TESIS DE LA UNIVERSIDAD
DE ZARAGOZA

2023

72

Abel Sancarlos González

Hybrid Twin in Complex System Settings

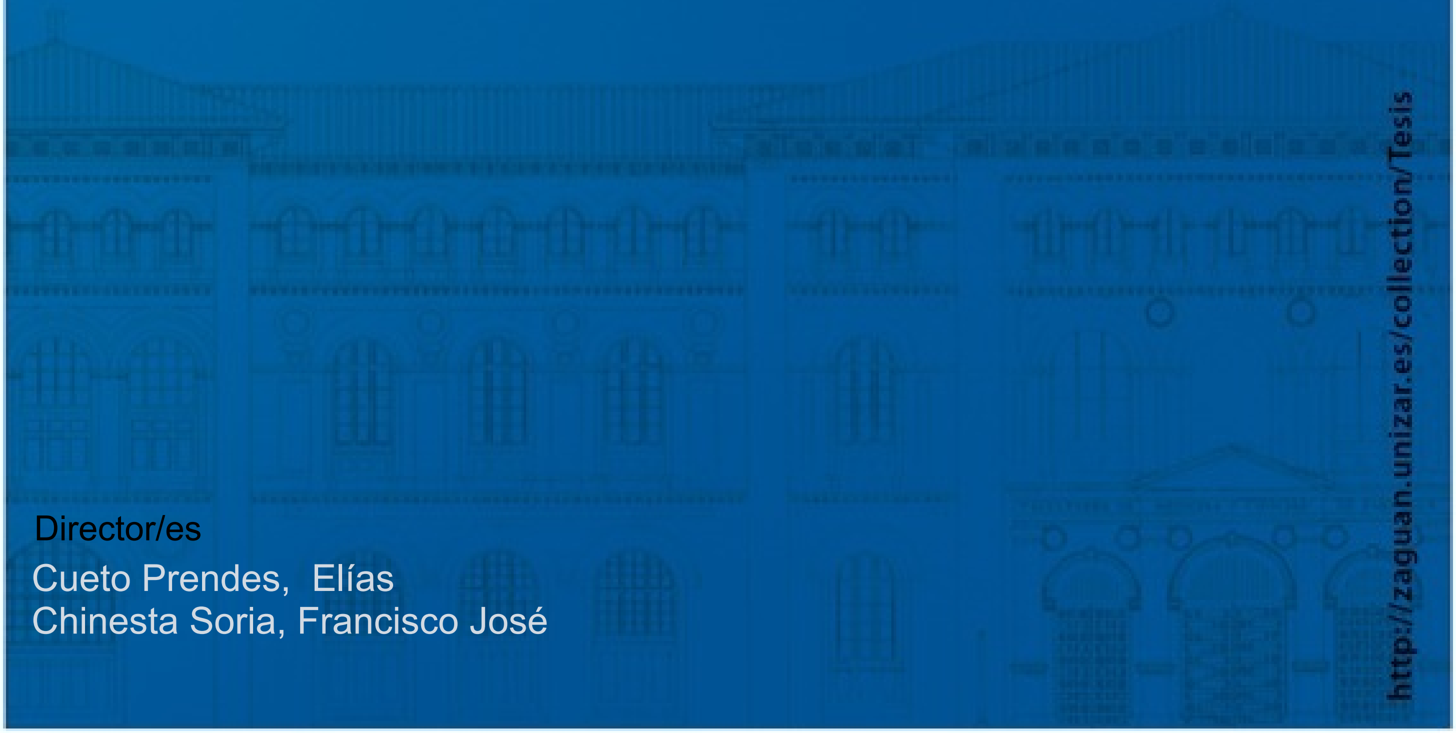

Director/es

Cueto Prendes, Elías
Chinesta Soria, Francisco José

ISSN 2254-7606

Prensas de la Universidad
Universidad Zaragoza

Servicio de Publicaciones

ISSN 2254-7606

Tesis Doctoral

HYBRID TWIN IN COMPLEX SYSTEM SETTINGS

Autor

Abel Sancarlos González

Director/es

Cueto Prendes, Elías
Chinesta Soria, Francisco José

UNIVERSIDAD DE ZARAGOZA
Escuela de Doctorado

2021

École Nationale Supérieure d'Arts et Métiers
Paris, France

Universidad de Zaragoza
Zaragoza, Spain

PHD THESIS

Hybrid Twin in Complex System Settings

Dissertation presented in fulfilment of the requirements for the degree of

PhD of the Universidad de Zaragoza
Doctor de la Universidad de Zaragoza

PhD of the ENSAM
Docteur de l'ENSAM

by
Abel SANCARLOS GONZALEZ

PhD Programme in Mechanical Engineering
September 2021

Doctoral Advisors:	Francisco CHINESTA	-	École Nationale Supérieure des Arts et Métiers
	Elías CUETO	-	Universidad de Zaragoza

Agradecimientos

Quiero dar las gracias, en primer lugar, a la persona que confió en mi desde un primer momento y que cimentó el camino para que yo me decidiera a realizar el doctorado: José Roger Folch. Muchísimas gracias por tu apoyo y tus consejos, tanto profesionales como personales, porque gracias a ti hoy en día soy una mejor persona.

También me gustaría dar las gracias a mis directores de tesis a quiénes puedo considerar mis padres científicos: Francisco Chinesta y Elías Cueto. Además de dirigir mi trabajo con gran sabiduría, han contribuido a formarme como persona y en animarme cuando más lo he necesitado. Su conocimiento y humor son tan extensos, que no sabría definir cuál es mayor. Creo que el entusiasmo científico, tanto de mis directores como el mío, ha hecho crear un clima maravilloso entre nosotros donde los avances científicos eran inevitables, pero donde, más importante, he estado muy a gusto. Quiero incluir también aquí a Emmanuelle Abisset-Chavanne, por acogerme durante mi estancia en Nantes, cuando apenas hablaba el idioma y orientarme en el nuevo país y equipo que me acogía.

Por otro lado, me gustaría también agradecer a la compañía ESI Group por confiar en este proyecto científico. Dentro de este grupo me gustaría hacer una especial mención a:

- A Anne Chambard y Jean Louis Duval, por su buen saber hacer como mis managers directos en la compañía.
- A Fatima Daim, Morgan Cameron, Mustapha Ziane tanto por su cálida bienvenida al grupo como por su ayuda dentro de la empresa, así como el magnífico ambiente que crearon cuando tuve la suerte de compartir mis experiencias con ellos. Mi estancia en ESI fue mucho mejor gracias a vuestra calidad humana.
- Isabelle Dugourd, por su apoyo constante e infinita amabilidad resolviendo y ayudándome en varios problemas burocráticos en el grupo.
- Al grupo de ESI - Nantes (Serge Laverdure, Jean-Sébastien Barreiro, Mokrane Hadj-Bachir, François-Xavier Jegaden y Mathias Ferraton) por su buena acogida en mi estancia en Nantes. También a Jean-Claude Kedzia y a Juliette Groulier por su buena acogida y profesionalidad en los proyectos en los que me vi involucrado con ellos.
- Al grupo de ESI-Hispania (Emilio Mencia, Carlos Terrés, Paula De Miguel, Juan Pedro Palacios, Monica Arroyo y Noelia Ballano) por su cálida y agradable acogida en mi estancia en Madrid.

- A Agathe Reille, que comenzó el doctorado conmigo y fue un gran pilar de apoyo al inicio de la aventura gracias a su simpatía y humor.

También me gustaría agradecer al equipo de la École Centrale de Nantes, en concreto al laboratorio del ICI por la buena acogida y trato que me dieron. Destacar a Luisa Silva, José Vicente Aguado, Domenico Borzacchiello, Kiran Sagar y José Manuel Navarro.

No dudaría en decir, que de lo mejor que me ha ocurrido durante el doctorado ha sido conocer gente de una calidad humana increíble y que me ha aportado experiencias que recordaré siempre dentro de mí. Entre estas personas, me gustaría hacer una mención **muy especial** a: Elena López, Carlos Sandino, Adrien Scheuer, Giacomo Quaranta, Clara Argerich, Rubén Ibáñez, Laura Oter y Ramiro Mena. Sin vosotros, este doctorado no hubiera sido lo mismo gracias a la buena atmósfera que se creó en el grupo y que prevaleció fuera de él, forjando una muy bonita relación de amistad. Además, agradeceré infinitamente vuestra inmensa ayuda en un momento muy delicado en la llegada a un nuevo país.

También me gustaría agradecer a Beatriz Moya y a Nicolas Hascoët. En concreto, me complacería destacar su infinita ayuda para hacer frente a los procesos burocráticos de sus respectivas universidades y su gran, agradable y apreciada compañía en los diferentes eventos científicos que hemos tenido la suerte de compartir y de disfrutar.

De la misma manera, querría dar las gracias a los amigos que he hecho durante el último año de doctorado: Víctor Champaney, Angelo Pasquale, Sevan Garois y Sergio Torregrosa.

De igual modo, me gustaría agradecer el apoyo de toda mi familia, especialmente de mis padres y mi hermana, por su apoyo, por su amor sin límite y porque no han dudado en confiar y creer en mí en ningún momento. También esta tesis va dedicada a mis abuelos, a los que no están y a Rosendo González, cuyo orgullo por su nieto espero que siga creciendo y que, pese a las circunstancias, me ha apoyado en todo como el que más.

Si hay a una persona a la que agradezco esta experiencia, más que a nadie, es a Anna Bueno. Sin ella, esto no hubiera sido posible y todo el documento aquí presente hubiera sido una mera elucubración. No hay tiempo ni dinero en el mundo (ni suficientes páginas en esta tesis) para expresar el amor y afecto que siento por ella. Esta aventura ha sido lo que ha sido gracias a ti y si esta tesis tiene una dedicatoria especial es la tuya.

De igual modo, quiero agradecer el apoyo de todos mis amigos. Agradezco también a los futuros lectores por tomarse el interés de leer este documento. Y si me dejo a alguien, también se lo agradezco. A todos, gracias de corazón,

Abstract

The benefits of a deep understanding of the technological and industrial processes of our world are unquestionable. Optimization, inverse analysis or simulation-based control are some of the procedures that can be carried out once the above knowledge is transformed into value for companies. This brings better technologies that end up greatly benefiting society. Think of a routine activity for many people today, such as taking a plane. All the above procedures are carried out in the plane design, on-board control and maintenance, culminating in a technologically resource-efficient product. This strong added value is what is driving Simulation Based Engineering Science (SBES) to make major improvements in these procedures, leading to noticeable breakthroughs in a wide variety of sectors (e.g. Healthcare, Telecommunications or Engineering, to cite only a few).

However, SBES is currently confronting several difficulties to provide accurate results in complex industrial scenarios. One is the high computational cost associated with many industrial problems which severely limits or even disables the key processes described above. Another problem is that in other applications, the more accurate (and also more highly-time consuming) models are not able to take into account all the details that govern the physical system under study, with observed deviations that seem to escape our understanding.

Therefore, in this context, novel numerical strategies and techniques are proposed throughout this manuscript to deal with the challenges that SBES is facing. To do that, different industrial scenarios are analyzed

The above panorama also brings a perfect opportunity to the so-called Dynamic Data Driven Application Systems (DDDAS), whose main objective is to merge classical simulation algorithms with data coming from experimental measures. This concept is envisaged thanks to the exhaustive development in Data Science. Within this scenario, data and simulations would no longer be uncoupled but rather they would form a symbiotic relationship which would achieve milestones inconceivable until these days. Indeed, data will no longer be understood as a static calibration of a given constitutive model but rather the model will be corrected dynamically as soon as experimental data and simulations tend to diverge.

For this reason, the present dissertation placed a particular emphasis on Model Order Reduction (MOR) techniques, as they are not only a tool to reduce computational complexity, but also a key element in meeting the real time constraints arising from the DDDAS framework.

Furthermore, this thesis presents new data-driven methodologies to enrich the so-called Hybrid Twin paradigm. A paradigm which is motivated because it makes DDDAS possible. How? by combining parametric solutions and the MOR framework with “on-the-fly” data-driven (i.e. machine learning) correction models.

Résumé

Les avantages d'une compréhension approfondie des processus technologiques et industriels de notre monde sont indiscutables. L'optimisation, l'analyse inverse ou le contrôle par simulation sont quelques-unes des procédures qui peuvent être mises en œuvre lorsque les connaissances susmentionnées sont transformées en valeur pour les entreprises. Il en résulte de meilleures technologies qui finissent par profiter grandement à la société. Pensez à une activité quotidienne pour de nombreuses personnes aujourd'hui, comme prendre l'avion. Toutes les procédures évoquées ci-dessus sont mises en œuvre dans la conception de l'avion, tel que le contrôle à bord et la maintenance, pour aboutir à un produit technologiquement efficace en termes de ressources. Cette forte valeur ajoutée est ce qui pousse les sciences de l'ingénieur basées sur la simulation (Simulation Based Engineering Science, SBES) à apporter des améliorations majeures à ces procédures, conduisant à des percées notables dans une grande variété de secteurs (comme par exemple la santé, les télécommunications ou l'ingénierie).

Cependant, les SBES sont actuellement confrontées à plusieurs difficultés pour fournir des résultats précis dans des scénarios industriels complexes. L'une d'elles est le coût de calcul élevé associé à de nombreux problèmes industriels, qui limite fortement, voire rend impossible, les processus clés décrits ci-dessus. Un autre problème apparaît dans d'autres applications, où les modèles plus précis (et aussi plus gourmands en temps) ne sont pas capables de prendre en compte tous les détails qui régissent le système physique étudié, avec des déviations observées qui semblent échapper à notre compréhension.

C'est pourquoi, dans ce contexte, de nouvelles stratégies et techniques numériques sont proposées tout au long de ce manuscrit pour relever les défis auxquels les SBES sont confrontées avec l'étude de différentes applications.

Le panorama ci-dessus offre également une opportunité parfaite pour les Dynamic Data Driven Application Systems (DDDAS), dont l'objectif principal est de fusionner les algorithmes de simulation classiques avec les données provenant de mesures expérimentales. Ce concept est envisagé grâce au développement exhaustif de la science des données. Dans ce scénario, les données et les simulations ne seraient plus découplées, mais formeraient une relation symbiotique qui permettrait d'atteindre des étapes inconcevables jusqu'à aujourd'hui. En effet, les données ne seront plus prises en compte pour un étalonnage statique d'un modèle constitutif donné, mais plutôt comme une correction dynamique dès que les données expérimentales et les simulations auront tendance à diverger.

C'est dans ce but que cette thèse met un accent particulier sur les techniques de réduction de modèles, car elles ne sont pas seulement un outil pour réduire la complexité de calcul, mais aussi un élément clé pour répondre aux contraintes de

temps réel découlant du cadre des DDDAS.

En outre, cette thèse présente de nouvelles méthodologies axées sur les données pour enrichir le paradigme dit des jumeaux hybrides. Un paradigme qui est motivé parce qu'il rend les DDDAS possible. Comment ? En combinant des solutions paramétriques et des techniques de réduction de modèles avec des corrections à la volée basés sur les données experimentales

Resumen

Los beneficios de un conocimiento profundo de los procesos tecnológicos e industriales de nuestro mundo son incuestionables. La optimización, el análisis inverso o el control basado en la simulación son algunos de los procedimientos que pueden llevarse a cabo una vez que los conocimientos anteriores se transforman en valor para las empresas. Con ello se consiguen mejores tecnologías que acaban beneficiando enormemente a la sociedad. Pensemos en una actividad rutinaria para muchas personas hoy en día, como coger un avión. Todos los procedimientos anteriores se llevan a cabo en el diseño del avión, en el control a bordo y en el mantenimiento, lo que culmina en un producto tecnológicamente eficiente en cuanto a recursos. Este alto valor añadido es lo que está impulsando a la Ciencia de la Ingeniería Basada en la Simulación (Simulation Based Engineering Science, SBES) a introducir importantes mejoras en estos procedimientos, lo que ha supuesto avances importantes en una gran variedad de sectores como la sanidad, las telecomunicaciones o la ingeniería.

Sin embargo, la SBES se enfrenta actualmente a varias dificultades para proporcionar resultados precisos en escenarios industriales complejos. Una de ellas es el elevado coste computacional asociado a muchos problemas industriales, que limita seriamente o incluso inhabilita los procesos clave descritos anteriormente. Otro problema es que, en otras aplicaciones, los modelos más precisos (que a su vez son los más caros computacionalmente) no son capaces de tener en cuenta todos los detalles que rigen el sistema físico estudiado, con desviaciones observadas que parecen escapar de nuestro conocimiento.

Por lo tanto, en este contexto, a lo largo de este manuscrito se proponen novedosas estrategias y técnicas numéricas para hacer frente a los retos a los que se enfrenta la SBES. Para ello, se analizan diferentes aplicaciones industriales.

El panorama anterior junto con el exhaustivo desarrollo producido en la Ciencia de Datos, brinda además una oportunidad perfecta para los denominados Dynamic Data Driven Application Systems (DDDAS), cuyo objetivo principal es fusionar los algoritmos clásicos de simulación con los datos procedentes de medidas experimentales. En este escenario, los datos y las simulaciones ya no estarían desacoplados, sino que formarían una relación simbiótica que alcanzaría hitos inconcebibles hasta estos días. Más en detalle, los datos ya no se entenderán como una calibración estática de un determinado modelo constitutivo, sino que el modelo se corregirá dinámicamente tan pronto como los datos experimentales y las simulaciones tiendan a diverger.

Por esta razón, la presente tesis ha hecho especial énfasis en las técnicas de reducción de modelos, ya que no sólo son una herramienta para reducir la complejidad computacional, sino también un elemento clave para cumplir con las

restricciones de tiempo real que surgen del marco de los DDDAS.

Además, esta tesis presenta nuevas metodologías basadas en datos para enriquecer el denominado paradigma *Hybrid Twin*. Un paradigma cuya motivación radica en su habilidad de posibilitar los DDDAS. ¿Cómo? combinando soluciones paramétricas y técnicas de reducción de modelos con correcciones dinámicas generadas “al vuelo” basadas en los datos experimentales recogidos en cada instante.

Contents

Introduction **1**

0.1 Context and Motivations 3
0.2 Objectives 12
0.3 Structure of the thesis 13
0.4 Scientific contributions 19
    0.4.1 Papers in international Journals 19
    0.4.2 Papers in German magazines 20
    0.4.3 Conference Proceedings 20
    0.4.4 International Conferences 20
    0.4.5 International ESI Conferences 21
    0.4.6 Batteries Europe Meetings 21
    0.4.7 Seminars given as a presenter 22
0.5 Scientific dissemination 22

I Fundamentals: Review of the main intrusive MOR techniques **23**

1 Advanced numerical techniques: intrusive Model Order Reduction techniques **25**

1.1 Introduction 26
1.2 Proper Orthogonal Decomposition 28
    1.2.1 Method of snapshots: Obtaining the POD basis 28
    1.2.2 POD reduced order models 30
1.3 Proper Generalized Decomposition 31
    1.3.1 Separated representation constructor 32
1.4 Summary 35

II Fundamentals: Presentation of novel non-intrusive and data-driven techniques. **37**

2 Novel reduced order formulations, algorithms and hybridation/dynamic techniques. **39**

2.1 Introduction 40
2.2 The Sparse Proper Generalized Decomposition 41
    2.2.1 Introduction 41
    2.2.2 s-PGD methodology: Basis of the technique 42

2.3 A novel sparse reduced order formulation: the s-PGD + RB strategy 44
2.4 A novel unwrapping algorithm for accurately addressing interpolation of complex numbers 47
2.4.1 Introduction to phase unwrapping 47
2.4.2 Proposed approach. Part I: Phase unwrapping in smooth parametric settings. 47
2.4.3 Proposed approach. Part II: Improving the robustness of phase unwrapping 51
2.4.4 Convergence 53
2.5 Novel hybridation and dynamic strategies 54
2.5.1 Introduction. 54
2.5.2 Hybrid Twins. The big picture. 55
2.5.3 An efficiently learning of dynamical systems: The stabilized DMD and DMDc techniques. 55
2.5.4 The DMD Dictionary strategy 59
2.6 Summary and Conclusions 61

3 Novel PGD strategies: PGD-based advanced nonlinear multiparametric regressions for constructing metamodels at the scarce-data limit. 63
3.1 Introduction 64
3.1.1 Chapter overview 64
3.1.2 Topic introduction 64
3.2 Regularized regressions: The regularized sparse PGD (rs-PGD) and the doubly sparse PGD (s^2-PGD) 68
3.2.1 Motivation 68
3.2.2 rs-PGD 69
3.2.3 s^2-PGD 71
3.3 The ANOVA-based sparse-PGD 72
3.3.1 Sensitivity analysis: Sobol coefficients 73
3.3.2 The *anchored* ANOVA 73
3.3.3 Combining the *anchored*-ANOVA with the sparse PGD 73
3.4 Results 74
3.4.1 Results for the rs-PGD approach 74
3.4.2 Checking the performances of s^2-PGD when addressing sparse solutions 76
3.4.3 ANOVA-PGD numerical results 81
3.5 Conclusions 84

III Industrial and Practical Applications 85

4 Advanced Multi-Parametric models for Electric Machines. 87
4.1 Introduction 89

- 4.1.1 Chapter overview 89
- 4.2 Multi-Parametric Electromagnetic Fields in Synchronous Machines by Using PGD-Based Fully Separated Representations 90
  - 4.2.1 Intrusive approach: Introduction 90
  - 4.2.2 Electromagnetic Equations 91
  - 4.2.3 Description of the Analyzed Motor 92
  - 4.2.4 PGD Physical Space Separated Solution 93
  - 4.2.5 PGD Parametric Solution 95
  - 4.2.6 Results 98
- 4.3 A novel sparse reduced order formulation for modeling electromagnetic forces in electric motors 104
  - 4.3.1 Non-intrusive approach: Introduction 104
  - 4.3.2 Analyzed motors 106
  - 4.3.3 Post-processing step. Computation of the radial force waves/magnetic pressure 107
  - 4.3.4 Reduced order model 109
  - 4.3.5 Results 109
- 4.4 Conclusions 126

5 Parametric electromagnetic analysis of radar based Advanced Driver Assistant Systems **129**
- 5.1 Introduction 130
  - 5.1.1 Chapter overview 130
  - 5.1.2 Topic introduction 130
- 5.2 Parametric Electromagnetic Fields 132
  - 5.2.1 Real-Imaginary Interpolation Versus Magnitude-Phase Interpolation 132
  - 5.2.2 Stratregy Proposed 133
- 5.3 Antena Modelling and Simulation Details 133
- 5.4 Results on the RADAR Problem 134
  - 5.4.1 Clarification. Phase Singularity 136
- 5.5 Conclusions 137

6 An aircraft Hybrid Twin: Learning stable reduced-order models for hybrid twins **139**
- 6.1 Introduction 140
  - 6.1.1 Chapter overview 140
  - 6.1.2 Topic introduction 140
- 6.2 System modeling 141
  - 6.2.1 Extracting the model of the system from scratch 141
  - 6.2.2 Enriching a physics-based model within the Hybrid Twin framework 142
- 6.3 Application to a dynamical system: The aircraft hybrid twin 142
  - 6.3.1 System to model and types of data. 142

6.3.2 Extracting a model from scratch using the GT data 143
6.3.3 Extracting a model from scratch using noisy data (PED). . . 151
6.3.4 Extracting the correction model. Hybrid Twin paradigm. . . 157
6.4 Conclusions 163

7 From ROM of electrochemistry to AI-based battery digital and hybrid twin 165
7.1 Introduction 167
7.1.1 Chapter overview 167
7.1.2 Topic introduction and chapter structure 168
7.2 Electrochemical model: Newman's P2D model 170
7.2.1 Newman's P2D model 170
7.2.2 Definitions of the State of Charge (SoC) 174
7.3 Solving Newman's P2D model 175
7.4 Proper Orthogonal Decomposition of the P2D model 176
7.4.1 Reasons to use the POD 176
7.4.2 POD of the electrochemical model 178
7.4.3 Results 180
7.5 PGD regression. Learning the cell behavior from data 184
7.5.1 Introduction 184
7.5.2 Proposed model 184
7.5.3 Results 187
7.6 Innovative planning algorithm with EV simulation and results 197
7.6.1 Introduction 197
7.6.2 Constructing a digital twin of the electric vehicle system . . . 197
7.6.3 Adapting driving behaviour in function of an accurate and fast computation of battery needs 202
7.6.4 Algorithm to select the best itinerary 210
7.6.5 BMS: cell balancing example 213
7.6.6 Summary results 216
7.7 Constructing a hybrid twin 216
7.7.1 Introduction 216
7.7.2 Dictionary Model for the Electrochemical Model: Correcting the gap 216
7.7.3 Results 218
7.8 Conclusions 228

Conclusions and Perspectives 229

A Translation of the Chapter on Conclusions and Perspectives 233
A.1 Conclusions et Perspectives 233
A.2 Conclusiones y perspectivas 236

B EM parameters **241**
B.1 Units 241
B.2 Induction motor 241
B.3 Synchronous machine. 242

C EM models **243**
C.1 Induction motor 243
C.2 Synchronous machine 244

D Nomenclature for the Electrochemical Model **245**

E Cell parameters and additional equations **247**

F Parameters used in the SimulationX model **249**

Bibliography **251**

List of Figures

1 Image of a crash test in the automotive industry. The image is property of the international company ESI group which authorised the diffusion in the present thesis. 4

2 Image of the simulation of a crash test in terms of passenger security. The image is property of the international company ESI group which authorised the diffusion in the present thesis. 4

3 Image of the haptic simulator developed with the Proper Generalized Decomposition (PGD) methodology. This simulator is able to provide the solution of a complex nonlinear mechanic problem one thousand times per second. Special thanks to the Applied Mechanics and Bioengineering group of the University of Zaragoza (specifically, Professor Elias Cueto) which authorised the diffusion of the image in the present thesis. 7

4 Image of the augmented reality environment developed with the methodology described in [Badías *et al.* 2020b]. Here, an augmented reality environment is set up where the mechanical interaction between real and virtual objects is computed in real-time with the precision of a high-fidelity solver (thanks to the MOR framework) but working at the speed of a video sequence. Special thanks to the Applied Mechanics and Bioengineering group of the University of Zaragoza (specifically, Dr. Alberto Badias and Professor Elias Cueto) which authorised the diffusion of the image in the present thesis. . . 9

5 Image of an augmented reality environment where the methodology described in [Moya *et al.* 2019, Moya *et al.* 2020a, Moya *et al.* 2021] is employed. The proposed method recognizes the precise type of fluid from video sequences and is able to predict future states of the dynamics for control and decision making. Note that MOR framework is employed to achieve real-time feedback. Special thanks to the Applied Mechanics and Bioengineering group of the University of Zaragoza (specifically, Bea Moya and Professor Elias Cueto) which authorised the diffusion of the image in the present thesis. 10

6 Figure to illustrate the Hybrid Twin (HT) concept. In this example, the Hybrid Twin (HT) is employed when trying to predict the variable y. Here, the Hybrid Twin (HT) response will be composed of the prediction of an accurate physics-based model, as well as the modeled on-line correction to delete the biased gap between measurements and predictions. As previously discussed, Reduced Order Models (ROMs) are used to run fast enough the accurate physics-based models. Note: MORT refers to model order reduction techniques 11

2.1 Approximating a unitary step function using global polynomials. In the first case, Chebyshev nodes are used to fit the polynomial. In the second case, equidistant nodes are used. 45
2.2 Example of successful phase unwrapping 47
2.3 Thought experiment: the function $y(x)$ is wanted to be unwrapped. Which of the possible blue points would you give as valid phase value for y_4? 48
2.4 Original wrapped function 49
2.5 Comparison of the proposed unwrapping procedure and the standard unwrapping function implemented in Matlab, in a coarse mesh consisting of 15 nodes. 50
2.6 Comparison of the proposed procedure and the Matlab unwrapping function in a coarse mesh consisting of 15 nodes with the $1/k_f$ factor 20% higher 50
2.7 Comparison of the proposed procedure and the Matlab unwrapping function in a coarse mesh consisting of 15 nodes with the $1/k_f$ factor 50% higher 51
2.8 Comparison of reduced-basis based unwrapping versus second derivative minimization based unwrapping on a test case exhibiting fast variations of the phase 53
2.9 Evolution of the phase error with the parameter sampling refinement. 54

3.1 Non-intrusive MOR techniques with the main sampling and approximation features, their pros (emphasized in the green text) and the cons (in red). 67
3.2 Comparing the reference (Eq. (3.22)) and its associated s-PGD and rs-PGD regressions, at points $(x_1, x_2, x_3 = 0, x_4 = 0, x_5 = 0.7071)$ . . 75
3.3 Comparing the reference (Eq. (3.22)) and its associated s-PGD and rs-PGD regressions, at points $(x_1, x_2, x_3 = -0.17069, x_4 = -0.17069, x_5 = -0.015517)$ 75
3.4 True dynamics and dynamics identified by the rs-PGD model 77
3.5 Comparison between rs-PGD predictions and true dynamics on the three-variable time evolution. 77
3.6 Plot of the original function and the training set (circles) used to construct the PGD models. 79

3.7 Problem defined in Eq. (3.24): Comparison of predicted s-PGD values with the reference ones in the testing set (the black line represents a perfect prediction) 79
3.8 Problem defined in Eq. (3.24): Comparison of predicted s^2-PGD values with the reference ones in the testing set (the black line represents a perfect prediction) 80
3.9 Problem defined in Eq. (3.25): Comparison of predicted s-PGD values with the reference ones in the testing set (the black line represents a perfect prediction) 81
3.10 Problem defined in Eq. (3.25): Comparison of predicted s^2-PGD values with the reference ones in the testing set (the black line represents a perfect prediction) 82
3.11 Comparing s-PGD and ANOVA-PGD regressions 82
3.12 Problem defined in Eq. (3.26): Comparison of predicted s-PGD values with the reference ones in the testing set (the black line represents a perfect prediction) 83
3.13 Problem defined in Eq. (3.26): Comparison of predicted ANOVA-PGD values with the reference ones in the testing set (the black line represents a perfect prediction) 83

4.1 Electric machine to simulate. The green arrow in the permanent magnets indicates the magnetization direction. 93
4.2 Mapping from the original geometry into the calculation one. 94
4.3 Fully separable domain used to compute the PGD solution laking use of the mapping detailed in Equations (4.9) and (4.10). 94
4.4 The integer values of the new s coordinate are placed in the positions shown in the figure. 95
4.5 The $h_i(t)$ functions are used to render separable the original non-separable geometries. 95
4.6 Illustration of $\phi_i^I(s)$ functions involved in Equation (4.14). 97
4.7 Illustration of functions $\psi_1^I(t)$ and $\psi_2^I(t)$ involved in Equation (4.14). 98
4.8 Functions $\phi_i^{II}(s)$ involved in Equation (4.15). 98
4.9 *Cont.* 100
4.9 Solution A_z for different combinations of the input parameters i_a, i_b, i_c, B_r and ρ. 100
4.10 Magnetic vector potential A_z in a section of the motor for $i_a = 1.5$ A, $i_b = 1.5$ A, $i_c = -3$ A, $B_r = 1.01$ T and $\rho = 0°$. 101
4.11 Relative error considering the PGD and the FEMM solution for the case $(s, t) \in$ (air gap), $i_a = i_b = i_c = 0$ A, $B_r = 1.01$ T, $\rho = 0$ (initial position). 101
4.12 Relative error considering the PGD and the FEMM solution for the case $(s, t) \in$ (air gap), $i_a = -1.5$ A, $i_b = 3$ A, $i_c = -1.5$ A, $B_r = 1.01$ T, $\rho = 0$ (initial position). 102

4.13 Relative error considering the PGD and the FEMM solution for the case $(s, t) \in$ (air gap), $i_a = i_b = i_c = 0$ A, $B_r = 1.01$ T, $\rho = 10$ deg. . 102
4.14 Magnetic pressure computed with the PGD solution for the case of Figure 4.11. 103
4.15 Fast Fourier Transform of the magnetic pressure depicted in Figure 4.14. 103
4.16 Conversion of electric energy into acoustic energy. 105
4.17 Induction motor geometry. 107
4.18 Synchronous machine: Complete geometry drawn in FEMM software. 108
4.19 Comparison between the s-PGD and FEMM model (linear B-H relationship) for the parameters $f = 40$ Hz, $s = 2.5$ %, $I_p = 3$ A, $f_h = 5 \cdot 40$ Hz, $s_h = 80.50$ %, $I_{ph} = 3/5$ A, $\gamma = 1$ degree 111
4.20 Alternating force components obtained with the parameters $f = 40$ Hz, $s = 2.5$ %, $I_p = 3$ A, $f_h = 5 \cdot 40$ Hz, $s_h = 80.50$ %, $I_{ph} = 3/5$ A, $\gamma = 1$ degre (linear B-H model). 112
4.21 Relative error of the s-PGD model (linear B-H relationship) to determine the real part of B_n for different untrained $\mathbf{z}_i$. Error criteria of Eq. (4.26) is used. 113
4.22 Relative error of the s-PGD model (linear B-H relationship) to determine the imaginary part of B_n for different untrained $\mathbf{z}_i$. Error criteria of Eq. (4.26) is used. 113
4.23 Comparison between the s-PGD and FEMM model (nonlinear B-H relationship) for a $\mathbf{z}_i$ belonging to the training set. Parameters $f = 10.4772$ Hz, $s = 5$ %, $I_p = 3.3858$ A, $\sigma = 47.6537$ MS/m, $\delta = 0.4876$ mm, $\gamma = 0$ degrees. The alternating force obtained during the post-processing step is also shown. 115
4.24 Comparison between the s-PGD and FEMM model (nonlinear B-H relationship) for a $\mathbf{z}_i \notin \mathcal{T}$. Parameters $f = 50$ Hz, $s = 3$ %, $I_p = 3.5$ A, $\sigma = 40$ MS/m, $\delta = 0.5$ mm, $\gamma = 0$ degrees. The alternating force obtained during the post-processing step is also shown. 116
4.25 Relative error of the s-PGD model (nonlinear B-H relationship) to determine the real part of B_n for different untrained $\mathbf{z}_i$. Error criteria of Eq. (4.26) is used. 117
4.26 Relative error of the s-PGD model (nonlinear B-H relationship) to determine the imaginary part of B_n for different untrained $\mathbf{z}_i$. Error criteria of Eq. (4.26) is used. 118
4.27 Sketch to visualize the parameters O_s, O_w, O_r and D_{O_s,O_r} 119
4.28 Induction obtained with the s-PGD model for the parameters: $\gamma = 0$ degrees, $I_p = 3$ A, $\tau = \pi/2$ rad, $\rho = 0$ 120
4.29 Radial force wave obtained with the s-PGD model for a set of parameters: $\gamma = 0$ degrees, $I_p = 13$ A, $\tau = \pi/2$ rad, $\rho = 0.5$ 120
4.30 Time evolution of the magnetic pressure wave obtained with the s-PGD supposing $N = 2000$ rpm. Set of parameters: $\gamma = 0$ degrees, $I_p = 13$ A, $\tau = \pi/2$ rad, $\rho = 0.5$ 121

4.31 Comparison between s-PGD and FEMM results. Set of the parameters (Top plot): $\gamma = 0$ degrees, $I_p = 3$ A, $\tau = \pi/2$ rad, $\rho = 0$. Set of the parameters (Bottom plot): $\gamma = 0$ degrees, $I_p = 13$ A, $\tau = \pi/2$ rad, $\rho = 0.5$. 122
4.32 Sensitivity of B_n and P_n for small changes in I_p. Operating point: $\gamma = 0$ degrees, $I_p = 0.5$ A, $\tau = \pi/2$ rad, $\rho = 0$. 123
4.33 Sensitivity of B_n and P_n for small changes in D_{O_s,O_r}. Operating point: $\gamma = 0$ degrees, $I_p = 0.5$ A, $\tau = \pi/2$ rad, $\rho = 0$. 124
4.34 Sensitivity of B_n and P_n for small changes in I_p. Operating point: $\gamma = 0$ degrees, $I_p = 20$ A, $\tau = \pi/2$ rad, $\rho = 0$ 124
4.35 Sensitivity of B_n and P_n for small changes in D_{O_s,O_r}. Operating point: $\gamma = 0$ degrees, $I_p = 20$ A, $\tau = \pi/2$ rad, $\rho = 0$. 125
4.36 Sensitivity of P_n (the modulus of the alternating component) for small changes in the parameters shown in the plot. The operating point is $f = 50$ Hz, $\gamma = 0$ degrees, $I_p = 3$ A, $s = 2.5$ %, $\sigma = 34.45$ MS/m, $\delta = 0.375$ mm. The region explored is $\alpha \in [22.2, 53.8]$ deg. is explored. 126

5.1 Example to illustrate the differences between Real-Imaginary and Magnitude-Phase interpolation. 132
5.2 Real and imaginary parts (top left and right respectively), magnitude and phase of E_z (bottom left ad right respectively) as a function of θ in one point of the geometry. 133
5.3 Radar antenna and radome. 134
5.4 Mean absolute error on the phase (°) of the E_z component over each patch of the antenna using the proposed method. 135
5.5 Mean absolute error on the phase (°) of the H_y component over each patch of the antenna using the proposed method. 135
5.6 Mean absolute error on the phase (°) of the E_z component over each patch of the antenna using the classical unwrapping algorithm. . . . 135
5.7 Mean absolute error on the phase (°) of the H_y component over each patch of the antenna using the classical unwrapping algorithm. . . . 136
5.8 Example of a smooth parametric curve on the complex plane (**left**) and the phase as a function of the parameter (**right**). 136

6.1 Comparison of the state evolution $\mathbf{z}(t) = [p_1, p_2, T_1, T_2, T_3, T_4, T_5, T_6]$ for a given flight between the Coarse model (CM) and the Ground truth (GT) 144
6.2 Comparison of the system evolution, $\mathbf{z}(t) = [p_1, p_2, T_1, T_2, T_3, T_4, T_5, T_6]$, for a given flight between the Ground truth (GT) and the pseudo-experimental (noisy) data, PED 145
6.3 Diagram illustrating the inputs and the state vector of the proposed DMDc model to reproduce the pruned data of the system. 145

6.4 Prediction of the GT data using the proposed technique for a flight which is not used in the training set. “GT" refers to GT data series described in Section 6.3.1 and “Pred" refers to the stabilized DMDc model obtained with the proposed approach discussed in Section 2.5.3 147

6.5 Error in the prediction of T_3, T_4, T_5 and T_6 for different flights which are not in the training set. The prediction error in variables T_5 and T_6 is higher than the other ones due to their fast time evolution . . . 148

6.6 Error in the prediction of p_1, p_2, T_1 and T_2 of the proposed technique for lights which are not in the training set 149

6.7 Error in the prediction of T_3 and T_4 of the proposed technique for flights which are not in the training set 150

6.8 GT data for the example in Section 6.3.2.2 152

6.9 Prediction $\mathbf{z}(t) = [p_1, p_2, T_1, T_2, T_3, T_4, T_5, T_6]$ of the GT obtained through DMDc. This prediction tries to reproduce the flight of Figure 6.8 but fails to provide with stable results 153

6.10 Comparison between the reference dynamics of Figure 6.8 and the prediction of the modified, stable DMDc model. Huge improvements are observed when comparing with Figure 6.9. The state vector of the system is $\mathbf{z}(t) = [p_1, p_2, T_1, T_2, T_3, T_4, T_5, T_6]$ 154

6.11 Comparison between the model obtained from scratch using PED data and the PED data itself. In this figure, the reconstruction of a flight contained in the training set is shown. “PED" refers to the pseudo-experimental data with noise described in Section 6.3.1 and “Pred" refers to the stabilized DMDc model obtained with the proposed approach discussed in Section 2.5.3. It can be observed that an excellent agreement is obtained for every variable while filtering the noise 155

6.12 Comparison between the model obtained from scratch using PED data and the PED data itself. In this figure, the reconstruction of a flight which is not contained in the training set is shown. “PED" refers to the pseudo-experimental data with noise described in Section 6.3.1 and “Pred" refers to the stabilized DMDc model obtained with the proposed approach discussed in Section 2.5.3. It can be observed that a good agreement is obtained for all the variables with the exception of T_5 and T_6 156

6.13 Diagram illustrating the HT concept. The HT is able to correct the discrepancy between the coarse model (CM) and the pseudo-experimental data (denoted by a superscript m, that is, the PED). Its prediction is here denoted by a superscript HT whereas the enrichment model is denoted by Δz. Note that z^m can be filtered to have a better estimate of the GT when applying the HT approach. 158

6.14 Prediction of the HT approach considering a flight in the testing set. “PED" refers to the pseudo-experimental data with noise described in Section 6.3.1 and “HT Pred" refers to the HT approach whose correction term corresponds to a stabilized DMDc model obtained with the methodology discussed in Section 2.5.3. The correction term was constructed using the PED. It can be observed that an excellent agreement is obtained for all the variables 159
6.15 Error of the HT approach (blue line) considering a flight which is not used for the training. The red line refers to the maximum error in the pseudo measurements (PED). The error criterion is defined in Eqs (6.11) (blue line) and (6.12) (red line) 160
6.16 Error of the HT approach (blue line) considering different flights which are not used for the training. The red line refers to the maximum error in the pseudo measurements. The error assigned to a flight is the mean value of the error defined in Eq. (6.11) 161
6.17 Sine wave with noise. In the plot, the maximum variation of the signal is indicated as well as the deviation caused by the noise to illustrate the concept used to define the error criterion 162

7.1 Schematic of electrochemical cell model with coupled solid diffusion submodel. 171
7.2 Schematic of the P2D model. 171
7.3 Detail of the solid diffusion submodel. The path of electrons and the graphs of $c_s(r)$ showed are the ones for the discharging process . . . 172
7.4 Scheme to solve the electrochemical model. 176
7.5 Improved scheme to solve the electrochemical model. 177
7.6 Reference mesh to obtain the finite difference formula when the spatial step changes. 180
7.7 Simulation of the reduced order model for the first cell. Comparison of the evolution in time between the POD model and the original, full-order electrochemical mode, of the different variables of the cell. The different SoC and cell voltages are compared and the input current used during the simulation is shown in the last picture. Legend: RM = Results of the full P2D model; POD = Results of the POD model. 181
7.8 Comparison of full- and reducer-order simulations of the second cell. . The different SoC and the cell voltage are compared and the input current used during the simulation is shown in the last picture. Legend: RM = Results of the full P2D model; POD = Results of the POD model. 182
7.9 Comparison of the reduced-order results with those provided by the software LIONSIMBA for the second cell. 183
7.10 Construction of a piece-wise linear intensity as a function of time. . . 185

7.11 Model of the parameterized interval. One regression is performed for each output. We will take for each output, the inputs which give us the best results. Here, subscript i refers to input values, while subscript o means output. Variable i refers to the current and the variable V refers to the voltage. 186
7.12 Comparison of the results between the s-PGD model and the POD model in a 5 minute itinerary. The s-PGD model is extracted based on itineraries of 5 minutes. $\Delta t = 15s$. 188
7.13 Error between the s-PGD model and the POD model in a 5 minute itinerary. The s-PGD model is extracted based on itineraries of 5 minutes. $\Delta t = 15s$ 189
7.14 Comparison of the results between the s-PGD model and the POD model in a 10 minute itinerary. The s-PGD model is extracted based on itineraries of 5 minutes. $\Delta t = 15s$ 190
7.15 Error between the s-PGD model and the POD model in a 10 minute itinerary. The s-PGD model is extracted based on itineraries of 5 minutes. $\Delta t = 15s$ 191
7.16 Comparison of the results between the s-PGD model and the POD model in a 10 minute itinerary. The s-PGD model is extracted based on itineraries of 10 minutes. $\Delta t = 5s$ 192
7.17 Error between the s-PGD model and the POD model in a 10 minute itinerary. The s-PGD model is extracted based on itineraries of 10 minutes. $\Delta t = 5s$ 193
7.18 Comparison of the results between the s-PGD model and the POD model in a 10-minute itinerary (critical SoC and c_e^{avg}). The s-PGD model is extracted based on itineraries of 10 minutes. $\Delta t = 2s$. . . . 195
7.19 Error between the s-PGD model and the POD model in a 10 minute itinerary (critical SoC and c_e^{avg}). The s-PGD model is extracted based on itineraries of 10 minutes. $\Delta t = 2s$. 196
7.20 Diagram showing the data flow for the s-PGD model when embedding in a SimulationX model. 198
7.21 Picture of the itinerary simulated by the SimulationX EV model. It corrsponds to a ten-minute itinerary between Avenida de Valencia, E-46891 El Palomar and Plaza Barranc Marques, E-46890 Agullent, both in Spain. 199
7.22 Velocity(position) of the itinerary 200
7.23 Velocity response demanded by the driver 201
7.24 Graphical view of the EV model created in SimulationX. In the red circle, the battery box created with the s-PGD solution is highlighted 202
7.25 Parameters of the SimulationX model created using the s-PGD solution 203
7.26 Cell voltage predicted by the s-PGD model during the simulated itinerary. 204
7.27 Voltage drop produced by the internal resistance in a cell during the simulated. itinerary 204

7.28 Comparison between the bulk SoC and the surface SoC in the ten-minute itinerary. 205
7.29 Comparison between the critical SoC and the c_e^{avg} in the negative electrode during the simulated itinerary. 205
7.30 Smoothing procedure of the reference driving cycle taken by the control $v(s)$ when high discharge/charge rates happens when accelerating. This is used by the second step (See Algorithm 2) of the general procedure to adapt the driving cycle. $v(s)$ and α refers to the values before the modification and $v'(s)$ and α' refers to the values after the modifciation. 207
7.31 In red: example itinerary taken for Section 7.6.3. It is also the example itinerary (number one) taken for Section 7.6.4 209
7.32 Initial reference speed for the example of Section 7.6.3. The SimulationX model translates the reference $v(s)$ to $v(t)$. It is important to note that this is not the real speed of the EV but the reference one taken by the control. We start with this type of reference curves to minimize the travel time. If problems arise, the smooth procedure is applied. 209
7.33 Reference speed after applying the algorithm of Section 7.6.3. Note that the SimulationX model translates the reference $v(s)$ to $v(t)$. . . 210
7.34 Time evolution of the surface (green line) and bulk (red line) SoC when taking speed curve of Figure 7.32. 211
7.35 Time evolution of the surface (green line) and bulk (red line) SoC when taking the modified speed curve of Figure 7.33. 211
7.36 In red: example itinerary (number two) taken for Section 7.6.4. . . . 212
7.37 In red: example itinerary (number three) taken for Section 7.6.4. . . 212
7.38 Diagram of the cell balancing strategy employed in Section 7.6.5. . . 213
7.39 Balancing of the cells during charging. In this figure, the bulk SoC of the two types of unbalanced cells is shown. After approx. 770 s, the cells are balanced. The charging is done using a constant current profile. 214
7.40 Balancing of the cells during charging. In this figure, the voltage of the two types of unbalanced cells is shown. The voltage of both blocks is equalised after the balancing process is finished. The charging is done using a constant current profile. 215
7.41 Diagram of the approach used to apply the DM for the battery model. 217
7.42 Voltage error of using the model extracted through the DM for 38 trajectories (without any on-line correction). The first ten trajectories correspond to the training set. The transition between the training set and the not-trained trajectories is highlighted with a red line . . 219
7.43 SoC error of using the model extracted through the DM for 38 trajectories (without any on-line correction). The first ten trajectories correspond to the training set. The transition between the training set and the not-trained trajectories is highlighted with a red line . . 220

7.44 Comparison of the results between the P2D model and the DM model for trajectory number 30. Here, the on-line correction term is not used. 221
7.45 Comparison of the results between the P2D model and the DM model for trajectory number 30. Here, the on-line correction is used. To update the on-line dictionary we impose the criteria to limit the maximum error to 0.65 % for the voltage. The vertical lines in the correction event plot indicate when the correction event happens. . . 222
7.46 The DM with on-line correction reacts in a region for which the model is not prepared. Results are shown for the voltage during a trajectory with an initial SoC of 85 % (not initially considered in the training set). To update the on-line dictionary, we imposed the criteria to limit the maximum error to 0.5 % for the voltage. 223
7.47 The DM with on-line correction reacts to a region in which the model is not prepared. Here we can see the results for the SoC for a trajectory with an initial SoC of 85 % (not trained for this scenario). To update the on-line dictionary we imposed the criteria to limit the maximum error to 0.035 % for the SoC. 224
7.48 The DM with on-line correction reacts to another trajectory with an initial SoC of 85 %. We can see that no correction is needed for the voltage in this second trajectory due to the on-line learning of the first one (Fig. 7.46). To update the on-line dictionary we imposed the criteria to limit the maximum error to 0.5 % for the voltage . . . 225
7.49 Number of corrections needed for different trajectories with an initial SoC of 85 % (for which the original model is not trained). To update the on-line dictionary we imposed the criteria to limit the maximum error to 0.035 % for the SoC and to 0.5 % for the voltage. 226
7.50 Number of corrections needed for different trajectories with an initial SoC of 42.7 % (for which the original model is not trained). To update the on-line dictionary we imposed the criteria to limit the maximum error to 0.035 % for the SoC and to 0.5 % for the voltage. 227

+

List of Tables

3.1 Initial rs-PGD model for $\dot{x}$ 78

7.1 Predictions for the example of Section 7.6.4 211

B.1 Table: units 241

D.1 Table: nomenclature 246

E.1 Table: cell parameters 247

F.1 Table: SimX parameters 249

Acronyms

ADAS Advanced Driver Assistant Systems

AI Artificial Intelligence

BMS Battery Management Systems

BVP boundary value problem

DDDAS Dynamic Data Driven Application Systems

DMD Dynamic Mode Decomposition

DMDc Dynamic Mode Decomposition with control

DoE Design of Experiments

EM Electric Motor

EV Electric Vehicle

FDM finite difference method

FEM finite element method

FVM finite volume method

HPC High Performance Computing

HT Hybrid Twin

ML Machine Learning

MOR Model Order Reduction

NVH noise vibration and harshness

PDEs Partial Differential Equations

PGD Proper Generalized Decomposition

POD Proper Orthogonal Decomposition

ROM reduced order model

ROMs Reduced Order Models

SBES Simulation Based Engineering Science

SSL Sparse Subspace Learning

Introduction

Abstract The benefits of a deep understanding of the technological and industrial processes of our world are unquestionable. Optimization, inverse analysis, simulation-based control or uncertainty propagation are some of the procedures that can be carried out once the above knowledge is transformed into value for companies and industries. This brings new technologies and better products that end up greatly benefiting society. Think of a routine activity for many people today, such as taking a plane. All the above procedures are carried out in the plane design, construction, on-board control and maintenance, culminating in a technologically resource-efficient product. This strong added value is what is driving Simulation Based Engineering Science (SBES) to make major improvements in these procedures, leading to noticeable breakthroughs in a wide variety of sectors and industries (e.g. Healthcare, Telecommunications or Engineering, to cite only a few).

However, SBES is currently confronting several difficulties to provide accurate results in complex industrial scenarios. One is the high computational cost associated with many industrial problems which severely limits or even disables the key processes described above. Another problem is that in other applications, the more accurate (and also more highly-time consuming) models are not able to take into account all the details that govern the physical system under study, with observed deviations that seem to escape our understanding.

Therefore, in this context, novel numerical strategies and techniques are proposed throughout this manuscript to deal with the challenges that SBES is facing. To do that, different industrial scenarios are analyzed

The above panorama also brings a perfect opportunity to the so-called Dynamic Data Driven Application Systems (DDDAS), whose main objective is to merge classical simulation algorithms with data coming from experimental measures in a dynamic way. This type of concepts can be envisaged thanks to the exhaustive development in both data-acquisition and data-storage systems as well as the unceasingly growing interest in concepts such as Big-Data, Machine Learning or Data-Analytics. Within this scenario, data and simulations would no longer be uncoupled but rather they would form a symbiotic relationship which would achieve milestones inconceivable until these days. Indeed, data will no longer be understood as a static calibration of a given constitutive model but rather the model will be corrected dynamically as soon as experimental data and simulations tend to diverge.

For this reason, the present dissertation placed a particular emphasis on Model Order Reduction (MOR) techniques, as they are not only a tool to reduce computational complexity, but also a key element in meeting the real time constraints arising from the DDDAS framework.

Furthermore, this thesis presents new data-driven methodologies to enrich the so-called Hybrid Twin paradigm. A paradigm which is motivated because it makes DDDAS possible. How? by combining parametric solutions and the MOR framework with "on-the-fly" data-driven (i.e. machine learning) correction models.

Contents

0.1 Context and Motivations 3

0.2 Objectives 12
0.3 Structure of the thesis 13
0.4 Scientific contributions 19
    0.4.1 Papers in international Journals 19
    0.4.2 Papers in German magazines 20
    0.4.3 Conference Proceedings 20
    0.4.4 International Conferences 20
    0.4.5 International ESI Conferences 21
    0.4.6 Batteries Europe Meetings 21
    0.4.7 Seminars given as a presenter 22
0.5 Scientific dissemination 22

0.1 Context and Motivations

Simulation Based Engineering Science (SBES) [Panel 2006] has pushed the field of computer simulation into a new era [Ibanez Pinillo 2019]. In fact, this discipline, which contains branches such as High Performance Computing, mathematical modeling or computational algorithms, has carried out major improvements in areas of industrial interest like optimization, multi-scale modelling, control and inverse analysis. These remarkable breakthroughs have been developed and applied in a wide variety of sectors such as engineering, automotive and aeronautics industries, healthcare or augmented reality, to cite only a few. However, despite the great success of SBES in a wide variety of fields, it currently faces several difficulties in providing accurate results in complex industrial problems. Therefore, this thesis proposes solutions to some of these problems as well as novel tools that will improve the performance and capabilities of the potential solutions to deal with challenging scenarios.

Specifically, the thesis context is framed within the advances in numerical simulation and data science. For this reason, the Model Order Reduction (MOR) framework as well as the concepts of virtual, digital, and hybrid twins[1] will now be briefly reviewed, while introducing the improvements, advances and challenges that have led to the emergence of each technology.

First of all, special mention should be made of numerical simulation. Indeed, numerical simulation constitues one of the three pillars of 20th century engineering, producing the age coined as the *third paradigm* of science [Hey *et al.* 2009, Chinesta *et al.* 2020]. Among the numerous numerical techniques; finite element, finite volume and finite difference techniques [Patankar 1980, Ida & Bastos 1992, Fish & Belytschko 2007] are worth mentioning as, among other things, they are still widely used nowadays. Although they differ in many technical aspects, their common goal is to transform a given set of Partial Differential Equations (PDEs) which describe a physical system into a discrete system of algebraic equations that is perfectly understandable by a computer. And it was this process of making the mathematical models understandable to computers that caused the revolution of “virtual twins”. In this revolution, the “virtual twins” are numerical simulations which emulate a physical system employing mathematical models to describe its complex behavior.

Nowadays, virtual twins are present in most scientific and engineering fields, allowing accurate designs and virtual evaluation of system responses, drastically reducing the number of experimental tests [Chinesta *et al.* 2020]. For instance, to illustrate an industrial scenario, imagine a crash test of a vehicle (See Figures 1 and 2). This test is a form of destructive testing usually performed in order to ensure safe design standards in examining, for instance, the ability of a structure to protect its occupants during an impact. Without virtual twins, an entire vehicle must be designed, built and destroyed for every test you want to run. As you can imagine this is extremely expensive. Fortunately, virtual twins come to the rescue, greatly reducing the number of experimental tests and consequently the costs for the company, which will generally only “destroy” the final design.

---

[1] There seems to be no consensus on the definition of the concepts of virtual, digital and hybrid twins. In this thesis, one possible distinction is suggested according to the references employed to write the manuscript as well as their respective characteristics. It is not the sole possibility and it is not intended to create any controversy in this respect.

Figure 1 – Image of a crash test in the automotive industry. The image is property of the international company ESI group which authorised the diffusion in the present thesis.

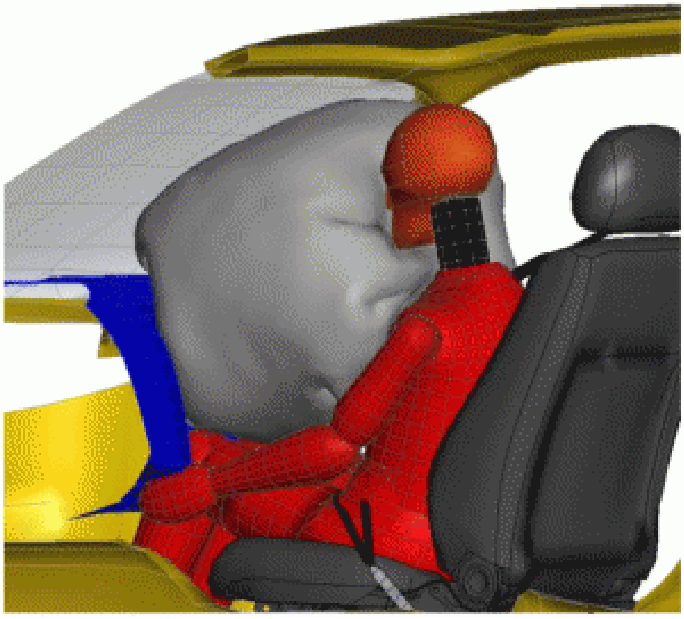

Figure 2 – Image of the simulation of a crash test in terms of passenger security. The image is property of the international company ESI group which authorised the diffusion in the present thesis.

Nevertheless, virtual twins have a disadvantage. Before solving a given problem, the different involved parameters must be introduced and the problem domain defined. Once the problem is solved, the different quantities of interest can be then computed. What does the above mean? It means that virtual twins are static [Quaranta 2019]: they are employed in the design of complex systems as well as their components, but they cannot accomodate or assimilate data in order to define Dynamic Data-Driven Application Systems (DDDAS) [Darema 2015]. Moreover, they rarely allow real-time feedback required in some applications on account of the characteristic time of standard simulation techniques. Furthermore, important industrial procedures such as optimization, inverse analysis or uncertainty propagation require enhancing the efficiency and computational cost of usual strategies because of the many direct calculations needed.

To alleviate some of the limitations, for instance, transfer functions are usually employed to achieve real-time control using an adapted representation of the system, appropriately relating inputs and outputs. Although these methods guarantee real time, their modelling of the system is too coarse compared to rich representations such as those carried out, for example, by finite elements (e.g. a 3D transient problem), which enable high-fidelity simulations. Nevertheless, as previously introduced, these rich modelling frameworks, perfectly valuable, for instance, for the system understanding; do not allow real-time on common computational platforms or deployed systems. And as mentioned earlier, they often do not have a computational cost or speed suitable enough for industrial interests such as optimisation or inverse analysis.

In this context, industry's desire for new simulation tools, as well as the need to speed up calculations, led to the birth of novel system modelling and simulation methodologies at the beginning of the 21st century. Here, one of major achievements are the model order reduction (MOR) techniques [Quaranta 2019, Ibanez Pinillo 2019, Chinesta *et al.* 2017]. In particular, they opened new possibilities to reach more efficient simulations. The MOR techniques which are being introduced here are called intrusive[2]. It is worth mentioning that when these intrusive MOR techniques are successfully applied to physics-based models, they continue to be well established and validated descriptions at hand. In fact, they act by simplifying the solution procedure without practically any sacrifice in the model solution accuracy, in view of accomodating accurate and fast (and in many cases real-time) predictions [Zlotnik *et al.* 2015, Chinesta *et al.* 2017, Quesada *et al.* 2018, Chinesta *et al.* 2020].

To illustrate the possibilities, two alternatives of the intrusive MOR framework are going to be described.

The first one consists in extracting off-line the most significant modes involved when expressing the model solution[3]. To do that, standard simulation methodologies are employed to see the main characteristics of the function. Then, the sought solution of similar problems is projected on that reduced space. And this is the key point, as the number of functions involved in the basis of the reduced space is usually low, just a few coefficients need to be computed for obtaining the problem solution. Therefore, at each iteration or time step, a discrete problem of very small size has to be solved instead. This way, this type of MOR techniques allow important time savings, of several orders of magnitude in some cases, making possible in several industrial scenarios to accomodate real-time constraints [Sempey *et al.* 2009, Ghnatios *et al.* 2012b, Chinesta & Ladevèze 2014, Nadal *et al.* 2015a, Chinesta *et al.* 2017].

On the other hand, the other common alternative is to compute a parametric solution,

---

[2] Chapter 1 will explain in detail the reason for this name as well as the differences with non-intrusive MOR techniques.

[3] For the unfamiliar reader, the modes can be understood as the main components for expressing the solution in a reduced base.

that is, a virtual chart that contains the solution of all possible scenarios. And not only that, but these different hypothetical cases can be particularized extremely fast for the given set of parameter values defined by the user. The computation of this parametric solution is performed in an off-line stage while employing all necessary computational resources, e.g. High Performance Computing (HPC), and available computing time. Once the parametric solution is constructed, it can be particularized on-line for the desired scenario employing light computatinal resources such as tablets or smartphones. This way, this strategy enables to perform efficient simulation, optimization, inverse analysis, uncertainty propagation and simulation-based control. Furthermore, it has been proved that this type of solutions can deal with real-time constraints in more than a few applications. And the main technique which allows that is the Proper Generalized Decomposition (PGD) [Dumon *et al.* 2011, Chinesta *et al.* 2011, Modesto *et al.* 2015, Chinesta *et al.* 2013b, Falco & Nouy 2012, Henneron & Clenet 2014, Chinesta & Ladevèze 2014, Chinesta & Cueto 2014, Cueto *et al.* 2016, Chinesta *et al.* 2013a, Bur *et al.* 2016, Chinesta *et al.* 2014]. In addition, this type of also allow to assimilate data collected from measurements, e.g. sensors, into the physics-based models.

To illustrate the capabilities of the aforementioned PGD technology, the example of Figure 3 is shown [Quesada *et al.* 2018]. In particular, virtual reality in the framework of computational surgery is explored to create a real-time, interactive simulation of tissue tearing during laparoscopic surgery. This is a challenging scenario because of the difficulties to obtain extremely fast feedback rates (500 Hz - 1 kHz) with physically realistic haptic rendering. In other words, the problem is to be able to solve a complex non-linear solid and/or fluids mechanic problem one thousand times per second. Therefore, to achieve the above goal, a multidimensional parametric problem is formulated and solved by means of the PGD method. Once the off-line solution is built, the high-dimensional parametric solution can be particularized with the aforementioned real-time constraints as well as being stored efficiently.

In parallel, the present century has also seen the data revolution in many fields including engineering. This way, massive data have been classified, visualized, curated, analyzed, ... with the aid of powerful methodologies developed in the fields of Artificial Intelligence (AI) and specifically, Machine Learning (ML). Great advancements has been carried out in techniques such as linear and nonlinear dimensionality reduction techniques based on manifold learning [Kambhatla & Leen 1997, Lee & Verleysen 2007, Schölkopf *et al.* 1998, Schölkopf *et al.* 1999, Zhang & Zha 2003, Roweis & Saul 2000] and data-driven models based on the use of decision threes [Breiman *et al.* 1984], random forests [Breiman 2001], gradient-boosted decision trees, linear and nonlinear regressions, and deep-learning techniques, among many others [Mallat 2016, LeCun *et al.* 2015, Schapire 1990, Wu *et al.* 2008, Schwarz 1978, Anandkumar *et al.* 2014, Parsa *et al.* 2018, Criminisi *et al.* 2011, Criminisi *et al.* 2012, Goodfellow *et al.* 2016, Raissi *et al.* 2017a, Raissi *et al.* 2017b, Raissi *et al.* 2019, Moitra 2018] .

Therefore, all the mentioned data-driven techniques, among others, gave arise the so-called *digital twins*. They can make possible, for instance, improved data-based predictive maintenance, efficient inspection and real-time decision making and/or control. These data-driven concepts are specially appealing for their computational complexity and consequently, when fast predictions are required. In particular, for applications requiring real-time feedback. The *digital twins* have been applied with success in a wide range of problems, but some issues appears in other industrial or scientific scenarios. Firstly, one of the main drawbacks when considering this conceptualization is usually that considerable time and efforts are required to guarantee an as rich as possible learning stage. For example,

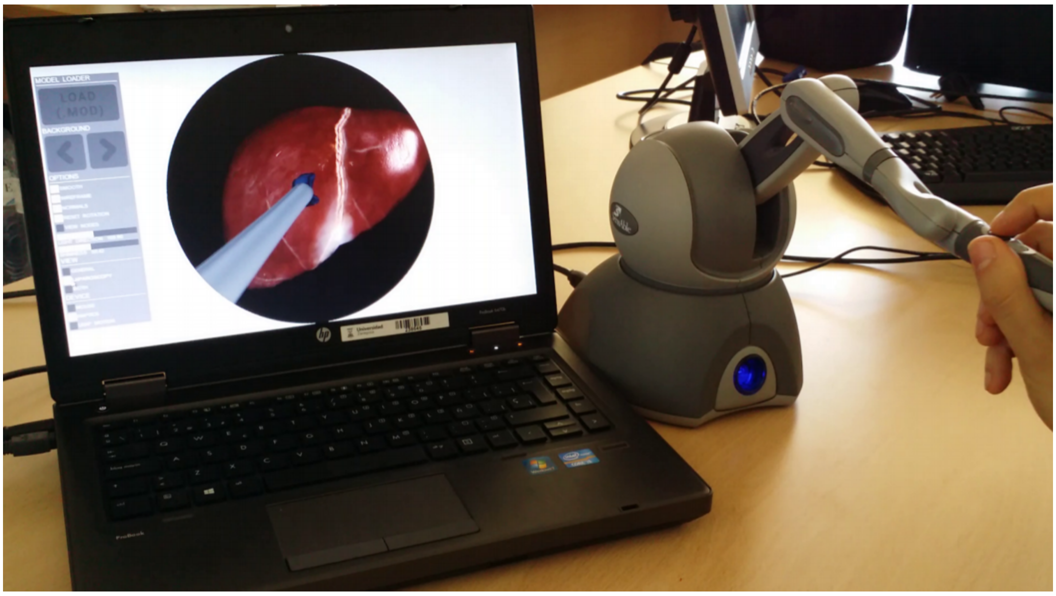

Figure 3 – Image of the haptic simulator developed with the PGD methodology. This simulator is able to provide the solution of a complex nonlinear mechanic problem one thousand times per second. Special thanks to the Applied Mechanics and Bioengineering group of the University of Zaragoza (specifically, Professor Elias Cueto) which authorised the diffusion of the image in the present thesis.

sometimes there is not enough data available or data is too expensive. In others, data are biased towards the dominant operating conditions extracted from measurements, thus losing guarantees that the model will perform well outside these main operating areas described by the experimental data. Therefore, the domain of applicability of the digital twins is generally narrower when compared with their physics-based counterpart.

For this reason, a valuable route to deal with the aforementioned problems is the following one: the employment of high-fidelity physics-based models accelerated with the MOR framework to ensure, for instance, real-time feedback. This way, the real-time solution of physically-based models allows to assimilate data collected from sensors as well as to calibrate them. Other advantage is that the produced model has usually a wider operating range that the ones produced just with sensor data.

This idea of accelerating highly-accurate physics-based models using the MOR framework has been tested and implemented successfully in many applications, often by using deployed computing devices such as Programmable Logic Controllers (PLCs), thus enabling better strategies for simulation-based control. In addition, to achieve the desired time or computational cost reduction, the MOR framework is sometimes combined with the previously introduced ML techniques (e.g. dimensionality reduction). Moreover, if intrusive MOR techniques such as the PGD present difficulties to be applied or are too intrusive[4] for the industrial software, the non-intrusive MOR techniques can be employed instead. This new type of MOR techniques was born in the following two

---

[4] In this work, the level of intrusiveness means the degree of changes required by the MOR framework, with respect to standard simulation techniques, in the mathematical procedure to solve an industrial problem. These changes should be programmed in softwares that are already implemented in the market and therefore they already has the confidence of the client as well as

circumstances: digital revolution and companies' reluctance to make major changes to their long-established software. One of the main characteristics of non-intrusive MOR techniques is that, in this case, the model is built mainly considering a data-driven approach, despite the fact that restrictions based on physical modelling can be incorporated. Other key feature is that non-intrusive MOR techniques are usually fed with data from high-fidelity physics-based models (normally called snapshots) rather than experimental data. This fact can sometimes be used to select the best snapshots to construct the model. Examples of these techniques are the Sparse Subspace Learning (SSL) and the s-PGD [Borzacchiello *et al.* 2019, Sapena-Bano *et al.* 2019, Ibáñez Pinillo *et al.* 2018]. Therefore, when they are employed, a careful selection of the snapshots from the highly accurate physics-based model is carried out to ensure sufficiently accurate performance and physics-based behaviour of the reduced order model (ROM). It has been proved that powerful models can be constructed by following this approach. One of the reasons is that data collected is not limited to the sensors but rather comes from the physical model, in order to reflect desired operation ranges that may not appear in experimental measurements. As with the intrusive MOR techniques like the PGD, such non-intrusive approaches can also be combined with other data-driven methodologies to boost performance (e.g. clustering techniques).

In addition, it is worthy to mention some of the applications where the physics-based models (accelerated with the MOR framework) and the data-driven methodologies are combined, e.g. augmented reality. An example to illustrate this fact is the one from [Badías *et al.* 2020b] (See Figure 4). Here, an augmented reality environment is set up where the mechanical interaction between real and virtual objects is computed in real-time with the precision of a high-fidelity solver but working at the speed of a video sequence. In this application, the MOR framework is employed to compute real-time physics predictions while ML, computer vision and computer graphics tools are merged to create the final augmented reality simulator. For the interested reader, other works considering augemented reality can be found in [Badias *et al.* 2020a, Badías *et al.* 2020b, Badías *et al.* 2019].

Furthermore, spetial mention should be made to the efforts to obtain data-driven models by imposing physics-based constraints. This allows us to conduct the learning stage towards compatible solutions derived from the physics knowledge. For instance, in [Moya *et al.* 2019, Moya *et al.* 2020a, Moya *et al.* 2021], several learning strategies for fluid sloshing problems based on data are described (See Figure 5). The key feature here is that the MOR framework within the ML tools are combined with a thermodinamically consistent integrator to guarantee the satisfaction of the laws of thermodynamics. In [Hernandez *et al.* 2021a], the concept is extended to neural networks.

After discussing the above examples, we have just seen the wide range of possibilities that the MOR framework open up for accelerating high-fidelity physical models as well as some innovative applications. However, problems have been reported when applied to other scenarios. Indeed, despite the fact that it has been proved that high-fidelity models accelerated with MOR techniques can perform under real-time (or almost real-time) by using reasonable computing platforms, unexpected difficulties can appear when they are integrated into data-driven applications systems. In particular, significant deviations between the predicted and observed responses have been noticed, thus potentially limiting their employment in many applications. In fact, the cause of this gap between measurements and predictions can be assigned to factors such as inacuracies in the employed models (they are not a perfectly description of the real system), in the determination of their parameters or in their time evolution.

---

several years of improvement and development.

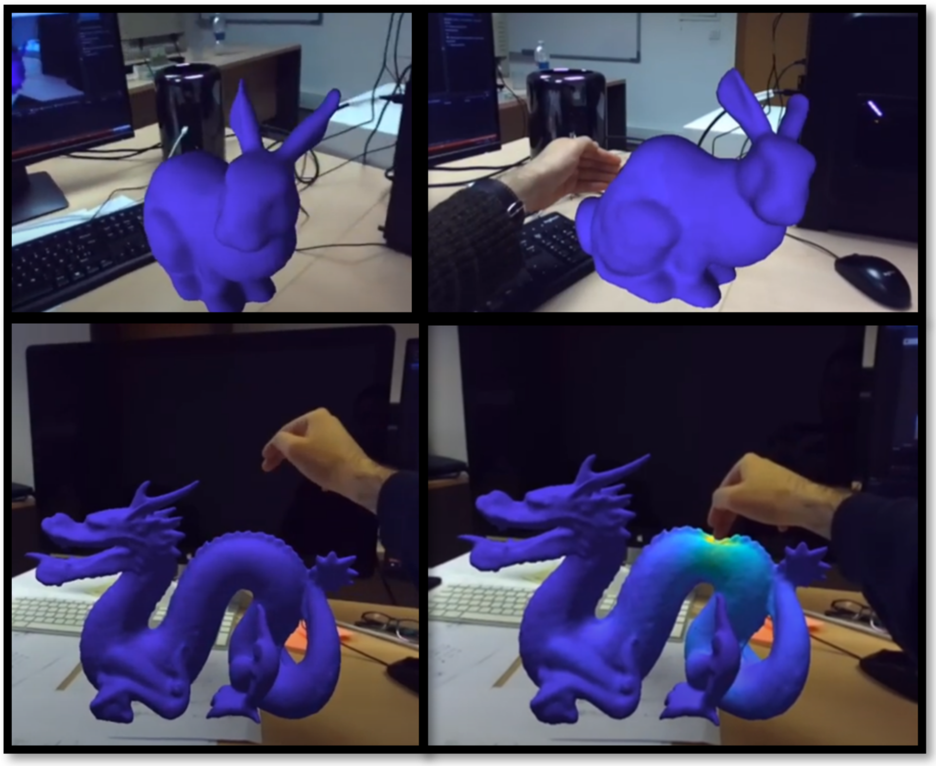

Figure 4 – Image of the augmented reality environment developed with the methodology described in [Badías *et al.* 2020b]. Here, an augmented reality environment is set up where the mechanical interaction between real and virtual objects is computed in real-time with the precision of a high-fidelity solver (thanks to the MOR framework) but working at the speed of a video sequence. Special thanks to the Applied Mechanics and Bioengineering group of the University of Zaragoza (specifically, Dr. Alberto Badias and Professor Elias Cueto) which authorised the diffusion of the image in the present thesis.

Indeed, as stated in [Quaranta 2019], a certain part of the deviation (its unbiased component in a statistical sense) can be considered as noise, but the remaining biased part proves the existence of a hidden model that operates but escapes to our understanding. To adress this issue, an appealing route can be proposed constructing "on-the-fly" data-driven models which can correct the gap between model prediction and measurement.

As a consequence, a new technology arises to deal with the above difficulties: the *Hybrid Twin* (HT) paradigm [Chinesta *et al.* 2020]. This technology combines physics-based models within a MOR framework (for accommodating real-time feedback) and data-driven models to correct the gap between predictions and measurements, thus enriching the Hybrid Twin (HT) (See Figure 6). This way, for instance, control strategies can be implemenged safely and more accurately since the HT concept enhance accuracy and allow the possibility to adress complex physical phenomena (such as degradation) by triggering data-driven corrections. Furthermore, this HT technology brings a perfect opportunity to the aforementioned Dynamic Data Driven Application Systems (DDDAS), whose main goal is to merge standard simulation algorithms with experimental data in a dynamic way. In

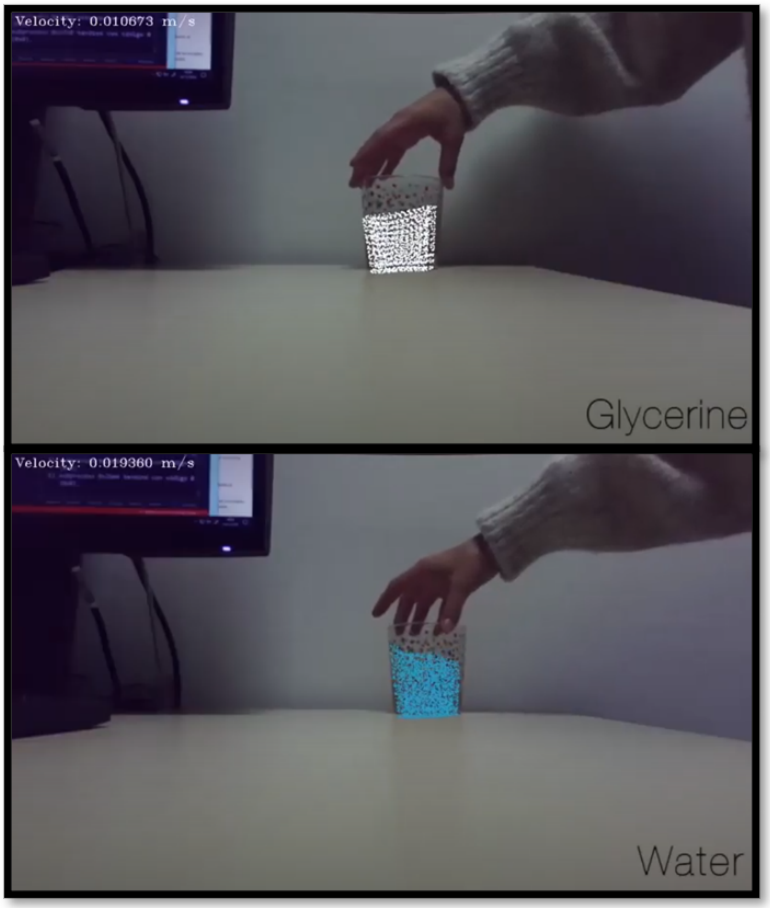

Figure 5 – Image of an augmented reality environment where the methodology described in [Moya *et al.* 2019, Moya *et al.* 2020a, Moya *et al.* 2021] is employed. The proposed method recognizes the precise type of fluid from video sequences and is able to predict future states of the dynamics for control and decision making. Note that MOR framework is employed to achieve real-time feedback. Special thanks to the Applied Mechanics and Bioengineering group of the University of Zaragoza (specifically, Bea Moya and Professor Elias Cueto) which authorised the diffusion of the image in the present thesis.

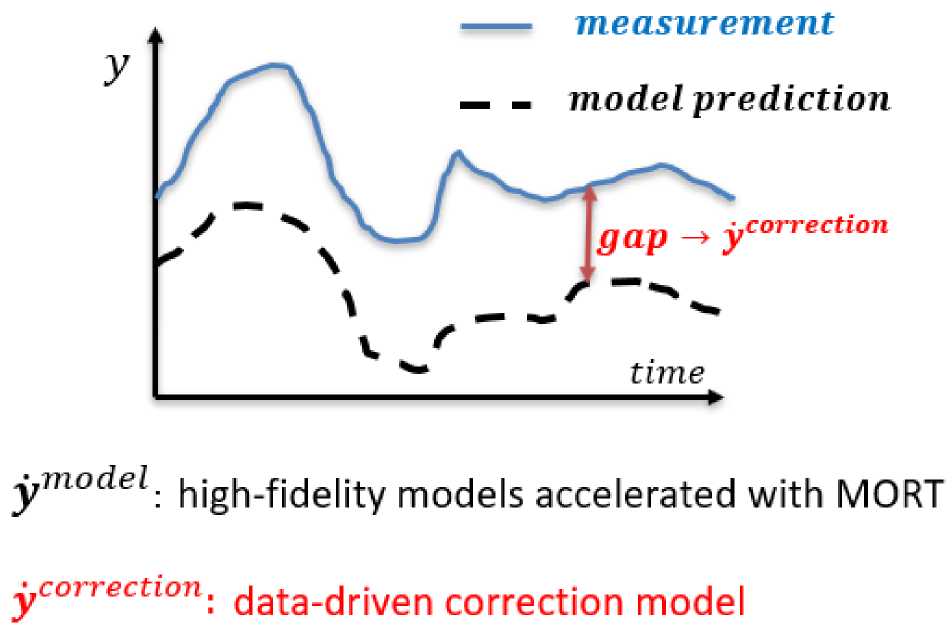

Figure 6 – Figure to illustrate the Hybrid Twin (HT) concept. In this example, the HT is employed when trying to predict the variable y. Here, the HT response will be composed of the prediction of an accurate physics-based model, as well as the modeled on-line correction to delete the biased gap between measurements and predictions. As previously discussed, Reduced Order Models (ROMs) are used to run fast enough the accurate physics-based models. Note: MORT refers to model order reduction techniques

this context, as stated in [Ibanez Pinillo 2019], data and simulations would no longer be uncoupled but rather they will create a symbiosis which can achieve milestones inconceivable until these days. In fact, data will no longer be understood as a static calibration of a given constitutive model but rather the model will be corrected dynamically as soon as data coming from measurements and simulations start to diverge. In other words, the HT makes DDDAS possible by combining HPC-based parametric solutions with "on-the-fly" data-driven correction models.

Therefore, as stated in [Chinesta *et al.* 2020], the HT satisfies the three main characteristics needed for a DDDAS:

- A simulation core able to solve complex mathematical problems representing physical models under real-time constraints [Ghnatios *et al.* 2012b];
- Advanced strategies able to proceed with data-assimilation, data-curation and data-driven modeling.
- A mechanism to online adapt the model to evolving environments.

Now, at this point, the review and introduction of the advances and challenges in the SBES field is finished. In particular, the technologies of virtual, digital, and hybrid twins as well as the MOR framework and data-driven methodologies were introduced and discussed.

And not only that but the motivations and industrial interests that led to the emergence of each technology are been illustrated, even with particular examples and achievements. Therefore, the motivation of the present thesis can already be clearly understood: to address the new challenges faced by these technologies with a particular focus on current industrial problems. To this end, new methodologies, algorithms and innovative solutions that can provide the desired business indicators will be proposed.

0.2 Objectives

The main goal of this work is to employ, develop and research new tools enabling virtual, digital and hybrid twins to address current industrial challenges. In other words, the core of this thesis is the improvement, enhancing and boosting of these new technologies[5]. In particular, the MOR and the Machine Learning (ML) framework will be explored, employed and enlarged. By doing so, the following objectives are going to be achieved:

- Enabling fast and real-time simulations of highly-time consuming and accurate physics-based models as well as developing advanced data-driven approaches in current challenging scenarios.
- Providing tools to address current key topics such as optimization, inverse analysis, uncertainty propagation and simulation-based control; which are enabled by the above methodologies thanks to the high decrease in computational complexity.
- Improving the construction as well as developing new tools for the creation of digital and hybrid twins, with a special emphasis on the latter.
- Enhancing a DDDAS framework by developing the HT concept in different applications.

These milestones are pursued by solving current industrial needs in challenging scenarios. In particular:

- Electric Vehicle Industry. Here, two main topics are analyzed:
    - Lithium-ion batteries.
        - Development and research of Reduced Order Models (ROMs) and data-driven models to enhance and construct the new required generation of Battery Management Systems (BMS) for the automotive industry as well as to address currently demanded applications.
        - Development of the first (to our knowledge) HT of a Li-ion battery.
        - Development of an innovative planning algorithm to make decisions as well as to adapt the driving behaviour based on predictions of the whole Electric Vehicle (EV). The micro-scale state of battery cells is wanted to be inferred
    - Electric motors. Development of novel MOR techniques to achieve fast and real-time predictions as well as high-dimensional parametric solutions for the electromagnetic field and force. This will help the design, analysis of performance and implementation of electric machines concerning industrial applications such as the noise, vibration, and harshness (NVH) in electric motors.

---

[5] In the previous section (Section 0.1), a detailed summary about the benefits of developing these technologies is caried out.

- Aeronautics industry. Development of a HT for the air distribution system of an aircraft. In this case, the model is constructed from real data supplied by Dassault Aviation. This work was done in the context of a project as part of the PEA MMT (Plan d'Etudes Amont Man Machine Teaming) financed by the DGA (Direction Générale de l'Armement).
- Radar-based Advanced Driver Assistant Systems (ADAS). Development of parametric solutions for electromagnetic wave propagation in radar applications as well as a suitable interpolation method for complex-valued fields which allows reducing the computational cost of this type of simulations by a great factor.

A more detailed description of the specific objectives for each industrial case as well as the achievements and proposed solutions are addressed in the corresponding chapter for each application.

In addition, in parallel:

- Research and development (R&D) of novel MOR techniques, algorithms and data-driven models. The objective is to improve the results when the current techniques suffer and to extend methodologies to new areas of interest.

Furthermore, the tools offered will lead to a competitive advantage which will boost competitiveness in a continuously growing industry. In fact, some the improvements of the present work can be also framed in the new Industry 4.0.

0.3 Structure of the thesis

As indicated in Section 0.1, there is an unceasingly growing interest in merging fields such as data science and science-based simulation engineering to derive knowledge from information and ultimately transform this knowledge into decision making. Furthermore, in this context, digital and hybrid twins are becoming increasingly popular to address current industrial needs such as optimization, inverse analysis or the new appealing routes like the ones coming from the DDDAS framework.

For this reason, and as further detailed in Section 0.2, the core of this thesis is the improvement, enhancing and boosting of this new technologies. And to do that, new non-intrusive MOR techniques and data-driven approximations are proposed to later, being applied in different scenarios to examine its viability and performance. In addition, a particular focus is given to the data-driven approaches enabling the HT.

Consequently, this work will be structured in the following three main parts, each of them composed of different chapters.

- ***Part I.*** *Fundamentals: Review of the main intrusive MOR techniques.*
  - ***Chapter 1:*** *Advanced numerical techniques: intrusive Model Order Reduction techniques.*
- ***Part II.*** *Fundamentals: Presentation of novel non-intrusive and data-driven techniques.*
  - ***Chapter 2:*** *Novel reduced order formulations, algorithms and hybridation/dynamic techniques.*
  - ***Chapter 3:*** *Novel PGD strategies: PGD-based advanced nonlinear multiparametric regressions for constructing metamodels at the scarce-data limit*

- ***Part III.*** *Industrial and Practical Applications*
  - ***Chapter 4:*** *Advanced Multi-Parametric models for Electric Machines.*
  - ***Chapter 5:*** *Parametric electromagnetic analysis of radar based Advanced Driver Assistant Systems.*
  - ***Chapter 6:*** *An aircraft Hybrid Twin: Learning stable reduced-order models for hybrid twins.*
  - ***Chapter 7:*** *From ROM of Electrochemistry to AI-based Battery Digital and Hybrid Twin.*

Chapter 1: Advanced numerical techniques: intrusive Model Order Reduction techniques.

In this chapter, a review of the main intrusive MOR techniques employed in this work are presented. Specifically, the Proper Orthogonal Decomposition (POD) and the Proper Generalized Decomposition (PGD). These techniques are used to empower and accelerate highly-time consuming physics-based models while maintaining good agreement. In addition, the PGD enables the construction of accurate high-dimensional parametric solutions, being able to construct virtual charts that can be particularized on-line under real-time constraints. During the present work, both techniques will be used in the following chapters to meet different objectives:

- First, the POD will be used to accelerate a highly-accurate physics-based model of a battery cell with an excellent agreement, thus enabling, among other targets, a quicker snapshot computation. Later, these snapshots will be employed to construct a ROM using more advanced MOR techniques discussed in Chapter 2.
- On the other hand, the intrusive PGD is used in Chapter 4 to construct a high-dimensional parametric solution for electromagnetic fields in synchronous machines. In this context, the domain of simulation is not suitable for a PGD separated representation, making its successful and efficient application to the problem challenging. However, in Chapter 4, a new suitable mapping is developed to transform the motor geometry in one amenable for a separated representation within the PGD framework.

Chapter 2. Novel reduced order formulations, algorithms and hybridation/dynamic techniques.

In this Chapter, the novel non-intrusive techniques developed in this thesis to face the industrial problems described in Chapters 4, 5, 6 and 7 are presented. In particular, the theoretical basis of these data-driven methodologies is detailed. Other techniques, such as those relevant to the understanding of the proposals presented, are also reviewed.

Firstly, this chapter begins by continuing and reviewing the theoretical foundations of the sparse PGD (s-PGD) from a machine learning point of view. In the following chapters, this technique will be employed to construct novel ROMs in different industrial applications. Furthermore, later on in Chapter 3, this framework will be taken as a basis for developing novel PGD methodologies to overcome the limitations of the current state of the art in challenging scenarios.

Secondly, this thesis introduces a novel sparse reduced order formulation combining the s-PGD with a Reduced Basis (RB) approach. We will see (in Chapter 4) how the proposed strategy can be employed to capture complex and challenging physical phenomena as well as to obtain a further data compression.

Next, a novel algorithm for phase-angle unwrapping for accurately addressing interpolation of complex numbers is proposed. This new and effective strategy was constructed during this thesis when addressing the problem encountered in Chapter 5 and compared with state-of-the-art techniques as the ones implemented in Matlab software [MathWorks 2020].

Subsequently, the techniques proposed for hybridization in the HT context are presented. Specifically, this thesis proposes two novel methodologies, the practical application of which is carried out in Chapters 6 and 7.

- The first one is a stabilization procedure for the Dynamic Mode Decomposition (DMD) and Dynamic Mode Decomposition with control (DMDc) techniques. The goal of this first technique is the computation of stable, fast and accurate corrections in the Hybrid Twin framework, regarding the delicate and important problem of stability.
- The second one is the DMD Dictionary strategy which allow us to address complex non-linear behaviors within the DMD framework. Moreover, this method is able to produce models that avoid over-fitting quite well, correcting only the operation ranges with more error.

In addition, prior to the mentioned new strategies, a big picture of the HT is discussed and the standard procedures for the DMD and DMDc are introduced.

To end up and to sum up, this chapter presents four disruptive and innovative methodologies: the s-PGD + RB strategy, a novel unwrapping algorithm, the stabilized DMD and DMDc techniques and the DMD Dictionary methodology.

Chapter 3. Novel PGD strategies: PGD-based advanced nonlinear multiparametric regressions for constructing metamodels at the scarce-data limit.

The following chapters (Chapters 4, 5, 6 and 7) will show the great results that can be obtained using the proposed non-intrusive ROMs and data-driven techniques to enable and improve digital and hybrid twins. The s-PGD technique deserves special mention because it is often able to construct high-dimensional parametric functions in the low data limit. This is crucial because, in many industrial applications, obtaining a large amount of data is unfeasible because of the curse of dimensionality or because of the expensiveness of data. However, in this framework, current techniques, such as the just referred s-PGD, do not always achieve good results when addressing high-dimensionality at the low data limit. The reason is that ensuring accuracy and avoiding overfitting constitutes a difficult challenge. Therefore, the present chapter aims at proposing and discussing different advanced regressions enabling and empowering the just referred features. In particular, this thesis proposes 3 novel PGD-based non-intrusive ROMs where their results are analyzed and discussed in this chapter:

- The first is based on an Elastic Net regularized formulation, called rs-PGD, combining Ridge and Lasso regressions, that make use, respectively, of the L2 and L1 norms. To avoid overfitting, the former favors specific solutions with smaller coefficients, while the last enforces the sparsest possible solution by retaining those contributing the most to the solution approximation. This technique can be employed to use richer approximation basis when compared to the s-PGD as well as to increase the generalization of the model when examining unseen scenarios

- Secondly, the doubly sparse regression, the so-called s^2-PGD technique will be introduced. The last makes use of the Lasso regularization (the one introduced above that looks for the sparsest approximation through the use of the L1-norm) while searching for the sparsest dimensions. This technique is able to identify sparse solutions when their sparse structure is composed according to the separated PGD representation.
- The third and last technique, the ANOVA-PGD, aims at allying orthogonal hierarchical bases with a more favorable scaling (with respect to the SSL [Borzacchiello *et al.* 2019]) of the amount of data with the approximation richness. For that purpose, separated representations and sparse approximations (eventually regularized) will be combined for addressing multiple correlation terms.

Discussions and results carried out will show that the proposed PGD-based methodologies can empower state-of-art surrogate models in the complex system settings described in the present chapter. Consequently, digital and hybrid twins will be improved when dealing with this type of scenarios which are highly appealing for industries.

Chapter 4: Advanced Multi-Parametric models for Electric Machines.

This chapter begins the third part of the thesis, which focuses on the application of the techniques presented and discussed previously. Thus, the fourth chapter address the creation of advanced and novel ROMs concerning rotating electric machines. In fact, it addresses the current need of fast, accurate and parametric models in this context. Nowadays, these solutions are highly demanded by the industry, especially with the recent developments in the Electric Vehicle (EV).

The following areas of work are addressed:

- A novel Reduced Order Model is obtained employing the intrusive PGD to construct a high-dimensional parametric solution for electromagnetic fields in synchronous machines. The proposed approach is capable to construct a virtual chart in a few minutes of off-line simulation and once constructed, a particular solution can be particularized on-line in less than a second. In this context, the domain of simulation is not suitable for a PGD separated representation, making its successful and efficient application to the problem challenging. However, in this Chapter 4, we develop a new suitable mapping to transform the motor geometry. Thus, the resultant new geometry will be more adapted to achieve good results within the PGD framework.
- A novel non-intrusive Model Order Reduction (MOR) strategy is employed to achieve fast and real-time predictions as well as high-dimensional parametric solutions for the electromagnetic force which will help the design, analysis of performance and implementation of electric machines concerning industrial applications such as the noise vibration and harshness (NVH) in electric motors. The approach allows to avoid the long-time simulations needed to analyze the electric machine at different operation points. In addition, it can be easily extended to predict other quantities of interest such as the torque or the fluxes. Moreover, it facilitates the computation and coupling of the motor model in other physical subsystems. Furthermore, this second proposal can also be used as an alternative of the first approach if an specific machine presents problems in the formulation of the intrusive PGD.

Chapter 5. Parametric electromagnetic analysis of radar based Advanced Driver Assistant Systems

Efficient and optimal design of radar-based ADAS (Advanced Driver Assistant Systems) requires performing a great number of electromagnetic simulations. Due to the nature of the problem, very fine meshes are required to accurately discretize the Partial Differential Equations (PDEs) involved. Thus, the computational cost of each simulation for a given choice of the design or operation parameters is highly time consuming (needing significant computational resources) compromising the efficiency of standard optimization algorithms. Making matters worse, another difficulty appears when non-intrusive MORs are applied in radar engineering. This is the interpolation of the complex-valued electric and magnetic fields. If an interpolation is sought for real and imaginary parts independently, spurious solutions appear. Therefore, it seems more reasonable to use the alternative formulation based on the amplitude and phase because both amplitude and phase functions are continuous in most practical cases. However, the use of an amplitude/phase description faces the difficulty related to the phase definition. Specifically, the problem is that the phase is not uniquely defined, and any other range $((k-1)\pi,(k+1)\pi]$ for $k \in \mathbb{Z}$ will be a valid interval to represent any complex number. Therefore, it is important to determine the interval $((k-1)\pi,(k+1)\pi]$ of each complex number where the phase function is continuous. This way, methodologies which tries to fix the above issue are created (and called "unwrapping strategies"). However, to be successful in the above strategies, sampling has to be quite dense. This, together with the high computational cost of each simulation put problems when constructing non-intrusive ROMs because of the amount of sampling points needed.

To alleviate the above-mentioned difficulties, this chapter proposes:

- A novel and powerful phase-angle unwrapping strategy to compute non-intrusive ROMs within the s-PGD rationale when sparse sampling is employed.

This is important because usual unwrapping algorithms only performs well when the data sampling is dense enough, but they fail in the sparse sampling case [Ben Abdallah & Abdelfattah 2015, Shanker & Zebker 2010, Costantini *et al.* 2012]. However, it is important to deal with this scenario because it is the framework involved when constructing high-dimensional parametric functions. Therefore, the most important achievement of this chapter is to propose a methodology able to conciliate unwrapping and sparse sampling.

Due to the above fact, this technique will considerably reduce the needed number of snapshots to create parametric ROMs with the s-PGD and thus accurately address the electric and magnetic fields interpolation.

Chapter 6. An aircraft Hybrid Twin: Learning stable reduced-order models for hybrid twins

This chapter of the thesis is devoted to the development of the Hybrid Twin (HT) methodology. Hybrid twins are a special type of digital twins able to learn and correct themselves once significant and persistent biases between data and predictions are found. To achieve this goal, the hybrid twins combine HPC-based parametric model solutions with "on-the-fly" data-driven constructed deviation-models, making DDDAS possible [Chinesta *et al.* 2020].

In any case, when addressing dynamical systems in the HT framework, it is important to guarantee the stability of the system when adding corrections to the physical model. It is worth noting that this is an important issue, because sometimes the best model, computed with state-of-the-art algorithms, completely fails to obtain a stable time-integrator. For example, when considering a dynamical model by the Dynamic Mode Decomposition (DMD) approach [Kutz *et al.* 2016, Schmid 2010], the feasible region constrained by the stability condition is nonconvex [Huang *et al.* 2016], and no general methodology exists to solve it. Therefore, this chapter is focused on the computation of stable, fast and accurate corrections in the Hybrid Twin framework. To do that and regarding the delicate and important problem of stability, this thesis proposes a new approach (where its mathematical details where introduced in Chapter 2), introducing several sub-variants and guaranteeing a low computational cost as well as the achievement of a stable time-integration.

The system analyzed to apply the HT concept within the new technique is an air distribution system of an aircraft. In this case, the model is constructed from real data supplied by the international company Dassault Aviation.

Furthermore, this research work was done in the context of a project as part of the PEA MMT (Plan d'Etudes Amont Man Machine Teaming) financed by the DGA (French Government Defense procurement and technology agency) and managed by French aircraft and jets manufacturer Dassault Aviation.

To end up, it is interesting to note that the final HT model was given to Dassault Aviation which decided, after the good results obtained, continuing in the research to implement the HT rationale in their systems.

Chapter 7. From ROM of Electrochemistry to AI-based Battery Digital and Hybrid Twin

Automotive industry is requiring novel sophisticated Battery Management Systems (BMS) to control and monitor the battery system to achieve benefits such as less battery degradation, better performance and more lifetime. The key to improve the BMSs is to employ more complex battery models on-board. However, they are highly-time consuming to be used. Therefore, three different methodologies are proposed to deal with the above problem, achieving great results as well as conceptualizing the HT procedure to follow when needed. These proposed techniques are applied to the most commonly used physics-based model (Newman's pseudo-2D model: [Doyle *et al.* 1993, Fuller *et al.* 1994, Doyle & Fuentes 2003]), each one for a different range of application.

- First, a POD model is used to greatly reduce the simulation time and the computational effort for the pseudo-2D model, while maintaining its accuracy. In this way, cell design, optimization of parameters, and simulation of battery packs can be done while saving time and computational resources. In addition, this model will be also employed to obtain the snapshots to create the following ROM.

- Next, a model is constructed from data by using the sparse-Proper Generalized Decomposition (s-PGD). It is shown that it achieves real-time performance for the whole Electric Vehicle (EV) system with a battery pack. In addition, this non-intrusive ROM can be used in a BMS without issues because of the simple algebraic expression obtained. A simulation of the EV with the proposed approach is demonstrated using the system simulation tool SimulationX [ESI ITI GmbH. Dresden, Germany]. To sum up, since a reduction in computational cost that is thousands of times lower is achieved with the s-PGD model (maintaining good accuracy), we have no problem in using the discussed approach for the above applications.

- Thus, this fact allowed to develop an innovative planning algorithm to make decisions based on predictions of the whole EV, taking into consideration this fast and accurate battery model. For example, the best possible itinerary is computed considering different battery criteria (where several itineraries are quickly simulated to select the best one). Or another example, the algorithm is also capable of proposing changes in the driving behavior if an itinerary is maintained but it detects that battery problems can arise. Moreover, the Digital Twin created using the s-PGD does not only allow for real-time simulations, but it can also correct its predictions taking into consideration the real driving conditions and the real driving cycle to change the planning in real-time
- Finally, a novel data-driven model is developed to extract an on-line model that corrects the gap between prediction and measurement, thus constructing the first (to our knowledge) hybrid twin of a Li-ion battery able to self-correct from data. To construct this data-driven model, this thesis proposes the novel procedure introduced in Chapter 2: “The DMD Dictionary strategy”. In addition, thanks to this model, the above gap can be corrected during the driving process, taking into consideration real-time restrictions.

To sum up, this chapter provides three different ROMs, covering different ranges of application as well as enabling the HT concept. Furthermore, an innovative planning algorithm is proposed where its big success is being able to make fast decisions as well as to adapt the driving behaviour employing the highly-accurate predictions provided by the s-PGD cell model.

0.4 Scientific contributions

These thesis works have generated the following publications:

0.4.1 Papers in international Journals

1. A. Sancarlos, M. Cameron, A. Abel, E. Cueto, J.L. Duval, F. Chinesta, “From ROM of Electrochemistry to AI-Based Battery Digital and Hybrid Twin,” *Archives of Computational Methods in Engineering* , vol. 28, pp. 979–1015, 2021. DOI: https://doi.org/10.1007/s11831-020-09404-6.
2. S. Vermiglio, V. Champaney, A. Sancarlos, F. Daim, J.C. Kedzia, J.L. Duval, P. Diez, F. Chinesta, “Parametric Electromagnetic Analysis of Radar-Based Advanced Driver Assistant Systems,” *Sensors*, vol. 20, issue 19, 2020. DOI: https://doi.org/10.3390/s20195686
3. A. Sancarlos, E. Cueto, F. Chinesta, J.L. Duval, “A novel sparse reduced order formulation for modeling electromagnetic forces in electric motors,” *SN Appl. Sci.*, vol. 3, issue 3, 2021. DOI: https://doi.org/10.1007/s42452-021-04310-3.
4. A. Sancarlos, C. Ghnatios, J.L. Duval, N. Zerbib, E. Cueto, F. Chinesta, “ Fast Computation of Multi-Parametric Electromagnetic Fields in Synchronous Machines by Using PGD-Based Fully Separated Representations,” *Energies*, vol. 14, issue 5, 2021. DOI: https://doi.org/10.3390/en14051454
5. A. Sancarlos, V. Champaney, J.L. Duval, E. Cueto, F. Chinesta, “PGD-Based Advanced Nonlinear Multiparametric Regressions for Constructing Metamodels at the Scarce-Data Limit,” *SIAM Journal on Scientific Computing*, Submitted.

6. A. Sancarlos, M. Cameron, J.M. Le Peuvedic, J. Groulier, E. Cueto, F. Chinesta, J.L. Duval, “ Learning stable reduced-order models for hybrid twins,” *Data-Centric Engineering*, In press.
7. T. Frahi, A. Sancarlos, M. Galle, X. Beaulieu, A. Chambard, A. Falco, E. Cueto, F. Chinesta, “ Monitoring weeder robots and anticipating their functioning by using advanced topological data analysis,” *Frontiers in Artificial Intelligence*, Submitted.

0.4.2 Papers in German magazines

This dissertation has generated the following publication in the magazine brand ATZ, the world’s leading specialist magazine for the automotive sector. In fact, ATZ is the internationally distributed technology magazine for decision-makers in automotive development and production and the must-read publication for technology-oriented management in the automotive industry. Specifically, the article was published in the magazine ATZextra dedicated to important topics focused on the German-speaking market:

1. F. Chinesta, A. Sancarlos, A. Abel, “Batteriemanagementsysteme mit Hybrid Twin für Lithium-Ionen-Batterien,” *ATZextra* , Springer Vieweg, vol. 26, Edition: Special issue 3/2021, pp. 20–23, Juni 2021. URL: `https://www.springerprofessional.de/batteriemanagementsysteme-mit-hybrid-twin-fuer-lithium-ionen-bat/19313538`.

Note:

- “Batteriemanagementsysteme mit Hybrid Twin für Lithium-Ionen-Batterien” is translated into “Battery management systems for lithium-ion batteries with Hybrid Twin”
- “Juni” is translated into “June”

0.4.3 Conference Proceedings

1. A. Sancarlos, P. De Miguel, M. Cameron, E. Cueto, F. Chinesta, J.L. Duval, “Battery Hybrid Twin in Electrical Vehicle Monitoring and Planning ,” *FISITA 2021 World Congress – Conference Proceedings*, 2021.
2. V. Champaney, A. Sancarlos, F. Chinesta, E. Cueto et al., “Hybrid Twins – a highway towards a performance-based engineering. Part I: Advanced Model Order Reduction enabling Real-Time Physics ,” *ESAFORM Conference Proceedings*, 2021. DOI: 10.25518/esaform21.2017.

0.4.4 International Conferences

1. A. Sancarlos, S. Clenet, T. Henneron, E. Cueto, F. Chinesta, J.L. Duval. *Novel and advanced numerical techniques for diagnosis and prognosis.* Mechanistic Machine Learning and Digital Twins for Computational Science, Engineering and Technology: MMLDT-CSET 2021. Hyatt Regency Mission Bay, San Diego, CA, US. 2021
2. V. Champaney, A. Sancarlos, F. Chinesta, E. Cueto, J.L. Duval, A. Chambard. *Hybrid Twins for empowering performance-based engineering. Part I. Real-time physics-based models.* Mechanistic Machine Learning and Digital Twins for Computational Science, Engineering and Technology: MMLDT-CSET 2021. Hyatt Regency Mission Bay, San Diego, CA, US. 2021

3. V. Champaney, A. Sancarlos, F. Chinesta, E. Cueto, J.L. Duval, A. Chambard. *Hybrid Twins for empowering performance-based engineering. Part II. Real-time data-driven models and hybridation.* Mechanistic Machine Learning and Digital Twins for Computational Science, Engineering and Technology: MMLDT-CSET 2021. Hyatt Regency Mission Bay, San Diego, CA, US. 2021
4. A. Sancarlos, P. De Miguel, M. Cameron, E. Cueto, F. Chinesta, J.L. Duval. *Battery Hybrid Twin in Electrical Vehicle Monitoring and Planning.* FISITA World Congress. Virtual Congress. 2021
5. A. Sancarlos, E. Cueto, F. Chinesta, J.L. Duval. *Empowering Multidimensional Data-Driven Metamodels: the doubly sparse Proper Generalized Decomposition (PGD) and the regularized sparse PGD.* VI ECCOMAS Young Investigators Conference: YIC 2021. Virtual Congress. 2021
6. A. Sancarlos, K. Bouayed, N. Zerbib, E. Cueto, F. Chinesta, J.L. Duval. *Fast Computation in Electric Motors for Design, Optimization and Prediction of Noise, Vibration and Harshness.* IX International Conference on Couled Problems in Science and Engineering: COUPLED. Virtual Congress. 2021
7. V. Champaney, A. Sancarlos, F. Chinesta, E. Cueto et al., *Hybrid Twins – a highway towards a performance-based engineering. Part I: Advanced Model Order Reduction enabling Real-Time Physics.* ESAFORM. Virtual Conference. 2021
8. A. Sancarlos, M. Cameron, E. Cueto, F. Chinesta, J.L. Duval. *Towards Battery Management Systems through Reduced Order Models and Machine Learning Techniques.* 14th World Congress in Computational Mechanics and ECCOMAS Congress: 14th WCCM-ECCOMAS Congress. Virtual Congress. 2021
9. A. Sancarlos, F. Chinesta, E. Cueto, J.L. Duval et al., *From Battery Cells Reduced Order Modeling to Real-time Planning and System Integration.* ADMOS. El Campello (Alicante), Spain. 2019
10. A. Sancarlos, F. Chinesta, E. Cueto, J.L. Duval et al., *Towards a Hybrid Twin paradigm for battery management system.* ECCM-ECFD 2018: 6th European Conference on Computational Mechanics and 7th European Conference on Computational Fluid Dynamics. Glasgow, UK. 2018

0.4.5 International ESI Conferences

1. A. Sancarlos, F. Chinesta, A. Abel.*From Battery Cells Reduced Order Modeling to Real-time Planning and System Integration.* PUCA – ESI Users' Forum. Tokyo, Japan. 2018

0.4.6 Batteries Europe Meetings

Nowadays, ESI Group is participating in the Batteries Europe project [Alliance 2019] which aims to bring together all relevant stakeholders in the European batteries research and innovation ecosystem in order to develop and support a competitive battery value chain in Europe. In my case, due to the battery research done in the present thesis, I am a representive of ESI Group in the following working groups:

1. WG1: New and Emerging Battery Technologies
2. WG3: Advanced Materials

3. WG4: Manufacturing and Cell Design

In addition, I participated in the following european meetings organised by the European Comission:

1. “WG1 Panel Meeting” of Batteries Europe which took place on October 4th 2019 in Helmholtz Institute Ulm (HIU), Germany.
2. “WG1 Meeting” of Batteries Europe which took place on February 27th 2020 in the European Comission, Brussels.
3. WG1-Batteries Europe web-meeting which took place on June 8th 2020.

0.4.7 Seminars given as a presenter

1. “Batteries & Model Order Reduction Techniques” which took place on January 20th 2020 in Lille, France. I gave this seminar of two hours in front of professors, post-docs and PhD students of the research team L2EP (Laboratory of Electrical Engineering and Power Electronics) and lead to fruitful discussion on model order reduction.
2. “Hybrid Twin Concept applied to Battery Management Systems” which took place on the 10th, 11th and 12th of February 2020 in Madrid, Spain. I gave this seminar of 27 hours to the Technical team ESI Group Hispania.S,L.

0.5 Scientific dissemination

Concerning the area of scientific dissemination, I participated in the French competition entitled “Ma thèse en 180 secondes (MT180s)” which is inspired in the Three minute thesis competition (3MT) founded by the University of Queensland (UQ). The idea is to cultivate students’ academic, presentation, and research communication skills as well as spreading the research topics carried out during the PhD. In fact, I reached the “finale HESAM Université édition 2021”. The participation was broadcasted live and recorded. The link to re-watch this thesis presentation on replay is: `https://www.youtube.com/watch?v=bzeXt1tHnN4&list=PL9j4_iHDzbySir44OHEuVocuVYHOvo5Pe&index=7`

Part I

Fundamentals: Review of the main intrusive MOR techniques

Chapter 1

Advanced numerical techniques: intrusive Model Order Reduction techniques

---

Abstract Model order reduction (MOR) techniques are methodologies for reducing the computational complexity of mathematical models in numerical simulations. They aim to lower the aforementioned complexity when it is not practical or feasible the employment of the full-order physics-based model to address the target needs (e.g. the set-up requirements for a given industrial application or physics experimentation). For instance, imagine an application where it is needed to compute the current torque of an electric motor in real-time with the accuracy of a finite element method (FEM) model. Thus, as the FEM model does not allow real-time feedback, a MOR technique can then be employed to obtain a ROM which satisfy the requirements for this application. Consequently, if an intrusive MOR technique is selected (the type presented in this Chapter), the mathematical formulation of the FEM model is changed accordingly. This way, we reached a key concept: instrusive MOR techniques need to reformulate the set of PDEs which define the prolem. Therefore, the "intrusiveness" comes from the fact that the mathematical problem and solver must be reformulated. Furthermore, these techniques have proven to be extremely powerful. They achieved to run simulations or Design of Experiments (DoE), which would last years using standard procedures (FEM or FDM for instance), in some minutes of off-line simulation. And not only that but, once the ROM is constructed, they can provide real-time feedback. Worthy of special mention is the intrusive Proper Generalized Decomposition (PGD), which allows to create virtual charts composed by high-dimensional parametric solutions while maintining an excellent agreement with the full order model. Furthermore, the key and top value of this technique is that it avoids the curse of dimensionality when computing this type of parametric functions which, by the way, can usually be particularized in real-time.

In this work, we are going to focus on two intrusive MOR techniques: the Proper Orthogonal Decomposition (POD) and the aforementioned PGD. **Specifically, the goal of this Chapter is to present the theoretical basis to employ the above techniques.** The reason is that they are going to be used in the following chapters (4, 5 and 7 respectively).

Contents

1.1 Introduction **26**
1.2 Proper Orthogonal Decomposition **28**
  1.2.1 Method of snapshots: Obtaining the POD basis 28
  1.2.2 POD reduced order models 30
1.3 Proper Generalized Decomposition **31**
  1.3.1 Separated representation constructor 32

1.4 Summary **35**

1.1 Introduction

Nowadays, numerical simulation is present in most scientific fields and engineering domains, making accurate designs and virtual evaluation of systems responses possible – drastically cutting the number of experimental tests [Panel 2006, Chinesta *et al.* 2020]. In fact, the success and wide range of application of techniques such as the FEM is undisputed.

However, in spite of this impressive progress made during the last decades in mathematical modelling and techniques of scientific computing, many problems in science and engineering remained and remain intractable [Panel 2006, Argerich 2020, Quaranta 2019, Chinesta *et al.* 2013a].

In fact, standard numerical tools (e.g., FEM [Ida & Bastos 1992, Fish & Belytschko 2007], FDM [Patankar 1980, Ida & Bastos 1992] or FVM [Patankar 1980]) can present serious difficulties or directly fail under different challenging scenarios. Among them, we can cite [Chinesta *et al.* 2013a, Chinesta *et al.* 2017]:

- Those related to highdimensional models (e.g., in dynamics of complex fluids, quantum chemistry), for which classical mesh-based approaches fail due to the exponential increase of the number of degrees of freedom.
- Those requiring many direct solutions of a given problem. For instance, optimization, inverse identification or uncertainty quantification. In this case, the computational cost to carry out the high number of simulations to perform the aforementioned tasks is limiting or prohibitive. This is further exacerbated when the accuracy of full order models is strongly desired.
- Those needing very fast solutions (i.e., for real-time simulation, simulation-based control). Here, the problem usually lies in the time cost of the full order or high-fidelity model which is far away from real-time constraints.

Therefore, we can conclude that standard numerical tools fail in some scenarios because their numerical complexity, or the restrictions imposed by different requirements (real-time on deployed platforms, for instance) make them unaffordable.

In this context, the intrusive Model Order Reduction framework was borned as an appeling route to offer new simulation alternatives by circumventing, or at least alleviating, otherwise intractable computational challenges.

In this Chapter, we present and describe the theoritical basis of two different intrusive MOR techniques.

Firstly, the Proper Orthogonal Decomposition is discussed as a general methodology for extracting the most significant characteristics of a system's behavior and representing them in a set of "POD basis vectors." These basis vectors then provide an efficient (typically low-dimensional) representation of the key system behavior, which proves useful in a variety of ways. The most common use is to project the system governing equations onto the reduced-order subspace defined by the POD basis vectors. This yields an explicit POD reduced model that can be solved in place of the original system. The POD basis is also able to provide a low-dimensional description in which to compute parametric interpolation as well as performing model adaptation. Due to its broad applicability to linear and nonlinear systems, the POD has become widely used in many different application domains. For instance, [Sempey *et al.* 2009, Carlberg & Farhat 2011, Allery *et al.* 2004, Carlberg & Farhat 2008, Allery 2002]. Furthermore, the POD technique has been developed and re-discovered in many branches of science under different names such as Principal Component Analysis (PCA) [F.R.S. 1901]. There is an extensive literature and POD has seen broad application across fields. Some review of POD and its applications can be found in [Dowell & Hall 2001, Benner *et al.* 2015]

Secondly, the intrusive PGD within its theoretical framework is presented. This methodology was borned as an excellent tool to handle the aforementioned list of features which cannot be solved employing direct, traditional numerical strategies. The cornerstone of the PGD is that it deals with the *curse of dimensionality*. Maybe, the reader unfamiliar with this phenomenan is wondering what is. Imagine, for example, the solution sought of a model defined in a space of dimension P using a standard mesh-based discretization technique, wherein N nodes are used for discretizing each space coordinate. The resulting number of nodes reaches the astronomical value of N^P. With $N = 10^3$ (a coarse description in practice) and $P = 5$ (a very simple model) the numerical complexity is 10^{15}, which is larger than the sum of the presumed number of stars contained in the Andromeda Galaxy plus the presumed number of galaxies in the observable universe! Making matters worse, imagine that you add the temporal dimension with the same discretization N: you will have to deal with an incremental procedure that involves the solution of a boundary value problem (BVP) of the above characteristics at each time step, that is, a total of 1000 BVP's with 10^{15} nodes. This is the previously introduced concept of *curse of dimensionality* and its effects are devastating in many areas of science and engineering. However, the PGD comes to the rescue avoiding the exponential complexity with respect to the problem dimension if the sought solution is well-expressed in the PGD framework. Specifically, the complexity of the PGD grows linearly with the problem's dimension.

For this reason, the PGD has allowed to solve parametric problems in phase spaces of one hundred dimensions with excellent agreement [Cueto *et al.* 2016]. Furthermore, it enabled to concept of high-fidelity parametric models defining virtual charts as a powerful tool to efficient optimization, inverse identification and real-time simulation. This parametric models follow an off-line/on-line strategy in which a high-dimensional parametric function is computed adding simulation settings (e.g., loads, boundary conditions, initial conditions, material properties, ...) as a extra-coordinates of the problem. Once the PGD solution is calculated in the off-line step, its on-line employment only requires particularizing the parametric solution for a desired set of parameter values. Consequently, this task can be performed very fast and repeatedly in real-time, by using light computing platforms such as smartphones or tablets [Bognet *et al.* 2012, Ghnatios *et al.* 2012b, Chinesta *et al.* 2013a]. In addition, inverse methods were addressed in [Gonzáles *et al.* 2012] in the context of real-time simulations and they were coupled with control strategies in [Ghnatios *et al.* 2012b] as a first step towards DDDAS.

In contrast to POD, which is *a posteriori* MOR technique, PGD is *a priori* methodology. For this reason, unlike *a posteriori* methods, PGD does not require snapshots or empirical realisations of the problem at hand to construct the ROM. Specifically, The PGD builds, by means of a successive enrichment strategy, a numerical approximation of the unknown fields in a separated form involving a priori unknown functions of individual or clustered coordinates of the problem.

As stated in [Cueto *et al.* 2016], the origin of Proper Generalized Decompositions, can be traced back to the so-called radial loading within the LATIN method [Ladeveze 1999] as a space-time separated representation in non-incremental structural mechanics solvers. Independently, Chinesta and coworkers in their seminal papers [Ammar *et al.* 2006, Ammar *et al.* 2007] developed a method for the solution of non-Newtonian fluid models defined in high-dimensional phase spaces that were soon identified as a generalization of the work by P. Ladeveze. PGD is constructed indeed upon a very old idea, the method of separation of variables or Fourier method for partial differential equations. But the main novelty lies in the ability of PGD for the construction of sums of separated functions a priori, i.e., without any prior knowledge on the solution nor the need for costly computer experiments or snapshots.

In addition to the references already cited, the following examples are suggested to the reader unfamiliar with the PGD for further research on the subject considering the great capabilities offered by this technology. For instance, PGD has enabled the development of efficient surgery simulators with haptic response [Niroomandi *et al.* 2013, Quesada *et al.* 2018] or it allowed complex simulations on handheld, deployed devices such as smartphones or tablets [Ghnatios *et al.* 2012b]. Furthermore, the PGD technology has important implications in augmented reality applications, paving the way to the possibility to include real-time simulations of complex physics.

1.2 Proper Orthogonal Decomposition

POD model reduction follows an offline-online strategy, where the reduced model is built once in the off-line phase and then used in the on-line phase. The off-line phase is concerned about the extraction and computing of the POD basis vectors in order to infer a low-dimensional description of the system. This involves:

- expensive simulations of the full model to generate the snapshots needed to compute the POD basis.
- projection of the full model onto the reduced subspace defined by the POD basis.
- if applicable: strategies to efficiently deal with nonlinear terms or/and parametric dependence

The first point is adressed in Section 1.2.1 while he other ones are revisited in Section 1.2.2.

1.2.1 Method of snapshots: Obtaining the POD basis

The following general full system model is considered:

$$\mathbf{E}(\boldsymbol{\mu})\frac{d\mathbf{u}}{dt} + \mathbf{G}(\boldsymbol{\mu})\mathbf{u} = f(\boldsymbol{\mu}, \mathbf{u}) \tag{1.1}$$

where $\mathbf{u} \in \mathbb{R}^n$ is the state vector of dimension n and $\boldsymbol{\mu} \in \mathbb{R}^{n_\mu}$ is a vector of n_μ parameters. The full model operators are $\mathbf{G}(\boldsymbol{\mu}) \in \mathbb{R}^{n\times n}$, $\mathbf{E}(\boldsymbol{\mu}) \in \mathbb{R}^{n\times n}$, and $f(\boldsymbol{\mu}, \mathbf{u}) \in \mathbb{R}^n$. The full system was written as a system of nonlinear ODEs to emphasize the general applicability of the POD technique.

It is worthy to mention that models of interest usually come from discretization of partial differential equations. For instance, if the following PDE is considered (with a single spatial variable):

$$u_t = \mathcal{L}u(x,t) + \mathcal{N}(u, u_x, u_{xx}; \boldsymbol{\mu}) \tag{1.2}$$

where $\mathcal{L}$ is a linear partial differential operator, $\mathcal{N}$ prescribes the generically non-linear evolution and:

$$u_t = \frac{\partial u}{\partial t},\ u_x = \frac{\partial u}{\partial x},\ u_{xx} = \frac{\partial}{\partial x}\Big(\frac{\partial u}{\partial x}\Big)$$

If a standard spatial discretization of Eq. (1.2) is carried out, evaluating the spatial variable x at $n >> 1$ points:

$$u_k = u(x_k, t), \text{ for } k = 1, \dots, n; \; u_x = \frac{u_{k+1} - u_{k-1}}{2\Delta x}; \; u_{xx} = \frac{u_{k+1} - 2u_k + u_{k-1}}{\Delta x^2}$$

Using standard finite-difference formulas, Eq. (1.2) is transformed in a equation which follows the general form of Eq. (1.1).

$$\frac{d\mathbf{u}}{dt} = \mathbf{L}\mathbf{u} + \mathbf{N}(\mathbf{u}, \boldsymbol{\mu}) \tag{1.3}$$

where: $\mathbf{u} = \begin{bmatrix} u_1 \\ \vdots \\ u_n \end{bmatrix}$, $\mathbf{L} \in \mathbb{R}^n$ and $\mathbf{N}(\cdot)$ prescribes the generically non-linear evolution.

Next, consider a set of n_s snapshots, $\mathbf{y}_1, \dots, \mathbf{y}_{n_s}$, which are state solutions computed at different instants in time and/or different parameter values. Here, $\mathbf{y}_j = \mathbf{u}(t_j; \boldsymbol{\mu}_j)$ denotes the j-th snapshot, where t_j and $\boldsymbol{\mu}_j$ are respectively the time and parameter values for the j-th snapshot.

In addition, let us consider $\mathbf{Y}$ as the matrix containing the n_s snapshots collected for our problem. Therefore, $\mathbf{Y} = [\mathbf{y}_1, \dots, \mathbf{y}_{n_s}] \in \mathbb{R}^{n \times n_s}$ is a matrix with rank $d \leq \min(n, n_s)$, where $\mathbf{y}_1, \dots, \mathbf{y}_{n_s}$ are column vectors. Further, let $\mathbf{Y} = \boldsymbol{\Xi}\boldsymbol{\Sigma}\mathbf{V}^\top$ be its singular value decomposition, where $\boldsymbol{\Xi} = [\boldsymbol{\xi}_1, \dots, \boldsymbol{\xi}_n] \in \mathbb{R}^{n \times n}$, $\mathbf{V} = [\mathbf{v}_1, \dots, \mathbf{v}_{n_s}] \in \mathbb{R}^{n_s \times n_s}$ are orthogonal matrices and the matrix $\boldsymbol{\Sigma} \in \mathbb{R}^{n \times n_s}$ has the form given by Eq. (1.5). Then for any $r = \{1, \dots, d\}$ the solution to following constrained optimization problem:

$$\begin{gathered} \max_{\tilde{\boldsymbol{\xi}}_1, \dots, \tilde{\boldsymbol{\xi}}_l \in \mathbb{R}^n} \sum_{i=1}^{r} \sum_{j=1}^{n_s} \left| \langle \mathbf{y}_j, \tilde{\boldsymbol{\xi}}_i \rangle_{\mathbb{R}^n} \right|^2, \\ \text{subject to } \langle \tilde{\boldsymbol{\xi}}_i, \tilde{\boldsymbol{\xi}}_j \rangle_{\mathbb{R}^n} = \delta_{ij} \text{ for } 1 \leq i, j \leq r, \end{gathered} \tag{1.4}$$

with the Kronecker Delta tensor defined as

$$\delta_{ij} = \begin{cases} 1, & \text{if } i = j, \\ 0, & \text{if } i \neq j, \end{cases}$$

is given by the singular vectors $\{\boldsymbol{\xi}_i\}_{i=1}^r$, i.e., by the first r columns of $\boldsymbol{\Xi}$. Moreover, the maximum value of Eq.(1.4) is given by the sum of the first r singular values of the diagonal matrix $\boldsymbol{\Sigma}$,

$$\begin{gathered} \boldsymbol{\Sigma} = \begin{pmatrix} \mathbf{D} & \mathbf{0} \\ \mathbf{0} & \mathbf{0} \end{pmatrix} \in \mathbb{R}^{n \times n_s}, \\ \mathbf{D} = \mathrm{diag}(\sigma_1, ..., \sigma_d) \in \mathbb{R}^{d \times d}. \end{gathered} \tag{1.5}$$

In Eq. (1.5), the diagonal entries are sorted in descending order.

The problem (1.4) consists in approximating all spatial coordinate vectors $\mathbf{y}_i$ of $\mathbf{Y}$ by a linear combination of normalized vectors as well as possible. The constraint of the problem serves to normalize the functions $\boldsymbol{\xi}_i$ and thus ensure the uniqueness of the solution. It also adds the property of orthonormality between the r functions which solves the problem.

The choice of r is usually based on heuristic considerations combined with observing the ratio between the modeled energy to the total energy contained in the system $\mathbf{Y}$, which is expressed by:

$$\zeta(r) = \frac{\sum_{i=1}^{r} \lambda_i}{\sum_{i=1}^{d} \lambda_i}. \tag{1.6}$$

Note also that $\sigma_i^2 = \lambda_i$.

In the present work, the constraint $1 > \zeta(r) > 0.9999$ is considered to construct the POD basis.

1.2.2 POD reduced order models

To derive the POD reduced model, the first step is to represent the full state in the reduced basis obtained in the previous Section:

$$\mathbf{u} \approx \boldsymbol{\Xi} \mathbf{u}_r \tag{1.7}$$

where $u_r \in \mathbb{R}^r$ is the reduced state vector containing the POD modal coefficients and $\boldsymbol{\Xi} \in \mathbb{R}^{n \times r}$ contains just the r columns employed to construct the POD model. Introducing the above approximation Eq. (1.7) into the full model equations leads to a residual, since generally the full order state will not lie exactly in the span of the reduced model basis. A Galerkin projection imposes orthogonality between the residual and the POD basis. Therefore, consider the Galerkin projection of the residual leading to the POD reduced model:

$$\mathbf{E}_r(\boldsymbol{\mu}) \frac{d\mathbf{u}_r}{dt} + \mathbf{G}_r(\boldsymbol{\mu}) \mathbf{u}_r = f_r(\boldsymbol{\mu}, \boldsymbol{\Xi} \mathbf{u}_r) \tag{1.8}$$

where the reduced model operators are $\mathbf{G}_r = \boldsymbol{\Xi}^\top \mathbf{G}\, \boldsymbol{\Xi} \in \mathbb{R}^{r \times r}$, $\mathbf{E}_r = \boldsymbol{\Xi}^\top \mathbf{E}\, \boldsymbol{\Xi} \in \mathbb{R}^{r \times r}$ and the nonlinear term is $f_r(\boldsymbol{\mu}, \mathbf{u}_r) = \boldsymbol{\Xi}^\top f(\boldsymbol{\mu}, \boldsymbol{\Xi} \mathbf{u}_r)$

If the non-linear term does not exist or it can be linearized, there are already huge advantages to be gained by using the above POD reduced model directly (Equation (1.8)). This is the case of the POD model of Chapter 7.

On the other hand, if f exists, it can be observed from Eq. (1.8) that the evaluation of $\mathbf{f}_r$ requires computations that involve the large dimension n, which can increase significantly the computational complexity when solving the POD reduced model. To deal with this problem, it is convenient to introduce an additional approximation that removes the direct dependence of f_r on $\boldsymbol{\Xi} \mathbf{u}_r$. The most successful methods to achieve this combine selective spatial sampling of $\mathbf{f}$ with an interpolation strategy. Among this class of methods, the Missing Point Estimation [Astrid *et al.* 2008] and Gauss Newton with approximated tensors (GNAT) [Carlberg *et al.* 2013] methods both build upon the gappy POD interpolation method [Everson & Sirovich 1995], while the Empirical Interpolation Method (EIM) of [Barrault *et al.* 2004] and its discrete variant, the Discrete Empirical Interpolation Method (DEIM) of [Chaturantabut & Sorensen 2010], conduct interpolation on a low dimensional basis for the nonlinear term. Furthermore, hyper-reduction methods are also developed to reduce the dimensionality (degrees of freedom) as well as the number of integration points of non-linear parameterized finite element models, thus addressing the non-linear term [Fritzen *et al.* 2016, Ryckelynck 2005, Hernández *et al.* 2014, Amsallem *et al.* 2014, Farhat *et al.* 2015, Chapman *et al.* 2017]. For the unfamiliar reader, the reading of the cited papers is suggested for a in-depth analysis of these methods.

To address an efficient handling of POD reduced model parametric dependence, it is also recommended the reading of [Benner *et al.* 2015] for a detailed discussion of the various ways of handling parametric dependence in ROMs.

It is also important to note that the selection of the snapshot set can affect significantly the POD basis and consequently, the resultant reduced order model. Optimal snapshot selection for the case of a time-dependent system is considered in [Kunisch, Karl & Volkwein, Stefan 2010], where the time locations of snapshots are chosen to minimize the error between the POD solution and the trajectory of the original dynamical system. In many cases the POD is used to create a ROM that targets a particular range of system behavior; in those cases, the snapshot set is chosen based on a sampling criterion of the full order model over the range of interest. Nevertheless, if the system depends on more than two-three parameters, difficulties can arise concerning the feasibility to obtain snapshots by brute-force sampling. In these scenarios, one can use sparse grid sampling or greedy sampling. For instance, [Bui-Thanh *et al.* 2008] use greedy sampling to derive a POD reduced model for a thermal problem with 21 parameters.

To end up, the reading of [Brunton & Kutz 2019] and [Chinesta *et al.* 2017] is strongly recommended for further information about research, advances and development concerning the POD.

1.3 Proper Generalized Decomposition

The cornerstone of the PGD is its ability to construct a solution composed of sums of separated functions *a priori*, i.e., without any prior knowledge on the solution nor the need for costly computer experiments or snapshots. To illustrate the PGD approach, the following example is considered. The sought function of a given PDE whose solution (u) is approximated in the PGD framework depending on space, time and a number n_μ of parameters, takes the form:

$$u(x,t,\mu_1,...,\mu_{n_\mu}) \approx u^M = \sum_{m=1}^{M} \vartheta_m^x(x)\cdot\vartheta_m^t(t)\cdot\vartheta_m^1(\mu_1)\cdots\vartheta_m^{n_\mu}(\mu_{n_\mu}) \tag{1.9}$$

where the functions ϑ_m^p are the ones determined during the PGD procedure and they are unknown *a priori*, μ_i refers to the parameters influencing the solution and M is the truncation level or number of modes.

In a more compact form, and considering a function with P dimensions $(s^1,...,s^P)$, the representation takes the form:

$$u^M(s^1,...,s^P) = \sum_{m=1}^{M}\prod_{p=1}^{P}\vartheta_m^p(s^p), \tag{1.10}$$

In fact, the PGD methodology can strongly alleviate the curse of dimensionality (by several orders of magnitude) through solving a Partial Differential Equation (PDE) or a set of PDEs in a high-dimensional space using the aforementioned separated representation. This allows the creation of high-dimensional and highly accurate multiparametric solutions that otherwise would be impossible to obtain.

To compute the above functions ϑ_m^p, a non-linear problem must be formulated. However, simple techniques have demonstrated to provide very good results [Dumon *et al.* 2011, Modesto *et al.* 2015, Nadal *et al.* 2015a, Zlotnik *et al.* 2015, Chinesta *et al.* 2010, Henneron & Clenet 2014, Chinesta *et al.* 2011, Cueto *et al.* 2016]. Usually, the approach is based on employing a greedy algorithm such that, once the approximation up to order $M-1$ is known, the new M-th order term is found using a non-linear solver (Picard, Newton, for instance). As stated in [Cueto *et al.* 2016], naive linearization strategies such as fixed point iterations usually provide very good results.

To illustrate how PGD deals with the curse of dimensionality, consider the following example. Imagine that N nodes are used to discretize each dimension Ω_j. Calling P to the total number of dimensions and M to the total number of modes (truncation level), the total number of unknowns for the PGD algorithm is $M \times N \times P$ instead of the N^P degrees of freedom involved in standard mesh-based discretizations. Furthermore, as stated in [Chinesta *et al.* 2013a], all numerical experiments carried out show that the number of terms M required to obtain an accurate solution is not a function of the problem dimension P, but it rather depends on the separable character of the exact solution. The PGD thus often avoids the exponential complexity with respect to the problem dimension. Indeed, usually a huge decrease in computational time is achieved to obtain highly accurate multi-parametric models that would otherwise be unimaginable.

Concerning dynamic problems, it is interesting to note the remarkable difference between the PGD strategy and traditional incremental time integration schemes. In fact, the PGD enables for a non-incremental solution of time-dependent problems. This way, time evolution is computed at the same time that the spatial response. In other words, the solution along the spatial dimensions is computed in the whole time interval simultaneously. This is significantly different from a standard, incremental solution procedure. If N_T is the total number of time steps needed to finish the numerical simulation, an incremental procedure involves the solution of a BVP in $\Omega_x \times \Omega_y \times \Omega_z$ at each time step, that is a total of N_T BVP's. This can be, in fact, a huge number as the time step Δt must be selected sufficiently small to guarantee the stability of the time-integration scheme. For this reason, in the scenario concerning 3D transient PDEs, the time savings when employing the PGD are able to be of many orders of magnitude.

Furthermore, it is worthy to mention that the PGD also allows additional features such as parametric domains or the possibility to add to the parametric models unusual variables such as loads, boundary condition or initial conditions, to cite only a few.

Next Section will detail the Separated representation constructor of the PGD.

1.3.1 Separated representation constructor

The problem formulation addressed in the present work (Section 4.2) involves the space and parameters separated representation. For the sake of completeness, this Section aims at illustrating in a simple case the construction of such a separated representation. This way, the followed mathematical procedure of the PGD can be detailed for the unfamiliar reader. For that purpose, we consider the 2D parametric problem

$$\nabla \cdot (\nabla u(x, y)) = g, \tag{1.11}$$

with uniform source term g, and homogeneous Dirichlet boundary conditions, defined in the separable domain $\Omega = \Omega_x \times \Omega_y$. We wish to compute *at once* a general solution of the problem for *all* values of g in a given interval of values Ω_g.

In the PGD framework, it is thus considered the source term g as an extra-coordinate, in addition to the space coordinates x and y. The problem (1.11) is now defined for $(x, y, g) \in \Omega_x \times \Omega_y \times \Omega_g$.

Thus, instead of solving a series of diffusion problems for different discrete values of the source term, we wish to solve at once a more general problem. The price to pay is of course an increase of the problem dimensionality. This is not a major issue for the PGD, whose computational complexity scales only linearly (and not exponentially) with the space dimension. Moreover, being the domain Ω separable, a fully separated representation can be envisaged, that reduces the parametric 2D problem to a sequence of three one-dimensional problems, the first involving the x-coordinate, the second the y-coordinate and the third and last, the g-extra-coordinate, as described in what follows.

The extended weighted residual form of (1.11) reads

$$\int_{\Omega_x\times\Omega_y\times\Omega_g} u^* \left(\frac{\partial^2 u}{\partial x^2}+\frac{\partial^2 u}{\partial y^2}-g\right) dx\ dy\ dg\ =\ 0, \tag{1.12}$$

for all suitable test functions u^*.

The separated form of the searched solution reads

$$u(x,y,g)=\sum_{m=1}^{N} X_m(x)Y_m(y)G_m(g), \tag{1.13}$$

where each term will be computed one at a time, enriching the PGD solution until reaching the convergence. Please note that, in order to facilitate the reading, the mathematical notation of the separated representation has been simplified in this example by doing $X_m = \vartheta_m^1$, $Y_m = \vartheta_m^2$ and $G_m = \vartheta_m^3$.

At step M of the PGD algorithm, the following approximation is assumed already calculated,

$$u^{M-1}(x,y,g)=\sum_{m=1}^{M-1} X_m(x)Y_m(y)G_m(g), \tag{1.14}$$

and wish to compute the functions involved in the M-mode, $X_M(x)$, $Y_M(y)$ and $G_M(g)$, according to

$$u^M = u^{M-1} + X_M(x)Y_M(y)G_M(g). \tag{1.15}$$

The weighted residual form (1.12) defines a non-linear problem which is solved iteratively. Each iteration k of the nonlinear solver consists of the three steps:

1. Compute $X_M^k(x)$ from the other two functions taken at the previous nonlinear iteration, i.e. $Y_M^{k-1}(y)$ and $G_M^{k-1}(g)$;
2. Compute $Y_M^k(y)$ from $X_M^k(x)$ and $G_M^{k-1}(g)$;
3. Compute $G_M^k(g)$ from $X_M^k(x)$ and $Y_M^k(y)$.

In what follows these three calculations are detailed.

- Computing $X_M^k(x)$ from $Y_M^{k-1}(y)$ and $G_M^{k-1}(g)$

  With the trial and test functions given by

$$u^{M,k}(x,y,g)=\sum_{m=1}^{M-1} X_m(x)Y_m(y)G_m(g) + X_M^k(x)Y_M^{k-1}(y)G_M^{k-1}(g), \tag{1.16}$$

  and

$$u^*(x,y,g)=X^*(x)Y_M^{k-1}(y)G_M^{k-1}(g), \tag{1.17}$$

  respectively, the weighted residual formulation reads

$$\int_{\Omega_x\times\Omega_y\times\Omega_g} X^*(x)Y_M^{k-1}(y)G_M^{k-1}(g)$$

$$\left(\frac{d^2X_M^k(x)}{dx^2}Y_M^{k-1}(y)G_M^{k-1}(g)+X_M^k(x)\frac{d^2Y_M^{k-1}(y)}{dy^2}G_M^{k-1}(g)\right)\ dx\ dy\ dg =$$

$$\int\limits_{\Omega_x \times \Omega_y \times \Omega_g} X^*(x) Y_M^{k-1}(y) G_M^{k-1}(g) \; \mathcal{R}^{M-1} \; dx \; dy \; dg, \tag{1.18}$$

where $\mathcal{R}^{M-1}$ is the residual related to $u^{M-1}(x,y,g)$,

$$\mathcal{R}^{M-1} = g - \sum_{m=1}^{M-1} \left(\frac{d^2 X_m(x)}{dx^2} Y_m(y) G_m(g) + X_m(x) \frac{d^2 Y_m(y)}{dy^2} G_m(g) \right). \tag{1.19}$$

Since all functions of the y-coordinate and the source term g-extra-coordinate are known, we can integrate (1.18) over $\Omega_y \times \Omega_g$, to obtain

$$\int\limits_{\Omega_x} X^*(x) \left(\alpha^{x,k} \frac{d^2 X_M^k(x)}{dx^2} + \beta^{x,k} X_M^k(x) - \gamma^{x,k} + \right.$$

$$\left. + \sum_{m=1}^{M-1} \left(\delta_m^{x,k} \frac{d^2 X_m(x)}{dx^2} + \xi_m^{x,k} X_m(x) \right) \right) \; dx \; = \; 0, \tag{1.20}$$

where coefficients $\alpha^{x,k}$, $\beta^{x,k}$, $\gamma^{x,k}$, $\delta_m^{x,k}$ and $\xi_m^{x,k}$ result from the integrals in $\Omega_y \times \Omega_g$ of the different products of functions $Y_m(y)$, $G_m(g)$, $Y_M^{k-1}(y)$ and G_M^{k-1} involved in Eq. (1.18).

With Eq. (1.20) valid for any function $X^*(x)$, we can extract its associated strong form

$$\alpha^{x,k} \frac{d^2 X_M^k(x)}{dx^2} + \beta^{x,k} X_M^k(x) = \gamma^{x,k} - \sum_{m=1}^{M-1} \left(\delta_m^{x,k} \frac{d^2 X_m(x)}{dx^2} + \xi_m^{x,k} X_m(x) \right), \tag{1.21}$$

whose solution results in the searched function $X_M^k(x)$.

- Computing $Y_M^k(y)$ from $X_M^k(x)$ and $G_M^{k-1}(g)$

  With the test function given by

$$u^*(x,y,g) = X_M^k(x) Y^*(y) G_M^{k-1}(g), \tag{1.22}$$

and following the same rationale than previously, after integrating the weighted residual form in $\Omega_x \times \Omega_g$ and extracting the resulting strong form, we obtain

$$\alpha^{y,k} \frac{d^2 Y_M^k(y)}{dy^2} + \beta^{y,k} Y_M^k(y) = \gamma^{y,k} - \sum_{m=1}^{M-1} \left(\delta_m^{y,k} \frac{d^2 Y_m(y)}{dy^2} + \xi_m^{y,k} Y_m(y) \right). \tag{1.23}$$

- Computing $G_M^k(g)$ from $X_M^k(x)$ and $Y_M^k(y)$

  Finally, with the test function given by

$$u^*(x,y,g) = X_M^k(x) Y_M^k(y) G^*(g), \tag{1.24}$$

and following the same rationale than previously, after integrating the weighted residual form in $\Omega_x \times \Omega_y$ and extracting the resulting strong form, we obtain

$$\beta^{g,k} G_M^k(g) = \gamma^{g,k} g - \sum_{m=1}^{M-1} \xi_m^{g,k} G_m(g). \tag{1.25}$$

The described alternating direction strategy can be started, for instance, from an arbitrary initial guess $(Y_M^0,\ K_M^0)$. Then, these non-linear iterations proceed until reaching a fixed point within a user-specified tolerance ϵ, i.e.:

$$\left\|X_M^k(x)\cdot Y_M^k(y)\cdot G_M^k(g) - X_M^{k-1}(x)\cdot Y_M^{k-1}(y)\cdot G_M^{k-1}(g)\right\| < \epsilon$$

or

$$\frac{\left\|X_M^k(x)\cdot Y_M^k(y)\cdot G_M^k(g) - X_M^{k-1}(x)\cdot Y_M^{k-1}(y)\cdot G_M^{k-1}(g)\right\|}{\left\|X_M^{k-1}(x)\cdot Y_M^{k-1}(y)\cdot G_M^{k-1}(g)\right\|} < \epsilon$$

where $\|\cdot\|$ is a suitable norm. The enrichement step M ends with the assignments $X_M(x) \leftarrow X_M^k(x)$, $Y_M(y) \leftarrow Y_M^k(y)$ and $G_M(g) \leftarrow G_M^k(g)$. Furthermore, the enrichment process itself stops when an appropiate measure of error $\mathcal{E}(M)$ becames small enough, i.e. $\mathcal{E}(M) < \tilde{\epsilon}$. As an example, one can use:

$$\mathcal{E}(M) = \frac{\|X_M(x)\cdot Y_M(y)\cdot G_M(g)\|}{\|X_1(x)\cdot Y_1(y)\cdot G_1(g)\|} \tag{1.26}$$

where $\|\cdot\|$ is a suitable norm. Selecting for example the L^2-norm:

$$\begin{aligned}\|X_M(x)\cdot Y_M(y)\cdot G_M(g)\|_2 &= \left(\int_{\Omega_x\times\Omega_y\times\Omega_g}\Big(X_M\cdot Y_M\cdot G_M\Big)^2\,dx\,dy\,dg\right)^{\frac{1}{2}}\\ &= \left(\int_{\Omega_x}\Big(X_M\Big)^2\,dx\right)^{\frac{1}{2}}\cdot\left(\int_{\Omega_y}\Big(Y_M\Big)^2\,dy\right)^{\frac{1}{2}}\cdot\left(\int_{\Omega_g}\Big(G_M\Big)^2\,dg\right)^{\frac{1}{2}}\end{aligned}$$

The aforementioned criterion (Eq. (1.26)) is based on the fact that the PGD constructor starts adding the most significant modes by progressively decreasing their importance at each enrichment. This way, the norm of the first mode (*a priori*, the most significant one) is compared with the current mode. If the norm of this newly computed mode is sufficiently small, the enrichment step is considered over because its inclusion in the final solution will not be significant.

Furthermore, one can apply other stopping criteria discussed in [Ladevèze & Chamoin 2011, Nadal *et al.* 2015b, de Almeida 2013, Chinesta *et al.* 2013a].

To end up, it is worthy to mention that following the same methodology, the discussed procedure can easily be extended for more complex settings such as the consideration of more parameters or the inclusion of the temporal dimension.

1.4 Summary

This chapter discussed the motivation of intrusive MOR techniques and it referenced its development in relation to the two techniques employed in the present work: the POD and the intrusive PGD. In additional, the achievements that can be obtained with the above techniques were highlighted as well as their differences and range of application.

A special focus was made on the theoretical basis of both techniques to understand how they are applied in Chapters 4, 5 and 7 of this thesis.

Concerning the POD, the method used to obtain the POD basis was shown in Section 1.2.1, and then its implementation in the mathematical equations was discussed in Section 1.2.2.

On the other hand, in Section 1.3.1, the PGD procedure is illustrated for a case which involves the space and parameters separated representation, which is the scenario adressed in Chapter 4.

This way, the information presented in this Chapter is sufficient to understand and follow the application of these techniques in the present work.

Furthermore, given the extensive literature and theory, references are also provided for further knowledge and for an in-depth analysis for those readers who are interested.

Part II

Fundamentals: Presentation of novel non-intrusive and data-driven techniques.

Chapter 2

Novel reduced order formulations, algorithms and hybridation/dynamic techniques.

Abstract Non-intrusive MOR techniques are mainly employed to approximate the numerical solution of parametric models. In fact, they are straightforwardly applicable to challenging problems characterized by nonlinearity or non affine weak forms. In addition, they can be interfaced with no particular effort to existing third party simulation software making them particularly appealing and adapted to practical engineering problems of industrial interest. They are also of crucial interest within the Dynamic Data Driven Application Systems framework. These techniques usually must face problems related to the expensiveness of data (economically or computationally). Specifically, data scarcity and sparsity. Nowadays, moreover, the demand of this type of solutions is skyrocketing due to the digital and data revolution and consequently novel approaches are being researched, tested and proposed to deal with the increasingly number of challenging scenarios. Thus, the present Chapter is going to present novel techniques to improve and enhance results in such cases (with the exception of the novel PGD methodologies which will be described in Chapter 3).

Furthermore, nowadays machine learning, artificial intelligence and Big Data are cutting-edge topics applied in a wide variety of fields. It becomes thus mandatory to explore the benefits of applying some of these techniques in the framework of this dissertation. In particular, this Chapter is going to present novel strategies to construct the HT paradigm. Specifically, the proposed approaches guarantee the employement of stable time-integrators to provide fast and accurate corrections as well as the ability to adress complex behaviours. This will bring substantial improvements and better possibilities for the DDDAS framework.

Contents

2.1 Introduction 40
2.2 The Sparse Proper Generalized Decomposition 41
    2.2.1 Introduction 41
    2.2.2 s-PGD methodology: Basis of the technique 42
2.3 A novel sparse reduced order formulation: the s-PGD + RB strategy 44
2.4 A novel unwrapping algorithm for accurately addressing interpolation of complex numbers 47
    2.4.1 Introduction to phase unwrapping 47
    2.4.2 Proposed approach. Part I: Phase unwrapping in smooth parametric settings. 47
        2.4.2.1 Description 47

2.4.2.2 Comparing the proposed algorithm with traditional unwrapping . . . 48
2.4.2.3 Robustness issues . . . 49
2.4.3 Proposed approach. Part II: Improving the robustness of phase unwrapping . . . 51
2.4.3.1 Introduction . . . 51
2.4.3.2 Reduced basis of the search space . . . 51
2.4.3.3 Phase unwrapping in the reduced search space . . . 52
2.4.3.4 Validation of the optimization procedure . . . 52
2.4.4 Convergence . . . 53
2.5 Novel hybridation and dynamic strategies . . . 54
2.5.1 Introduction. . . . 54
2.5.2 Hybrid Twins. The big picture. . . . 55
2.5.3 An efficiently learning of dynamical systems: The stabilized DMD and DMDc techniques. . . . 55
2.5.4 The DMD Dictionary strategy . . . 59
2.6 Summary and Conclusions . . . 61

2.1 Introduction

The motivation, context and advances which led to the emergence of the non-intrusive and data-driven techniques was exposed in Section 0.1 of the Introduction Chapter.

In this Chapter, the novel non-intrusive techniques developed during this dissertation to face the industrial problems described in Chapters 4, 5, 6 and 7 are presented. In particular, the theoretical basis of these data-driven methodologies is detailed. Other techniques, such as those relevant to the understanding of the proposals presented, are also reviewed.

Firstly, this chapter begins by continuing and reviewing the theoretical foundations of the sparse PGD (s-PGD) from a machine learning point of view. In the following chapters, this technique will be employed to construct novel ROMs in different industrial applications. Furthermore, later on in Chapter 3, this framework will be taken as a basis for developing novel PGD methodologies to overcome the limitations of the current state of the art in challenging scenarios.

Secondly, this thesis introduces a novel sparse reduced order formulation combining the s-PGD with a Reduced Basis (RB) approach. We will see (in Chapter 4) how the proposed strategy can be employed to capture complex and challenging physical phenomena as well as to obtain a further data compression.

Next, a novel algorithm for phase-angle unwrapping for accurately addressing interpolation of complex numbers is proposed. This new and effective strategy was constructed during this thesis when addressing the problem encountered in Chapter 5 and compared with state-of-the-art techniques as the ones implemented in Matlab software [MathWorks 2020].

Subsequently, the techniques proposed for hybridization in the HT context are presented. Specifically, this thesis proposes two novel methodologies, the practical application of which is carried out in Chapters 6 and 7.

- The first one is a stabilization procedure for the DMD and DMDc techniques. The goal of this first methodology is the computation of stable, fast and accurate corrections in the Hybrid Twin framework, regarding the delicate and important problem of stability. In addition, several sub-variants are introduced to guarantee a low computational cost as well as the achievement of a stable time-integration.

- The second one is the DMD Dictionary strategy which allow us to address complex non-linear behaviors within the DMD framework. Moreover, this method is able to produce models that avoid over-fitting quite well, correcting only the operation ranges with more error.

Moreover, prior to the mentioned new strategies, a big picture of the HT is discussed and the standard procedures for the DMD and DMDc are introduced.

To end up and to sum up, this chapter presents four disruptive and innovative methodologies:

- A novel sparse reduced order formulation combining the s-PGD with a Reduced Basis (RB) approach: the s-PGD + RB strategy. (Section 2.3)
- A novel unwrapping algorithm for accurately addressing interpolation of complex numbers. (Section 2.4)
- The stabilized DMD and DMDc techniques. (Section 2.5.3)
- The DMD Dictionary strategy. (Section 2.5.4)

These topics contain the theoretical part addressed in the following published articles, which constitute this chapter:

1. A. Sancarlos, M. Cameron, A. Abel, E. Cueto, J.L. Duval, F. Chinesta, "From ROM of Electrochemistry to AI-Based Battery Digital and Hybrid Twin," *Archives of Computational Methods in Engineering* , vol. 28, pp. 979–1015, 2021. DOI: https://doi.org/10.1007/s11831-020-09404-6.
2. S. Vermiglio, V. Champaney, A. Sancarlos, F. Daim, J.C. Kedzia, J.L. Duval, P. Diez, F. Chinesta, "Parametric Electromagnetic Analysis of Radar-Based Advanced Driver Assistant Systems," *Sensors*, vol. 20, issue 19, 2020. DOI: https://doi.org/10.3390/s20195686
3. A. Sancarlos, E. Cueto, F. Chinesta, J.L. Duval, "A novel sparse reduced order formulation for modeling electromagnetic forces in electric motors," *SN Appl. Sci.*, vol. 3, issue 3, 2021. DOI: https://doi.org/10.1007/s42452-021-04310-3.
4. A. Sancarlos, M. Cameron, J.M. Le Peuvedic, J. Groulier, E. Cueto, F. Chinesta, J.L. Duval, " Learning stable reduced-order models for hybrid twins," *Data-Centric Engineering*, Submitted.

2.2 The Sparse Proper Generalized Decomposition

2.2.1 Introduction

This Section presents an overview of the sparse Proper Generalized Decomposition (s-PGD in what follows) to generate response surface based on scattered data. This type of methodologies are of crucial importance within the data-driven framework whenever the data has to be interpolated/extrapolated to infer behaviours at locations where there are no experimental measurements. Initially, the s-PGD was presented as a combination of the PGD rationale together with a collocation procedure [Ibáñez Pinillo *et al.* 2018, Ibanez Pinillo 2019]. However, in this dissertation, we present this technique in a different way, that is, from a machine learning point of view. This will allow us to lay the groundwork for developing new PGD techniques (see Chapter 3) to boost performance in challenging scenarios. It is worthy to mention that this technique is employed when constructing high-dimensional parametric models. In fact, if an usual response surface-like approach is chosen under this setting, a large sampling effort is to be expected, that grows exponentially with the number of parameters. For this reason, a method able to circumvent the so-called curse of dimensionality should be used [Laughlin & Pines 2000]. This is one of the contexts where the s-PGD has one of its greatest strengths. The reason is that this methology alleviates the curse of dimensionality by means of the separation of variables and it makes use of the data only at the experimental sample points.

2.2.2 s-PGD methodology: Basis of the technique

The reader unfamiliar with the standard Proper Generalized Decomposition (PGD) method for solving PDEs, is directed to review the Chapter 1 of the present thesis. In this Section a brief exposition of the s-PGD is presented from a regression point of view. After discussing the s-PGD basis, the novel approach will be presented in Section 2.3. Here, let us consider an unknown function:

$$f(s^1, ..., s^P) : \Omega \subset \mathbb{R}^P \to \mathbb{R},$$

which depends on P different variables, considered as dimensions of the state space s^p, $p = 1, \dots, P$.

The sparse PGD (s-PGD) approach tries to approximate the function f using a separated (tensor) representation. As in standard PGD procedures, it expresses the function f using a sum of products of one-dimensional functions each one involving one dimension. Each sum is called a mode.

In the context of regression problems, the goal is to find a function $\tilde{f}$ which minimizes the distance to the sought function

$$\tilde{f} = \arg\min_{f^*} \sum_{i=1}^{n_t} \| f(\mathbf{s}_i) - f^*(\mathbf{s}_i) \| , \tag{2.1}$$

and that takes the separated form

$$\tilde{f}(s^1, ..., s^P) = \sum_{m=1}^{M} \prod_{p=1}^{P} \vartheta_m^p(s^p), \tag{2.2}$$

where M is the number of modes and ϑ_m^p is the one-dimensional function of the mode m and dimension p. n_t is the number of sampling points to perform the regression and $\mathbf{s}_i$ are the different vectors which contain the data points of the training set. $\|\cdot\|$ is the chosen norm to measure the distance between two points.

The other objective is that the function $\tilde{f}$ has to perform as well in the training set as in other possible test sets. This second goal is more difficult to achieve, yet is more important because this evaluates the predictive ability of the model $\tilde{f}$, that is, the capacity to have good predictions when the model is fed with untrained data. Achieving this is particularly difficult when confronted with a high-dimensional problem, which provides sparse data.

The s-PGD methodology is based on creating a function $\tilde{f}$ with the separated form expressed by (2.2). Then, the functions $\{\vartheta_m^p\}_{m=1}^{M}$ for each p are formed by a linear combination of a set of basis functions:

$$\vartheta_m^p(s^p) = \sum_{j=1}^{D} N_{j,m}^p(s^p) a_{j,m}^p = (\mathbf{N}_m^p)^\top \mathbf{a}_m^p, \tag{2.3}$$

where D represents the degrees of freedom of the chosen approximation. In addition, $\mathbf{N}_m^p$ is a column vector with the set of basis functions for the p dimension and the m-th mode and $\mathbf{a}_m^p$ is a column vector with the coefficients for the p dimension and the m-th mode. The important issue here is to know which set of basis functions are best suited for the problem at hand. For example, a Fourier basis or a polynomial basis can be selected.

The determination of the coefficients in each one-dimensional function for each mode $m = 1, \ldots, M$ is done by employing a greedy algorithm such that, once the approximation up to order $M-1$ is known, the new M-th order term is found using a non-linear solver (Picard, Newton, for instance):

$$\tilde{f}^M = \sum_{m=1}^{M-1} \prod_{p=1}^{P} \vartheta_m^p(s^p) + \prod_{p=1}^{P} \vartheta_M^p(s^p). \tag{2.4}$$

A standard choice is to select the same basis for each one of the modes:

$$\mathbf{N}_1^p = \mathbf{N}_2^p = \ldots = \mathbf{N}_M^p, \text{ for } p = 1, \ldots, P. \tag{2.5}$$

This choice may seem reasonable, however it may not be appropriate when dealing with non-structured sparse data.

It is known that the cardinality of the interpolation basis must not exceed the maximum rank provided by the training set. Indeed, this constraint, which provides an upper bound to build the interpolation basis, only guarantees that the minimization is satisfied by the training set, without saying anything of the other points. Hence, if there is not an abundance of sampling points in the training set, in the low-data limit, high oscillations may appear out of these measured points because of the increased risk of overfitting. Usually, this is an undesirable effect because it affects the predictive ability of the constructed regression model.

In order to tackle this problem, the s-PGD uses the Modal Adaptivity Strategy (MAS) to take advantage of the greedy PGD algorithm. The idea is to minimize spurious oscillations out of the training set by starting the PGD algorithm looking for modes with low order degree. When it is observed that the residual decreases slowly or stagnates, higher order approximation functions are introduced. By doing this, oscillations are reduced, since a higher-order basis will try to capture only what remains in the residual.

To deploy the strategy, an indicator and a stopping criterion has to be defined. Many different strategies can be envisaged. Here, it is employed that defined in references [Ibáñez Pinillo *et al.* 2018, Ibanez Pinillo 2019], where the methodology of the s-PGD is deeply described. Following that reference, the following norm is used for the PGD residual in the present work:

$$\mathcal{R}_T^M = \frac{1}{\sqrt{n_t}} \sqrt{\sum_{i=1}^{n_t} \left(f(\mathbf{s}_i) - \tilde{f}^M(\mathbf{s}_i) \right)^2}, \tag{2.6}$$

where $\mathcal{R}_T^M$ is the residual of the PGD solution of M modes in the training set T and $\tilde{f}^M$ is the PGD solution composed of M modes.

Then, for each $\tilde{f}^M$, it is defined,

$$\Delta\mathcal{R}_T^M = \mathcal{R}_T^M - \mathcal{R}_T^{M-1} < \epsilon_r, \tag{2.7}$$

where ϵ_r is a tolerance defining the resilience of the s-PGD to increase the cardinality of the interpolation basis. The lower ϵ_r is, the more resilient the method is to increase the cardinality.

For the interested reader, the aforementioned reference [Ibanez Pinillo 2019] is recommended for further information.

2.3 A novel sparse reduced order formulation: the s-PGD + RB strategy

Regarding the compactness, robustness and simplicity of the PGD models obtained by the s-PGD technique, global polynomial basis are usually selected to use the s-PGD explained in Section 2.2 (although other options such as Kriging interpolants are also employed).

As it is well known, polynomials are differentiable functions for all arguments. Therefore, trying to capture a differentiable function using polynomials is, above all, a consistent idea because the function which wants to be captured has the same properties that the basis where is projected.

In fact, according to the Weierstrass approximation theorem, if f is a continuous real-valued function on $[a, b]$, for a given ϵ, then there exists a polynomial p on $[a, b]$ such that:

$$\mid f(x) - p(x) \mid < \epsilon, \tag{2.8}$$

for all $x \in [a, b]$. In words, any continuous function on a closed and bounded interval can be uniformly approximated on that interval by polynomials to any degree of accuracy. However, sometimes the function which is trying to be captured is not a differentiable function in some points or even presents discontinuities.

In this case, global polynomials are far away to be the best choice to approach this type of functions because they are, in fact, very poor at interpolating discontinuities. To demonstrate this, Figure 2.1 shows the interpolation of the unit step function with 16 points using a 15th-degree polynomial.

Two different solutions to the problem can be envisaged. The first one is to use piecewise polynomial interpolation. This way, we can use different polynomials to approach the function at the right and at the left of the discontinuity. For example, the step function of the previous example will be composed of:

$$f(x) = \begin{cases} 0 & x \in [-1, 0], \\ 1 & x \in (0, 1], \end{cases} \tag{2.9}$$

which are zero degree polynomials. However, an issue of this type of approaches is its rank deficiency when combined with the sparsity used in the s-PGD [Ibáñez Pinillo *et al.* 2018].

Other possible solution is to use a basis (which can contain discontinuous functions) whose linear combination produces the class of discontinuities of our problem in the right places.

For instance, a basis composed of different step functions can be used to approximate the unitary step function discussed during this example.

In the industrial problem that the present work is dealing with in Chapter 4 (Section 4.3), discontinuities change their place in space when changing some values in the parameter space. Therefore, the previous discussed basis approach is prefered to deal with the discontinuity problem.

Other issue is that if we try to capture a non-regular function of this type without having preliminary knowledge of the system, a lot of nodes are needed to detect where and how these singular points are present in the dimension where this behaviour happens.

Therefore, to deal with the previous discussed issues, the following approach is proposed:

1. Find the spatial dimension(s) where singular points are placed.
2. Detect parameter(s) which can change location of the singular points along spatial dimension/s.

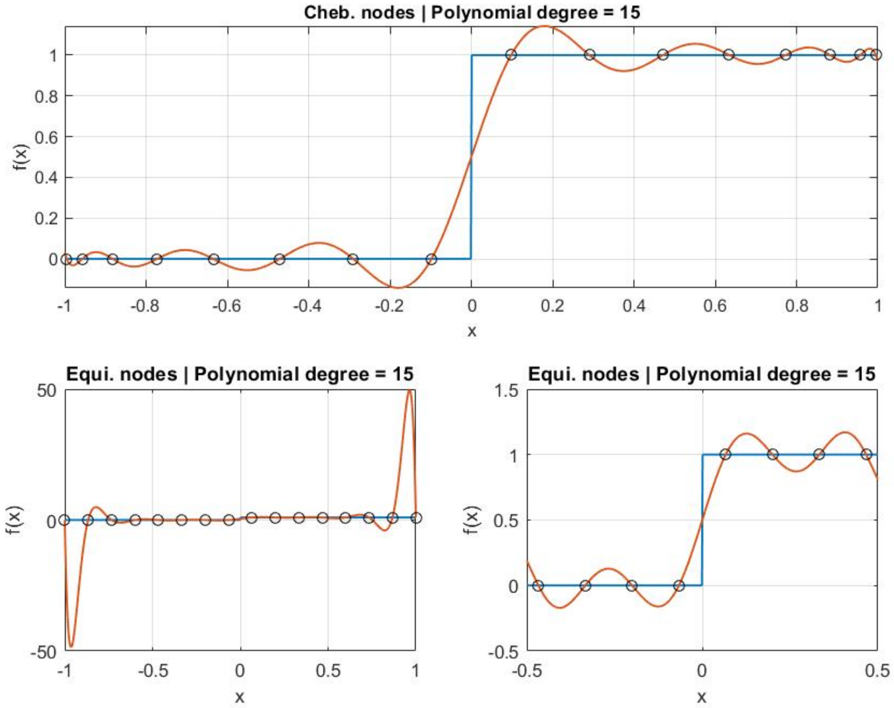

Figure 2.1 – Approximating a unitary step function using global polynomials. In the first case, Chebyshev nodes are used to fit the polynomial. In the second case, equidistant nodes are used.

3. Construct a RB considering the non-regular dimensions found in steps one and two. Not sparse sampling will be used along the dimension/s contained in the RB.

To insert the RB in the PGD procedure, we propose to reformulate the regression problem in the following way, where without loss of generality only one dimension (s^1) is assumed causing troubles:

$$\tilde{f}(s^1, ..., s^P) = \beta^1(s^2, \ldots, s^P) \cdot N_1(s^1) + \quad \cdots \quad + \beta^r(s^2, \ldots, s^P) \cdot N_r(s^1), \tag{2.10}$$

where:

$$\beta^j(s^2, \ldots, s^P) = \sum_{m=1}^{M_j} \prod_{p=2}^{P} \vartheta^p_{m,j}(s^p), \quad j = 1, 2, \ldots, r. \tag{2.11}$$

$N_1(s^1), \ldots, N_r(s^1)$ form the RB obtained with the SVD (see Section 1.2.1) along the s^1 dimension, the $\beta^j(s^2, \ldots, s^P)$ terms represent the unknown functions for the s-PGD problem for a given N_j, M_j is the number of modes used to decompose β^j and $\sum_{j=1}^{r} M_j$ is the total number of modes of the ROM.

The training set is then used to obtain the reduced basis as well as the value of the β^j coefficients in the training points. In addition, once these points are obtained, the s-PGD procedure is used to obtain the separated representation of these functions using polynomial basis according to Eq.(2.11). To obtain the RB, the method of snapshots, revisited in Section 1.2.1, is employed according to the discussion that follows.

Defining $\mathbf{z}_i$ as a point in the dimensions $(s^2, \ldots, s^P)$ then, the set $\mathcal{Y}$ of one-dimensional functions, created by the points belonging to the training set $\mathcal{T}$, can be defined as:

$$\mathcal{Y} = \{f(s^1, \mathbf{z}_i) : \mathbf{z}_i \in \mathcal{T}\}. \tag{2.12}$$

Therefore, the set $\mathcal{Y}$ is created collecting the one-dimensional functions for the different points which are selected for the training set $\mathcal{T}$ to do the regression via s-PGD.

Consequently, the snapshots in $\mathcal{Y}$ are the ones used to construct the matrix $\mathbf{Y}$ (see Section 1.2.1). Then, the SVD can be used to extract a reduced basis $\{\mathbf{N}_m\}_{m=1}^r$, which best approximates the set $\mathcal{Y}$.

Furthermore, the methodology described above can also be applied to address other types of problems. For instance, if one wants to create a parametric model for a crash test (See Figure 1), the solution in spatial coordinates may be hardly separable in the PGD framework. In these cases, a more interesting route is to not separate the spatial dimensions and create a reduced basis for compressing the snapshot information along these coordinates. In this case, the procedure described in Eq. (2.10) would also be employed with a reduced basis for the spatial dimensions.

To end up, an important issue is the choice of arguments of the parametric model. They must be independent or poorly correlated to avoid increasing the redundancy and the complexity of the model without necessity.

Industrial and technical knowledge can be used to determine the appropriate choice of variables as it is the case in this work. If not, a Manifold Learning (such as kernel-PCA, [Schölkopf *et al.* 1999]) or a dimensionality reduction technique (viz. Topological Data Analysis, [Wasserman 2018]) can be applied to reduce unnecessary variables. In addition, the ANOVA analysis can also be carried out to determine the importance of each input to keep the most relevant ones.

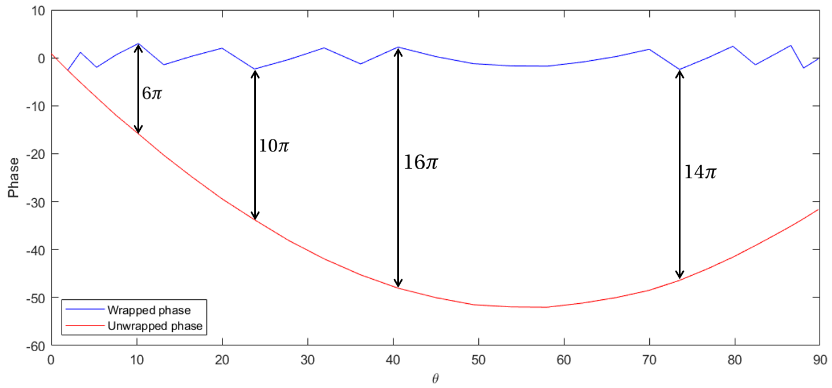

Figure 2.2 – Example of successful phase unwrapping

2.4 A novel unwrapping algorithm for accurately addressing interpolation of complex numbers

2.4.1 Introduction to phase unwrapping

Let $\psi(\theta)$ be a complex function which depends on a parameter θ and let $\text{Arg}(\cdot)$ be the function which returns the phase value of a complex number in the interval $(-\pi, \pi]$. Note that the argument of a complex number is not uniquely defined, and any other range $((k-1)\pi, (k+1)\pi]$ for $k \in \mathbb{Z}$ will be a valid interval. Usually, the phase value of the signal/physics-system can be expressed, in most practical cases, as a continuous function $\phi(\theta)$. However, the $\text{Arg}(\cdot)$ function will keep the phase in $(-\pi, \pi]$ even if the sought phase values leaves it, creating strange discontinuities. Consequently, trying to interpolate the phase function when such discontinuities happen results in a poor interpolation performance.

Therefore, the term phase unwrapping refers to the reconstruction of a "physically-meaningful" representation of the phase (as a function of the parameter θ) by adding multiples of 2π to some of its values in order to make it a continuous function. This step is very important because it determines the number of periods between two successive values of θ, regardless of the interpolation method used. Then, the unwrapped phase can be defined as the unique representation of the phase which can lead to a correct continuous interpolation. Unwrapping has been extensively addressed, the interested reader is referred to [Costantini *et al.* 2012, Shanker & Zebker 2010] and the numerous references therein.

The goal is to find a sequence $(k_n)_{1\leq n\leq N_\theta} \in \mathbb{Z}^{N_\theta}$, such that the unwrapped phase $\phi \in \mathbb{R}^{N_\theta}$ verifies:

$$\forall n \in [1, N_\theta], \quad \phi_n = \text{Arg}(\psi(\theta_n)) + 2k_n\pi$$

under some regularity constraint. Note that in the above expression N_θ refers to the number of points in the θ discretization.

2.4.2 Proposed approach. Part I: Phase unwrapping in smooth parametric settings.

2.4.2.1 Description

The proposed solution consists of assuming the derivative of the phase does not vary too much, or, to put it another way, that the second derivative remains small. The selection

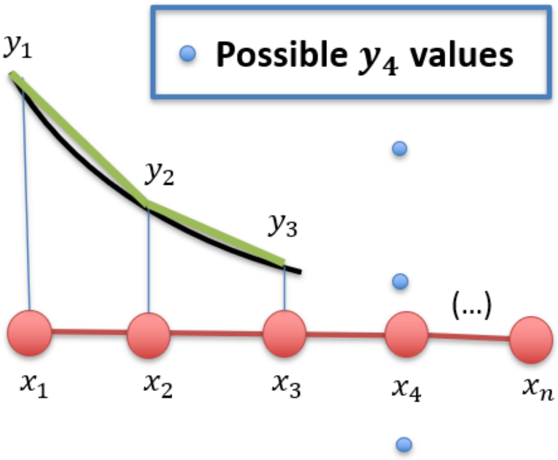

Figure 2.3 – Thought experiment: the function $y(x)$ is wanted to be unwrapped. Which of the possible blue points would you give as valid phase value for y_4?

of this criterion can be interpreted as a way to impose smoothness on the reconstructed construction, as smoothing splines do when penalizing the second derivative. Then, the reason of this choice is straightforward: smooth solutions can be interpolated more easily and with fewer data points.

The above hypothesis leads to a minimization of the variation of the derivative using a finite differences scheme to compute sequentially the values of the unwrapped phase:

$$\begin{aligned} & k_1 = 0, \\ & k_2 = \underset{k\in\mathbb{Z}}{\operatorname{argmin}} \quad \left|\operatorname{Arg}(\psi(\theta_2)) + 2k\pi - \phi_1\right|, \\ \forall n \geq 3, \quad & k_n = \underset{k\in\mathbb{Z}}{\operatorname{argmin}} \quad \left|\frac{\operatorname{Arg}(\psi(\theta_{n+1})) + 2k\pi - \phi_n}{\theta_{n+1} - \theta_n} - \frac{\phi_n - \phi_{n-1}}{\theta_n - \theta_{n-1}}\right|. \end{aligned} \tag{2.13}$$

Note that θ_2 must be chosen close enough to θ_1 to ensure $|\phi_2 - \phi_1| < \pi$. This algorithm can also be run in descending n order, for example to avoid initialization in a noisy area.

Imagine the following thought experiment to better understand conceptually the idea of the algorithm. Assume that the function $y(x)$ of the Figure 2.3 is wanted to be unwrapped. Which of the possible blue points would you give as valid phase value for y_4? Intuitively, we would select the middle one, that is, the one that minimizes the change of the first derivative in the function.

The proposed phase unwrapping algorithm, once applied to a problem, produces a very smooth curve, which allows great performance for interpolation (Fig. 2.2).

2.4.2.2 Comparing the proposed algorithm with traditional unwrapping

To illustrate the advantages of the just introduced methodology, the function having as unwrapped form

$$\phi = (\theta + 10)(\theta - 90)(\theta - 45)/k_f \tag{2.14}$$

with $k_f = 3000$, is considered.

Figure 2.4 depicts the wrapped counterpart of the above function. For unwrapping it, the proposed algorithm is compared with the standard procedure included in the commercial

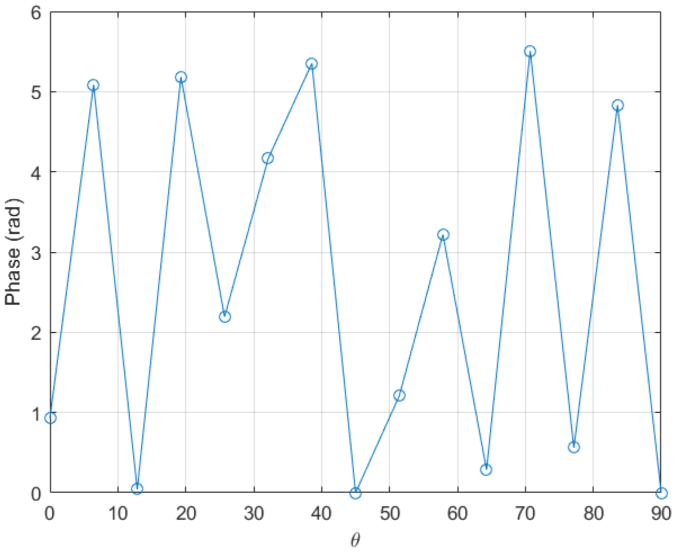

Figure 2.4 – Original wrapped function

.

software Matlab, the unwrap() function. The Matlab function applies when the difference between consecutive angles is greater than π, and shifts the angles by adding multiples of $\pm 2\pi$ until the difference becomes less than π [MathWorks 2020]. As noticed that function achieves a good unwrapping if a fine enough mesh is used (involving more than 35 nodes). However, the Matlab function fails to perform correctly in the case of coarser meshes (less than 30 nodes).

On the other hand, the procedure proposed in this dissertation achieves good results with only 15 nodes, as it can be seen in Figure 2.5, with the associated computing time saving.

In order to check the performances when the derivatives involved in the solution increase, the previous function is considered while increasing the factor $1/k_f$ of 20 % and 50 %, with the same coarse mesh consisting of 15 nodes. The comparison is shown in Figures 2.6 and 2.7. As it can be noticed, the proposed procedure seems quite robust when compared with traditional unwrapping.

2.4.2.3 Robustness issues

We have just seen how the proposed algorithm can improve the results of standard commercial libraries. In fact, it performs extremely well on relatively smooth data. However the robustness can be improved when dealing with more difficult scenarios. For instance:

1. Even with very regular data, the phase can have a chaotic behavior when the magnitude is close to zero, which means that the hypothesis on the regularity of the phase is not valid.
2. Since the different phase values are computed sequentially using the previous ones, local irregularities result in high global error.

However, because a failure of the method is caused by the invalidity of the hypothesis,

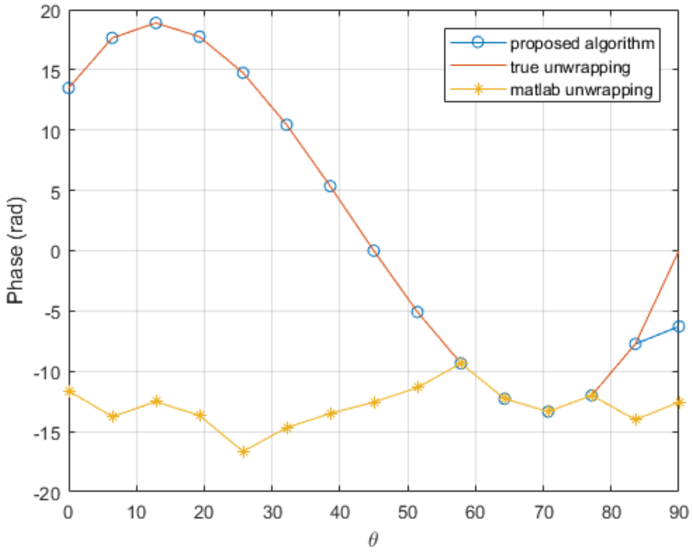

Figure 2.5 – Comparison of the proposed unwrapping procedure and the standard unwrapping function implemented in Matlab, in a coarse mesh consisting of 15 nodes.

.

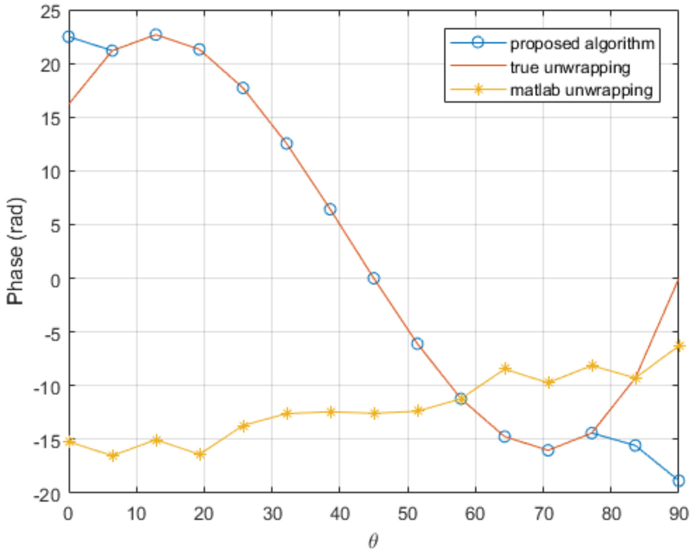

Figure 2.6 – Comparison of the proposed procedure and the Matlab unwrapping function in a coarse mesh consisting of 15 nodes with the $1/k_f$ factor 20% higher

.

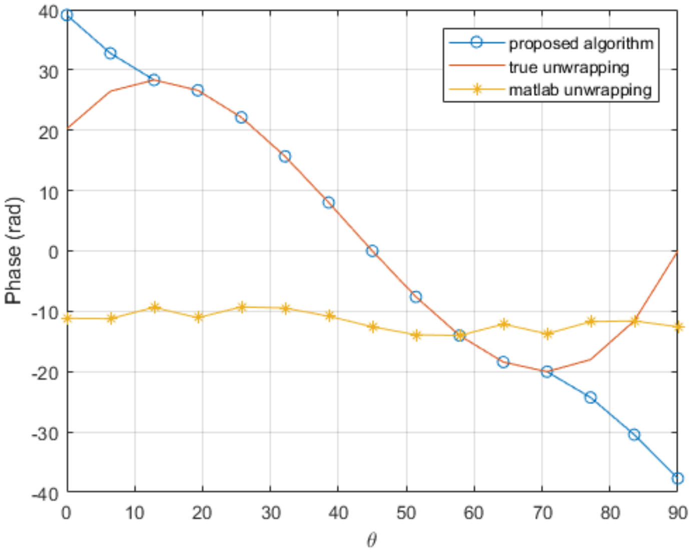

Figure 2.7 – Comparison of the proposed procedure and the Matlab unwrapping function in a coarse mesh consisting of 15 nodes with the $1/k_f$ factor 50% higher

computing the finite differences approximation of the second derivative of the phase is a good way to detect when the unwrapping fails.

To end up, next section is going to add improvements and increase the robustness of the methodology by focusing on the industrial problem addressed in Chapter 5.

2.4.3 Proposed approach. Part II: Improving the robustness of phase unwrapping

2.4.3.1 Introduction

Imagine a three-dimensional spatial problem where a complex function is defined for each point in space. The proposed phase unwrapping can be attempted on all N points in the spatial discretization and accepted or rejected by setting a threshold for the values of the second derivative as described in Section 2.4.2.

Thus, a part of the geometry has therefore been dealt with. In this section, it is discussed how to use these solved points to correct the phase unwrapping in the rest of the geometry.

Moreover, the improvement discussed in this section can be also employed to deal with difficult functions when it is known that the solution can be expressed in a certain basis.

2.4.3.2 Reduced basis of the search space

The proposed algorithm is based on computing the phase unwrapping in a reduced search space. To do that, a reduced basis must be extracted. Taking as a reference the three-dimensional example described in the previous section 2.4.3.1 , the following process can be employed to obtain the reduced basis.

Note that for the process which is going to be described, the complex function to unwrap will be the electromagnetic field.

Firstly, the geometry can be divided into subdomains inside which the variations of the electromagnetic field are small. In each subdomain, the search space is reduced using the proper orthogonalized decomposition (POD) computed with the method of the snapshots where the snapshots are the unwrapped phases from the points in the subdomain which are already solved. As it will be checked in the application addressed in Chapter 5, the local coherence of the electromagnetic field allows the POD to have a very low dimension, typically 2 or 3, denoted in the following as r.

2.4.3.3 Phase unwrapping in the reduced search space

Out of all the possible configurations of the phase, we are looking for the one closest to the reduced search space. This can be expressed as a minimization problem:

$$\min_{\substack{k \in \mathbb{Z}^{N_\theta} \\ \alpha \in \mathbb{R}^r}} \left\| \mathrm{Arg}(\psi) + 2\pi k - \sum_{i=1}^{r} \alpha_i w_i \right\|, \tag{2.15}$$

where $(w_i)_{i=1..r}$ are the basis vectors of the search space and $(\alpha_i)_{i=1..r}$ are the vector coefficients with respect to this base.

The search of k can easily be limited to $[k_-, k_+]^{N_\theta} \subset \mathbb{Z}^{N_\theta}$, k_- and k_+ being two integers which depend on the size of the unwrapping. However, this problem can still be very hard to solve hence we will approximate the resolution.

The proposed algorithm to work around this high complexity follows three main steps:

1. Using only a few of the raw phase values, generate a discrete subset of the search space which is likely to be close to the optimal solution.
2. Fit the rest of the phase values to each curve of this subset by adding or subtracting multiples of 2π.
3. Select the configuration which allowed for the best fit.

Thus, r points $(\theta_{n_1}, ..., \theta_{n_r})$ are chosen from the θ discretization. For $(k_{n_1}, ..., k_{n_r}) \in [k_-, k_+]^r$, we can find the unique curve in the search space which can be fit to the r points $(\mathrm{Arg}(\psi_{n_1}) + 2\pi k_{n_1}, ..., \mathrm{Arg}(\psi_{n_r}) + 2\pi k_{n_r})$, by solving for the coefficients α_i:

$$\forall j \in [\![1, r]\!], \quad \sum_{i=1}^{r} \alpha_i w_i(\theta_{n_j}) = \mathrm{Arg}(\psi_{n_j}) + 2\pi k_{n_j} \tag{2.16}$$

In practice, we choose the n_r-tuple $(\theta_{n_1}, ..., \theta_{n_r})$ minimizing the condition number of the linear system represented by Equation (2.16). Let $\alpha_i : (k_{n_1}, ..., k_{n_r}) \mapsto \alpha_i(k_{n_1}, ..., k_{n_r})$ be the function that associates with each configuration the vector coefficients solution to the linear system (2.16). We can now solve instead of (2.15) the following problem:

$$\min_{(k_{n_1}, ..., k_{n_r}) \in [k_-, k_+]^r} \quad \min_{k \in \mathbb{Z}^{N_\theta}} \left\| \mathrm{Arg}(\psi) + 2\pi k - \sum_{i=1}^{r} \alpha_i(k_{n_1}, ..., k_{n_r}) w_i \right\|. \tag{2.17}$$

2.4.3.4 Validation of the optimization procedure

We consider the following phase function:

$$\phi(\theta) = 8\pi \sin(4\theta) - 4.5\pi \sin(8\theta) + \sin(12\theta)$$

involving 30 points in the discretization of the θ parametric coordinate.

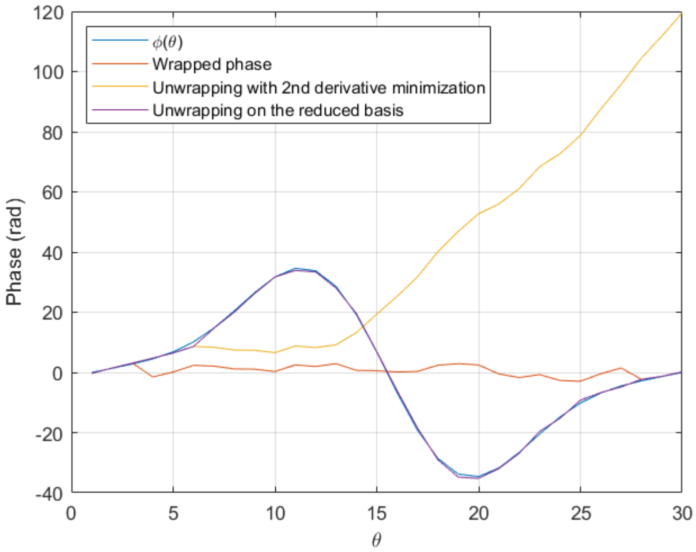

Figure 2.8 – Comparison of reduced-basis based unwrapping versus second derivative minimization based unwrapping on a test case exhibiting fast variations of the phase

Once it is artificially wrapped, both the standard unwrapping algorithm and the procedure proposed in this chapter based on the second derivative, fail to unwrap it.

Assuming we have computed the reduced basis consisting of the three functions $(\sin(4\theta), \sin(8\theta), \sin(12\theta))$, we attempt to unwrap $\text{Arg}\left(e^{i\phi(\theta)+\mathcal{N}(0,0.5)}\right)$ using the just described optimization procedure. The unwrapped phase is exactly the sum of $\phi(\theta)$ and the added noise, as Figure (2.8) proves.

2.4.4 Convergence

Since the simulations of radar devices of Chapter 5 are too expensive, in this section we consider a simpler problem able to provide the required data for performing the convergence analysis.

Thus, we consider the Helmholtz problem with damping in a 2D rectangular domain Ω, that looks for $u(x, y)$ verifying

$$\begin{cases} \Delta u + (i\nu\omega - \omega^2)u = f & \text{in } \Omega \\ \dfrac{\partial u}{\partial n} = 0 & \text{on } \partial\Omega \end{cases} \tag{2.18}$$

where $\Omega = [0, 9] \times [0, 2]$, $\omega = 10$, $\nu = 1$ and $f(x, y; \theta) = e^{120i(cos(\theta)x+sin(\theta)y)}$.

We discretize and solve this problem using the Finite Element Method for a number of values of θ and interpolate the solution (complex field) for $\theta = 3°$.

Then, we compare the phase of the interpolated field to the phase of the solution obtained with the FEM, whose difference is depicted in Fig. 2.9).

The previous figure proves the convergence of the proposed strategy when enriching the sampling. It can also be noticed that a quite sparse sampling suffices for reaching an acceptable accuracy.

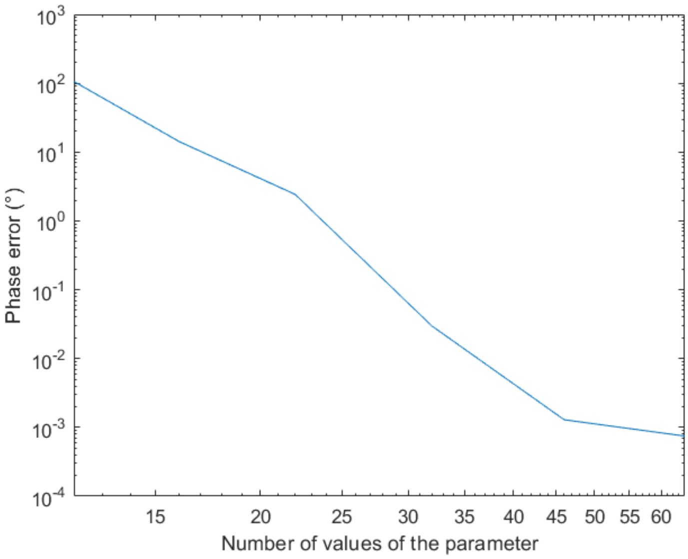

Figure 2.9 – Evolution of the phase error with the parameter sampling refinement.

2.5 Novel hybridation and dynamic strategies

2.5.1 Introduction.

In Section 0.1, the importance of the development of the HT paradigm was discussed as well as its applications. This methodology is not only a way to better predict the evolution of complex dynamical systems but is one of the cornerstones for the implementation of DDDAS nowadays. For these reasons, it is so important to have the right numerical tools to make the previous paradigm a reality.

Consequently, in the following sections, two novel techniques for hybridization are proposed to address different scenarios in the HT framework. These methodologies learn efficiently dynamic systems from data. Therefore, precisely speaking, they can also be used outside the HT concept. Nevertheless, in the present dissertation, these methodologies are focused on obtaining the dynamically evolving correction model of the HT. The proposed techniques are:

- **The stabilized DMD and DMDc techniques**. The goal here is the computation of stable, fast and accurate corrections in the Hybrid Twin framework, regarding the delicate and important problem of stability. In addition, several sub-variants are introduced to guarantee a low computational cost as well as the achievement of a stable time-integration.

- **The DMD Dictionary strategy**. This method allow us to address complex non-linear behaviors within the DMD framework. Moreover, this method is able to produce models that avoid over-fitting quite well, correcting only the operation ranges with more error.

Now, before presenting the aforementioned techniques, a more detailed mathematical presentation of the HT is given in the following section.

2.5.2 Hybrid Twins. The big picture.

Each dynamical system can be characterized by the time evolution of its state vector, that is, the vector which contains the value of the variables needed to describe the system. The Hybrid Twin (HT) focuses on describing this evolution as well as possible, by taking into consideration that the physics-based model does not always fit the measurements exactly.

HTs are based on the idea that biased deviations (between the model and the measurements) show hidden physics—in other words, ignorance—and therefore, these deviations require a particular treatment. They will be modeled on-line by assimilating collected data. This correction on-the-fly is done using data-driven deviation models. On the other hand, the unbiased deviation contribution is associated to noise and it is addressed by using adequate filters. The interested reader can consult [Gonzalez *et al.* 2018b] or [Moya *et al.* 2019] for previous applications of this rationale.

In what follows the state vector at time t is denoted by $\mathbf{z}(t)$ and its time evolution by $\dot{\mathbf{z}}(t)$. A HT can thus be represented then by the following equation:

$$\dot{\mathbf{z}}(t) \approx \dot{\mathbf{z}}(t)^{\text{model}} + \dot{\mathbf{z}}(t)^{\text{correction}}. \tag{2.19}$$

In a HT framework [Chinesta *et al.* 2018] the dynamical evolution of the system will be represented as

$$\dot{\mathbf{z}}(t) = \mathbf{P}(\mathbf{z}, t; \mu) + \mathbf{B}(\mathbf{z}, t) + \mathbf{E}(\mathbf{z}, t) + \mathbf{R}(t), \tag{2.20}$$

thus establishing that the rate of change of the state vector encompasses different contributions:

- The physics-based model $\mathbf{P}(\mathbf{z}, t; \mu)$, used to describe the dynamical system. Its contribution depends on a number of model parameters μ. This can be cast in the form of a ROM to ensure real-time feedback, namely, a PRM (Parametric Reduced Model) where the values of the involved parameters are identified from the assimilated-data.
- A data-based model correction $\mathbf{B}(\mathbf{z}, t)$, describing the gap between prediction and measurement.
- External actions $\mathbf{E}(\mathbf{z}, t)$, introduced into the system dynamics in order to drive the model solution towards the desired target. It must be noted that the term $\mathbf{E}$ could depend on the model parameters μ or it may not depend on $\mathbf{z}$.
- The unbiased noise $\mathbf{R}(t)$, that has been traditionally addressed using appropriate filters [Chinesta *et al.* 2018] [González *et al.* 2017]. This terms also includes external actions for which there is no possible prediction.

It is worth noting that the physics-based model $\mathbf{P}$ is calibrated on-line to adapt its output to the measurements, and the data-driven model correction $\mathbf{B}$ is constructed on-the-fly.

In the above definition, the adjective Hybrid comes from $\mathbf{B}(\mathbf{z}, t)$. The reason is that the model is composed of two contributions: one, $\mathbf{P}$, coming from a physics-based model—even if it is calibrated from data—and the other, $\mathbf{B}$, constructed from scratch from data. This double nature distinguishes digital twins from their hybrid counterparts.

2.5.3 An efficiently learning of dynamical systems: The stabilized DMD and DMDc techniques.

Frequently, difficulties to learn stable models arise when learning linear dynamical systems, specially when dealing with high-dimensional data. This is an important issue to deal with because of the growing importance of the data-driven approximations. For instance, it is usual to search the best linear approach of a set of high-dimensional data to make, for example, fast predictions of the system or to develop control strategies. In fact, there is a growing success of techniques such as the DMD to discover dynamical systems from high-dimensional data [Schmid 2010, Kutz *et al.* 2016]. This success steams from its capability of providing an accurate decomposition of a complex system into spatiotemporal coherent structures while constructing the model dynamics evolving on a low-rank subspace.

However, when operating in the above scenarios, sometimes the best model computed with state-of-the-art algorithms fails to obtain a stable time-integration. In fact, for a given set of data, the problem to guarantee a stable system is defined by Eq. (2.23) below but, unfortunately, the feasible region constrained by the spectral radius is nonconvex and no general methodology exists to solve it [Huang *et al.* 2016]. Moreover, if a fast procedure is needed to obtain a correction model in a real-time application, this problem is further exacerbated.

For these reasons, this dissertation proposes a methodology to compute a stable model for a given dataset at low computational cost. The strategy is discussed for a DMD model and for a DMD with control (DMDc) model. In addition, other strategies are discussed.

Let us assume the following dynamical systems defined in Eqs (2.21) and (2.22), the first one without considering inputs,

$$\mathbf{z}_{k+1} = \mathbf{M}_z \mathbf{z}_k, \tag{2.21}$$

and the second one considering inputs,

$$\mathbf{z}_{k+1} = \begin{bmatrix} \mathbf{M}_z & \mathbf{M}_u \end{bmatrix} \begin{bmatrix} \mathbf{z}_k \\ \mathbf{u}_k \end{bmatrix} = \tilde{\mathbf{M}} \tilde{\mathbf{z}}_k, \tag{2.22}$$

where $\mathbf{z}_k \in \mathbb{R}^{\mathtt{D_z}}$ is the vector representing the state of our dynamical system at time step k, $\mathbf{u}_k \in \mathbb{R}^{\mathtt{D_u}}$ is a vector with the inputs of the system at time step k, $\mathbf{M}_z \in \mathbb{R}^{\mathtt{D_z} \times \mathtt{D_z}}$ and $\mathbf{M}_u \in \mathbb{R}^{\mathtt{D_u} \times \mathtt{D_u}}$ are the matrices defining the time evolution of the system. To guarantee stability in the above systems, the following condition must be satisfied:

$$\rho(\mathbf{M}_z) \leq 1, \tag{2.23}$$

where $\rho(\cdot)$ denotes the spectral radius.

Therefore, in relation to Eq. (2.22), the solution minimizes

$$\left\| \mathbf{X}_1 - \tilde{\mathbf{M}} \tilde{\mathbf{X}}_0 \right\|_F^2 \quad \text{s.t.} \quad \rho(\mathbf{M}_z) \leq 1, \tag{2.24}$$

with

$$\begin{aligned} \tilde{\mathbf{X}}_0 &= \begin{bmatrix} \tilde{\mathbf{z}}_0, & \tilde{\mathbf{z}}_1, & \dots, & \tilde{\mathbf{z}}_{n_s-1} \end{bmatrix}, \\ \mathbf{X}_1 &= \begin{bmatrix} \mathbf{z}_1, & \mathbf{z}_2, & \dots, & \mathbf{z}_{n_s} \end{bmatrix}, \end{aligned}$$

where n_s is the number of different snapshots for the training and the matrices $\tilde{\mathbf{X}}_0$ and $\mathbf{X}_1$ contain the data to construct the model. In them, each column corresponds to a snapshot of the system at a given time instant.

Unfortunately, as already said, the feasible region constrained by $\rho(\mathbf{M}_z) \leq 1$ is nonconvex and no general methodology exists to solve it [Huang *et al.* 2016]. This can lead to the problems already discussed where an unstable model is obtained or, in other cases, simply an extremely bad model is extracted due to a failure of the optimization methodology employed.

The proposed approach, which can always guarantee the creation of a stable model, is based on an observation of the following inequality, which is satisfied by any matrix norm:

$$\rho(\mathbf{A}) \leq \|\mathbf{A}\| \,. \tag{2.25}$$

To prove it, let ω be an eigenvalue of $\mathbf{A}$, and let $\mathbf{x} \neq 0$ be a corresponding eigenvector. From $\mathbf{A}\mathbf{x} = \omega\mathbf{x}$, we have:

$$\mathbf{A}\mathbf{X} = \omega\mathbf{X},$$

where $\mathbf{X} = [\mathbf{x}, \cdots, \mathbf{x}]$.

It follows that

$$\|\omega\mathbf{X}\| = |\omega| \, \|\mathbf{X}\| \,,$$

and taking into account that

$$\|\mathbf{A}\mathbf{X}\| \leq \|\mathbf{A}\| \, \|\mathbf{X}\| \,,$$

it follows that

$$|\omega| \, \|\mathbf{X}\| \leq \|\mathbf{A}\| \, \|\mathbf{X}\| \,.$$

Simplifying the above expression by $\|\mathbf{X}\|$ (> 0) gives:

$$|\omega| \leq \|\mathbf{A}\| \,,$$

that taking the maximum over all eigenvalues ω gives the desired proof.

Taking for the reasoning the following induced norm,

$$\|\mathbf{A}\|_1 = \max_{1 \leq j \leq m_1} \sum_{i=1}^{m_2} |a_{ij}|,$$

where m_1 is the number of columns, and m_2 is the number of rows—which is simply the maximum absolute column sum of the matrix. It can be observed that by decreasing the absolute value of the matrix coefficients, a smaller matrix norm is obtained, and if it is decreased sufficiently, a smaller $\rho(\mathbf{A})$ is got, because of Eq. (2.25).

Therefore, the idea to obtain a stable system is to shrink the matrix coefficients of $\mathbf{M}_z$. In fact, this dissertation proposes to do so by using the ridge regression [Hastie *et al.* 2009], also known as a special case of the Tikhonov regularization. Many advantages can be obtained from this choice. For instance, a closed mathematical expression is obtained. This implies that there is no need to use complex optimization procedures (that can fail to converge). In addition, there is a low added computational cost when changing the Ordinary Least Squares (OLS) problem to the ridge one.

This way, a new feature and use is proved for the ridge regression. Ridge regression was employed in a certain way for regression of dynamical systems, see e.g. [Erichson *et al.* 2019], but just to use the classical function of ridge: to deal with ill-posed problems. Now, we have extended the employment of the technique to a broader problem area: the construction of stable dynamical systems.

To reformulate the resolution of the systems (2.21) and (2.22), and then extend the procedure for the DMDc (a more general version of the DMD considering control inputs), two options are envisaged. The first one is solving the following problem:

$$\begin{aligned}\hat{\mathbf{M}} &= \arg\min_{\mathbf{M}_z} \left\{ \|\mathbf{X}_1 - \mathbf{M}_z\mathbf{X}_0\|_F^2 + \lambda^2 \|\mathbf{M}_z\|_F^2 \right\} \\ &= \arg\min_{\mathbf{M}_z} \left\| \begin{bmatrix}\mathbf{X}_1 & \mathbf{0}\end{bmatrix} - \mathbf{M}_z \begin{bmatrix}\mathbf{X}_0 & \lambda\mathbf{I}\end{bmatrix} \right\|_F^2 = \arg\min_{\mathbf{M}_z} \left\|\bar{\mathbf{X}}_1 - \mathbf{M}_z\bar{\mathbf{X}}_{01}\right\|_F^2 ,\end{aligned} \tag{2.26}$$

where:

$$\mathbf{X}_0 = \begin{bmatrix} \mathbf{z}_0, & \mathbf{z}_1, & ..., & \mathbf{z}_{n_s-1} \end{bmatrix},$$

$\bar{\mathbf{X}}_1$ and $\bar{\mathbf{X}}_{01}$ are the augmented matrices, $\mathbf{I}$ is an identity matrix of size $\mathtt{D_z} \times \mathtt{D_z}$ and $\mathbf{0}$ is a zero matrix of size $\mathtt{D_z} \times \mathtt{D_z}$.

The solution of the above problem can be computed using the Moore-Penrose pseudoinverse, therefore:

$$\hat{\mathbf{M}} = \bar{\mathbf{X}}_1(\bar{\mathbf{X}}_{01})^{\dagger},$$

where † is the the Moore-Penrose pseudoinverse.

A second procedure to solve Eq. (2.26) is to employ a ridge regression for each variable to be predicted.

Concerning the system (2.22),

$$\begin{aligned} \hat{\mathbf{M}} = \underset{\tilde{\mathbf{M}}}{\arg\min} \left\{ \left\| \mathbf{X}_1 - \tilde{\mathbf{M}}\tilde{\mathbf{X}}_0 \right\|_F^2 + \lambda^2 \left\| \mathbf{M}_z \right\|_F^2 \right\} \\ = \underset{\tilde{\mathbf{M}}}{\arg\min} \left\| \begin{bmatrix} \mathbf{X}_1 & \mathbf{0}_1 \end{bmatrix} - \tilde{\mathbf{M}} \begin{bmatrix} \mathbf{X}_0 & \lambda\mathbf{I} \\ \mathbf{U}_0 & \mathbf{0}_2 \end{bmatrix} \right\|_F^2 = \underset{\tilde{\mathbf{M}}}{\arg\min} \left\| \bar{\mathbf{X}}_1 - \tilde{\mathbf{M}}\bar{\mathbf{X}}_{02} \right\|_F^2, \end{aligned} \quad (2.27)$$

where:

$$\mathbf{U}_0 = \begin{bmatrix} \mathbf{u}_1, & \mathbf{u}_2, & \ldots, & \mathbf{u}_{n_{s-1}} \end{bmatrix},$$

$\bar{\mathbf{X}}_1$ and $\bar{\mathbf{X}}_{02}$ are the augmented matrices, $\mathbf{I}$ is an identity matrix of size $\mathtt{D_z} \times \mathtt{D_z}$, $\mathbf{0}_1$ is a zero matrix of size $\mathtt{D_z} \times \mathtt{D_z}$ and $\mathbf{0}_2$ is a zero matrix of size $\mathtt{D_u} \times \mathtt{D_z}$.

In addition, the same procedures used to solve system (2.26) can be used to solve (2.27), either the Moore-Penrose pseudoinverse or the individual ridge regressions.

The above model can be extended in the context of high-dimensional systems when using the DMDc taking the formulation expressed in Eq. (2.27). To do that, we take the Singular Value Decomposition (SVD) of matrix $\bar{\mathbf{X}}_{02} = \tilde{\mathbf{\Xi}}\tilde{\mathbf{\Sigma}}\tilde{\mathbf{V}}^*$ (where the star symbol * indicates the conjugate transpose). Therefore:

$$\tilde{\mathbf{M}} = \bar{\mathbf{X}}_1(\bar{\mathbf{X}}_{02})^{\dagger} = \bar{\mathbf{X}}_1\tilde{\mathbf{V}}\tilde{\mathbf{\Sigma}}^{-1}\tilde{\mathbf{\Xi}}^*.$$

Approximations of the operators $\mathbf{M}_z$ and $\mathbf{M}_u$ can be found as follows:

$$\tilde{\mathbf{M}} = \begin{bmatrix} \mathbf{M}_z, & \mathbf{M}_u \end{bmatrix} = \begin{bmatrix} \bar{\mathbf{X}}_1\tilde{\mathbf{V}}\tilde{\mathbf{\Sigma}}^{-1}\tilde{\mathbf{\Xi}}_1^*, & \bar{\mathbf{X}}_1\tilde{\mathbf{V}}\tilde{\mathbf{\Sigma}}^{-1}\tilde{\mathbf{\Xi}}_2^* \end{bmatrix},$$

where $\tilde{r}$ is the truncation value of the SVD applied to decompose matrix $\bar{\mathbf{X}}_{02} = \tilde{\mathbf{\Xi}}\tilde{\mathbf{\Sigma}}\tilde{\mathbf{V}}^*$, $\tilde{\mathbf{\Xi}}^* = \begin{bmatrix} \tilde{\mathbf{\Xi}}_1^*, & \tilde{\mathbf{\Xi}}_2^* \end{bmatrix}$, and the sizes of $\tilde{\mathbf{\Xi}}_1^*$ and $\tilde{\mathbf{\Xi}}_2^*$ are $\tilde{r} \times \mathtt{D_z}$ and $\tilde{r} \times \mathtt{D_u}$ respectively.

For high-dimensional systems ($\mathtt{D_z} \gg 1$) a reduced-order approximation can be solved for instead, leading to a more tractable computational model. Thus, a transformation to a lower-dimensional subspace on which the dynamics evolve is sought.

The output space $\bar{\mathbf{X}}_1$ is chosen to find the reduced-order subspace. Consequently, the SVD of $\bar{\mathbf{X}}_1$ is defined as

$$\bar{\mathbf{X}}_1 = \mathbf{\Xi}\mathbf{\Sigma}\mathbf{V}^*,$$

where the truncation value for this SVD will be denoted as r. Please note that usually both SVDs will have different truncation values.

Then, by employing the change of coordinates $\mathbf{z} = \mathbf{\Xi}\,\hat{\mathbf{z}}$ (or equivalently $\hat{\mathbf{z}} = \mathbf{\Xi}^*\,\mathbf{z}$), the following reduced-order approximations can be obtained,

$$\mathbf{z}_{k+1} = \mathbf{M}_z\mathbf{z}_k + \mathbf{M}_u\mathbf{u}_k,$$

$$\boldsymbol{\Xi}\,\hat{\mathbf{z}}_{k+1} = \mathbf{M}_z\,\boldsymbol{\Xi}\,\hat{\mathbf{z}}_k + \mathbf{M}_u\,\mathbf{u}_k,$$

so that

$$\hat{\mathbf{z}}_{k+1} = \hat{\mathbf{M}}_z\,\hat{\mathbf{z}}_k + \hat{\mathbf{M}}_u\,\mathbf{u}_k, \tag{2.28}$$

where:

$$\hat{\mathbf{M}}_z = \boldsymbol{\Xi}^*\bar{\mathbf{X}}_1\tilde{\mathbf{V}}\tilde{\boldsymbol{\Sigma}}^{-1}\tilde{\boldsymbol{\Xi}}_1^*\boldsymbol{\Xi},$$

$$\hat{\mathbf{M}}_u = \boldsymbol{\Xi}^*\bar{\mathbf{X}}_1\tilde{\mathbf{V}}\tilde{\boldsymbol{\Sigma}}^{-1}\tilde{\boldsymbol{\Xi}}_2^*,$$

and the sizes of $\hat{\mathbf{M}}_z$ and $\hat{\mathbf{M}}_u$ are $r \times r$ and $r \times \mathtt{D}_\mathtt{u}$ respectively.

To select the penalty factor, when the standard procedure leads to a matrix that violates the stability condition, several options can be envisaged. Here, this thesis proposes to use the bisection method (which guarantees convergence toward the solution) or the regula falsi method (to speed up the process). Of course, faster algorithms can be used such as the Illinois algorithm, but our experience suggests that the former ones are enough in practice.

For example, if the bisection method is selected, the zero of the following function is sought:

$$f(\lambda) = \rho_{\text{desired}} - \rho(\mathbf{M}_z(\lambda)), \tag{2.29}$$

where ρ_{desired} is a chosen value very close to one, representing the target when the initial constructed model violates the stability condition.

Taking into consideration that the bracketing interval at step k of the algorithm is $[\lambda_k^a, \lambda_k^b]$, then the Eq. (2.30) is employed to compute the new solution estimate for the penalty λ_k^c at step k:

$$\lambda_k^c = \frac{\lambda_k^a + \lambda_k^b}{2}. \tag{2.30}$$

If $f(\lambda_k^c)$ is satisfactory, the iteration stops. If this is not the case, the sign of $f(\lambda_k^c)$ is examinated and the bracking interval is updated for the following iteration so that there is a zero crossing within the new interval.

2.5.4 The DMD Dictionary strategy

The Dictionary Model (DM) starts with the supposition that we are dealing with a nonlinear dynamical system. So, we consider a nonlinear dynamical system:

$$\dot{\mathbf{z}}(t) = \mathbf{f}(\mathbf{u}, \mathbf{z}, t; \boldsymbol{\mu}), \tag{2.31}$$

where $\mathbf{z} \in \mathbb{R}^{\mathtt{D}_\mathtt{z}}$ is the vector representing the state of our dynamical system at time t, and $\boldsymbol{\mu}$ contains parameters of the system. $\mathbf{u} \in \mathbb{R}^{\mathtt{D}_\mathtt{u}}$ is a vector with the inputs of the system, and $\mathbf{f}$ represents the dynamics as a function of $\mathbf{u}$, $\mathbf{z}$, t and $\boldsymbol{\mu}$.

The discrete-time system is:

$$\mathbf{z}_{k+1} = \mathbf{f}(\mathbf{u}_k, \mathbf{z}_k, t_k; \boldsymbol{\mu}). \tag{2.32}$$

If we assume that the system is linear,

$$\mathbf{z}_{k+1} = \mathbf{M}_z(\boldsymbol{\mu}) \cdot \mathbf{z}_k + \mathbf{M}_u(\boldsymbol{\mu}) \cdot \mathbf{u}_k, \tag{2.33}$$

where $\mathbf{z}_k \in \mathbb{R}^{\mathtt{D}_\mathtt{z}}$, $\mathbf{u}_k \in \mathbb{R}^{\mathtt{D}_\mathtt{u}}$, $\mathbf{M}_z(\boldsymbol{\mu}) \in \mathbb{R}^{\mathtt{D}_\mathtt{z} \times \mathtt{D}_\mathtt{z}}$ and $\mathbf{M}_u(\boldsymbol{\mu}) \in \mathbb{R}^{\mathtt{D}_\mathtt{z} \times \mathtt{D}_\mathtt{u}}$. The operator $\mathbf{M}_z(\mu)$ describes the dynamics of the unforced system while the operator $\mathbf{M}_u(\mu)$ characterizes the impact of the input $\mathbf{u}_k$ on the state $\mathbf{z}_{k+1}$.

The idea of the DM is to approximate the nonlinear behavior of Eq. (2.32) with locally linear approaches in terms of $\mathbf{z}_k$. To do this, the operators $\mathbf{M}_z$ and $\mathbf{M}_u$ of Eq. (2.33) must depend on $\mathbf{z}_k$. Therefore, the dynamical system described by the DM is:

$$\mathbf{z}_{k+1} = \mathbf{M}_z(\mathbf{z}_k, \boldsymbol{\mu}) \cdot \mathbf{z}_k + \mathbf{M}_u(\mathbf{z}_k, \boldsymbol{\mu}) \cdot \mathbf{u}_k. \tag{2.34}$$

This implies that there is a set of matrices $\mathcal{S}$ that must be obtained to describe the nonlinear behavior.

$$\mathcal{S} = \{\mathcal{Z}_1, ..., \mathcal{Z}_I\}\,; \mathcal{Z}_i = \left\{\mathbf{M}_z^i, \mathbf{M}_u^i\right\}. \tag{2.35}$$

Please, note that the superscript in $\mathbf{M}_z^i$ and $\mathbf{M}_u^i$ does not indicate exponentation, but it indicates the i-th matrix pair instead.

The set $\mathcal{S}$ is the "dictionary", which allows us to reproduce a nonlinear model as a combination of local linear approaches.

It must be noted that if a pair of operators $\left\{\mathbf{M}_z^i, \mathbf{M}_u^i\right\}$ is needed for each $\mathbf{z}_k$, the method can be unfeasible because of the large amount of memory needed to store $\mathcal{S}$, and also because of the large size of the training set needed to obtain $\mathcal{S}$.

For this reason, this method will work well if each $\mathcal{Z}_i$ can be used in a wide range of state vectors $\mathbf{z}_k$. If this is not the case, it is useful to look for a transformation $\mathbf{g}(\cdot)$, which transforms the evolution of the state vectors in a more linear behaviour $\mathbf{g}(\mathbf{z}_k)$. The Support Vector Machine (SVM) [Burges 1998] and kernel methods [Baudat & Anouar 2001, Ham *et al.* 2004, Hofmann *et al.* 2008] provide a number of techniques for constructing the feature space $\mathbf{g}(\mathbf{z}_k)$.

Here, a methodology based on the Dynamic Mode Decomposition (DMD) ideas [Kutz *et al.* 2016] is proposed. The discrete equation for a local dynamical system must be rewritten as:

$$\mathbf{z}_{k+1} = \begin{bmatrix} \mathbf{M}_z^i & \mathbf{M}_u^i \end{bmatrix} \cdot \begin{bmatrix} \mathbf{z}_k \\ \mathbf{u}_k \end{bmatrix} = \tilde{\mathbf{M}}^i \cdot \tilde{\mathbf{z}}_k. \tag{2.36}$$

Then, if we have n_s different snapshots for a given local linear system, we define the matrix $\tilde{\mathbf{X}}_0 \in \mathbb{R}^{(\mathtt{D_z}+\mathtt{D_u})\times(n_s-1)}$ and the matrix $\mathbf{X}_1 \in \mathbb{R}^{(\mathtt{D_z})\times(n_s-1)}$ as:

$$\tilde{\mathbf{X}}_0 = \begin{bmatrix} \tilde{\mathbf{z}}_1, & \tilde{\mathbf{z}}_2, & ..., & \tilde{\mathbf{z}}_{n_s-1} \end{bmatrix}, \tag{2.37}$$

$$\mathbf{X}_1 = \begin{bmatrix} \mathbf{z}_2, & \mathbf{z}_3, & ..., & \mathbf{z}_{n_s} \end{bmatrix}, \tag{2.38}$$

where each column corresponds to a snapshot. Therefore, the transition matrix $\tilde{\mathbf{M}}^i$ is learned to minimize the state reconstruction error:

$$\min \left\| \mathbf{X}_1 - \tilde{\mathbf{M}}^i \cdot \tilde{\mathbf{X}}_0 \right\|_F^2. \tag{2.39}$$

However, to guarantee stability, the Eq. (2.39) must be reformulated as:

$$\min \left\| \mathbf{X}_1 - \tilde{\mathbf{M}}^i \cdot \tilde{\mathbf{X}}_0 \right\|_F^2 \quad \text{s. t.} \quad \rho(\mathbf{M}_z) \leq 1 \tag{2.40}$$

where $\rho(\cdot)$ denotes the spectral radius.

As it was discussed, the above problem can be efficiently solved by means of the technique proposed in Section 2.5.3. Further information about this type of problems can be found in [Huang *et al.* 2016, Huang *et al.* 2017, Kawashima & Matsuyama 2005]

A training set $\mathcal{T}$ composed of a collection of snapshots $\left\{\tilde{\mathbf{z}}_1, \ldots, \tilde{\mathbf{z}}_{N_f}\right\}$ of different simulations must be obtained. To decide the snapshots to obtain each local linear dynamical system, two methodologies are proposed.

The first one is to split each simulation time in intervals $(\mathcal{I}_1, ..., \mathcal{I}_N)$, where the linearization process is deemed good enough. Then, the collected snapshots $\{\tilde{\mathbf{z}}_1, \ldots, \tilde{\mathbf{z}}_{N_I}\}$ of each interval $\mathcal{I}_i$ are assigned to belong to the linear dynamical system obtained in their interval $\mathcal{I}_i$.

The second one is to use the k-means clustering [Arthur & Vassilvitskii 2007, Lloyd 2006] algorithm to obtain the linear dynamical system of each cluster. In this second approach, given a set of snapshots $\left\{\tilde{\mathbf{z}}_1, \ldots, \tilde{\mathbf{z}}_{N_f}\right\}$, k-means clustering aims to partition the N_f observations into Υ ($\Upsilon \leq N_f$) sets $\mathcal{K} = \{\mathcal{K}_1, \ldots, \mathcal{K}_\Upsilon\}$ so as to minimize the within-cluster sum of squares:

$$\underset{\mathcal{K}}{\arg\min} \sum_{i=1}^{k} \sum_{\tilde{\mathbf{z}} \in \mathcal{K}_i} \|\tilde{\mathbf{z}} - \boldsymbol{\nu}_i\|^2 , \tag{2.41}$$

where $\boldsymbol{\nu}_i$ is the mean of points in $\mathcal{K}_i$.

Other techniques like the ones based on Hierarchical Clustering can be used. Here, techniques such as k-means clustering are preferrred because they can be applied to large volumes of data without difficulties.

2.6 Summary and Conclusions

After reviewing the s-PGD, this chapter introduced and discussed the theoretical basis for four new non-intrusive strategies proposed in the present dissertation:

1. A novel sparse reduced order formulation combining the s-PGD with a Reduced Basis (RB) approach: the s-PGD + RB.
2. A novel unwrapping algorithm for accurately addressing interpolation of complex numbers.
3. The stabilized DMD and DMDc techniques.
4. The DMD Dictionary strategy.

where the motivation for each of the above proposals is also set out in the corresponding section.

The first two methodologies are focused on obtaining parametric models while the last two are focused on obtaining the evolution of dynamic systems.

In addition, a study and analysis of the novel unwrapping algorithm was carried out in which a validation of the procedure, a comparison with traditional unwrapping and a convergence analysis were discussed. The results showed that a great reduction in the number of needed snapshots can be achieved. In addition, it was proved that the proposed approach can outperform current commercial software as well as provide good results in complex settings. Furthermore, Chapter 5 discusses an industrial application where the advantages for a specific problem are observed.

The results of the other three methodologies will be observed in the next chapters, where they will be directly analysed when applied to a concrete industrial problem.

On the other hand, the results of the methodologies three and four are addressed in the Chapters 6 and 7, respectively. In particular, they are going to be employed inside the HT framework

Chapter 3

Novel PGD strategies: PGD-based advanced nonlinear multiparametric regressions for constructing metamodels at the scarce-data limit.

Abstract Regressions created from experimental or simulated data enable the construction of metamodels, widely used in a variety of engineering applications. Many engineering problems involve multi-parametric physics whose corresponding multi-parametric solutions can be viewed as a sort of computational vademecum that, once computed offline, can be then used in a variety of real-time engineering applications including optimization, inverse analysis, uncertainty propagation or simulation based control. Sometimes, these multi-parametric problems can be solved by using advanced model order reduction —MOR— techniques. However, when the solution of these multi-parametric problems becomes cumbersome, one possibility consists in solving the problem for a sample of the parametric values, and then creating a regression from all the computed solutions, to finally infer the solution for any choice of the problem parameters. However, addressing high-dimensionality at the low data limit, ensuring accuracy and avoiding overfitting constitutes a difficult challenge. The present chapter aims at proposing and discussing different PGD-based advanced regressions enabling the just referred features.

Contents

3.1 Introduction **64**
  3.1.1 Chapter overview 64
  3.1.2 Topic introduction 64
3.2 Regularized regressions: The regularized sparse PGD (rs-PGD) and the doubly sparse PGD (s^2-PGD) **68**
  3.2.1 Motivation 68
  3.2.2 rs-PGD 69
  3.2.3 s^2-PGD 71
3.3 The ANOVA-based sparse-PGD **72**
  3.3.1 Sensitivity analysis: Sobol coefficients 73
  3.3.2 The *anchored* ANOVA 73
  3.3.3 Combining the *anchored*-ANOVA with the sparse PGD . . . 73
3.4 Results **74**
  3.4.1 Results for the rs-PGD approach 74

3.4.1.1 A first example involving a five dimensional polynomial 74
3.4.1.2 A second example involving five dimensions with trigonometric and logarithmic functions 76
3.4.1.3 Results on the chaotic Lorenz system. 76
3.4.2 Checking the performances of s^2-PGD when addressing sparse solutions 76
3.4.2.1 A first example involving sparsity in one dimension 78
3.4.2.2 A second example involving more dimensions 80
3.4.3 ANOVA-PGD numerical results 81
3.5 Conclusions 84

3.1 Introduction

3.1.1 Chapter overview

This chapter starts by presenting an overview of different methodologies to generate response surfaces at the scarce-data limit and in the context of scattered data. These methodologies are of crucial importance within the data-driven framework whenever the data has to be interpolated/extrapolated to infer behaviours at locations where there are no experimental measurements. For instance, many engineering problems require the construction of multi-parametric solutions to address a wide variety of engineering applications. In many cases, as discussed in the Introduction Chapter and in Chapter 2, these solutions are computed employing non-intrusive procedures such as the s-PGD. In fact, several chapters of this dissertation use this technique. However, industrial scenarios are found where state-of-the-art techniques fail to provide a suitable solution. Therefore, this chapter proposes and discusses novel PGD-based advanced regressions to improve the model's quality under these difficult circumstances.

Before starting the discussion, it is important to mention that the topic presented in this chapter as well as its results correspond to the following submitted paper:

- A. Sancarlos, V. Champaney, J.L. Duval, E. Cueto, F. Chinesta, "PGD-Based Advanced Nonlinear Multiparametric Regressions for Constructing Metamodels at the Scarce-Data Limit," *SIAM Journal on Scientific Computing*, Submitted.

3.1.2 Topic introduction

Model Order Reduction —MOR— techniques express the solution of a given problem (expressed as a partial differential equation —PDE—, for instance) into a reduced basis with strong physical or mathematical content. Very often, these bases are extracted from solutions of the problem at hand obtained offline. This can be done, for instance, by invoking the proper orthogonal decomposition —POD— or the reduced basis method —RBM—[Chinesta *et al.* 2017]. When computing with a reduced basis, the solution complexity scales with the size of this basis, which is in general much smaller than the size of the multi-purpose approximation basis associated with the finite element method —FEM—, whose size scales with the number of nodes in the mesh.

Even if the use of a reduced basis implies a certain loss of generality, it enables impressive computing time savings and, as soon as the problem solution continues living in the space spanned by the reduced basis, the computed solution remains accurate enough. Obviously, as soon as one is interested in a solution that can not be accurately approximated within the space spanned by that reduced basis, the solution will be computed fast, but its accuracy is expected to be poor. To improve generality while ensuring accuracy, an appealing route consists of constructing the reduced basis and solving the problem simultaneously, as the Proper Generalized Decomposition —PGD— does [Chinesta *et al.* 2017]. However, this option can become very intrusive in different applications.

To alleviate intrusiveness, non-intrusive procedures were proposed. They proceed by constructing the parametric solution of the parametric problem from a number of high-fidelity solutions performed offline. In general, these are very expensive from the computing time viewpoint, for different choices of the model parameters that constitutes the design of experiments —DoE—.

Among these techniques we can mention standard polynomial approximations on sparsely sampled parametric domains. Despite its simplicity, its use is not to be taken lightly. The use of orthogonal polynomial bases, with their associated Gauss-Lobatto points as DoE, allows us to obtain very accurate approximations. However, the sampling (DoE) increases exponentially with either the number of dimensions of the considered polynomial degree. Using randomly sampled DoE, or considering an approximation too rich with respect to the available amount of data (underdetermined approximation problem), results in noticeable overfitting effects. A way of attenuating these unfavorable effects, consists in using an approximation basis avoiding over-oscillating phenomena, as kriging approximations, for instance perform successfully [Papritz & Stein 1999], being a major protagonist of the so-called surrogate models (or metamodels) [Forrester *et al.* 2008, P. Jiang *et al.* 2020]. Another possibility consists in restricting polynomial approximations to a low degree, e.g., linear or moderately nonlinear regressions.

Other tentatives concern the proper orthogonal decomposition with interpolation —PODI—[Ly & Tran 2001], where usual regressions for expressing the dependence of the modal coefficients on the parameters are employed. Within the PGD rationale, Sparse Subspace Learning —SSL—[Borzacchiello *et al.* 2019] interpolates the pre-computed solutions related to the DoE associated to an structured grid (Gauss-Lobatto points) over the whole parametric space, by considering a hierarchical approximation basis for interpolating the precomputed solutions. This ensures the separated representation of the interpolated parametric solution. A sparsely sampled counterpart, the so-called sparse PGD, s-PGD, was proposed in [Ibáñez Pinillo *et al.* 2018].

The main limitations of SSL-based regression procedures is the volume of data, which increases exponentially with the number of parameters involved in the model. Thus, when considering $\mathtt{P}$ parameters, the lowest approximation level, the so-called *0-level*, which consists in a multi-linear approximation (the product of a linear approximation along each parametric dimension), needs $2^{\mathtt{P}}$ data (each datum coming in fact from a high fidelity solution). On the other hand, s-PGD reduces the amount of required data, by considering a sparse sampling. However, the fact of combining higher degree approximations (induced by the separated representations) with very reduced amount of data, exacerbates the risk of overfitting. To avoid overfitting, in [Ibáñez Pinillo *et al.* 2018] the authors proposed the use of adaptive approximation bases, the so-called Modal adaptive Strategy —MAS—, whose degree is kept to a minimum in the first PGD modes (first terms of the finite sum decomposition expressing the variables separation which is at the heart of the PGD). This degree is then increased progressively for the calculation of higher level modes. Other choices of the approximation bases were also considered for limiting these spurious over-oscillating behaviors, as for example the employ of kriging. The s-PGD can thus be viewed as a nonlinear regression that makes use of the separation of variables. This enables its use in multi-parametric settings.

Regressions are widely employed in artificial intelligence in general, and more particularly in supervised scientific machine learning [Udrescu *et al.* 2020, Brunton *et al.* 2016, Hernández *et al.* 2021b], in the development of cognitive or hybrid digital twins [Moya *et al.* 2020b, Sancarlos *et al.* 2020, Chinesta *et al.* 2020] or even in the field of neuroscience [Shiffrin *et al.* 2020]. Regression can thus be seen as the main ingredient in the automatic construction of models of the surrounding physical reality. This is of utmost importance in the construction of an artificial intelligence able to maneuver in the physical world [Moya *et al.* 2020a, Moya *et al.* 2019].

The main issues related to the implementation of regression in the low-data limit concern nonlinear behaviors in multi-parametric settings. This last factor leads to the so-called curse of dimensionality, i.e., the exponential growth in the number of degrees of freedom (equivalently, the number of necessary sampling points in the phase space) that is necessary to obtain accurate results [Laughlin & Pines 2000].

When constructing models, it is always important to keep them as simple as possible. In other words, parsimonious models are always preferable to more complex ones. This principle, known as Occam's razor [Udrescu *et al.* 2020, Brunton *et al.* 2016], implies that simpler explanations should be preferred among all the available ones to explain any physical phenomenon. In the literature this is achieved by imposing sparsity in the regression [Ibanez *et al.* 2019, Ibáñez Pinillo *et al.* 2018, Hernandez *et al.* 2021a, Brunton *et al.* 2016]. To obtain parsimonious models able to address sparsity, it is thus convenient to perform regression by combining L2 and L1 norms.

This chapter aims at proposing robust, general, frugal and accurate regression methodologies able to operate in separated representation settings. For that purpose, three techniques will be proposed and analyzed. The first is based on an Elastic Net regularized formulation, called rs-PGD, combining Ridge and Lasso regressions, that make use, respectively, of the L2 and L1 norms. Both use a rich approximation basis and, to avoid overfitting, the former favors specific solutions with smaller coefficients, while the last enforces the sparsest possible solution by retaining those contributing the most to the solution approximation.

Then, the doubly sparse regression, the so-called s^2-PGD technique will be introduced. The last makes use of the Lasso regularization (the one introduced above that looks for the sparsest approximation through the use of the L1-norm) while searching for the sparsest dimensions.

The third and last technique, the ANOVA-PGD, aims at allying orthogonal hierarchical bases with a more favorable scaling (with respect to the SSL) of the amount of data with the approximation richness. For that purpose, separated representations and sparse approximations (eventually regularized) will be combined for addressing multiple correlation terms.

Figure 5.2 sketches the just referred regression strategies, with the main sampling and approximation features, their pros (emphasized in the green text) and the cons (in red). The future works will address the scalability to address industrial problems involving extremely large solutions as well as the general workflow for allying them for the solution of a given problem.

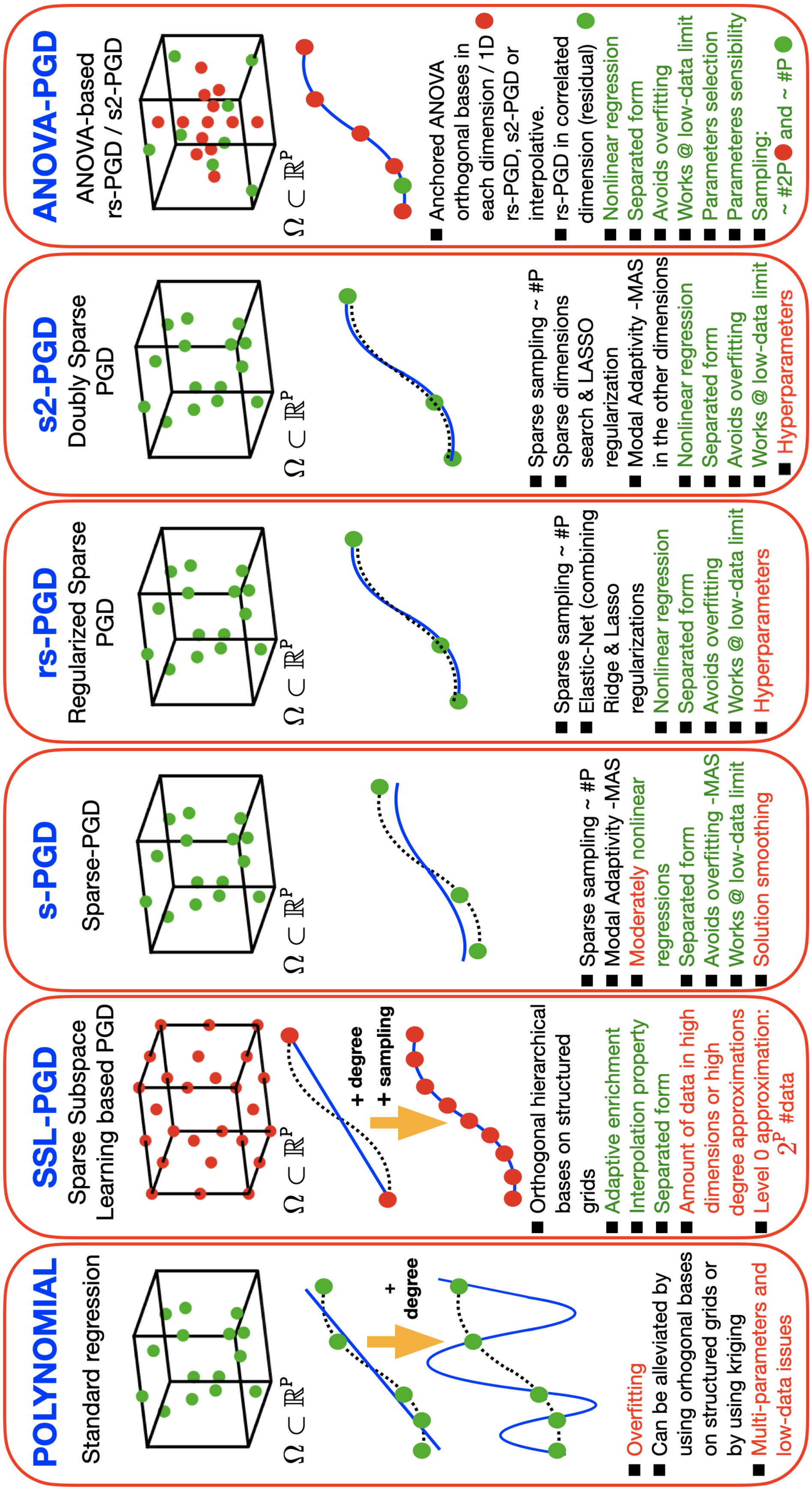

Figure 3.1 – Non-intrusive MOR techniques with the main sampling and approximation features, their pros (emphasized in the green text) and the cons (in red).

3.2 Regularized regressions: The regularized sparse PGD (rs-PGD) and the doubly sparse PGD (s^2-PGD)

In this Section, the novel numerical techniques, the regularized sparse PGD (rs-PGD) and the doubly-sparse PGD (s^2-PGD), are presented and discussed. The content is divided according to the following subsections:

- In subsection 3.2.1, the motivation from which the proposed methodologies are developed, is presented.
- In subsection 3.2.2, the regularized PGD is presented starting from the concepts discussed in Section 3.2.1 and Section 2.2 from Chapter 2.
- In subsection 3.2.3, the s^2-PGD is presented starting from the concepts presented in 3.2.2, 3.2.1 and Section 2.2 from Chapter 2.

3.2.1 Motivation

The rs-PGD and the s^2-PGD are constructed from the theoretical background of the s-PGD in the context of regression problems. In addition, an overview of the s-PGD was presented in Section 2.2.

As it was discussed, the objective of the s-PGD is a particular form of *machine learning* where the final goal is to approximate the unknown parametric function f by the s-PGD approach $\tilde{f}$ trained in some sampling points. The most challenging feature is to improve the predictive ability of the model $\tilde{f}$, that is, the capacity to provide good predictions when the model is fed with previously unseen data. Achieving this is particularly difficult when confronted with a high-dimensional problem, for which data is nearly always sparse and/or scarce.

Indeed, the regression problem described by Eq. (2.1) only guarantees that the minimization is satisfied by the training set, without saying anything at different sampling points. Hence, if there is not an abundance of sampling points in the training set, in the low-data limit, high oscillations may appear out of these measured points because of the increased risk of overfitting. Usually, this is an undesirable effect because it affects the predictive ability of the constructed regression model.

In order to tackle this problem, the s-PGD uses the Modal Adaptivity Strategy (MAS) to take advantage of the greedy PGD algorithm. The idea is to minimize spurious oscillations out of the training set by starting the PGD algorithm looking for modes with low degree. When it is observed that the residual decreases slowly or stagnates, higher order approximation functions are introduced. By doing this, oscillations are reduced, since a higher-order basis will try to capture only what remains in the residual.

The MAS has proved to be a good strategy to improve significantly the s-PGD performance in many problems, see for instance [Ibanez Pinillo 2019, Argerich 2020, Sancarlos *et al.* 2020]. However, it has some limitations. For example, it has been observed that the desired accuracy is not achieved before reaching overfitting or the algorithm stops too early when using MAS in some cases. This last issue implies a PGD solution composed of low order approximation functions, thus not getting an as rich as desired function.

In addition, in problems where just a few terms of the interpolation basis are present (that is, there are just some sparse non-zero elements in the interpolation basis to be determined), the strategy fails in recognizing the true model and therefore converging to other one whose predictive performances are bad.

To solve these difficulties, the rs-PGD and the s^2-PGD are proposed in what follows. Specifically, the first one is used to increase the predictive capacity beyond the s-PGD capabilities and the second one is used to sparse identification and variable selection to construct parsimonious models with great explanatory and predictive capabilities.

3.2.2 rs-PGD

For the ease of the exposition and representation but without loss of generality, let us continue by assuming that the unknown objective function $f(x, y)$ lives in $\mathbb{R}^2$,

$$f(x, y) : \Omega \subset \mathbb{R}^2 \to \mathbb{R},$$

and that it is to be recovered from scarce data.

The goal is therefore to find a function $\tilde{f}^M$ which minimizes the distance to the sought function:

$$\tilde{f}^M = \arg\min_{f^*} \sum_{i=1}^{n_t} \| f(x_i, y_i) - f^*(x_i, y_i) \|_2^2 ,$$

and that takes the separated form

$$\tilde{f}^M(x, y) = \sum_{m=1}^{M} X_m(x) \cdot Y_m(y) = \sum_{m=1}^{M} \Big((\mathbf{N}_m^x)^\top \mathbf{a}_m^x \cdot (\mathbf{N}_m^y)^\top \mathbf{a}_m^y \Big),$$

where n_t is the number of sampling points employed to train the model (training set). Here, the superscript M is employed to highlight the rank of the sought function. How to determine the precise value of M will be detailed hereafter.

In the PGD framework, an iterative scheme based on an alternating direction strategy is usually used to solve the resulting non-linear problem —note that we look for products of one-dimensional functions— and compute $\mathbf{a}_M^x$ and $\mathbf{a}_M^y$. This strategy computes $\mathbf{a}_M^{x,k}$ from $\mathbf{a}_M^{y,k-1}$ and $\mathbf{a}_M^{y,k}$ from $\mathbf{a}_M^{x,k}$ where $\mathbf{a}_M^{y,k}$ indicates the values of $\mathbf{a}_M^y$ at iteration k of the nonlinear iteration algorithm. The iterations proceed until reaching a fixed point according to a user-specified tolerance.

Defining $\mathbf{N}_m^x(x_i)$ and $\mathbf{N}_m^y(y_i)$ as the vectors containing the evaluation of the interpolation basis of the m^{th} mode at x_i and y_i, respectively, we can write the following matrix equations defining the systems to solve:

$$\mathbf{M}_x \cdot \mathbf{a}_M^x = \mathbf{r}, \tag{3.1}$$

$$\mathbf{M}_y \cdot \mathbf{a}_M^y = \mathbf{r}, \tag{3.2}$$

where:

$$\mathbf{r} = \begin{pmatrix} f(x_1, y_1) - \tilde{f}^{M-1}(x_1, y_1) \\ \vdots \\ f(x_{n_t}, y_{n_t}) - \tilde{f}^{M-1}(x_{n_t}, y_{n_t}) \end{pmatrix},$$

$$\mathbf{M}_x = \begin{pmatrix} (\mathbf{N}_M^y(y_1))^\top \mathbf{a}_M^y \cdot (\mathbf{N}_M^x(x_1))^\top \\ \vdots \\ (\mathbf{N}_M^y(y_{n_t}))^\top \mathbf{a}_M^y \cdot (\mathbf{N}_M^x(x_{n_t}))^\top \end{pmatrix},$$

$$\mathbf{M}_y = \begin{pmatrix} (\mathbf{N}_M^x(x_1))^\top \mathbf{a}_M^x \cdot (\mathbf{N}_M^y(y_1))^\top \\ \vdots \\ (\mathbf{N}_M^x(x_{n_t}))^\top \mathbf{a}_M^x \cdot (\mathbf{N}_M^y(y_{n_t}))^\top \end{pmatrix}.$$

If Eq. (3.1) and (3.2) are solved in the Ordinary Least Squares (OLS) sense:

$$\mathbf{a}_M^x = (\mathbf{M}_x^\top \mathbf{M}_x)^{-1} \cdot \mathbf{M}_x^\top \mathbf{r}, \tag{3.3}$$

$$\mathbf{a}_M^y = (\mathbf{M}_y^\top \mathbf{M}_y)^{-1} \cdot \mathbf{M}_y^\top \mathbf{r} \tag{3.4}$$

which give us the usual matrix equations in the OLS context.

The rs-PGD is based on putting a penalty term when solving (3.1) and (3.2) with the following objectives:

- To reduce overfitting.
- To deal with strong multicollinearity, namely when the OLS regression problem is ill-posed.

Note that the overfitting problem can easily arise in the s-PGD context when high-order approximations (that separated representations exacerbate) are employed because of the usual unstructured low data regime used to train the model. This issue strongly affects the model's ability to perform on new, unseen sets. Therefore, the idea of using the penalty term consists in improving the model's ability to perform on new samples at the cost of increasing the bias or the error model in the training set for a given set of basis functions.

Different regularizations can be envisaged depending on the properties of the problem such as the Tikhonov regularization or the Elastic Net regularization.

For the sake of simplicity but without loss of generality, we start introducing the ridge regression regularization (a special case of the Tikhonov regularization) that will be generalized later to lead to the Elastic Net redularization.

For this purpose, we first rewrite Eqs. (3.3) and (3.4):

$$\mathbf{a}_M^x = (\mathbf{M}_x^\top \mathbf{M}_x - \lambda \mathbf{I})^{-1} \cdot \mathbf{M}_x^\top \mathbf{r} \tag{3.5}$$

$$\mathbf{a}_M^y = (\mathbf{M}_y^\top \mathbf{M}_y - \lambda \mathbf{I})^{-1} \cdot \mathbf{M}_y^\top \mathbf{r}, \tag{3.6}$$

where λ is the penalty factor and $\mathbf{I}$ is the identity matrix. In this case, both dimensions are equally penalized but different penalty factors could be considered depending on the considered dimension, as well as penalizing only the most conflictive one.

The regularized problems associated to Eqs. (3.5) and (3.6) are:

$$\mathbf{a}_M^x = \arg\min_{\mathbf{a}_M^{x*}} \left\{ \|\mathbf{r} - \mathbf{M}_x \mathbf{a}_M^{x*}\|_2^2 + \lambda \|\mathbf{a}_M^{x*}\|_2^2 \right\}, \tag{3.7}$$

$$\mathbf{a}_M^y = \arg\min_{\mathbf{a}_M^{y*}} \left\{ \|\mathbf{r} - \mathbf{M}_y \mathbf{a}_M^{y*}\|_2^2 + \lambda \|\mathbf{a}_M^{y*}\|_2^2 \right\}, \tag{3.8}$$

where the problem is divided in solving a ridge regression problem for each dimension when computing $\mathbf{a}_M^x$ and $\mathbf{a}_M^y$ during the alternate direction fixed point strategy.

The interpretation of employing Eqs. (3.7) and (3.8) during the PGD iterative scheme can be thought of as an attempt of solving the following problem within the PGD rationale:

$$\tilde{f}^M(\mathbf{a}_M^x, \mathbf{a}_M^y) = \arg\min_{\mathbf{a}_M^{x*}, \mathbf{a}_M^{y*}} \left\{ \left\| f - \tilde{f}^M(\mathbf{a}_M^{x*}, \mathbf{a}_M^{y*}) \right\|_2^2 + \lambda \|\mathbf{a}_M^{x*}\|_2^2 + \lambda \|\mathbf{a}_M^{y*}\|_2^2 \right\}, \tag{3.9}$$

where $\|\cdot\|_2$ is the Euclidean norm, and $\tilde{f}^M$ is the function defined in (2.4) where the new M-th order term of the model is sought.

As the terminology used in this section shows, a regularization problem is formulated at each enrichment step. Thus, we are looking for the best penalty factor at each updating stage, adapting the regularization whenever the approach is enriched. Other possibilities can be envisaged but this one seems the one which offers the best results according to our numerical experiments.

A null intercept term was assumed for $\mathbf{a}_M^x$ and $\mathbf{a}_M^y$ in the deduction of equations (3.5), (3.6), (3.7) and (3.8). If this term is going to be included, it can be treated as in standard ridge procedures when solving the corresponding linear regularized regression problem for each dimension during the alternating direction strategy.

As we are generally looking for the mode with best predictive abilities in each enrichment, the proposed criterion to choose λ is to perform a k-fold cross-validation and select the value of λ that minimizes the cross-validated sum of squared residuals (or some other measure). It is also possible to use the "one-standard error" rule (heuristic) with cross-validation, in which we choose the most penalized model whose error is no more than one standard error above the error of the best model. Such a rule acknowledges the fact that the tradeoff curve is estimated with error, and hence takes a conservative approach [Hastie *et al.* 2009].

If enough data is available, the split of the training set in two subgroups is equally a reasonable option to select λ and in addition, computationally less demanding. In this case, one subgroup is employed for constructing the model and the other one to evaluate the predictive ability and then to select λ accordingly.

The Elastic Net regularization results of including a L1-norm regularization, from which Eqs. (3.7)-(3.8) and Eq. (3.9) become:

$$\mathbf{a}_M^x = \arg\min_{\mathbf{a}_M^{x*}} \left\{ \|\mathbf{r} - \mathbf{M}_x \mathbf{a}_M^{x*}\|_2^2 + \lambda \left[(1-\alpha) \|\mathbf{a}_M^{x*}\|_2^2 + \alpha \|\mathbf{a}_M^{x*}\|_1 \right] \right\}, \tag{3.10}$$

$$\mathbf{a}_M^y = \arg\min_{\mathbf{a}_M^{y*}} \left\{ \|\mathbf{r} - \mathbf{M}_y \mathbf{a}_M^{y*}\|_2^2 + \lambda \left[(1-\alpha) \|\mathbf{a}_M^{y*}\|_2^2 + \alpha \|\mathbf{a}_M^{y*}\|_1 \right] \right\}, \tag{3.11}$$

and

$$\begin{aligned} \tilde{f}^M(\mathbf{a}_M^x, \mathbf{a}_M^y) = \arg\min_{\mathbf{a}_M^{x*}, \mathbf{a}_M^{y*}} & \left\{ \left\| f - \tilde{f}^M(\mathbf{a}_M^{x*}, \mathbf{a}_M^{y*}) \right\|_2^2 \right. \\ + & \left. \lambda \left[(1-\alpha) \left(\|\mathbf{a}_M^{x*}\|_2^2 + \|\mathbf{a}_M^{y*}\|_2^2 \right) + \alpha \left(\|\mathbf{a}_M^{x*}\|_1 + \|\mathbf{a}_M^{y*}\|_1 \right) \right] \right\}, \end{aligned} \tag{3.12}$$

respectively, where $\alpha \in [0, 1)$ and λ are the penalty factors. These coefficients could be also different for the different dimensions, and as before, other appealing option consists on penalizing only the most conflictive dimension. The limit cases $\alpha = 0$ and $\alpha = 1$ result in the Ridge and Lasso regressions respectively.

3.2.3 s^2-PGD

For the ease of the exposition and representation but without loss of generality, let us continue by assuming the same two-dimensional unknown function discussed in Section 3.2.2.

Here, we are dealing with a solution which admits a sparse solution for a certain basis using the PGD separated form (2.2). In this case, the goal is to identify the correct non-zero coefficients at each enrichment step in order to guide the approach to the correct separated representation.

Without a roadmap to select these nonzero coefficients, the traditional s-PGD fails to capture the true relationship between the model's features as well as its final response.

Furthermore, if high-order terms appear in the searched function, this issues become even worse leading to serious overfitting issues.

Let us consider the theory discussed in the previous section but now considering the L1 regularization with the idea to promote sparsity in the overall solution of the nonlinear regression problem:

$$\tilde{f}^M(\mathbf{a}_M^x, \mathbf{a}_M^y) = \underset{\mathbf{a}_M^{x*}, \mathbf{a}_M^{y*}}{\arg\min} \left\{ \left\| f - \tilde{f}^M(\mathbf{a}_M^{x*}, \mathbf{a}_M^{y*}) \right\|_2^2 + \lambda \left\| \mathbf{a}_M^{x*} \right\|_1 + \lambda \left\| \mathbf{a}_M^{y*} \right\|_1 \right\}. \tag{3.13}$$

This formulation is convenient because the nonlinear problem can be solved using the PGD constructor, with an alternate direction fixed point strategy, where a LASSO regression problem is considered in each dimension.

Therefore, the regression problems for the iterative scheme will be:

$$\mathbf{a}_M^x = \underset{\mathbf{a}_M^{x*}}{\arg\min} \left\{ \left\| \mathbf{r} - \mathbf{M}_x \mathbf{a}_M^{x*} \right\|_2^2 + \lambda \left\| \mathbf{a}_M^{x*} \right\|_1 \right\}, \tag{3.14}$$

$$\mathbf{a}_M^y = \underset{\mathbf{a}_M^{y*}}{\arg\min} \left\{ \left\| \mathbf{r} - \mathbf{M}_y \mathbf{a}_M^{y*} \right\|_2^2 + \lambda \left\| \mathbf{a}_M^{y*} \right\|_1 \right\}, \tag{3.15}$$

that consists of solving a LASSO regression problem for each dimension when computing $\mathbf{a}_M^x$ and $\mathbf{a}_M^y$ within the alternate direction fixed point strategy. Moreover, as previously discussed, in the present case again, both dimensions are equally penalized but different penalty factors could be envisaged.

As we are iteratively solving a LASSO problem, we will end up with sparse solutions for each one-dimensional function choosing the right penalty factor. Again, a null itercept term was assumed.

In case of looking for sparsity just in the x dimension, only Eq. (3.14) applies for computing coefficients $\mathbf{a}_M^x$, whereas coefficients $\mathbf{a}_M^y$ are calculated by invoking the standard s-PGD or the rs-PGD, addressed in the previous section.

To determine λ, we first refer the reader to the discussion of the previous section. Then, the following considerations applied in the case of the doubly sparse PGD:

- Before selecting the model enrichment according to the predictive criterion, a filter is considered taking only the models with a minimum sparsity criterion $\|\mathbf{a}_M^x\|_0 \leq \chi_x^{lim}$. If sparsity is also desired in y direction, χ_y^{lim} will be defined accordingly. Note: We define $\|\cdot\|_0$ by $\|\mathbf{x}\|_0 = \#\{i : \mathbf{x}_i \neq 0\}$. This notation is considered even if it is actually not a norm.
- Once the aforementioned model selection is performed, the OLS methodology is employed with the detected non-zero elements to obtain the correct mode update. The reason of this step is that LASSO regression terms are in general not accurate, and so it may be necessary to de-bias the obtained values. Remember that the LASSO shrinkage causes the estimates of the non-zero coefficients to be biased towards zero and in general they are not consistent [Brunton & Kutz 2019] [Hastie *et al.* 2009].

3.3 The ANOVA-based sparse-PGD

The ANOVA decomposition of a function of P variables $f(s^1, \ldots, s^P) : \Omega \subset \mathbb{R}^P \to \mathbb{R}$ is an orthogonal decomposition based on the analysis of variance, a statistical model designed for data analysis. Thus, the function $f(\mathbf{s})$ can be written as a sum of orthogonal functions:

$$f(\mathbf{s}) = f_0 + \sum_{i=1}^{P} f_i(s^i) + \sum_{i_1=1}^{P} \sum_{i_2=i_1}^{P} f_{i_1,i_2}(s^{i_1}, s^{i_2}) + \ldots + f_{1,2,\ldots d}(s^1, s^2, \ldots, s^P), \tag{3.16}$$

satisfying

$$\mathbb{E}_i(f_{i_1,\ldots,i_k}(s^{i_1},\ldots,x^{i_k}))=0, \tag{3.17}$$

where $\mathbb{E}_i$ refers to the expectation with respect to any coordinate i in the set $(i_1,\ldots,i_k)$, $1\le k\le P$. This property results in the orthogonality of functions involved in the previous decomposition.

To prove it, consider for example a simple 2D case with, $\mathbf{s}=(x,y)$, $f(\mathbf{s})\equiv f(x,y)$. Thus, with $\mathbb{E}_x(f_x(x))=0$, $\mathbb{E}_x(f_{x,y}(x,y))=0$ and $\mathbb{E}_y(f_{x,y}(x,y))=0$, we have $\mathbb{E}_{x,y}(f_{x,y}(x,y)f_x(x))=\mathbb{E}_x\{\mathbb{E}_y(f_{x,y}(x,y))\ f_x(x)\}=0$.

The number of function involved in the decomposition (without considering the constant term) is 2^P-1, and they can be parametrized by the integer n, $n=1,\ldots,2^P-1$. The different functions involved in the ANOVA decomposition can be expressed from expectations according to:

$$\begin{cases}\mathbb{E}(f(\mathbf{s}))=f_0\\ \mathbb{E}(f(\mathbf{s}|s^i))=f_i(s^i)+f_0\\ \mathbb{E}(f(\mathbf{s}|s^i,s^j))=f_{i,j}(s^i,s^j)+f_i(s^i)+f_j(s^j)+f_0\\ \vdots\end{cases} \tag{3.18}$$

where $\mathbb{E}(f(\mathbf{s}|s^i))$ refers to the integration on all the variables except s^i.

3.3.1 Sensitivity analysis: Sobol coefficients

The variance of $f(\mathbf{s})$, $\mathrm{Var}(f(\mathbf{s}))$, taking into account the orthogonality of the functions involved in the ANOVA decomposition, reads

$$\mathrm{Var}(f(\mathbf{s}))=\sum_{n=1}^{2^P-1}\mathbb{E}\left(f_n(\mathbf{s}_n)\right)^2=\sum_{n=0}^{2^P-1}\mathrm{Var}_n, \tag{3.19}$$

that allows defining the so-called Sobol sensitivity coefficients $\mathcal{S}_n$

$$\mathcal{S}_n=\frac{\mathrm{Var}_n}{\mathrm{Var}(f(\mathbf{s}))}. \tag{3.20}$$

3.3.2 The *anchored* ANOVA

Multidimensional settings imply expensive calculations for computing the multidimensional expectations. For alleviating those costly computations we introduce the so-called anchor point $\mathbf{c}$ such that $f_0=f(\mathbf{c})$. Then, in the definition of the functions involved in the ANOVA decomposition, the expectations are replaced by $f(\mathbf{c}|\mathbf{s}_n)$, that is, the particularization of the function in the anchor point, except for those coordinates involved in $\mathbf{s}_n$.

3.3.3 Combining the *anchored*-ANOVA with the sparse PGD

A valuable strategy consists in: (i) first, using the standard *anchored*-ANOVA for evaluating the functions depending on each dimension $f_i(s^i)$, $i=1,\ldots,P$, by suing an adequate sampling, a sort of multidimensional cross centered at the anchor point $\mathbf{c}$. In each dimension, $f_i(s^i)$ can be approximated by using any variable approximation, eventually the regularized ones discussed in the previous sections. Then, (ii) one could compute the residual $f'(\mathbf{s})$:

$$f'(\mathbf{s})=f(\mathbf{s})-f_0-\sum_{i=1}^{P}f_i(s^i), \tag{3.21}$$

and finally, (iii) using the rs-PGD, or the s^2-PGD, for approximating that residual $f'(\mathbf{s})$ that contains the different correlations. In that case, an enhanced sparse-sampling can be considered, trying to approach as much as possible the points involved in the sparse sampling to the borders of the parametric domain.

3.4 Results

In this section, the results of using the above techniques are shown for different cases. First, in Section 3.4.1, the error reduction is shown when using the rs-PGD comparing with the classical procedure (s-PGD). Then, in Section 3.4.2, sparse identification and error reduction is presented when using the s^2-PGD comparing with the standard sparse procedure (s-PGD). Finally, Section 3.4.3 employes the analysis of variance and combines it with regularized approximations to define an original and powerful regression methodology.

3.4.1 Results for the rs-PGD approach

The following examples considers the Elastic Net Regularization. For that purpose, an α parameter is employed for combining the Ridge and Lasso regression. The α parameter is selected by running the algorithm several times for different α values, and then choosing the one which has better predictive performances.

3.4.1.1 A first example involving a five dimensional polynomial

In the first example, we are trying to approximate the five-dimensional function

$$f(x_1, x_2, x_3, x_4, x_5) = (8x_1^3 - 6x_1 - 0.5x_2)^2 + (4x_3^3 - 3x_3 - 0.25x_4)^2 + 0.1(2x_5^2 - 1). \quad (3.22)$$

The above function is intended to be reconstructed in the domain $\Omega = [-0.51, 0.51]^5$. The sampling for the training set contains 160 points. Therefore, only these points are used to construct the model either using the s-PGD or the rs-PGD methodology. In addition, the Latin hypercube sampling (LHS) is used to generate this set of data.

On the other hand, a testing set of 54000 untrained points is considered to compare the results between techniques when predicting unseen scenarios. This second set will be used to study the predictive ability of both models once they are finally constructed.

A standard MAS employing up to 4th degree polynomials for both the s-PGD and the rs-PGD is considered. To measure the error of both methodologies in the testing set, the following error criterion is used:

$$\text{err}_{\text{pgd}} = \frac{\|\mathbf{z} - \mathbf{z}_{\text{pgd}}\|_2}{\|\mathbf{z}\|_2}; \qquad \text{err}_{\text{rpgd}} = \frac{\|\mathbf{z} - \mathbf{z}_{\text{rpgd}}\|_2}{\|\mathbf{z}\|_2};$$

where $\mathbf{z}$ is the vector containing the values of $f(x_1, x_2, x_3, x_4, x_5)$ in the testing set, $\mathbf{z}_{pgd}$ and $\mathbf{z}_{rpgd}$ are the vectors containing the prediction in the testing set of both methodologies (s-PGD and rs-PGD, respectively).

After employing the discussed techniques in the above conditions, we obtain in this example that the error is reduced by 52.38 % using the rs-PGD with $\alpha = 0.1$.

To perceive the improvements and the overfitting reduction, in Figure 3.2, we show a plot of the original function $f(x_1, x_2, x_3 = 0, x_4 = 0, x_5 = 0.7071)$. It can be noticed that the rs-PGD corrects the shape of the function in the indicated areas in Fig. 3.2, improving the performance of the regression.

This improvement occurs over the whole five-dimensional domain. Other result is shown in Figure 3.3 that depicts $f(x_1, x_2, x_3 = -0.17069, x_4 = -0.17069, x_5 = -0.015517)$.

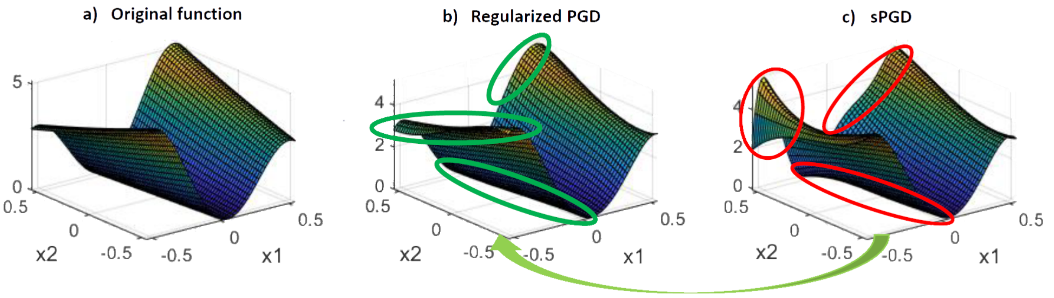

Figure 3.2 – Comparing the reference (Eq. (3.22)) and its associated s-PGD and rs-PGD regressions, at points $(x_1, x_2, x_3 = 0, x_4 = 0, x_5 = 0.7071)$

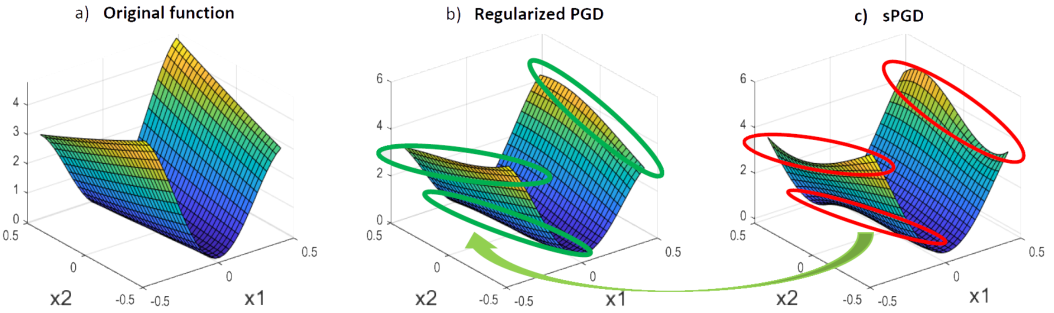

Figure 3.3 – Comparing the reference (Eq. (3.22)) and its associated s-PGD and rs-PGD regressions, at points $(x_1, x_2, x_3 = -0.17069, x_4 = -0.17069, x_5 = -0.015517)$

3.4.1.2 A second example involving five dimensions with trigonometric and logarithmic functions

In this second example, we are trying to approximate the function:

$$\begin{aligned} f(x_1,x_2,x_3,x_4,x_5) = \cos(x_1x_2)\Big[&\big(\sin(2x_3)-3.14\big)\log(3x_4+1.5)\cos(x_5) \\ &+\exp(x_4)\cosh(x_3)\sinh(x_5)\Big], \end{aligned} \tag{3.23}$$

by using the rs-PGD with polynomials. The above function is intended to be reconstructed in the domain $\Omega = [-1,1]^5$.

In this case, the sampling for the training set contains 290 points. Therefore, only these points are used to construct the model either by using the s-PGD or the rs-PGD methodology. In addition, the Latin hypercube sampling is used to generate this set of data.

On the other hand, a testing set of 2000 untrained points is available to compare the results when predicting unseen scenarios. Again a standard MAS is employed reaching 4th degree polynomials in both, the s-PGD and the rs-PGD. An error reduction of about 47% is accomplished with $\alpha = 0.5$.

3.4.1.3 Results on the chaotic Lorenz system.

As a last example, we consider a canonical model for chaotic dynamics, the Lorentz system [Brunton *et al.* 2015, Lorenz 1963]:

$$\begin{aligned} \dot{x} &= \sigma(y-x) \\ \dot{y} &= x(\rho-z)-y \\ \dot{z} &= xy-\beta z \end{aligned}$$

with parameters $\sigma = 10$, $\rho = 28$ and $\beta = 8/3$.

Data are collected using a sampling without replacement in the interval $t \in [0,20]$ until completing a set of 102 points. These 102 points will be divided in two sets: the construction set and the validation set. The first one will be used to compute the regression coefficients and the other one to select the hyperparameters. Furthermore, the ridge regularization is employed as well as the MAS for the rs-PGD when identifying the dynamics. As in other instances, the Chebyshev basis is used in the one-dimensional approximations.

The rs-PGD successfully detects the important non-zero coefficients with an error below 0.02 % in the construction and validation set for the three variables. As an illustration, the initial identified coefficients for $\dot{x}$ are shown in Table 3.1. As we can observe, the theoretical zero coefficients are not always exactly zero but they are very small. However, we are dealing with a chaotic dynamics where very small deviations on the identified parameters can produce huge deviations in the long-time predictions.

For this reason, once the rs-PGD solution is computed, a filter based on the sequential thresholded least-squares (STLS) can be applied on the remaining coefficients, aiming at removing the coefficients below a given threshold, and then the least squares procedure applies again to recompute the coefficients, for obtaining a very accurate regression, as Figs. 3.4 and 3.5 prove.

3.4.2 Checking the performances of s^2-PGD when addressing sparse solutions

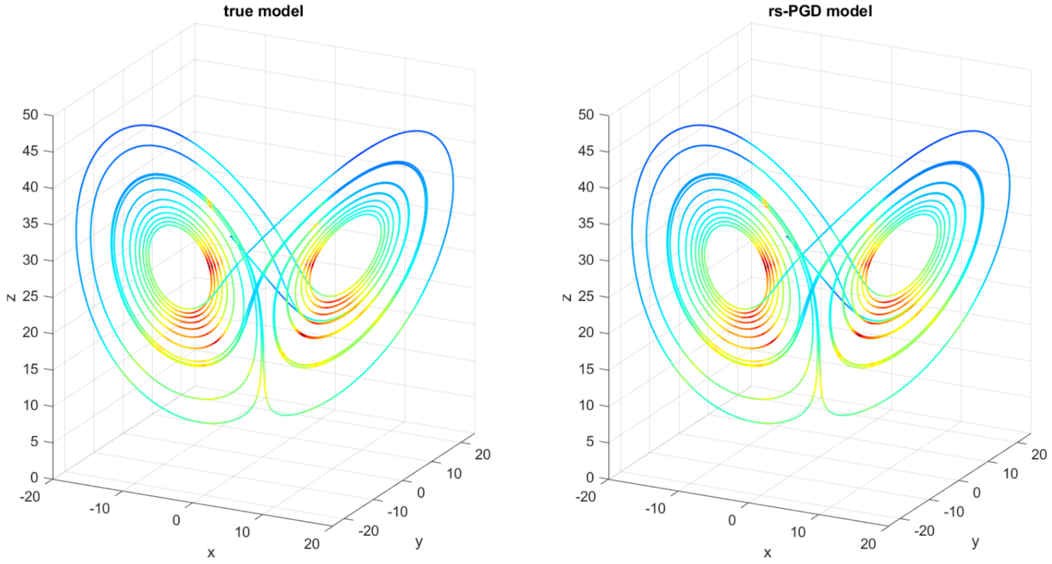

Figure 3.4 – True dynamics and dynamics identified by the rs-PGD model

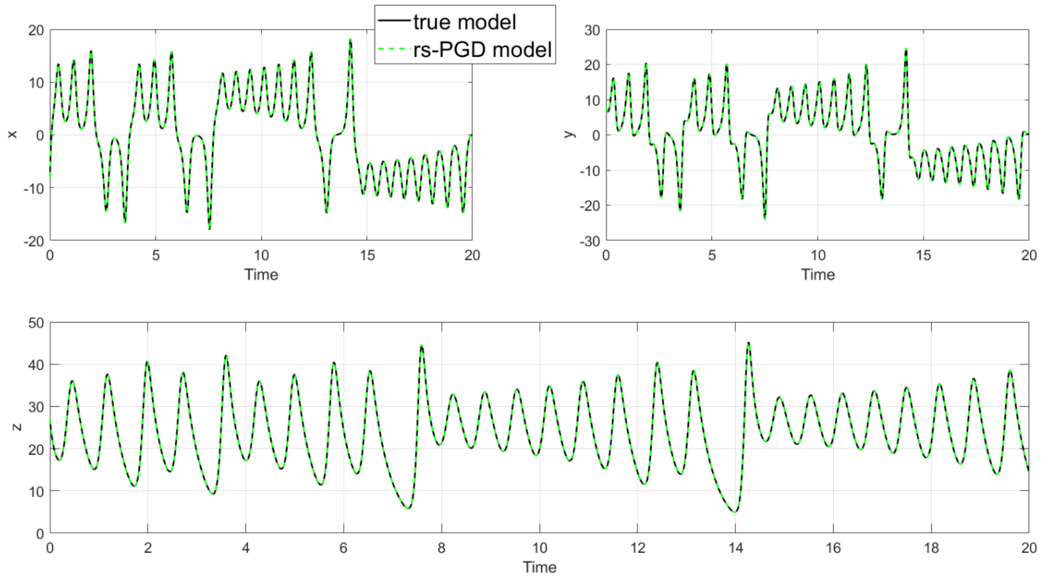

Figure 3.5 – Comparison between rs-PGD predictions and true dynamics on the three-variable time evolution.

	$\dot{x}$
$\{' \, '\}$	$\{[8.7112e-04]\}$
$\{'x'\}$	$\{[-9.9997]\}$
$\{'y'\}$	$\{[9.9996]\}$
$\{'z'\}$	$\{[0]\}$
$\{'xy'\}$	$\{[-1.3783e-05]\}$
$\{'xz'\}$	$\{[0]\}$
$\{'yz'\}$	$\{[0]\}$
$\{'xyz'\}$	$\{[0]\}$

Table 3.1 – Initial rs-PGD model for $\dot{x}$

3.4.2.1 A first example involving sparsity in one dimension

In the first example of this Section, we are trying to approximate the function:

$$f(x_1, x_2, x_3) = (\sin(2x_1) - 3.14)T_5(x_2) + \exp(x_3)\cosh(x_1), \tag{3.24}$$

by using a Chebyshev basis for the one-dimensional functions of the PGD. The above function is intended to be reconstructed in the domain $\Omega = [-1, 1]^3$.

Moreover, the sampling for the training set is created using a sparse grid based on the Smolyak quadrature rule of level 3 based on the Clenshaw-Curtis univariate quadrature rule [Kaarnioja 2013, Beddek 2012]. Therefore, only these points are used to construct the model either using the s-PGD or the s^2-PGD methodology. In figure 3.6, the mesh used for the training set is shown.

On the other hand, a testing set of 27000 untrained points is available to compare the results between techniques when predicting unseen scenarios. This second set will be used to study the predictive ability of both models once they are finally constructed.

The conditions to employ the s^2-PGD in this example are the following. A basis reaching eighth-degree polynomials is chosen for the sparse dimension. Moreover, a standard MAS-based s-PGD is used, reaching 4th degree polynomials along the non-sparse dimensions.

In Figure 3.7, the results of the standard s-PGD are shown. In this case, we can see that the predictions are bad because this methodology completely fails in finding this type of sparse solutions. This is one of the problems that the s-PGD is facing and we propose to solve with the s^2-PGD.

In addition, if we observe the s-PGD solution we can see that all the possible elements are nonzero, so it fails in identifying the sparsity. To detect sparsity, three simulations of the s^2-PGD are carried out, penalizing a different dimension at each iteration. Consequently, the model with best predictive ability (out of the training set) will be the selected one. As expected, the chosen model is the one obtained when penalizing the x_2 dimension.

In Figure 3.8, the results of the s^2-PGD are presented. As we can observe, predictions are almost perfect. If we examine the solution, we can see that the model is correctly identified using four modes, that is, four sums of the PGD decomposition.

The errors concerning the s-PGD and the s^2-PGD solutions are respectively $\text{err}_{pgd} = 141$ % and $\text{err}_{s^2pgd} = 0.56$ %.

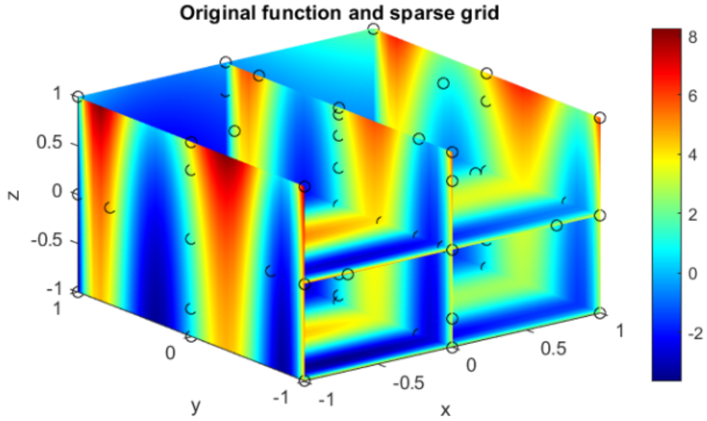

Figure 3.6 – Plot of the original function and the training set (circles) used to construct the PGD models.

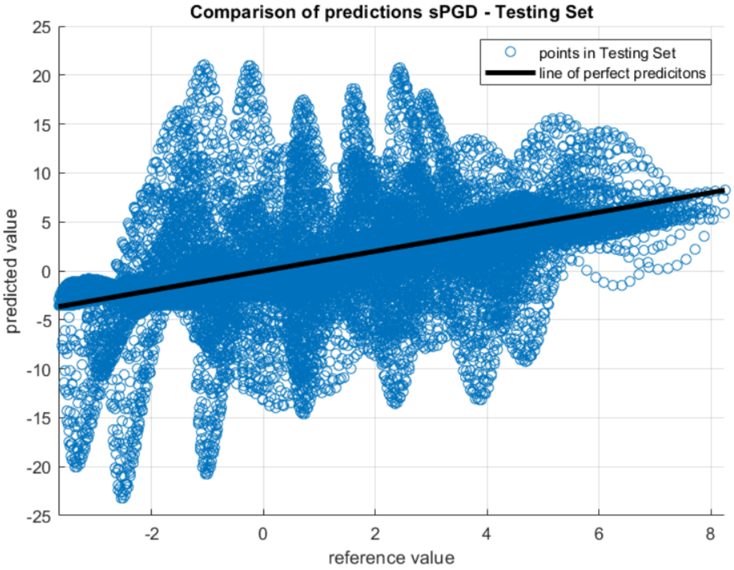

Figure 3.7 – Problem defined in Eq. (3.24): Comparison of predicted s-PGD values with the reference ones in the testing set (the black line represents a perfect prediction)

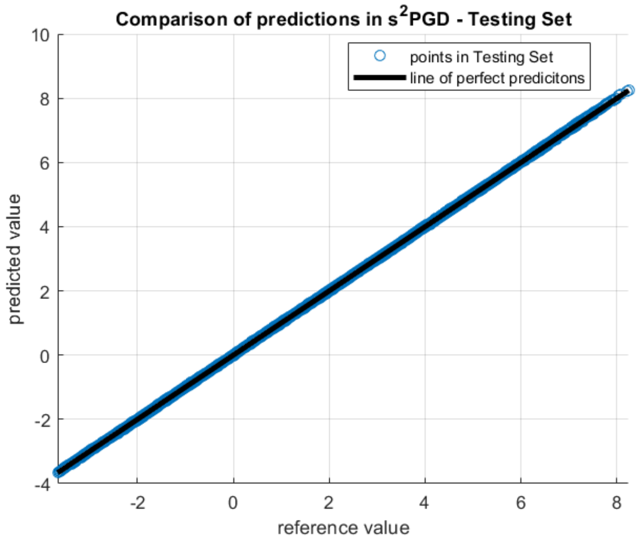

Figure 3.8 – Problem defined in Eq. (3.24): Comparison of predicted s^2-PGD values with the reference ones in the testing set (the black line represents a perfect prediction)

3.4.2.2 A second example involving more dimensions

In this case we consider the approximations problem of function

$$f(x_1,x_2,x_3,x_4,x_5) = \big[T_5(x_1) + 2T_1(x_1)\big]\big[T_2(x_2) + 2T_4(x_2)\big] \\ \Big[\big(\sin(2x_3) - 3.14\big)\log(3x_4 + 1.5)\cos(x_5) + \exp(x_4)\cosh(x_3)\sinh(x_5)\Big] \quad (3.25)$$

by using a Chebyshev approximation basis for the one-dimensional functions involved in the PGD constructor.

The above function is intended to be reconstructed in the domain $\Omega = [-1,1]^5$. The sampling for the training set contains 290 points. In addition, the Latin hypercube sampling is used to generate this random set of data.

On the other hand, a testing set of 2000 untrained points is available to compare the results between techniques when predicting unseen scenarios. As in the previous examples, this second set will be used to study the predictive ability of both models once they are finally constructed.

Concerning the s^2-PGD a basis reaching sixth-degree polynomials is chosen for the sparse dimensions. Moreover, a standard MAS is used, up-to 4th degree polynomials, in the non-sparse dimensions.

In Figure 3.9, the results of the standard s-PGD are shown. In this case, we can see that the predictions are bad. This is due to the wrong identification of the non-zero elements in the separated representation, which causes overfitting problems.

To detect sparsity, five different simulations of the s^2-PGD are carried out, penalizing one different dimension each time. Consequently, the model with best predictive ability (out of the training set) will be the selected one. As expected, the chosen model is the one obtained when penalizing the x_1 dimension. The reason is that in this case, we observe that the correct non-zero terms for x_1 and x_2 are identified just penalizing x_1.

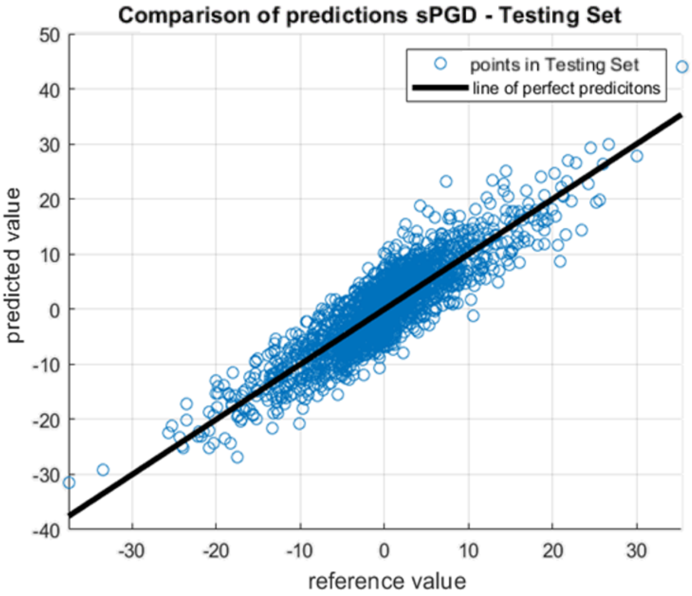

Figure 3.9 – Problem defined in Eq. (3.25): Comparison of predicted s-PGD values with the reference ones in the testing set (the black line represents a perfect prediction)

In Figure 3.10, the results of the s^2-PGD are presented. An exellent agreement between the real function and the proposed approach is observed. Furthermore, if we examine the s^2-PGD solution, we can see that the model have correctly identified the non-zero elements. In addition, this PGD solution needed 104 modes, that is, 104 sums of the PGD decomposition, solution that can be re-compacted by invoking again the PGD [Chinesta *et al.* 2013a].

Finally, the errors concerning the s-PGD and the s^2-PGD solutions are respectively $\text{err}_{pgd} = 46.39$ % and $\text{err}_{s^2pgd} = 2.4$ %.

3.4.3 ANOVA-PGD numerical results

ANOVA-PGD regression consists of applying regression techniques (such as standard interpolation, s-PGD, rs-PGD or s^2-PGD) separately to the different terms (or groups of terms) in the ANOVA decomposition. This strategy suggests the MAS since it enforces some simplicity in the first modes, even if here richer approximations can be envisaged, but it also provides other benefits through the orthogonality of the decomposition and the opportunity to work in a low dimension setting, as previously expossed.

Here, we consider the numerical test related to the 2D function

$$f(x, y) = -2\cos(3x^{1.75}) + 10\log(y - 0.6)^4 + 6\cos(x)(y - 0.3y^2), \tag{3.26}$$

that perfectly fits the ANOVA structure, despite the functional complexity of the terms involving the coordinates x and y, $2\cos(3x^{1.75})$ and $10\log(y - 0.6)^4$ respectively, and the one coupling both coordinates, $6\cos(x)(y - 0.3y^2)$.

When considering the ANOVA-based sampling consisting of the center point of the parametric domain acting as the anchor $\mathbf{c} = (x_c, y_c)$, 10 additional points in the first

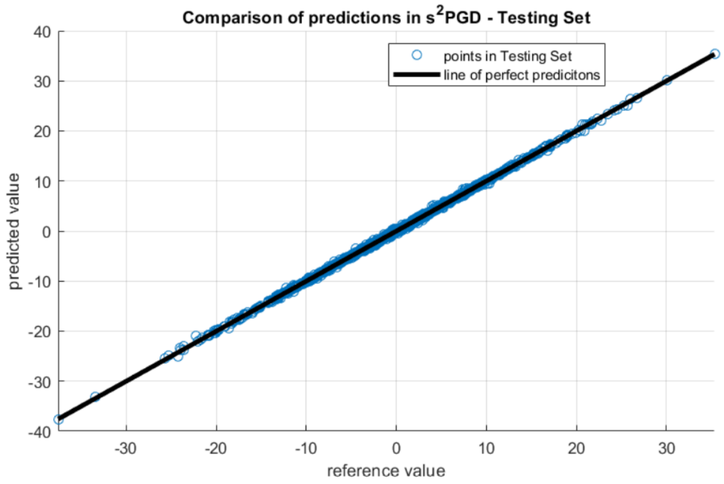

Figure 3.10 – Problem defined in Eq. (3.25): Comparison of predicted s^2-PGD values with the reference ones in the testing set (the black line represents a perfect prediction)

dimension (of the form (x, y_c)) and 10 additional points in the second dimension (of the form (x_c, y)), functions $f_x(x)$ and $f_y(y)$ were calculated with a cubic spline interpolation. Then, a standard 2D nonlinear regression using basis functions of the form $(x - x_c)^m (y - y_c)^n$, $m, n \geq 1$ (due to the low dimensionality of the treated problem the employ of separated representations is not needed) was employed for calculating the term $f_{x,y}(x, y)$ using 4 sample points.

The constructed solution is depicted in Fig. 3.11 where it is compared with the exact solution as well as with the solution obtained by using the standard s-PGD (with a Latin Hypercube Sampling containing 25 points), while Figs. 3.12 and 3.13 compare the predictions and the reference values. From all these results, excellent performances of the ANOVA-based regression can be stressed.

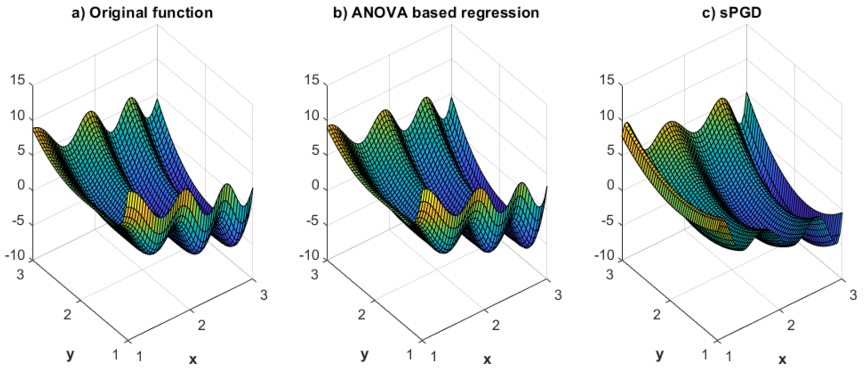

Figure 3.11 – Comparing s-PGD and ANOVA-PGD regressions

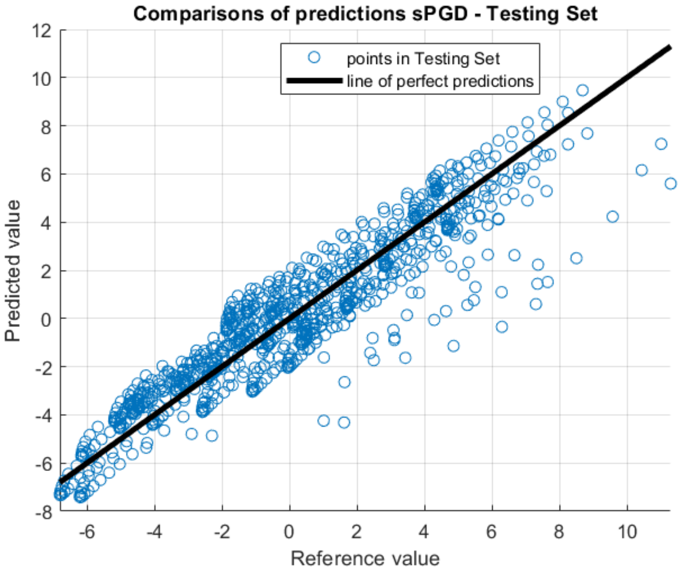

Figure 3.12 – Problem defined in Eq. (3.26): Comparison of predicted s-PGD values with the reference ones in the testing set (the black line represents a perfect prediction)

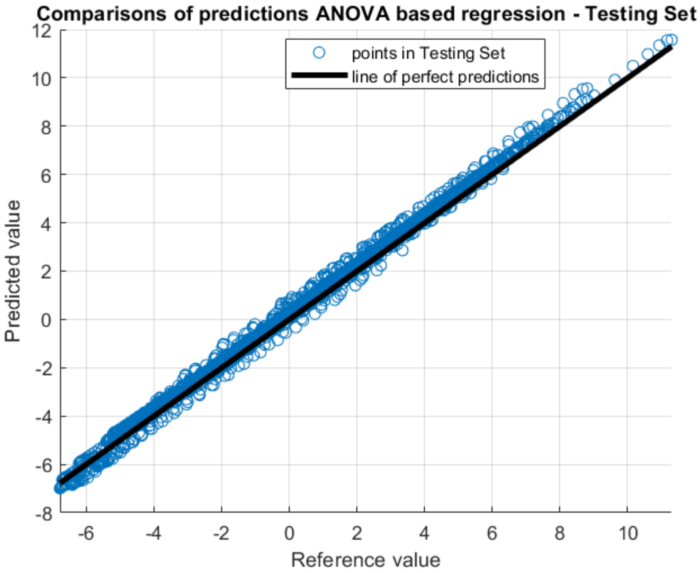

Figure 3.13 – Problem defined in Eq. (3.26): Comparison of predicted ANOVA-PGD values with the reference ones in the testing set (the black line represents a perfect prediction)

3.5 Conclusions

In this chapter, three different data-driven regression techniques are introduced, the first two, the so-called rs-PGD and s^2-PGD, that consist of a regularization of the usual sparse PGD, and the third, that combines analysis of variance features with sparse separated representations. It has been shown and discussed, through different examples, how they can improve significantly the existing sparse s-PGD performance, reducing overfitting and achieving great explanatory predictive capabilities when dealing with unseen scenarios.

Furthermore, the s^2-PGD can be employed to sparse identification and variable selection when the s-PGD fails. The comparison of Figures 3.7 and 3.8 is an example of the substantial improvements under this rationale.

In addition, the suitability of the s-PGD to deal with the challenging scenarios concerning the low-data regime context and high-dimensional parametric functions was previously proved in [Ibáñez Pinillo *et al.* 2018] and [Ibanez Pinillo 2019]. Therefore, the improvements carried out by these new techniques opens the door to construct better high-performance ROMs in this difficult context. Moreover, this is really appealing because of the increasing industrial interest of obtaining accurate models under these circumstances.

Part III

Industrial and Practical Applications

CHAPTER 4

Advanced Multi-Parametric models for Electric Machines.

Abstract At present, industry is permanently looking for fast and accurate solutions in electric machines such as electric motors and generators, and trends such as the Electric Vehicle (EV) or the self-driving car are producing a lot of investment in that direction. The reason for this seems clear: achieving these goals will improve the final design's performance and economic competitiveness. In fact, a great portion of numerical simulations concerning real-life problems face difficulties in design, optimization and control due to the complexity of the system, high computational costs, and storage requirement. In order to deal with the above issues, two reduced order models are proposed. Consequently, high-dimensional parametric solutions are obtained to quickly determine the response of the electric machine with accuracy. In this way, a huge benefit is obtained when tasks such as optimization, inverse analysis or simulation-based control are performed. Although the techniques described here have a wide range of application, this work has a special focus on the treatment of noise and vibration of electric motors in the EV, the industrial application that motivated this work.

Contents

4.1 Introduction 89
  4.1.1 Chapter overview 89
4.2 Multi-Parametric Electromagnetic Fields in Synchronous Machines by Using PGD-Based Fully Separated Representations 90
  4.2.1 Intrusive approach: Introduction 90
  4.2.2 Electromagnetic Equations 91
  4.2.3 Description of the Analyzed Motor 92
  4.2.4 PGD Physical Space Separated Solution 93
  4.2.5 PGD Parametric Solution 95
  4.2.6 Results 98
4.3 A novel sparse reduced order formulation for modeling electromagnetic forces in electric motors 104
  4.3.1 Non-intrusive approach: Introduction 104
  4.3.2 Analyzed motors 106
    4.3.2.1 Induction motor 106
    4.3.2.2 Synchronous motor 107
  4.3.3 Post-processing step. Computation of the radial force waves/magnetic pressure 107
  4.3.4 Reduced order model 109
  4.3.5 Results 109
    4.3.5.1 Induction Motor. Linear B-H 109

4.3.5.2 Induction Motor. Nonlinear B-H 114
4.3.5.3 Synchronous motor 114
4.3.5.4 Sensitivity analysis of the parametric solutions . . . 119
4.4 Conclusions 126

4.1 Introduction

4.1.1 Chapter overview

This chapter address an important industrial application nowadays: the need of fast, accurate and parametric models for electric machines. These solutions are highly demanded by the industry, especially with the recent developments in the Electric Vehicle (EV).

In this context, the following two areas of work are addressed:

- A novel Reduced Order Model is obtained employing the intrusive PGD to construct a high-dimensional parametric solution for electromagnetic fields in synchronous machines (Section 4.2). The proposed approach is capable to construct this parametric solution in a few minutes of off-line simulation and once constructed, a particular solution can be particularized on-line in less than a second. In particular, the result is a virtual chart allowing real-time evaluation of the magnetic vector potential as a function of the operation point of the motor, or even as a function of constructive parameters, such as the remanent flux in permanent magnets. This is possible thanks to the use of a fully separated representation in which the solution is written from a series of functions of the space and parameters coordinates, with full space separation made possible by the use of an adapted geometrical mapping. In this context, the domain of simulation is not suitable for a PGD separated representation, making its successful and efficient application to the problem challenging. However, in this dissertation, a new suitable mapping is developed to transform the motor geometry. Thus, the resultant new geometry will be more adapted to achieve good results within the PGD framework.
- A novel non-intrusive Model Order Reduction (MOR) strategy is employed to achieve fast and real-time predictions as well as high-dimensional parametric solutions for the electromagnetic force which will help the design, analysis of performance and implementation of electric machines concerning industrial applications such as the noise, vibration, and harshness in electric motors (Section 4.3). The approach allows to avoid the long-time simulations needed to analyze the electric machine at different operation points. In addition, it can be easily extended to predict other quantities of interest such as the torque or the fluxes. Moreover, it facilitates the computation and coupling of the motor model in other physical subsystems. Specifically, the novel formulation employed is the one proposed in Section 2.3 of this dissertation. Here, the sparse Proper Generalized Decomposition procedure is combined with a Reduced Basis approach, which is used to fit correctly the Reduced Order Model with the numerical simulations as well as to obtain a further data compression. This technique can be applied to construct a regression model from high-dimensional data. These data can come, for example, from Finite Element simulations.

As we have just introduced, two different advanced ROMs are developed in this chapter to meet current industrial requirements. The first one based on the intrusive PGD (Chapter 1) and the second one based on the novel reduced ordered formulation described in Section 2.3, that is, the s-PGD+RB strategy.

If two approaches are proposed one could wonder when we should use each one. The first one (intrusive PGD) is recommended when possible or when the intrusiveness is not an issue. On the other hand, the s-PGD+RB strategy is recommended when complex geometries cannot be addressed by the proposed change of coordinates or when complex geometrical parameters present difficulties in the formulation of the intrusive PGD. For instance, eccentricity in the rotor can be an issue for the intrusive PGD.

The chapter is divided into two main sections describing each technique (Section 4.2 and Section 4.3), as well as a concluding section that presents the overall conclusions of the work. In addition, at the beginning of aforementioned Sections 4.2 and 4.3, the topic and the content is introduced in detail for the corresponding ROM as well as showing the internal structure of the section. In the aformentioned introductions, a special focus on the topic of noise and vibration of electric motors is done becasue it is the industrial application that motivated this work.

This chapter and all the results presented in it correspond to the published papers:

- A. Sancarlos, C. Ghnatios, J.L. Duval, N. Zerbib, E. Cueto, F. Chinesta, " Fast Computation of Multi-Parametric Electromagnetic Fields in Synchronous Machines by Using PGD-Based Fully Separated Representations," *Energies*, vol. 14, issue 5, 2021. DOI: https://doi.org/10.3390/en14051454
- A. Sancarlos, E. Cueto, F. Chinesta, J.L. Duval, "A novel sparse reduced order formulation for modeling electromagnetic forces in electric motors," *SN Appl. Sci.*, vol. 3, issue 3, 2021. DOI: https://doi.org/10.1007/s42452-021-04310-3.

4.2 Multi-Parametric Electromagnetic Fields in Synchronous Machines by Using PGD-Based Fully Separated Representations

4.2.1 Intrusive approach: Introduction

Numerical tools such as the Finite Element Method (FEM) or the Finite Difference Method (FDM) are powerful and excellent methodologies for analyzing static and dynamical systems. Despite this, a great portion of numerical simulations concerning real-life problems face difficulties in design, optimization and control due to the complexity of the system, high computational costs, and storage requirement [Farzamfar *et al.* 2016, M. Sudheer Kumar & Apparao 2015].

At present, industry is permanently looking for fast and accurate solutions in electric motors and generators, and trends such as the Electric Vehicle or the self-driving car are producing a lot of investment in that direction. The reason for this seems clear: achieving these goals will improve the final design's performance and economic competitiveness.

To address this need, a model order reduction technique that employs the Proper Generalized Decomposition (PGD) is developed. This method alleviates the curse of dimensionality through solving a Partial Differential Equation (PDE) or a set of PDEs in a high-dimensional space within minutes, using a separated representation of the multiparametric solution. Moreover, this technique has solved unfeasible high-dimensional problems with high accuracy, and its abilities have been proven in many previous works as discussed in Chapter 1 and the numerous references therein, where these parametric solutions were employed for predicting, optimizing, propagating uncertainty, performing inverse analysis and simulation-based control, all under the stringent real-time constraint. For the sake of completeness, the intrusive PGD procedure for constructing spatial and parametric separated representations was revisited in Section 1.3.1 of Chapter 1.

PGD was previously applied in electromagnetics, such as, for instance, design of earthing systems [Pérez 2013], the computation of impedance in industrial busbar systems [Sancarlos-González *et al.* 2017, Sancarlos 2017], the analysis of magnetoelectric devices [Chaqués Herraiz 2015, Henneron & Clenet 2017] or simulation and optimization of smart grids [Malik 2017] . However, the complex non-separable geometry of electric motors limited its use for efficiently expressing the solution by separating the space coordinates. Furthermore, there is also a numerical challenge when introducing the rotor movement as a parameter in the PGD framework. In this Chapter, a framework to efficiently employ the PGD for a Permanent-Magnet Synchronous Motor (PMSM) is set up. To overcome the complex geometries limitation, an adapted mapping of the real geometry into a suitable separable domain is proposed. Such mappings were previously successfully employed to deal with apparently non-separable domains [Ghnatios *et al.* 2021, Ghnatios *et al.* 2019a].

To evaluate the obtained PGD solutions, the finite element software FEMM is employed [Meeker 2018]. The main aim of using FEMM is twofold. First, it aims to make the results more accessible to the community for checking, with FEMM being an open-source finite-element analysis software package. Second, it aims to have a good reference to rely on. Furthermore, despite the fact that the PGD is currently a mature technique in the area of computational mechanics, the application of PGD-based techniques in electromagnetism constitutes a very active research area at present.

The main contributions of this first proposed ROM, developed in the present Sections 4.2.4 and 4.2.5 are: (i) the introduction of a very efficient geometrical mapping, able to separable render the motor geometry, enabling the application of the PGD-based space-separated representation; (ii) the introduction of other parameters as model extra-parameters, enabling the construction of parametric solutions to be efficiently used in a variety of engineering applications. The attained computational efficiency is impressive, attaining, thanks to the separated representation constructor, resolutions equivalent to 10^{23} FEM degrees of freedom, within few minutes, on a standard laptop, performances which are unattainable when using more usual multi-purpose discretization techniques.

Therefore, the present Section is organized as follows. In subsection 4.2.2, the physical equations are presented to focus on a two-dimensional steady-state analysis of a PMSM. Next, in subsection 4.2.3, the simulated motor is presented where the main parameters/features are introduced. Then, in subsection 4.2.4, the formulation for the separated PGD representation in space is presented. Furthermore, in subsection 4.2.5, the formulation to add the parameters as extra-coordinates in the PGD framework is shown. Finally, in subsection 4.2.6 the results are shown and the conclusions will be addressed in the conclusions of the Chapter, in Section 4.4.

4.2.2 Electromagnetic Equations

A two-dimensional steady-state analysis (magneto-static analysis) is employed to analyze the synchronous machine.

In three-phase motors, as in the other polyphase configurations of the synchronous machines, the stator-produced magnetomotive force (MMF) rotates at synchronous speed. Since the rotor is also rotating at synchronous speed in the steady state, an observer on the rotor experiences a constant field ($\frac{\partial \mathbf{B}}{\partial t} = \mathbf{0}$), and, therefore, there are no eddy currents on the rotor.

On the other hand, an observer on the stator experiences a time-varying field with a characteristic frequency. Since the stator is laminated and the stator windings are stranded and transposed, the eddy currents are limited and can be neglected in the field computation.

Taking into consideration the above assumptions, let us start with Ampere's law

$$\nabla \times \mathbf{H} = \mathbf{J}, \tag{4.1}$$

where ∇ is the nabla operator, $\mathbf{J}$ is the electric current density and $\mathbf{H}$ is the magnetic H-field. In addition, the magnetic flux density ($\mathbf{B}$-field) is related to the magnetic field strength (**H**-field) using

$$\mathbf{B} = \mu_0 \left(\mu_r \mathbf{H} + \mathbf{M} \right), \tag{4.2}$$

where $\mathbf{M}$ is the magnetization vector, μ_r is the relative magnetic permeability and μ_0 is the magnetic permeability of free space. Noting that $\nu = \frac{1}{\mu_0 \mu_r}$ and combining Equations (4.1) and (4.2), one obtains

$$\nabla \times (\nu \mathbf{B}) = \mathbf{J} + \nabla \times (\nu \mu_0 \mathbf{M}). \tag{4.3}$$

Using the Helmholtz decomposition and noting that $\nabla \cdot \mathbf{B} = 0$, the B-field can be expressed as

$$\mathbf{B} = \nabla \times \mathbf{A}, \tag{4.4}$$

with $\mathbf{A}$ is the magnetic vector potential, leading to

$$\nabla \times (\nu \nabla \times \mathbf{A}) = \mathbf{J} + \nabla \times (\nu \mu_0 \mathbf{M}). \tag{4.5}$$

Note that eventhough the gauge condition should be defined for 3D, the condition is automatically satisfied for 2D problems. To define the integral form of the problem, $\mathbf{W}$ is used as the test function

$$\int_\Omega \nabla \times (\nu \nabla \times \mathbf{A} - \nu \mu_0 \mathbf{M}) \cdot \mathbf{W} d\Omega = \int_\Omega \mathbf{J} \cdot \mathbf{W} d\Omega. \tag{4.6}$$

As detailed in [Salon 1995], after using some vector identities and the divergence theorem, the results are

$$\int_\Omega \nu \left(\nabla \times \mathbf{A} \right) \cdot \left(\nabla \times \mathbf{W} \right) d\Omega = \int_\Omega \nu \mu_0 \mathbf{M} \cdot \left(\nabla \times \mathbf{W} \right) d\Omega + \int_\Omega \mathbf{W} \cdot \mathbf{J} d\Omega, \tag{4.7}$$

that in the 2D case reads

$$\int_\Omega \nu \left(\frac{\partial A_z}{\partial x} \frac{\partial W}{\partial x} + \frac{\partial A_z}{\partial y} \frac{\partial W}{\partial y} \right) d\Omega = \int_\Omega \left(\nu \mu_0 \left(M_x \frac{\partial W}{\partial y} - M_y \frac{\partial W}{\partial x} \right) + J_z W \right) d\Omega \tag{4.8}$$

4.2.3 Description of the Analyzed Motor

As a proof of concept, the (Permanent-Magnet Synchronous Machine) PMSM with the following characteristics is going to be analyzed:

- Three-phase supply. This is an eight-pole machine (i.e., p = 4).
- The winding configuration for one pole of the machine is: A+, B−, C+ (the three slots from 0 to 45 geometrical degrees).
- Turns/Slot: 46.
- In addition, the complete geometry of the machine is shown in Figure 4.1.

For the interested reader, further details of the machine parameters and materials can be found in the Appendix B as well as in the FEMM software manual [Meeker 2018] where this example is borrowed.

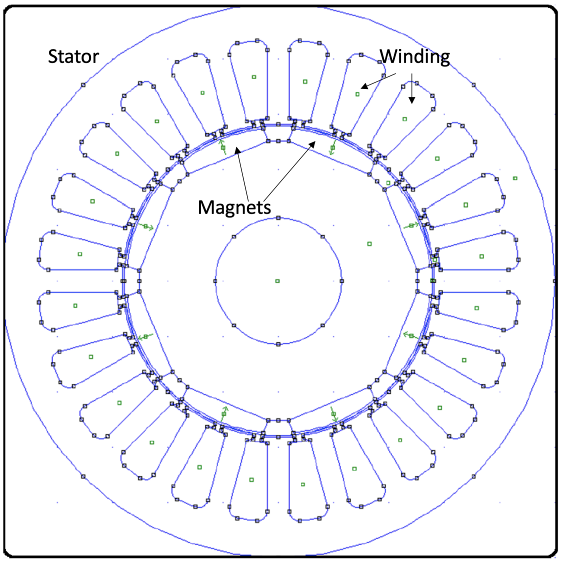

Figure 4.1 – Electric machine to simulate. The green arrow in the permanent magnets indicates the magnetization direction.

4.2.4 PGD Physical Space Separated Solution

The domain of simulation is not suitable for a PGD-separated representation using Cartesian (x, y) coordinates because of the lack of plane symmetries (see Figure 4.1). Previous techniques were developed to deal with such complexity using the PGD framework [Ghnatios *et al.* 2012a]. However, in this work, a new suitable mapping to transform the motor geometry into the one shown in Figures 4.2 and 4.3 is developed. The advantage is that the resultant geometry is amenable for a separated representation within the PGD framework.

The first step to achieving this goal is to perform a mapping to the polar coordinates (R, θ) using

$$\begin{cases} R = \sqrt{x^2 + y^2}, \\ \theta = arctg\left(\frac{y}{x}\right), \end{cases} \tag{4.9}$$

where *arctg* is the inverse trigonometric function arctangent.

Then, a second mapping is used to transform the resulting non-fully separable domain into a prismatic, easily separable one, (s, t), such as $s \in [1, 7]$ and $t \in [0, 2\pi)$, using the following transformation, for $i = 2, \ldots, 7$

$$\begin{cases} R(s \in [i-1, i], t) = [s - (i-1)] \cdot (h_i(t) - h_{i-1}(t)) + h_{i-1}(t) \\ \theta(s, t \in [0, 2\pi)) = t \end{cases}, \tag{4.10}$$

where s and t are the new coordinates and i is computed rounding up the s value to the next integer. In addition, the integers of the s coordinate are placed strategically, as shown in Figure 4.4, and the definition of $h_i(t)$ functions is illustrated in Figure 4.5.

Using the associated Jacobians and the chain rule, one can rewrite the weak form (4.8) into the (s, t) domain. More details about this technique can be found in [Ghnatios *et al.* 2021, Ghnatios *et al.* 2019a, Ghnatios *et al.* 2019b].

The domain depicted in Figure 4.3 can be easily expressible by using a fully space-separated representation within the PGD rationale, by expressing in the same way the material properties, e.g.,

$$\nu(s,t) = \sum_{k=1}^{n} \mathcal{S}_k(s)\mathcal{T}_k(t), \tag{4.11}$$

where n is the number of needed products.

By replacing the mapping into Equation (4.8), one may find the final weak form of the problem by using the corresponding 1D-1D meshes defined in s and t one-dimensional domains. The separated representations of the other known functions J_z and $\mathbf{M}$ is detailed in the next section.

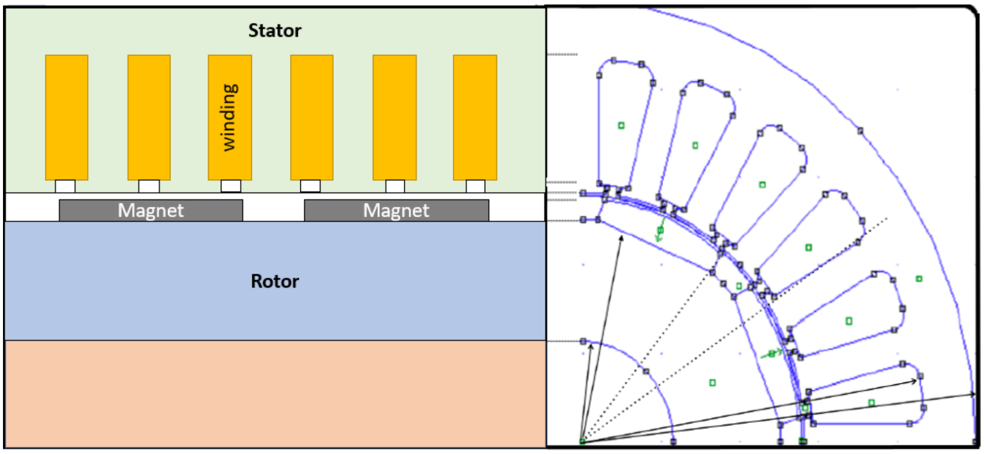

Figure 4.2 – Mapping from the original geometry into the calculation one.

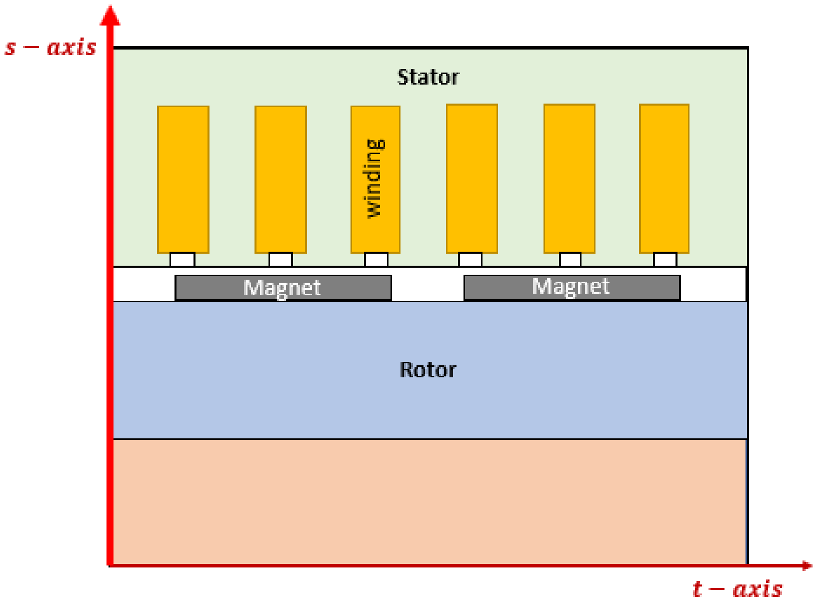

Figure 4.3 – Fully separable domain used to compute the PGD solution laking use of the mapping detailed in Equations (4.9) and (4.10).

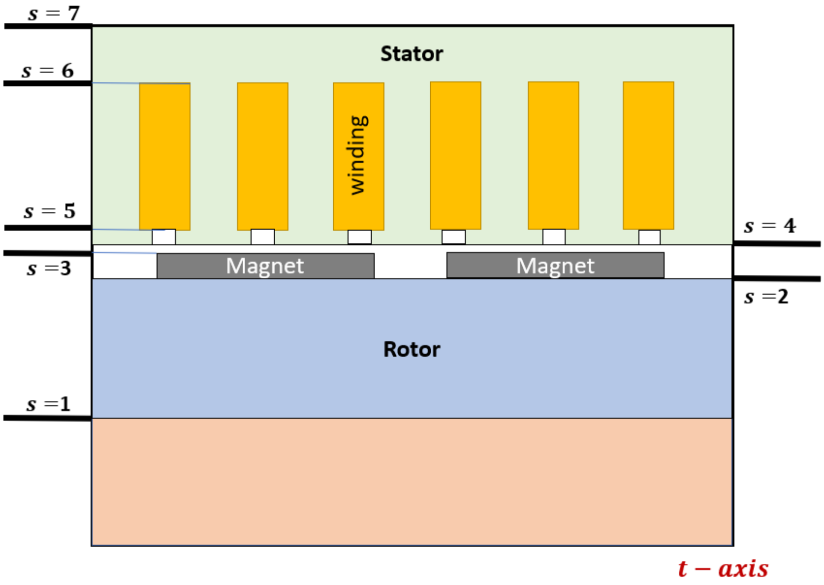

Figure 4.4 – The integer values of the new s coordinate are placed in the positions shown in the figure.

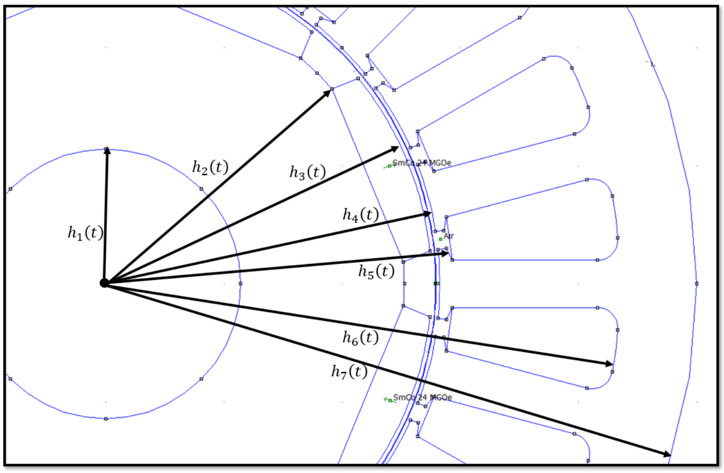

Figure 4.5 – The $h_i(t)$ functions are used to render separable the original non-separable geometries.

4.2.5 PGD Parametric Solution

With the solution performance significantly improved from the fully space-separated representation (s, t), the next natural step within the PGD rationale consists of introducing a number of model parameters as model extra-coordinates for calculating a multi-parametric solution of the vector potential.

The chosen parameters to be added to the space coordinates s and t are i_a, i_b, i_c, ρ and B_r, where B_r indicates the modulus of the remanent magnetization in the permanent magnets, with $B_r = \mu_0 \|\mathbf{M}\|$, while i_a, i_b, i_c are the currents of the three-phase system. In addition, ρ indicates the rotor position of the machine. Moreover, for addressing the third dimension (the z-coordinate), when the 3D domain does not correspond to the 2D section extrusion, an appropriate mapping should be considered. In what follows, an extruded 3D domain, by extruding the 2D section along the z-coordinate axis, is considered.

Therefore, the first step is to obtain the parametric solution $A_z(s,t,z,i_a,i_b,i_c,B_r)$. When applying the PGD procedure, this function is assumed to be expressed as a finite sum of products of one-dimensional functions

$$A_z(s,t,z,i_a,i_b,i_c,B_r) = \sum_{m=1}^{M} \vartheta^1_m(s)\vartheta^2_m(t)\vartheta^3_m(z)\vartheta^4_m(i_a)\vartheta^5_m(i_b)\vartheta^6_m(i_c)\vartheta^7_m(B_r), \tag{4.12}$$

where M is the total number of sums and $\{\vartheta^1_m, \cdots, \vartheta^7_m\}$ are the sought functions for the m^{th} mode.

In addition, a PGD solution was obtained for different rotor positions, expressed by the coordinate ρ. Thus, an additional discretization is associated to the ρ coordinate. Specifically, 91 nodes are considered for discretizing the $\pi/2$ angular interval, and, consequently, the corresponding number of solutions is performed.

Therefore, the final and most general parametric solution reads

$$A_z(s,t,z,i_a,i_b,i_c,B_r,\rho) = \begin{cases} A_z(s,t,z,i_a,i_b,i_c,B_r,\rho_1), & \rho = 0, \\ \vdots & \\ A_z(s,t,z,i_a,i_b,i_c,B_r,\rho_{91}), & \rho = 90, \end{cases} \tag{4.13}$$

where the terms $A_z(s,t,z,i_a,i_b,i_c,B_r,\rho_k)$ are the different computed PGD solutions. Only ninety degrees of the rotation were simulated, as the rest can be found using the symmetry of the problem.

On top of the physical space-separated solution, the electric current densities, as well as the permanent magnets, are modeled as extra coordinates of the problem. To achieve the required model, the electric current density J_z, as well as the modulus of the magnetization vector $\mathbf{M}$, are modeled as a function of the new space coordinates (s,t,z) as well as the corresponding additional parameters. Therefore, J_z reads

$$J_z(s,t,z,i_a,i_b,i_c,B_r,\rho_k) = \sum_{i=1}^{6} \phi^I_i(s)\psi^I_i(t)\mathcal{J}_i, \tag{4.14}$$

where, according to Figures 4.6 and 4.7

$$\phi^I_i(s) = \begin{cases} 0, & \text{if } 1 \le s < 5, \\ 1, & \text{if } 5 \le s \le 6, \\ 0, & \text{if } 6 < s \le 7, \end{cases}$$

and

$$\psi^I_i(t) = \begin{cases} 1, & \text{for the corresponding winding position,} \\ 0, & \text{for the rest of the domain,} \end{cases}$$

with $\mathcal{J}_i$ taking the corresponding values of J_z depending on the winding label: A, $-B$, C, $-A$, B and $-C$. In addition, they are arranged in the following way: $\mathcal{J}_1$ and $\mathcal{J}_4$ are one-dimensional functions depending on i_c (with the relation $\mathcal{J}_1 = -\mathcal{J}_4$), $\mathcal{J}_2$ and $\mathcal{J}_5$ are one-dimensional functions depending on i_b (with the relation $\mathcal{J}_2 = -\mathcal{J}_5$) and $\mathcal{J}_3$ and $\mathcal{J}_6$ are one-dimensional functions depending on i_a (with the relation $\mathcal{J}_3 = -\mathcal{J}_6$).

Similarly, $\mathbf{M}$ can be expressed with a finite sum involving the number of permanent magnets N_M, according to

$$\mathbf{M}(s,t,z,i_a,i_b,i_c,B_r,\rho_k) = \frac{B_r}{\mu_0}\sum_{i=1}^{N_M}\phi_i^{II}(s)\psi_i^{II}(t)\hat{\mathbf{m}}_i(s,t), \tag{4.15}$$

where $\hat{\mathbf{m}}_i$ is the unit vector defining the magnetization direction of the i-magnet, according to Figure 4.8, and the characteristic functions defining the location of each magnet read

$$\phi_i^{II}(s) = \begin{cases} 0, & \text{if } 1 \leq s < 2, \\ 1, & \text{if } 2 \leq s \leq 3, \\ 0, & \text{if } 3 < s \leq 7, \end{cases}$$

$$\psi_i^{II}(t) = \begin{cases} 1, & \text{within the magnet location in the even numbers of magnets,} \\ -1, & \text{within the magnet location in the odd numbers of magnets.} \\ 0, & \text{for the rest of the domain.} \end{cases}$$

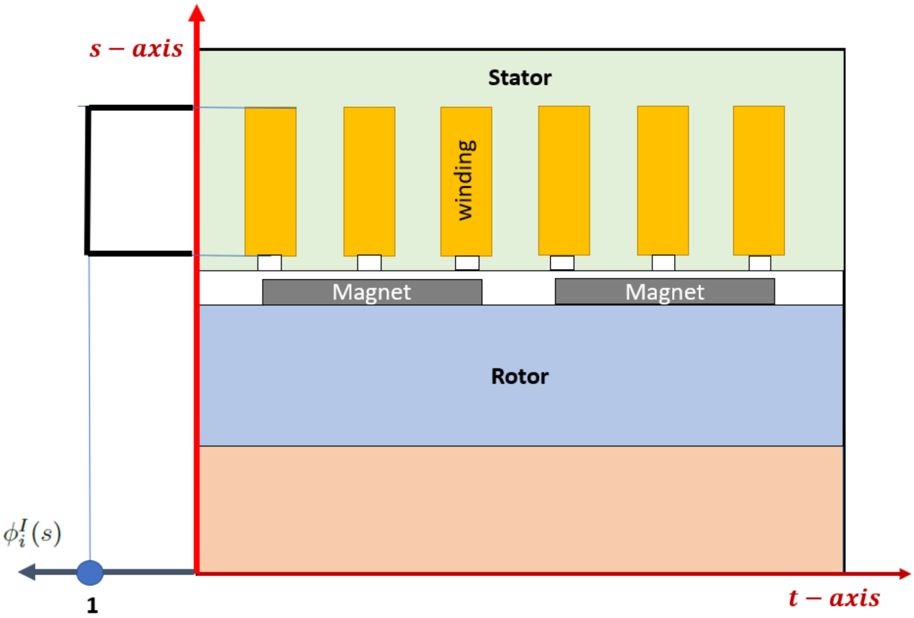

Figure 4.6 – Illustration of $\phi_i^I(s)$ functions involved in Equation (4.14).

Considering the coordinate transformation presented in Section 4.2.4 and the approximations just introduced, the problem can be formulated and solved using the standard PGD procedure described in Section 1.3.1. For the unfamiliar reader, further information can be found in [Ghnatios 2012, Ghnatios *et al.* 2017, Cueto *et al.* 2014] and the references therein.

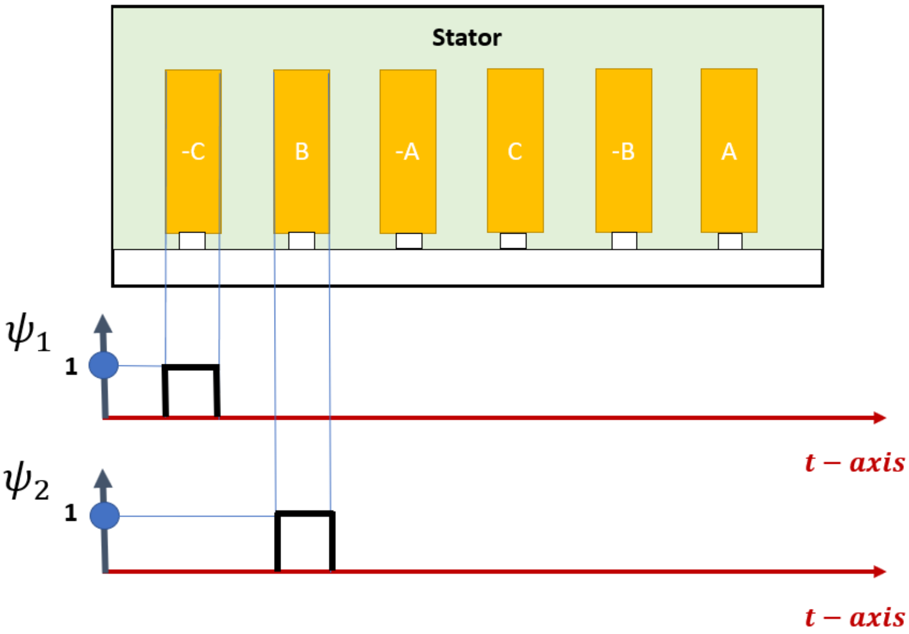

Figure 4.7 – Illustration of functions $\psi_1^I(t)$ and $\psi_2^I(t)$ involved in Equation (4.14).

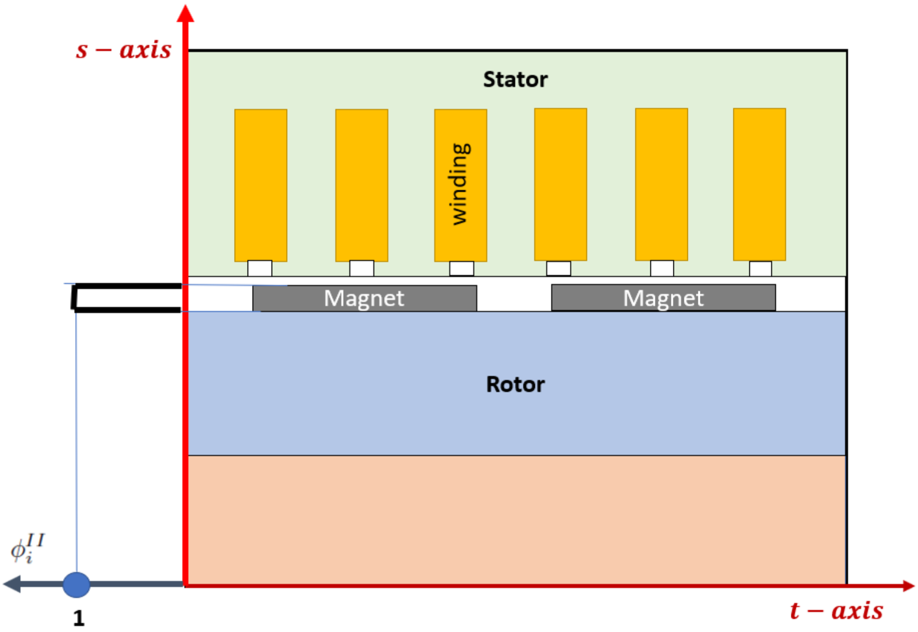

Figure 4.8 – Functions $\phi_i^{II}(s)$ involved in Equation (4.15).

4.2.6 Results

This section aims to analyze the motor sketched in Figure 4.1, whose parameters were reported in Section 4.2.3. As was indicated in the previous section (Equation (4.13)), a PGD parametric solution is created for each discretized rotor position ρ_k (from ρ_1 to ρ_{91}).

The results focus on one of the industrial applications where this type of solution is highly demanded: the evaluation of the electromagnetic force involved in noise and vibration analysis of electric motors. Here, the solution is specifically sought in the air-gap area to obtain the B-field in this region, and then estimate the magnetic pressure using the Maxwell stress tensor.

As it will be discussed in Section 4.3.3, in the vibro-acoustic analysis, the following expressions are usually employed [Pile *et al.* 2018, Xu *et al.* 2018, Haas & Ellermann 2017]:

$$P_n(\alpha, t) = \frac{1}{2\mu} B_n^2(\alpha, t), \tag{4.16}$$

$$P_\tau(\alpha, t) \approx 0, \tag{4.17}$$

where P refers to the magnetic pressure, α is the angle of a polar coordinate system pointing to the selected air-gap point, subscript n refers to the radial component in the air-gap midline and the subscript τ refers to the tangential component in the air-gap midline.

Figure 4.9 shows the magnetic vector potential A_z in a section of the simulated motor for different combinations of the input parameters i_a, i_b, i_c, B_r and ρ, illustrated in the physical (x, y) domain. Figure 4.10 illustrates the 3D results in a section of the motor assumed a simple section extrusion for a given combination of the parameters, to keep the 2D problem formulation. Even if solving the 2D magnetic problem in the 3D domain does not contribute to the solution, this remains invariant along the z-coordinate; its consideration here only aims to prove that the fully space separation can very efficiently address extremely rich 3D configurations.

Figures 4.11–4.13 compare the PGD solution with the one obtained by using the open-source software FEMM (assuming the FEMM solution as the reference one). An excellent agreement can be seen between the PGD-based mutli-parametric solution and the reference one. However, each PGD-based parametric solution (for each rotor position, ρ_k) is computed by using a standard laptop, in about 12 minutes, for a resolution equivalent to 10^8 different FEM simulations (the number of possible parameter choices), each of them involving an equivalent spatial resolution of 175 million nodes (degrees of freedom). Solving that number of extremely rich problems by using a standard finite element discretization becomes unreasonable. The computational efficiency increases even more when considering more parameters in the parametric solution. This constitutes the most appealing feature of PGD-based separated representations; in the present case, concerning both the 3D space (resulting in three one-dimensional approximations) and the model parameters assumed here model extra-coordinates, and are also expressed in a separated form.

As indicated previously, once the field solution is obtained, the post-processing step to obtain the magnetic pressure on the stator surface is performed, as Figures 4.14 and 4.15 reveal.

Furthermore, a comparison between the PGD and the FEMM solution is carried out on the torque, which is one of the most important quantities of interest when analyzing, for instance, the torque-speed curve. Random points of the parametric solution were checked, observing that this error was below 2% (relative error computed considering the FEMM solution as a reference).

This functionality is particularly valuable in electrical vehicles, when looking for a compromise between the torque and the normal force applied on the stator (that causes vibration and its induced noise).

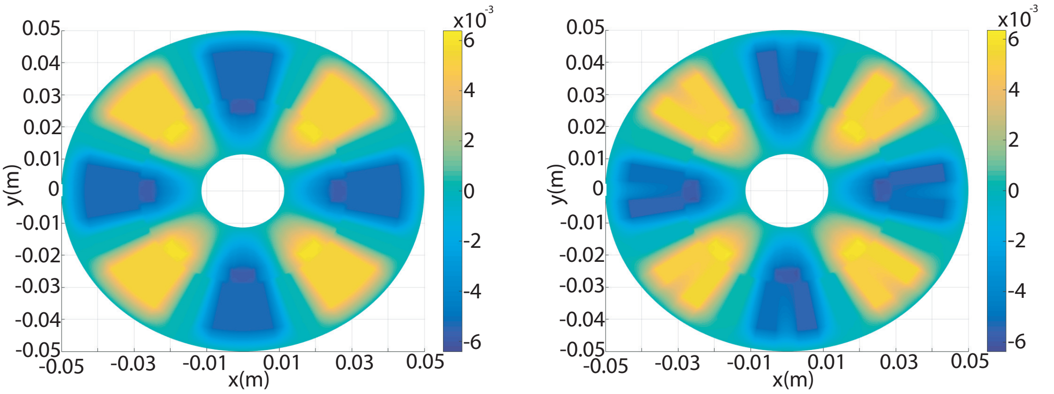

(a) $i_a = 0$ A, $i_b = 0$ A, $i_c = 0$ A, $B_r = 1.01$ T and $\rho = 0°$

(b) $i_a = -1.5$ A, $i_b = 3$ A, $i_c = -1.5$ A, $B_r = 1.01$ T and $\rho = 0°$

Figure 4.9 – *Cont.*

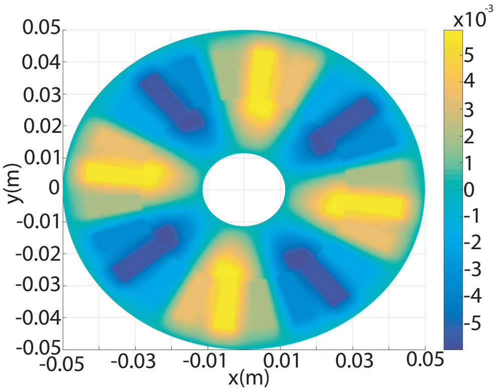

(b) $i_a = 0$ A, $i_b = 0$ A, $i_c = 0$ A, $B_r = 1.01$ T and $\rho = 10°$

Figure 4.9 – Solution A_z for different combinations of the input parameters i_a, i_b, i_c, B_r and ρ.

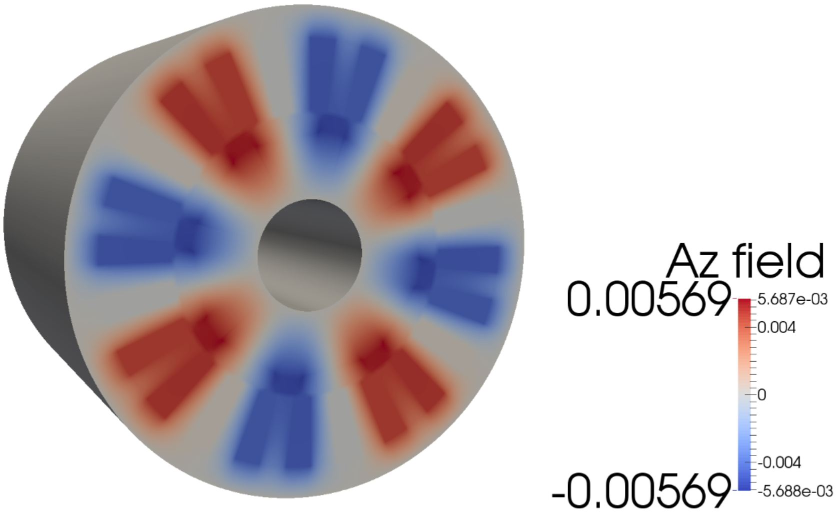

Figure 4.10 – Magnetic vector potential A_z in a section of the motor for $i_a = 1.5$ A, $i_b = 1.5$ A, $i_c = -3$ A, $B_r = 1.01$ T and $\rho = 0°$.

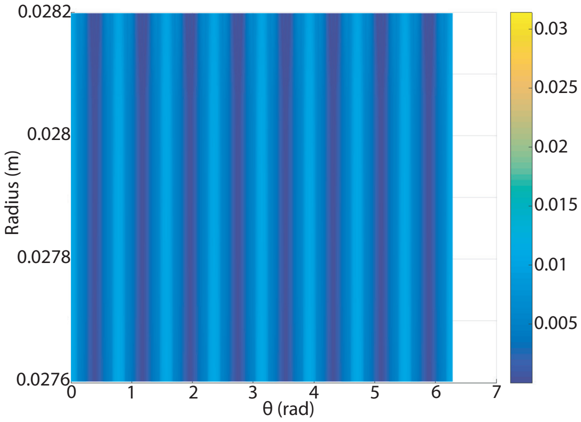

Figure 4.11 – Relative error considering the PGD and the FEMM solution for the case $(s, t) \in$ (air gap), $i_a = i_b = i_c = 0$ A, $B_r = 1.01$ T, $\rho = 0$ (initial position).

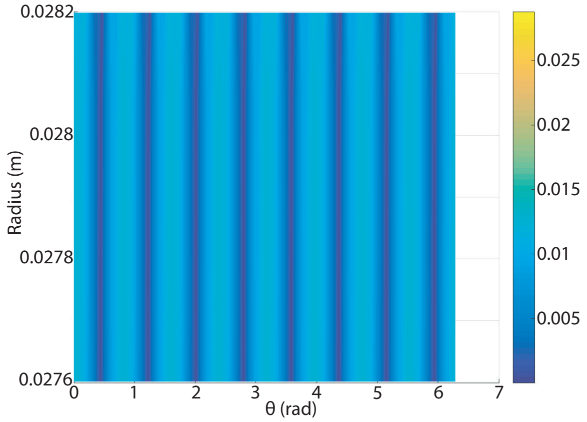

Figure 4.12 – Relative error considering the PGD and the FEMM solution for the case $(s,t) \in$ (air gap), $i_a = -1.5$ A, $i_b = 3$ A, $i_c = -1.5$ A, $B_r = 1.01$ T, $\rho = 0$ (initial position).

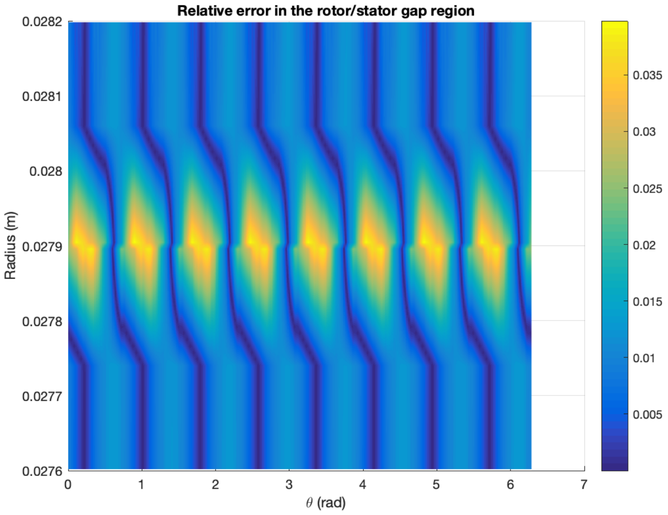

Figure 4.13 – Relative error considering the PGD and the FEMM solution for the case $(s,t) \in$ (air gap), $i_a = i_b = i_c = 0$ A, $B_r = 1.01$ T, $\rho = 10$ deg.

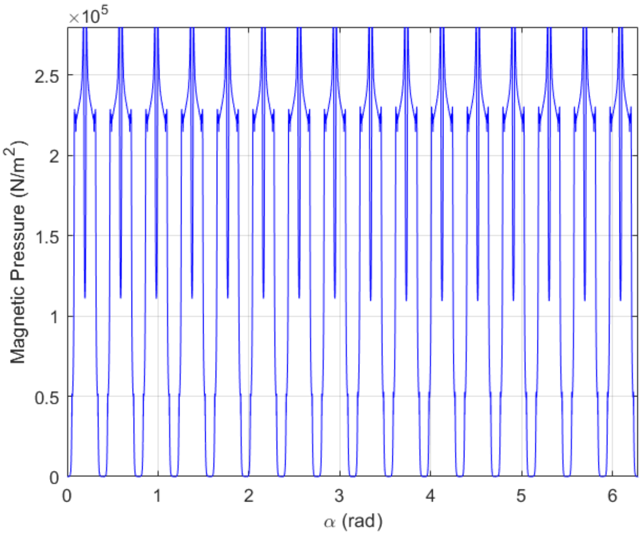

Figure 4.14 – Magnetic pressure computed with the PGD solution for the case of Figure 4.11.

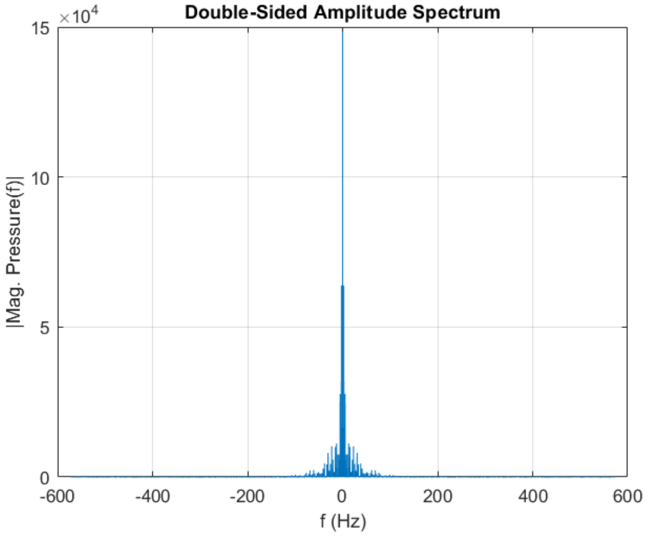

Figure 4.15 – Fast Fourier Transform of the magnetic pressure depicted in Figure 4.14.

The torque directly derives from the computed solution, as described in [Bianchi 2005], according to

$$T = \frac{D-g}{2}\frac{L}{\mu_0}\int_{l_g} B_n B_\tau dl, \tag{4.18}$$

where B_n is the radial component of the flux density (normal to the line l_g), B_τ is the azimuthal component of the flux density (tangential to the air-gap midline l_g), D is the inner stator diameter, L is the active length of the rotor in the axial direction and g is the air-gap.

Finally, it is important to note that computing a derivative of the parametric solution is easily done in the PGD framework as a pure solution post-processing, by simply taking the derivatives of the one-dimensional functions involved in the separated representation. For the interested reader, an application of this property is carried out in Section 4.3.5.4 where a sensitivity analysis of a PGD solution is performed.

4.3 A novel sparse reduced order formulation for modeling electromagnetic forces in electric motors

4.3.1 Non-intrusive approach: Introduction

The electric powertrain is drastically growing its importance in industry, specifically in the automotive one, because of different reasons. One of them is the environmental and energy regulations laid out in United Nations Climate Change Conference held in Paris in 2015 [Cli 2015, Kumar *et al.* 2017]. In addition, the development of technologies such as Electric Vehicles (EVs), Hybrid Electric Vehicles (HEVs) or self-driving cars encourages even more the research and development in this area.

Furthermore, an important effort of research in this direction of both companies and national governments (such as USA or China) is carried out in the last years. For example, in Europe, the creation of The European Technology & Innovation Platform (ETIP) on batteries, named BatteRIes Europe [Alliance 2019], clarifies and envisages even more the importance of the electric powertrain and the EVs in our next years.

Due to this interest, it is mandatory to analyze the Vehicle Noise, Vibration and Harshness (NVH) because contrary to popular costumers' belief, EVs are not silent at all. It is true that they can present lower overall levels comparing to Internal Combustion Engines (ICEs) but unfortunately, they have high-frequency and tonal content that makes the electric motor noise annoying if this issue is not addressed correctly [Mazgaonkar *et al.* 2019, Dupont & Bouvet 2013].

The noise in the EV can be divided in 4 main sources: powertrain noise, wind noise, tire/road noise, and ancillary noise (where the first is one of the most significant). For this reason, it is so important to analyze the electric powertrain, specially, the electric motor in the NVH studies.

As it is shown in different sources [Dupont & Saucy 2019, Bai 2018] , vibration and noise produced by electrical machines can be divided into three categories [Gieras *et al.* 2006] : electromagnetic vibration and noise, mechanical noise (related to the mechanical assembly, in particular bearings) and aerodynamic noise (they are mainly caused by aerodynamic forces in ventilation components of the motor).

Adding complexity to the analysis, the electromagnetic vibration and noise of electric motors is a multi-physics problem, involving multiple fields including electromagnetism, structural dynamics and acoustics.

Electromagnetic-induced vibration and noise of an electric motor is mainly caused by radial force waves [Bai 2018] on the stator surface as said in [Gieras *et al.* 2006] and [Jean-Baptiste & Bouvet 2012]. [Xu *et al.* 2018] and [Haas & Ellermann 2017] also agree on this. In addition, this calculation is one of the most highly-time consuming and challenging. Consequently, Reduced Order Models (ROMs) are an appealing alternative to compute these force waves which will be the input for the other stages of the NVH analysis, as illustrated in Figure 4.16.

Contemporary electric motors are designed with higher magnetic flux density in the air gap which produces higher radial magnetic forces acting on the stator. This can lead to a

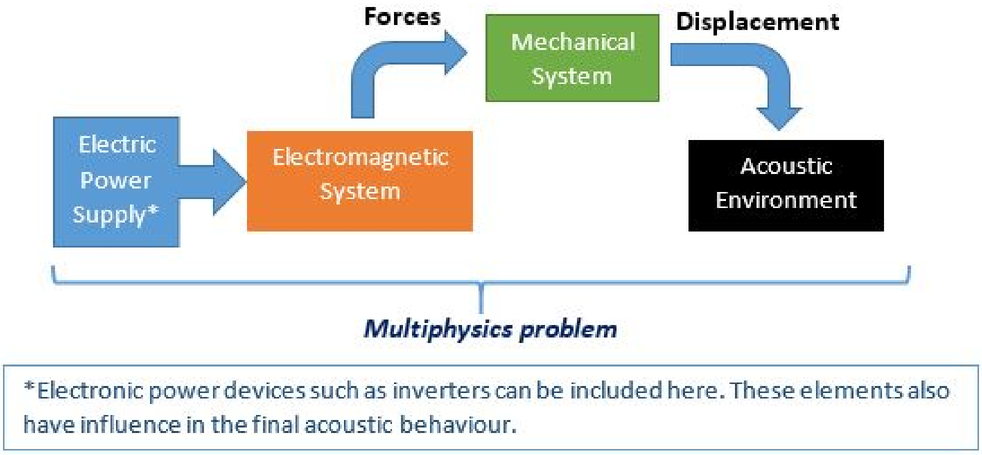

Figure 4.16 – Conversion of electric energy into acoustic energy.

rise of vibration and acoustic problems. [Gieras *et al.* 2006, Bai 2018, Xu *et al.* 2018].

Even worse, the relatively small-size and lightweight design for motors, the large electromagnetic forces as well as the poor rigidity of motor structures increase this serious problem of electromagnetic vibration and noise which will affect the riding comfort. Therefore, it is clearly justified to incorporate in the design the requirements of noise and vibration to avoid large retrofit expenses when the overall performance is being optimized/balanced as said in [Gieras *et al.* 2006] and [Dupont & Saucy 2019]. [Jean-Baptiste & Bouvet 2012] and [Kumar *et al.* 2017] also agree on this.

A possible gateway for enabling more efficient designs could be the simulation of complex models of the electric machine. However, although it is a valid option in some cases, it can be problematic when a detailed analysis of the machine is being carried out or the machine is beeing simulated with the other physical systems which interact with it.

The reasons are the following ones. On the one hand, a lot of simulations are needed to analyze the NVH behavior of a motor, thus being required faster simulations without losing excessively accuracy. On the other hand, these complex models cannot be used to analyze the whole EV system because of the difficulties to couple the machine model with the other subsystems. Nevertheless, this system simulation is important in the analysis because the real inputs for the motor are computed and the entire vehicle system is modeled (within the so-called system engineering) obtaining the predictive responses of the different subsystems when interacting with each other.

Therefore, the main aim of the discussion of the following sections is to open the door towards the use of simple, accurate and fast ROMs to predict the electromagnetic forces on the stator surface which is one of the most challenging and highly time consuming steps of the NVH analysis. For this reason, the methodology proposed in this Section 4.3 can be used to compute these force waves in almost real-time (because of the simple algebraic expression to be manipulated) and with accuracy respect to the finite element model (FEM) where it is based.

To get to the point, the ROM proposed here is based on the novel formulation proposed in Section 2.3 of this dissertation: The s-PGD+RB strategy. Here, the sparse Proper Generalized Decomposition [Ibáñez Pinillo *et al.* 2018] procedure is combined with a Reduced Basis approach, which is used to fit correctly the Reduced Order Model with the numerical simulations as well as to obtain a further data compression.

The proposed technique can be applied to construct a regression model constructed from data. This data can come for example from a Finite Element Method (FEM) software. Moreover, it is perfectly suitable to create a high-dimensional function to give us the electromagnetic force or pressure considering many parameters, including the geometric ones.

Moreover, the s-PGD+RB strategy can easily be extended to other quantities of interest (QoI) such as the torque or the flux to obtain a complete ROM of the machine as it is carried out in Section 4.2, where all the QoI can be computed from the PGD solution. For this reason, the s-PGD+RB methodology is also presented as an alternative to the aforementioned method proposed in 4.2 when it cannot be applied due to the issues discussed in section 4.4.

One of the main advantages of this technique is that it deals with the well-known course of dimensionality issue allowing to have good results with only few snapshots, that is, high fidelity solutions. This way, given some snapshots, the regression model can be constructed using mainly polynomials, therefore once the model is constructed the responses are computed immediately because of the simple expression obtained.

Furthermore, the non-intrusive methodology proposed in this chapter can easily be extended to other type of motors and modeling frameworks as well as other industrial problems.

To illustrate the process, the *s*-PGD-RB procedure is applied to construct three different ROMs. To compute them, two types of motor are analyzed: an induction motor and a synchronous machine presented in Section 4.3.2. As in previous Section 4.2, the open source software Finite Element Method Magnetics (FEMM) [Meeker 2018] is used to obtain the pseudo experimental data. In Section 4.3.4, the proposed approach is presented and discussed.

The results obtained as well as a comparison study between the *s*-PGD and FEMM predictions are presented in Section 4.3.5 to evaluate the accuracy of the ROM.

Finally, in Section 4.4 the conclusions of the present work are discussed.

4.3.2 Analyzed motors

4.3.2.1 Induction motor

As a proof of concept, the induction motor with the following characteristics is going to be analyzed:

- 2 HP motor, 50 Hz, 3-phase supply. It is a 4-pole machine (i.e., p = 2).
- The winding configuration for one pole of the machine is: A+, A+, A+, C-, C-, C-, B+, B+, B+ (the nine slots from 0 to 90 geometrical degrees).
- There are a total of 36 slots on the stator and 28 slots on the rotor. A total of 44 turns sit inside each stator slot.
- In addition, the complete geometry of the machine is shown in Figure 4.17.

For the interested reader, further details of the machine parameters and materials can be found in the Appendix B as well as in the FEMM software manual [Meeker 2018] where this example is borrowed.

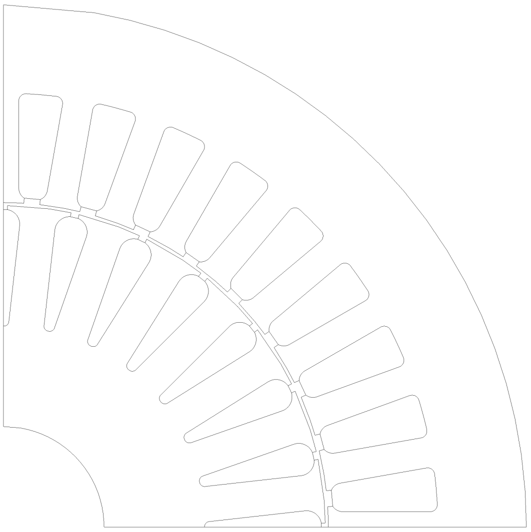

Figure 4.17 – Induction motor geometry.

In addition, the above machine is analyzed by employing a 2D current-based formulation for a squirrel-cage induction motor. This way, the results are adapted and can be reproduced using the free FEMM software and its capabilities.

For the interested reader, further details of the modeling framework employed by FEMM can be found in Appendix C.

4.3.2.2 Synchronous motor

The synchronous machine previously described in Section 4.2.3 is also employed to test the non-intrusive methodology. In addition, the formulation used to analyze this machine was introduced in Section 4.2.2 when the weak form was presented to apply the intrusive PGD. Moreover, the Appendix C is added detailing the strong form employed in FEMM as well as the choice of certain modeling details according to the electric machine references consulted.

In addition to the information given in Section 4.2.3, a screenshot of the complete geometry is shown in Figure 4.18.

4.3.3 Post-processing step. Computation of the radial force waves/magnetic pressure

As it was introduced in Section 4.3.1, the main goal is to obtain accurate and fast ROMs to predict electromagnetic forces on the stator surface. For this reason, here the post-processing step to obtain them is detailed.

Once the PDE describing the distribution and evolution of the magnetic vector potential is solved, the B field must be obtained from the expression:

$$\mathbf{B} = \nabla \times \mathbf{A}, \tag{4.19}$$

and then, the Maxwell stress tensor is used to compute the forces.

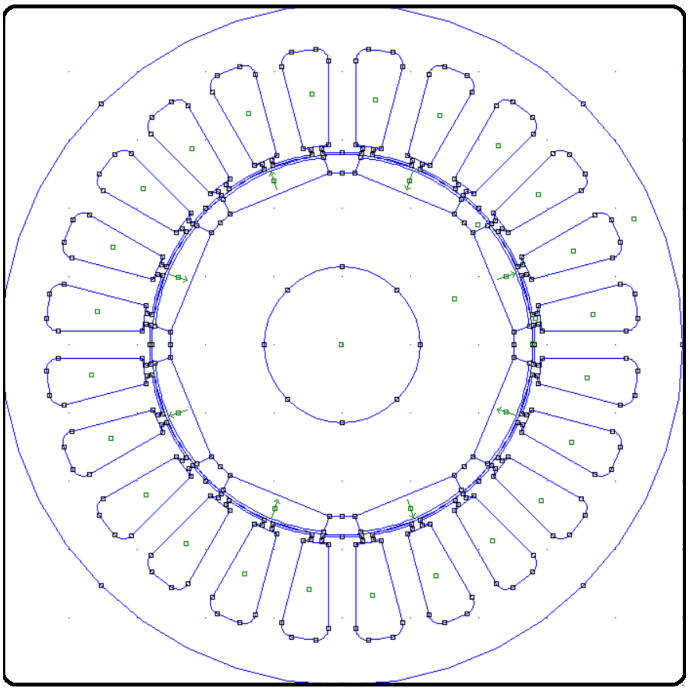

Figure 4.18 – Synchronous machine: Complete geometry drawn in FEMM software.

In this work it is used, for the sake of simplicity, the approach applied to the path at constant radius in the middle of the air gap [Sathyan *et al.* 2020]. Other possibilities can be envisaged. For example, in [Pile *et al.* 2018], the Maxwell stress tensor is used and compared under different paths. However, it is important to highlight that using a more complicated post-processing will not affect the fast computational features of the final ROM obtained in this work.

The normal and tangential components of magnetic pressure are:

$$P_n(\alpha,t) = \frac{1}{2\mu}\Big(B_n^2(\alpha,t) - B_\tau^2(\alpha,t)\Big), \tag{4.20}$$

$$P_\tau(\alpha,t) = \frac{1}{\mu}B_n(\alpha,t)B_\tau(\alpha,t), \tag{4.21}$$

where α is the angle of a polar coordinate system pointing to the selected air-gap point, subscript n refers to the radial component in the air-gap midline and the subscript τ refers to the tangential component in the air-gap midline.

In the vibro-acoustic context, simplifying assumptions are often added neglecting the tangential terms. The reason is that the tangential component of the flux density is much smaller than the normal component [Pile *et al.* 2018, Xu *et al.* 2018, Haas & Ellermann 2017]. This leads to:

$$P_n(\alpha,t) = \frac{1}{2\mu}B_n^2(\alpha,t), \tag{4.22}$$

$$P_\tau(\alpha,t) \approx 0. \tag{4.23}$$

4.3.4 Reduced order model

As already mentioned in Section 4.3.1, the ROM described here aims at proposing a new methodology to obtain accurately the electromagnetic forces on the stator surface (specifically the magnetic pressure) in almost real-time for any choice of a given set of parameters. The reason is that this is one of the most challenging steps of the vibro-acoustic analysis as it was discussed in Section 4.3.1.

In fact, the proposed approach allow us to obtain the force or magnetic pressure immediately when changing different parameters of the problem such as conductivities or the operation point of the motor, for instance. This methodology opens the door to a more efficient vibro-acoustic analysis during the design and optimization process of the Electric Machine as well as to improve the prediction capacities when the whole vehicle system is considered. Furthermore, the procedure can be easily extended to other QoI to create the desired ROM for the machine.

As it was introduced in Section 4.1.1 and 4.3.1, the ROM is made of a regression combining both the s-PGD and the RB techniques. This new formulation is called the s-PGD + RB strategy. In Section 2.2, the s-PGD technique is exposed. This methodology will allow us to achieve excellent results when dealing with high-dimensional spaces and sparse data. This technique is specially convenient because only sparse data is available when dealing with high-dimensional problems [Ibáñez Pinillo *et al.* 2018]. This allows us to cope with the curse of dimensionality.

Then, as it will be discussed in Section 2.3, because of the presence of localized behaviors and discontinuities in the computed solutions, more than interpolating the solution itself, we consider the construction of a RB which will be used for the regression procedure. The RB is inserted in the s-PGD formulation, creating the ROM described in Section 2.3. In the same section, the rationale for the use of such a formulation is detailed without losing sight of the present industrial application.

Now, in the next section and in order to test the technique, different ROMs will be built with the proposed strategy for different machines and modeling frameworks.

4.3.5 Results

In this section, the results of the proposed ROMs for each motor and modeling framework are presented.

In addition, to illustrate some of the advantages concerning the separated representation of the PGD, a sensitivity analysis is carried in Section 4.3.5.4 to measure the impact of each variable.

Furthermore, a study comparing the error between the ROM and the FEM software FEMM is carried out to check the accuracy of the proposed approach.

4.3.5.1 Induction Motor. Linear B-H

The approach shown is based on a current-based model where a balanced three-phase system is supposed for both the fundamental and the harmonic component of the current. The searched PGD function is:

$$B_n(\alpha, f, s, I_p, f_h, s_h, I_{ph}, \gamma); \quad B_n \in \mathbb{C}, \tag{4.24}$$

where α refers to an angle pointing to a node in the air-gap midline, f is the supply frequency, s is the slip, I_p is the current peak value of the fundamental frequency of the source, f_h is the harmonic frequency of the source, $s_h = \frac{f_h-(1-s)f}{f_h}$ is a redefined slip concerning the harmonic component, I_{ph} is the current peak value of the harmonic component, and γ is the relative rotor position in relation to stator.

In this Section, the problematic dimensions discussed in Section 2.3 are γ and α. Therefore, the RB procedure will be applied in these dimensions as explained in the reformulation of Section 2.3.

To obtain the above function, a multi-PGD procedure is used to decompose the function in more than one PGD solution. Consequently, the searched function is now:

$$B_n(\alpha, f, s, I_p, f_h, s_h, I_{ph}, \gamma) = \tilde{f}_1(\alpha, f, s, I_p, \gamma) + \tilde{f}_2(\alpha, f_h, s_h, I_{ph}, \gamma), \tag{4.25}$$

where the s-PGD technique will be used first for $\tilde{f}_1$ and then for $\tilde{f}_2$.

The first PGD search will focus on the range of parameters of the fundamental component of the source and the second one regarding the harmonic one.

Considering the extraction of snapshots the following remark must be considered to approach the problem.

As the system is considered linear (Linear B-H relationship), the total response is the sum of the responses obtained from each source considered separately (superposition theorem). Therefore, the chosen approach is to analyse harmonic content separately, considering each source component independently and then adding each time response to B_n. Finally, when the total $B_n(t)$ is obtained, the post-processing of Eq. (4.22) must be carried out.

To compare the results for different $\mathbf{z}_i$ along the α dimension, the following expressions are used:

$$\begin{aligned} \text{err}_i^{\text{real}} &= \frac{\left\|\text{real}(B_n^{\text{PGD}}(\alpha, \mathbf{z}_i)) - \text{real}(B_n^{\text{exp}}(\alpha, \mathbf{z}_i))\right\|_2}{\|\text{real}(B_n^{\text{exp}}(\alpha, \mathbf{z}_i))\|_2}, \\ \text{err}_i^{\text{imag}} &= \frac{\left\|\text{imag}(B_n^{\text{PGD}}(\alpha, \mathbf{z}_i)) - \text{imag}(B_n^{\text{exp}}(\alpha, \mathbf{z}_i))\right\|_2}{\|\text{imag}(B_n^{\text{exp}}(\alpha, \mathbf{z}_i))\|_2}, \end{aligned} \tag{4.26}$$

where the superscript PGD denotes the results obtained by the s-PGD and the superscript “exp” denotes the experimental measurements (pseudo-experimental results obtained in this case by the FEMM software).

Furthermore, to sample the training set, different Latin Hypercubes (LHs) are taken using a grid composed of Chebyshev nodes along dimensions $f, s, I_p, f_h, s_h, I_{ph}$. In addition, eight hours are used to obtain the training set in the offline stage.

In Figure 4.19, a comparison between the expperimental and PGD results for a $\mathbf{z}_i \notin \mathcal{T}$. For this plot, the error measured as Eq. (4.26) is $\text{err}_i^{\text{real}} = 0.000355$, $\text{err}_i^{\text{imag}} = 0.000341$; and $\text{err}_i^{\text{real}} = 0.000037$, $\text{err}_i^{\text{imag}} = 0.000029$ for the induction component caused by the harmonic. On the other hand, the error in the training set measured as Eq. (4.26) is always lower than 10^{-5}.

In addition, the alternating force (specifically, the alternating magnetic pressure) for the selection of parameters used in Figure 4.19 is shown in Figure 4.20. This force is obtained combining the different sine/cosine waves of the B-field in Eq. (4.22).

In Figures 4.21 and 4.22, the error for Eq. (4.24) for some $\mathbf{z}_i \notin \mathcal{T}$ can be seen. As it can be noticed, an excellent agreement between FEMM and PGD results is achieved even outside the training set. The main advantage is that the PGD model computes induction and force for a given $\mathbf{z}_i$ in less than 0.1 seconds independently of the computational cost of the Finite Element solutions used for the snapshots.

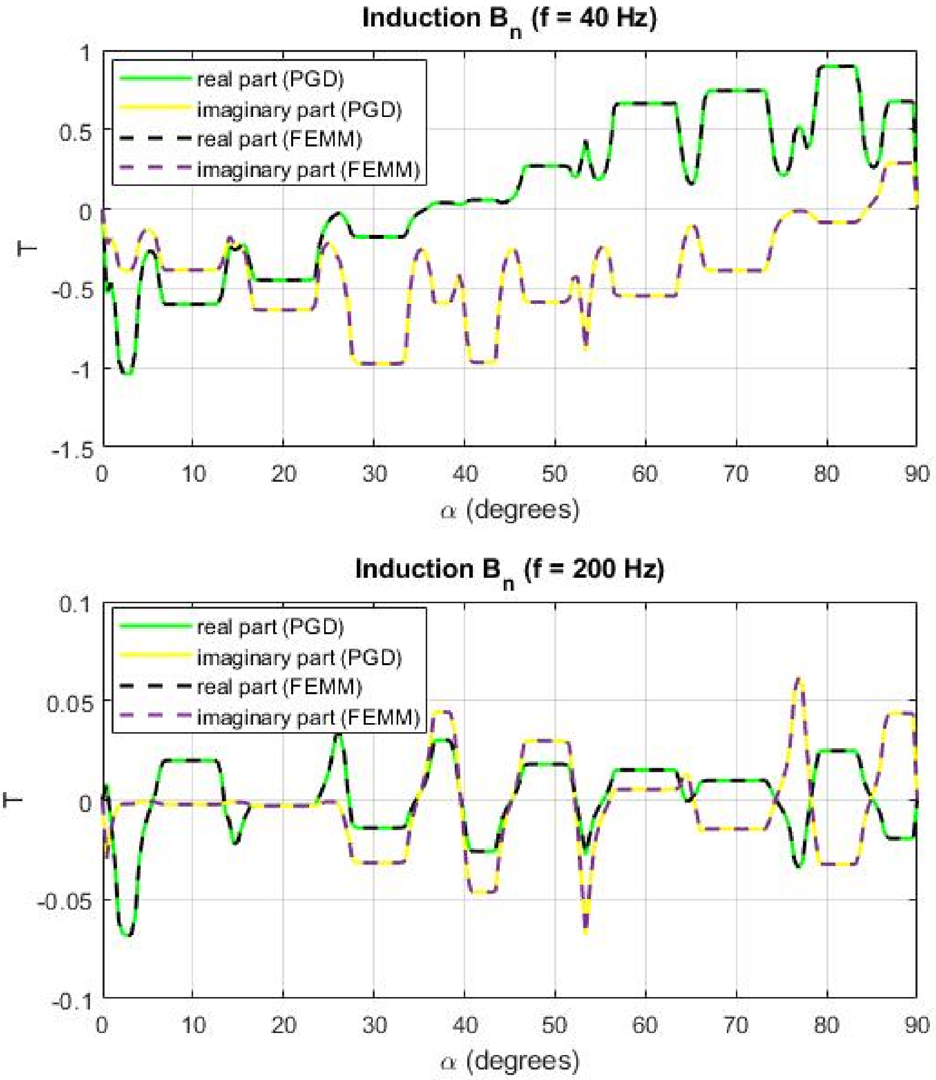

Figure 4.19 – Comparison between the s-PGD and FEMM model (linear B-H relationship) for the parameters $f = 40$ Hz, $s = 2.5$ %, $I_p = 3$ A, $f_h = 5 \cdot 40$ Hz, $s_h = 80.50$ %, $I_{ph} = 3/5$ A, $\gamma = 1$ degree

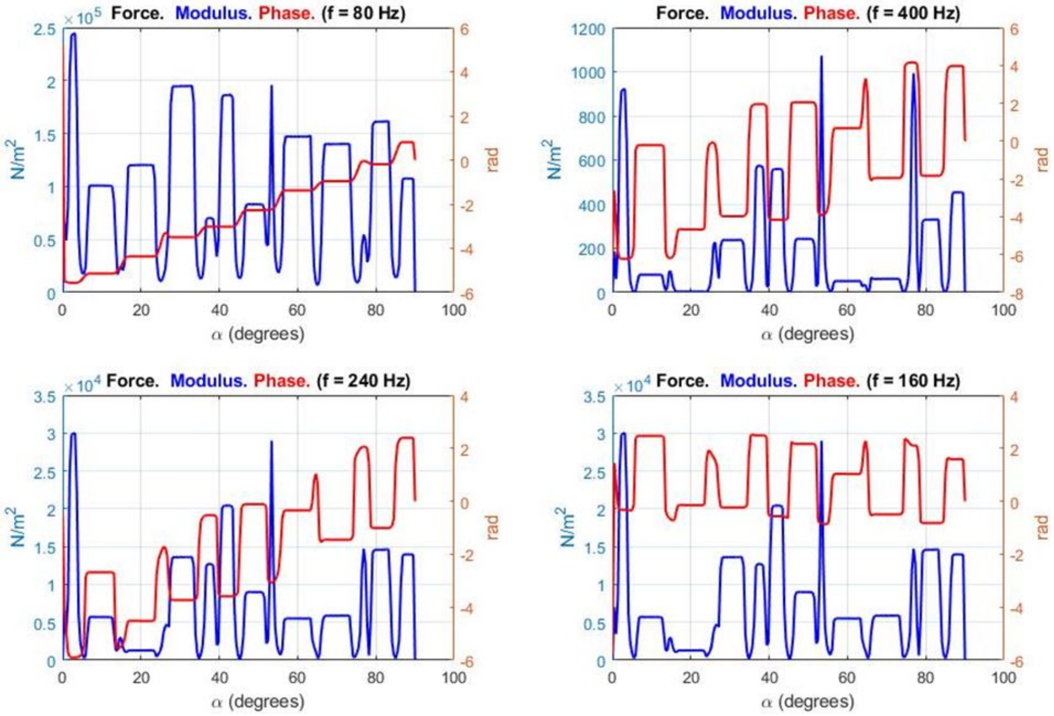

Figure 4.20 – Alternating force components obtained with the parameters $f = 40$ Hz, $s = 2.5$ %, $I_p = 3$ A, $f_h = 5 \cdot 40$ Hz, $s_h = 80.50$ %, $I_{ph} = 3/5$ A, $\gamma = 1$ degre (linear B-H model).

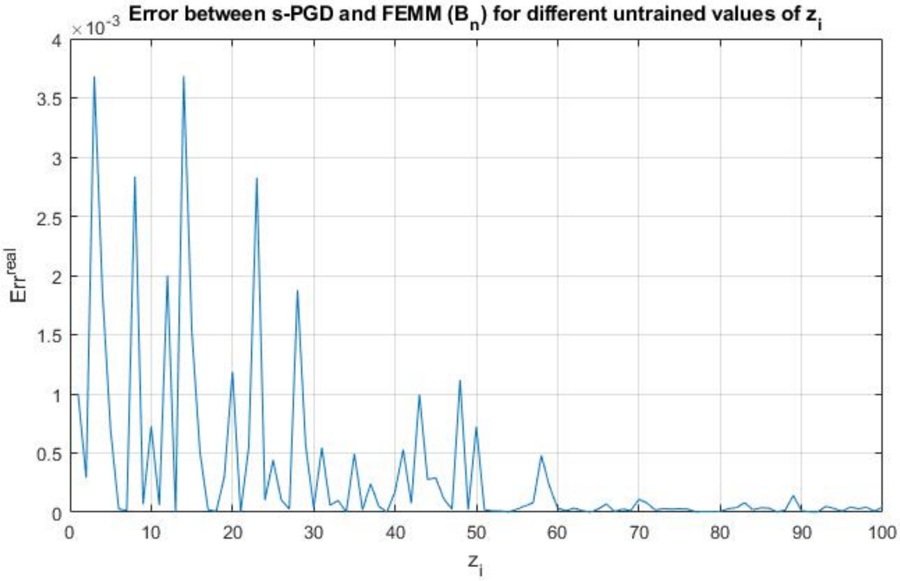

Figure 4.21 – Relative error of the s-PGD model (linear B-H relationship) to determine the real part of B_n for different untrained $\mathbf{z}_i$. Error criteria of Eq. (4.26) is used.

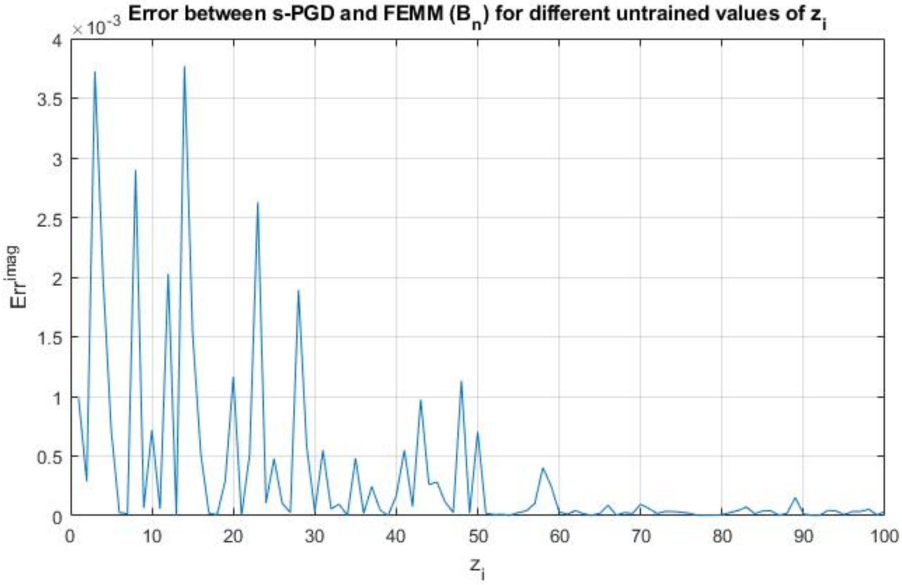

Figure 4.22 – Relative error of the s-PGD model (linear B-H relationship) to determine the imaginary part of B_n for different untrained $\mathbf{z}_i$. Error criteria of Eq. (4.26) is used.

4.3.5.2 Induction Motor. Nonlinear B-H

The approach shown here is also based on a current based model. In addition, perfect sine wave current functions are supposed for the balanced three-phase system. In this case, the searched PGD function is:

$$B_n(\alpha, f, s, I_p, \sigma, \delta, \gamma); \quad B_n \in \mathbb{C}, \tag{4.27}$$

where σ is the bar conductivity and δ is the air gap of the electric machine.

In this Section, the problematic dimensions described in Section 2.3 are α and γ. Therefore, the RB procedure will be applied in this dimension as explained in the reformulation of Section 2.3.

Furthermore, to sample the training set, different Latin Hypercubes (LHs) are taken using a grid composed of Chebyshev nodes along dimensions $f, s, I_p, \sigma, \delta$. In addition, nine hours are used to obtain the training set in the offline stage.

In Figure 4.23, a comparison for Eq. (4.27) is shown for a $\mathbf{z}_i$ belonging to the training set. For this plot, the error measured as Eq. (4.26) is $\mathrm{err}_i^{\mathrm{real}} = 0.0008$ and $\mathrm{err}_i^{\mathrm{imag}} = 0.001$.

In Figure 4.24, a comparison between the FEMM and PGD results for a $\mathbf{z}_i \notin \mathcal{T}$. For this plot, the error measured as Eq. (4.26) is $\mathrm{err}_i^{\mathrm{real}} = 0.009$ and $\mathrm{err}_i^{\mathrm{imag}} = 0.012$. In addition, the alternating magnetic pressure related to this B-field can be seen.

In Figures 4.25 and 4.26, the error for Eq. (4.27) for some $\mathbf{z}_i \notin \mathcal{T}$ can be observed. As it can be seen in these figures, excellent agreement between FEMM and PGD results is achieved outside the training set.

The main advantage is that the PGD model computes induction and force for a given $\mathbf{z}_i$ in less than 0.1 seconds indepentently of the computational cost of the Finite Element solutions used for the snapshots.

It is important to highlight that the computational cost of the PGD model is independent of the one of the FEM software used for the snapshots. Hence, if the computational cost of the FEM software was some days, the time needed for the PGD still would be less than 0.1 seconds.

4.3.5.3 Synchronous motor

The approach shown is based on a current based model. In addition, perfect sine wave current functions are supposed for the balanced three-phase system. In addition, a nonlinear B-H relationship is used for the materials.

The searched PGD function is:

$$B_n(\alpha, \gamma, I_p, \tau, \rho); \quad B_n \in \mathbb{R}, \tag{4.28}$$

where α refers to an angle pointing to a node in the air-gap midline, γ is the relative rotor position in relation to stator, I_p is the current peak value of the fundamental frequency of the source, τ is the torque angle, namely, the phase difference between rotor and stator magnetic fields and ρ is a parameter defining the dynamic eccentricity of the machine ($\rho = \frac{D_{O_s,O_r}}{\delta}$; where O_s is the stator symmetry center which in this eccentricity is equals to the rotor rotation center O_w, O_r is the rotor symmetrical axis, D_{O_s,O_r} is the distance between O_s and O_r and δ is the uniform air-gap length when there is no eccentricity). The above eccentricity parameters can be seen in Figure 4.27.

In this Section, the problematic dimensions described in Section 2.3 are α and γ. Therefore, the RB procedure will be applied in these dimensions as explained in the reformulation of Section 2.3.

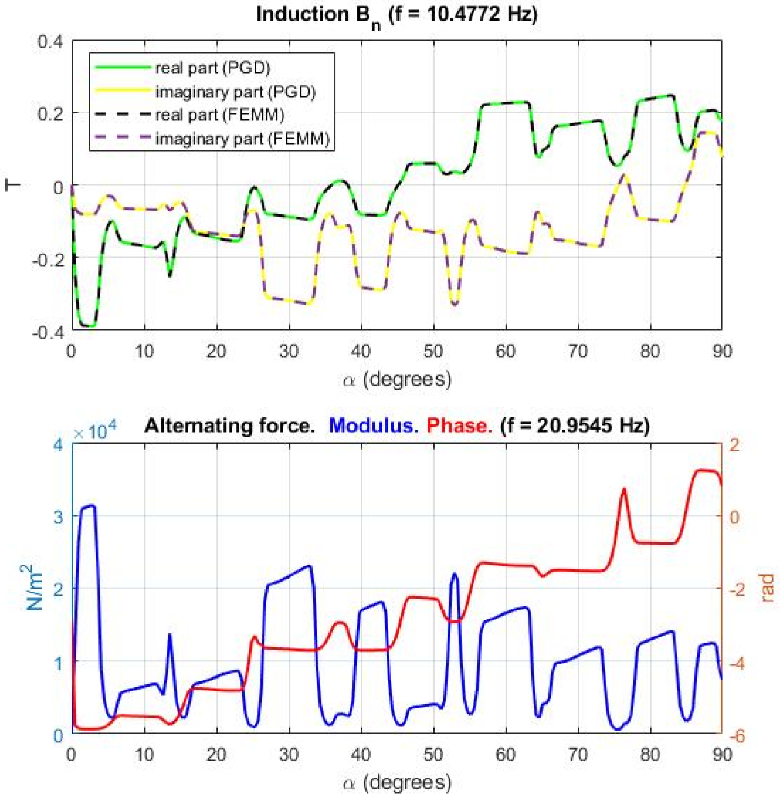

Figure 4.23 – Comparison between the s-PGD and FEMM model (nonlinear B-H relationship) for a $\mathbf{z}_i$ belonging to the training set. Parameters $f = 10.4772$ Hz, $s = 5$ %, $I_p = 3.3858$ A, $\sigma = 47.6537$ MS/m, $\delta = 0.4876$ mm, $\gamma = 0$ degrees. The alternating force obtained during the post-processing step is also shown.

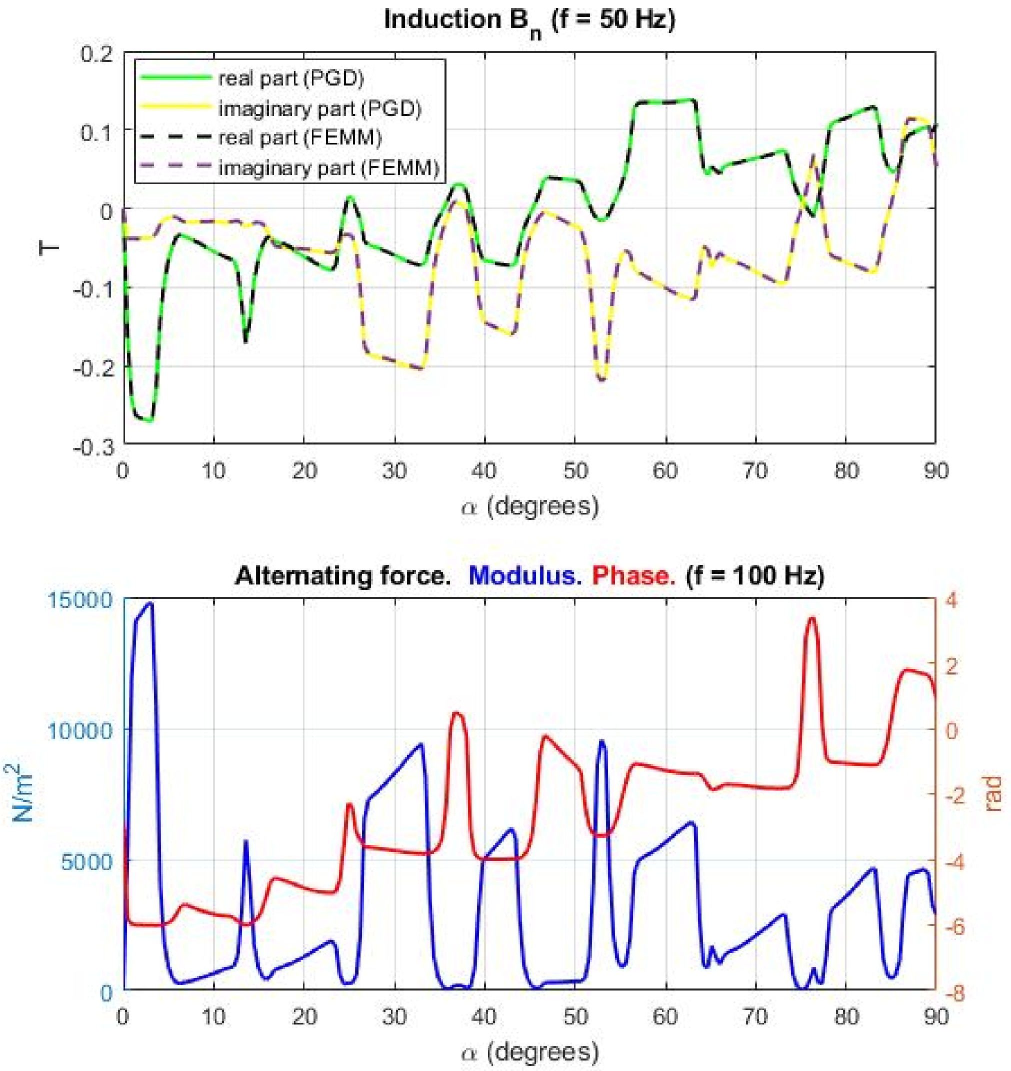

Figure 4.24 – Comparison between the s-PGD and FEMM model (nonlinear B-H relationship) for a $\mathbf{z}_i \notin \mathcal{T}$. Parameters $f = 50$ Hz, $s = 3$ %, $I_p = 3.5$ A, $\sigma = 40$ MS/m, $\delta = 0.5$ mm, $\gamma = 0$ degrees. The alternating force obtained during the post-processing step is also shown.

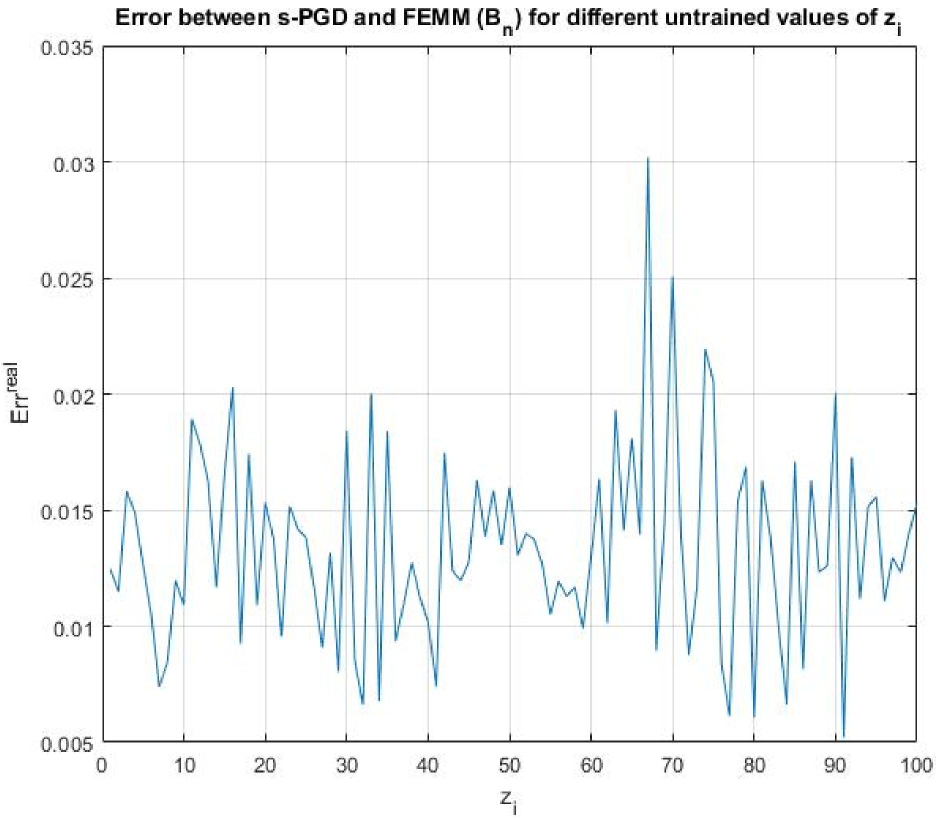

Figure 4.25 – Relative error of the s-PGD model (nonlinear B-H relationship) to determine the real part of B_n for different untrained $\mathbf{z}_i$. Error criteria of Eq. (4.26) is used.

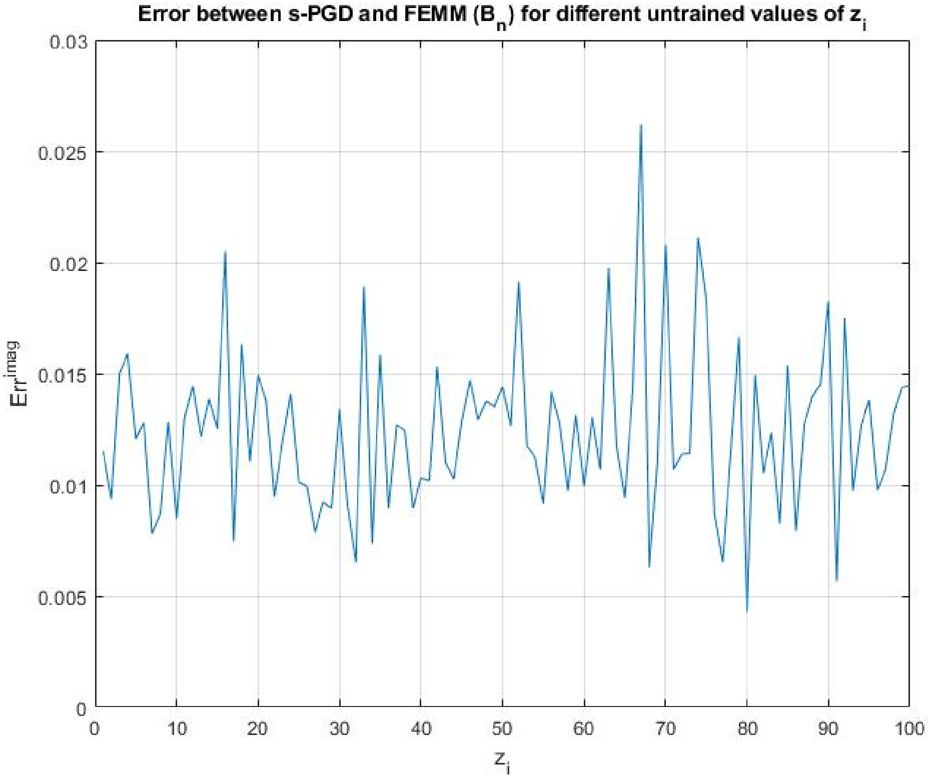

Figure 4.26 – Relative error of the s-PGD model (nonlinear B-H relationship) to determine the imaginary part of B_n for different untrained $\mathbf{z}_i$. Error criteria of Eq. (4.26) is used.

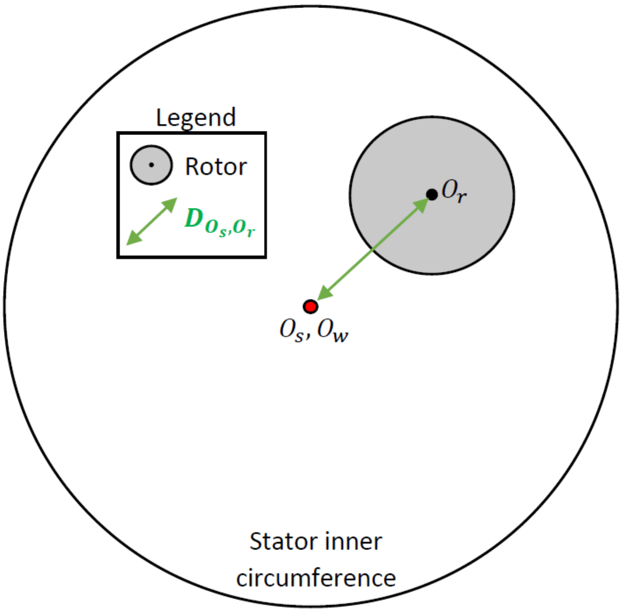

Figure 4.27 – Sketch to visualize the parameters O_s, O_w, O_r and D_{O_s,O_r}

Furthermore, to sample the training set, different Latin Hypercubes (LHs) are taken using a grid composed of Chebyshev nodes with the exception of γ (where it is preferred to use equidistant nodes for each parameter combination to complete a 180-degree turn). In addition, eight hours are used to obtain the training set in the offline stage.

In Figures 4.28 and 4.29, the induction and the magnetic pressure are depicted for two points $\mathbf{z}_1, \mathbf{z}_2 \notin \mathcal{T}$. The error associated according to Eq. (4.26) is respectively $\text{err}_1^{\text{real}} = 0.01$ and $\text{err}_2^{\text{real}} = 0.009$.

In Figure 4.30, we can see the time evolution of the magnetic pressure of figure 4.29 supposing a rotor and synchronous speed of $N = 2000$ rpm in steady state.

In Figure 4.31, a comparison of the results between FEMM and the PGD are shown to analyze the error of the proposed ROM.

As it can be seen, the error analysis for this PGD solution has similar results to the other PGD functions obtained for the induction motor.

Finally, as in the other cases, the big advantage is that the PGD model computes induction and force for a given $\mathbf{z}_i$ in less than 0.1 seconds and with accuracy indepentently of the computational cost of the Finite Element solutions used for the snapshots.

4.3.5.4 Sensitivity analysis of the parametric solutions

Sensitivity analysis is often interesting in parametric models because of:

- the need to characterize how sensitive the response is with respect to uncertainties in the input data; for example, manufacturing tolerances or material properties.
- the need to characterize how sensitive the response is in function of the operation point of the system.
- the need to make changes to improve the performance of a design and want to find out which changes that are most efficient for attaining the expected goals.

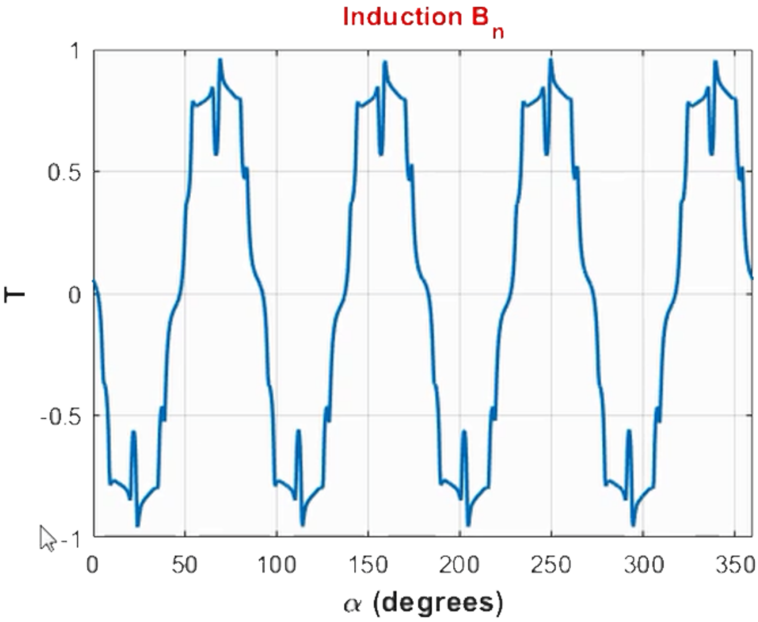

Figure 4.28 – Induction obtained with the s-PGD model for the parameters: $\gamma = 0$ degrees, $I_p = 3$ A, $\tau = \pi/2$ rad, $\rho = 0$

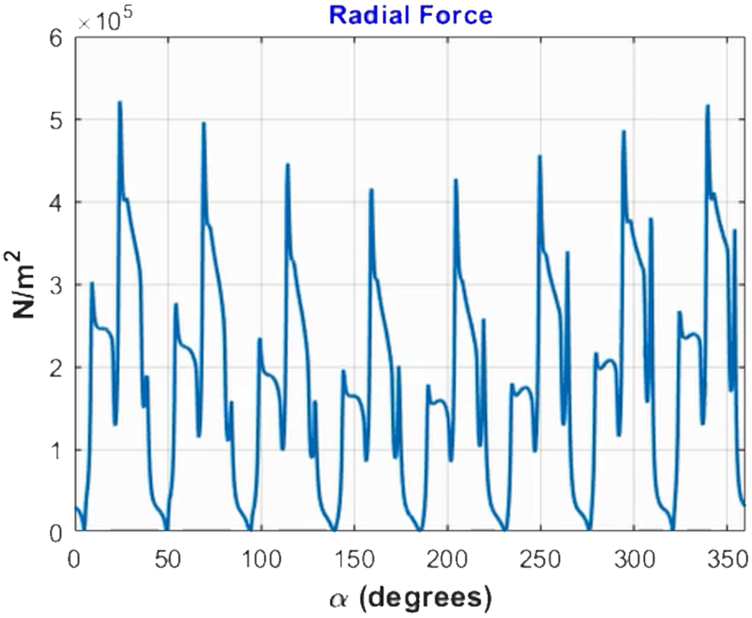

Figure 4.29 – Radial force wave obtained with the s-PGD model for a set of parameters: $\gamma = 0$ degrees, $I_p = 13$ A, $\tau = \pi/2$ rad, $\rho = 0.5$

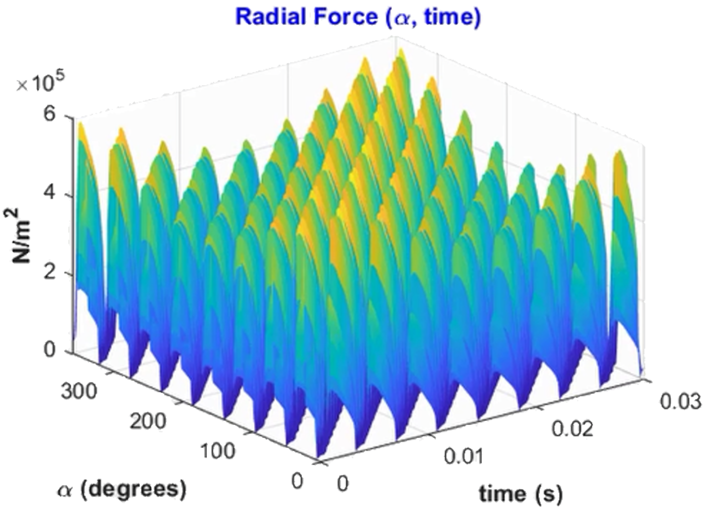

Figure 4.30 – Time evolution of the magnetic pressure wave obtained with the s-PGD supposing $N = 2000$ rpm. Set of parameters: $\gamma = 0$ degrees, $I_p = 13$ A, $\tau = \pi/2$ rad, $\rho = 0.5$

As a result, it seems evident that the importance of doing this type of analysis arises in industrial applications like the one treated in this chapter. The most appealing point is that the ROMs constructed with the separated representation proposed in this work make easier performing this analysis. The reason is that computing partial derivatives in the separated representation is translated to compute the derivatives of one-dimensional functions. As the vast part of the one-dimensional functions used in the ROMs are polynomials, the computation remains quite simple and with low-computational cost enabling online real-time calculations.

To illustrate the procedure, imagine a PGD solution concerning 3 parameters:

$$\tilde{f}^M = \sum_{m=1}^{M} X_m(x)\Theta_m^1(\theta_1)\Theta_m^2(\theta_2)\Theta_m^3(\theta_3),$$

where we want to analyze the how sensitive is the solution around the nominal point $\theta_1 = a_1, \theta_2 = a_2, \theta_3 = a_3$. Then, the partial derivatives $\frac{\partial \tilde{f}^M}{\partial \theta_1}(x, a_1, a_2, a_3)$, $\frac{\partial \tilde{f}^M}{\partial \theta_2}(x, a_1, a_2, a_3)$ and $\frac{\partial \tilde{f}^M}{\partial \theta_3}(x, a_1, a_2, a_3)$ are computed as:

$$\frac{\partial \tilde{f}^M}{\partial \theta_1}(x, a_1, a_2, a_3) = \sum_{m=1}^{M} X_m(x)\frac{\partial \Theta_m^1}{\partial \theta_1}(a_1)\Theta_m^2(a_2)\Theta_m^3(a_3),$$

$$\frac{\partial \tilde{f}^M}{\partial \theta_2}(x, a_1, a_2, a_3) = \sum_{m=1}^{M} X_m(x)\Theta_m^1(a_1)\frac{\partial \Theta_m^2}{\partial \theta_2}(a_2)\Theta_m^3(a_3),$$

$$\frac{\partial \tilde{f}^M}{\partial \theta_3}(x, a_1, a_2, a_3) = \sum_{m=1}^{M} X_m(x)\Theta_m^1(a_1)\Theta_m^2(a_2)\frac{\partial \Theta_m^3}{\partial \theta_3}(a_3),$$

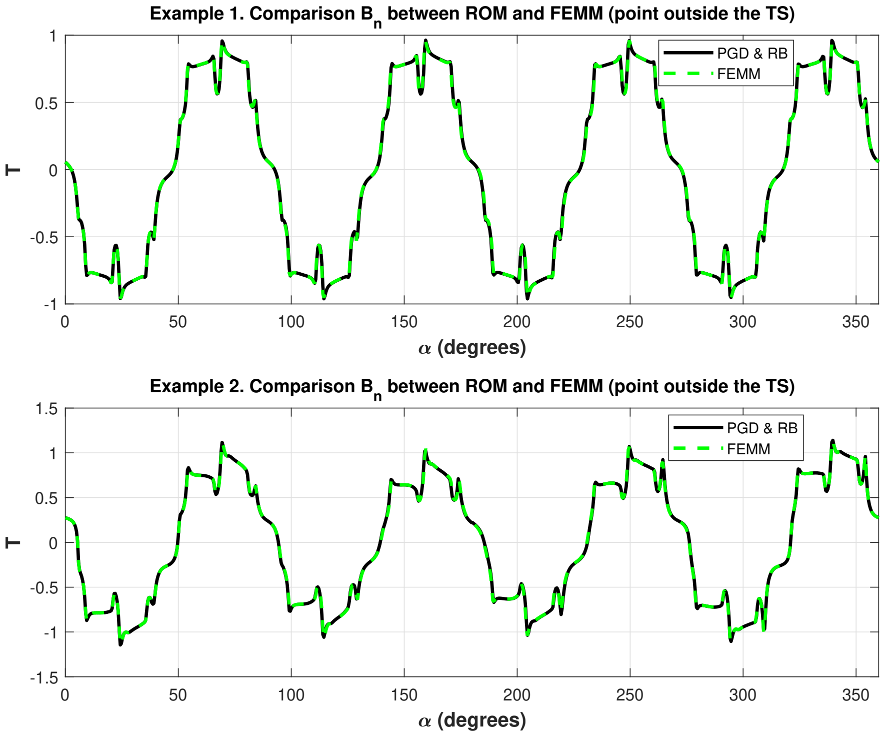

Figure 4.31 – Comparison between s-PGD and FEMM results. Set of the parameters (Top plot): $\gamma = 0$ degrees, $I_p = 3$ A, $\tau = \pi/2$ rad, $\rho = 0$. Set of the parameters (Bottom plot): $\gamma = 0$ degrees, $I_p = 13$ A, $\tau = \pi/2$ rad, $\rho = 0.5$.

where the magnitude of the partial derivative indicates the sensitivity of the solution for the given parameter in the analysed point (higher magnitude corresponds to higher sensitivity). In addition, the sign of the partial derivative indicates the direct or indirect relationship between the function value and the parameter.

Higher-order derivatives and also derivatives concerning different parameters are also possible. It is important to note that the sensitivities are a field, offering large information, beyond the behavior around the operating point.

Since the ROMs are based in the B-field, the sensitivity relation between magnetic pressure and the B-field for a given parameter θ_i is (using Eq. (4.22)):

$$\frac{\partial P_n}{\partial \theta_i}(\alpha) = \frac{1}{\mu} \cdot B_n \frac{\partial B_n}{\partial \theta_i}(\alpha). \tag{4.29}$$

Now, as an example of use, some analysis that can be carried out with the extracted ROMs are shown in different regions of the domain. In the first example, we are going to focus on the synchronous machine. Here, the sensitivity of the solution for the parameters I_p and ρ is explored in an area of interest $\alpha \in [134.7, 224.8]$ deg. under the conditions: high current and no eccentricity, high current and eccentricity, low current and no eccentricity, and low current and eccentricity.

In Figures 4.32, 4.33, 4.34 and 4.35 the sensitivity is compared with two operating points changing its I_p from 0.5 A to 20 A. Here, we can observe how much a little change in the eccentricity or in the current peak value affects the magnetic pressure as well as the B-field for both cases. In this operating points, adding eccentricities in the order of 0 - 0.25 mm does not change a lot the sensitivity behavior.

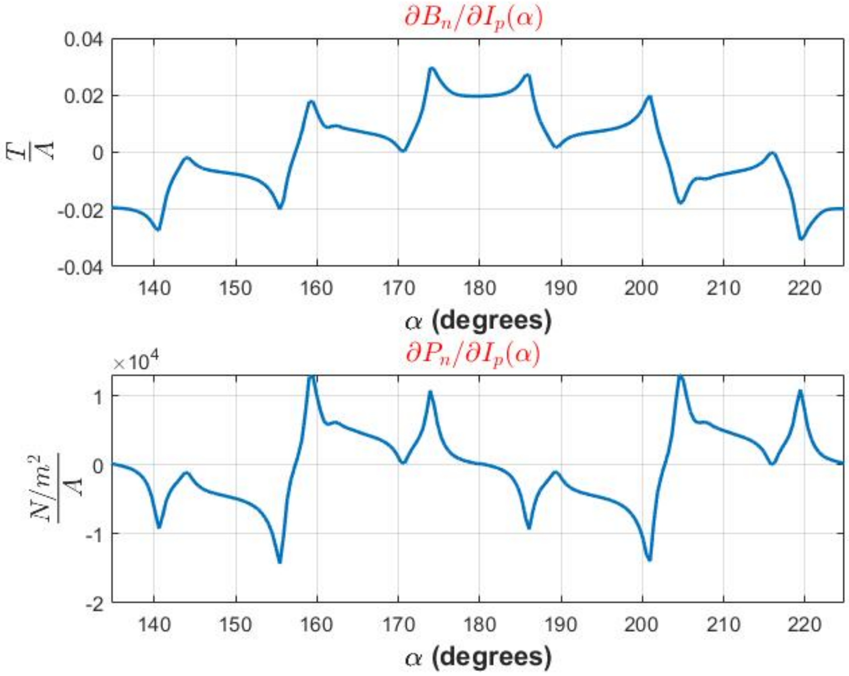

Figure 4.32 – Sensitivity of B_n and P_n for small changes in I_p. Operating point: $\gamma = 0$ degrees, $I_p = 0.5$ A, $\tau = \pi/2$ rad, $\rho = 0$.

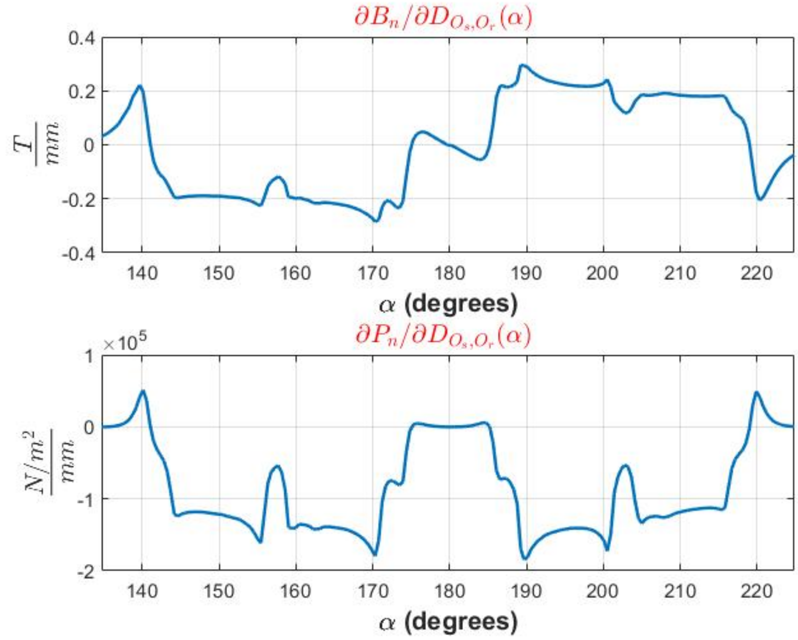

Figure 4.33 – Sensitivity of B_n and P_n for small changes in D_{O_s,O_r}. Operating point: $\gamma = 0$ degrees, $I_p = 0.5$ A, $\tau = \pi/2$ rad, $\rho = 0$.

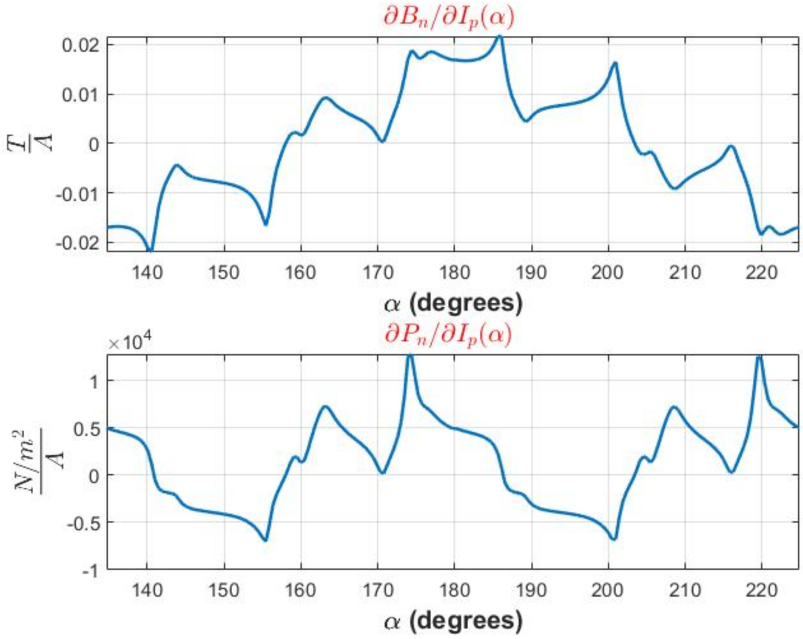

Figure 4.34 – Sensitivity of B_n and P_n for small changes in I_p. Operating point: $\gamma = 0$ degrees, $I_p = 20$ A, $\tau = \pi/2$ rad, $\rho = 0$

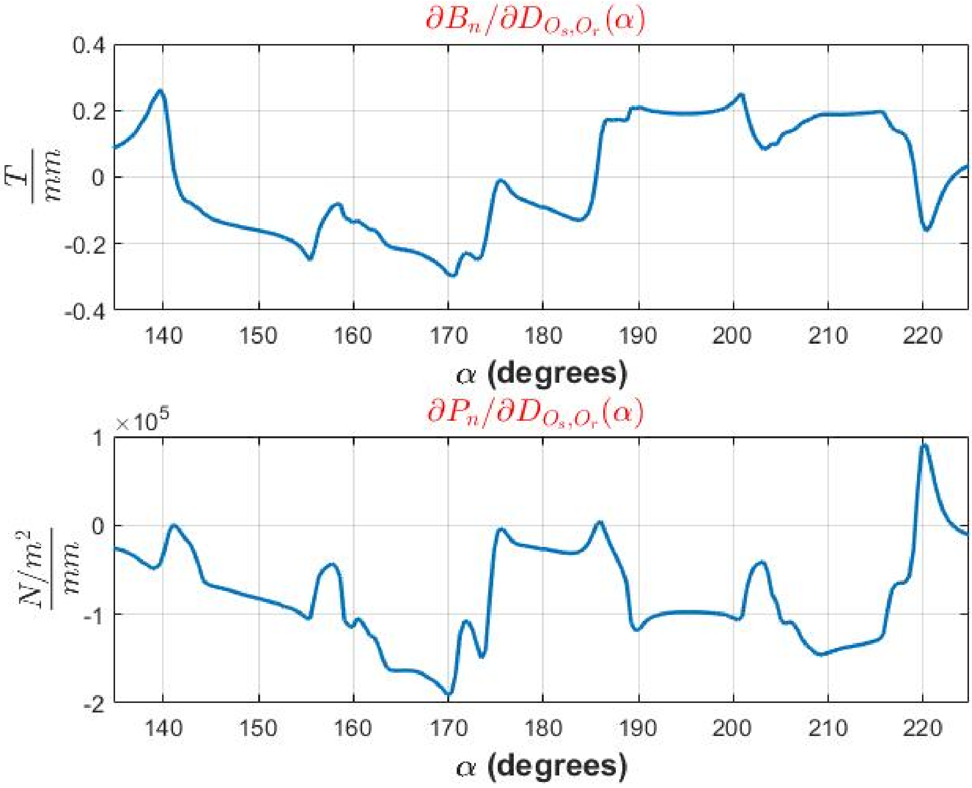

Figure 4.35 – Sensitivity of B_n and P_n for small changes in D_{O_s,O_r}. Operating point: $\gamma = 0$ degrees, $I_p = 20$ A, $\tau = \pi/2$ rad, $\rho = 0$.

The second example is reported in figure 4.36 concerning the induction motor. Here, the sensitivity of the solution for five parameters is explored under a nominal operation point. Also, the sensitivity of the conductivity when its value is not well known was studied concluding that this uncertainty does not affect strongly the variables of interest.

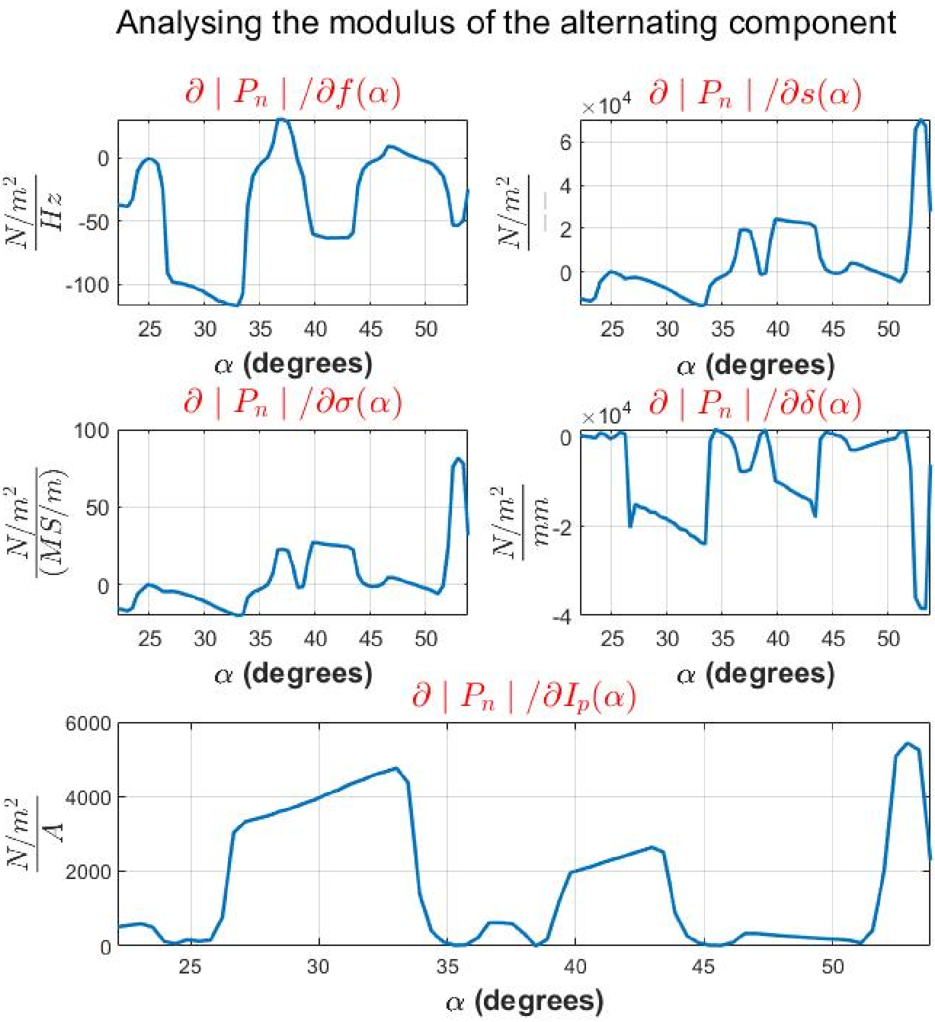

Figure 4.36 – Sensitivity of P_n (the modulus of the alternating component) for small changes in the parameters shown in the plot. The operating point is $f = 50$ Hz, $\gamma = 0$ degrees, $I_p = 3$ A, $s = 2.5$ %, $\sigma = 34.45$ MS/m, $\delta = 0.375$ mm. The region explored is $\alpha \in [22.2, 53.8]$ deg. is explored.

4.4 Conclusions

Two different advanced ROMs for rotating electrical machines are developed in this chapter to meet current industrial requirements. The first one based on the intrusive PGD and the second one based on the s-PGD+RB strategy.

The first one is recommended when possible or when the intrusiveness is not an issue, due to the fact that the equations are mathematically solved for all possible combinations of the parameter values. On the other hand, the s-PGD+RB strategy is recommended when complex geometries cannot be addressed by the proposed change of coordinates or when complex geometrical parameters present difficulties in the formulation of the intrusive PGD. For instance, eccentricity.

With respect to the PGD ROM, a double separation of variables, involving both the space coordinates and the model parameters, was carried out within the PGD rationale, and was applied to the analysis of electric motors, in particular, synchronous machines. To test the proposal, a two-dimensional steady state analysis (magneto-static analysis) of a PMSM was studied. In addition, an efficient coordinate transformation was proposed, which was able to proceed with a full space separation that reduced the 3D domain description from a series of one-dimensional approximations.

In this study, an excellent agreement between the FEMM software and the PGD results was noticed. The great benefit of employing the PGD is that high-dimensional parametric functions can be efficiently constructed with low computational cost. Furthermore, the proposed approach can empower the design, optimization or inverse analysis of this type of machines because once the PGD solution is obtained in the off-line stage, it can be particularized online under the stringent real-time constraints.

On the other hand, with respect to the s-PGD+RB ROM, it can be observed that the results of the FEMM software are reproduced with a high accuracy. A reduction in the computational time and resources needed to obtain parametric electromagnetic forces is achieved. In fact, the computational cost can be carried out by a standard laptop in less than 0.1 seconds. Consequently, the saving in computational time and resources opens a door for design, analysis, optimization and simulation of NVH in electric motors under this rationale in the electromagnetic step. In addition, the proposed ROM facilitates the integration and coupling of the force computation in electric motors to other systems (such as the EV system) because of the simplicity of the obtained algebraic expression.

It is worthy to mention that the extremely low computational cost of the s-PGD+RB ROM is independent of the complexity of the model used to offline obtain the snapshots. In this work, the formulation available in the free software FEMM was employed.

Furthermore, richer finite element models can be used to obtain the electromagnetic forces to construct the ROM without major difficulties. Although it is true that using these models to obtain the snapshots for the off-line stage is more time consuming, the computing time needed for the ROM once it is constructed (on-line stage) still would not be affected (much smaller than a second).

Chapter 5

Parametric electromagnetic analysis of radar based Advanced Driver Assistant Systems

Abstract Efficient and optimal design of radar-based Advanced Driver Assistant Systems (ADAS) needs the evaluation of many different electromagnetic solutions for evaluating the impact of the radome on the electromagnetic wave propagation. Because of the very high frequency at which these devices operate, with the associated extremely small wavelength, very fine meshes are needed to accurately discretize the electromagnetic equations. Thus, the computational cost of each numerical solution for a given choice of the design or operation parameters, is high (CPU time consuming and needing significant computational resources) compromising the efficiency of standard optimization algorithms. In order to alleviate the just referred difficulties the present chapter proposes an approach based on the use of reduced order modeling, in particular the construction of a parametric solution by employing a non-intrusive formulation of the Proper Generalized Decomposition, combined with a powerful phase-angle unwrapping strategy for accurately addressing the electric and magnetic fields interpolation, contributing to improve the design, the calibration and the operational use of those systems.

Contents

5.1 Introduction . . . 130
- 5.1.1 Chapter overview . . . 130
- 5.1.2 Topic introduction . . . 130

5.2 Parametric Electromagnetic Fields . . . 132
- 5.2.1 Real-Imaginary Interpolation Versus Magnitude-Phase Interpolation . . . 132
- 5.2.2 Stratregy Proposed . . . 133

5.3 Antena Modelling and Simulation Details . . . 133

5.4 Results on the RADAR Problem . . . 134
- 5.4.1 Clarification. Phase Singularity . . . 136

5.5 Conclusions . . . 137

5.1 Introduction

5.1.1 Chapter overview

This chapter presents an industrial application where the novel unwrapping algorithm proposed in Section 2.4 is employed (Chapter 2). The main goal is to significantly reduce the number of snappshots needed to obtain a valid surrogate model for the radar application, to allow, for instance, parametric models. Fulfilling the above objective has a very high added value due to the high computational cost of obtaining the snapshots (i.e. simulations are higly time-consuming).

Therefore, once the unwrappping is computed, non-intrusive MOR techniques can be used to obtain a response surface. In particular, the s-PGD procedure is recommended in this chapter to mitigate the curse of dimensionality as well as to reduce intrusiveness. An analysis of the results is carried out to observe the improvements of the proposed strategy.

Before starting the discussion, it is important to mention that the industrial application presented in this chapter as well as its results correspond to the second published paper shown in Chapter 2 when presenting the unwrapping algorithm.

5.1.2 Topic introduction

Radar is a widely employed technology which relies on wave propagation to detect surrounding objects. It consists in emitting a radio wave from a transmitter and measuring the reflected wave with a receiving antenna. The data collected from this measurement can provide information about a detected object such as its location or its nature. An in-depth analysis of the electromagnetic field may be necessary to ensure the information inferred from the data is valid.

Radio waves are oscillations of the electromagnetic field and can therefore be computed by solving Maxwell's equations. In the present work the electromagnetic problem is solved using the Finite Differences Time Domain (FDTD) method implemented in CEM One®, a commercial software provided by ESI Group, then computing the discrete Fourier transform of the result to obtain the solution in the frequency domain.

The fundamentals of radar technology is nowadays used in many driver assistance systems, needing for a precise quantification of performances and limitations [Winner *et al.* 2016]. Its design and use need addressing many topics, raging from waveform design, propagation and pattern recognition [Rohling 2006, Stateczny *et al.* 2019, Schnabel *et al.* 2013], with challenges and opportunities that are driving their evolution [Steinbaeck *et al.* 2017]. However, its use is not limited to driver assistance, this technology is nowadays largely employed in many domains like short-range localization [Peng & Li 2019], monitoring worker activity [Cardillo & Caddemi 2019a], aids for visually impaired people [Cardillo & Caddemi 2019b], physiological monitoring [Gao *et al.* 2016], non-contact identity authentication [Islam *et al.* 2020], among many others. Signal pollution is not excluded and sometimes it must be repaired before making use of it [Rodriguez & Li 2019].

In outdoor applications, the transmitter and antenna are placed behind a radome, a shell made of a dielectric material designed to protect the electric components against the weather. Although dielectric materials are radio-wave transparent, they have an altering effect on the electromagnetic field and must therefore be taken into account when analyzing the data. Simulation of radio wave propagation through the radome provides knowledge of the latter's precise influence on the system accuracy and performances. Thus, an important issue concerns the effect of bumpers on the radar performances, topic that attracted great interest [Blöecher *et al.* 2012, Vasanelli *et al.* 2017, Harter *et al.* 2016, Pfeiffer & Biebl 2009, Buitrago *et al.* 2019, Norouzian *et al.* 2016]. In the just referred works the coupling radar-radome effects (e.g., attenuation, signal pollution, ...) was investigated but a parametric numerical modeling was not considered.

In the present chapter, we address precisely the analysis of that coupling, depending on the radar orientation, however because of the high frequency, the spatial mesh resolution for describing the solution of Maxwell equations leads to extremely fine meshes, with the consequent impact on the computing time. Simulation details are included in Section 5.3.

To alleviate that issue, we investigate the use of model order reduction (MOR) techniques that successfully accomplished numerous parametric studies in other engineering domains. Model order reduction has been successfully applied in problems involving dynamics and waves within the so-called projection formulation, needing for a certain degree of intrusiveness when using commercial softwares. Thus, the radial approximation proposed in [Ladevèze 1989] was extended to mid-frequency dynamics within the so-called variational theory of complex rays [Ladevèze *et al.* 2001]. In [Modesto *et al.* 2015], a parametric solution of the Helmholtz equation was successfully obtained using the usual rank-one greedy PGD constructor. In [Amsallem & Farhat 2008] authors proposed a consistent reduced bases interpolation.

Non-intrusive formulations were proposed for constructing parametric solutions from a number of high-fidelity simulations performed for different choices of the model parameters, while trying to reduce as much as possible the size of the sampling for addressing multi-parametric models [Chkifa *et al.* 2014, Borzacchiello *et al.* 2019]. In those circumstances, usual surrogate models exhibit limitations when the number of parameters increases, and alternative technologies combining two main ingredients, the separation of variables and sparse sampling and approximations, appeared and proved their performances [Borzacchiello *et al.* 2019, Ibáñez Pinillo *et al.* 2018].

When these techniques were employed in radar engineering different difficulties appeared. The first related to the fact that the sampling scales with the characteristic length of the solution, that is with the wavelength, extremely small. On the other hand interpolation of complex-valued electric and magnetic fields produces spurious solutions. Thus, for example, the average of $1 + 0i$ and $-1 + 0i$ results $0 + 0i$, even if one is expecting having $0 + i$ (See Figure 5.1).

This limitation was solved by employing and alternative formulation based on the amplitude and phase. For example, in the scenario just described, the average of $1|0$ and $1|\pi$ results $1|\pi/2$, result that seems more physically consistent.

However, the use of an amplitude/phase description faces the difficulty related to its 2π periodicity, and the associated spurious discontinuities found when combining a phase close to 2π, e.g., $2\pi - \theta$ ($\theta > 0$, very small), with another very close too, e.g., $2\pi + \theta'$ ($\theta' > 0$, very small), but that being higher than 2π reduces to θ', originating the just referred spurious discontinuity: $2\pi - \theta \to \theta'$. Even if this issue was addressed in many works that proposed the use of the so-called unwrapping, usual unwrapping algorithms only performs well when the data sampling is dense enough, but they fail in the sparse sampling case [Ben Abdallah & Abdelfattah 2015, Shanker & Zebker 2010, Costantini *et al.* 2012] .

The present chapter proposes a technique able to conciliate unwrapping and sparse sampling.

Now, the problem statement and the proposed strategy are introduced in Section 5.2.

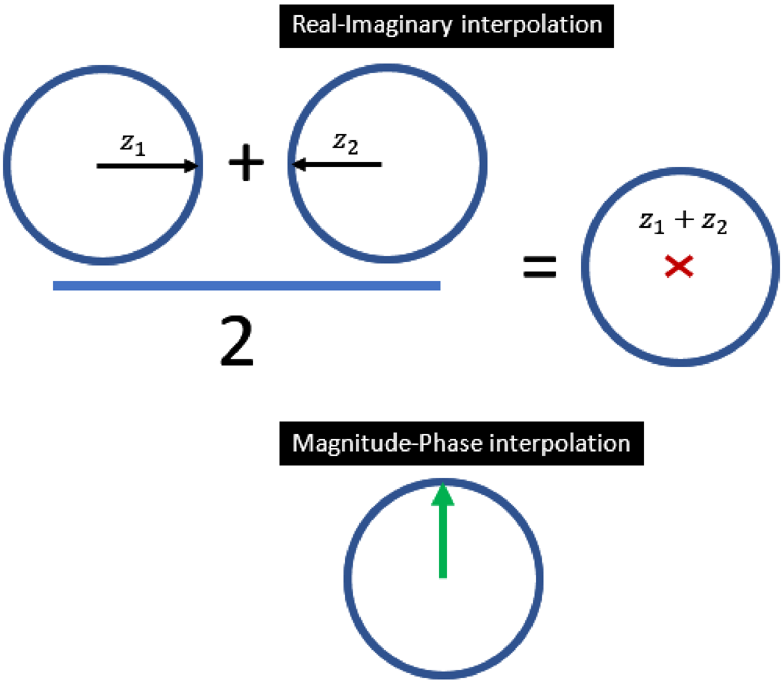

Figure 5.1 – Example to illustrate the differences between Real-Imaginary and Magnitude-Phase interpolation.

5.2 Parametric Electromagnetic Fields

In the present context, the transmitter emits waves at a constant frequency in a direction denoted by an angle θ between $0°$ and $90°$. For each component of the electric and magnetic fields, the data generated by the simulations consists of an array of $N \times N_\theta$ values, N being the number of points in the spatial discretization and N_θ the number of points in the angular discretization. The aim of this work is to provide a method to determine through the values of the electromagnetic field in all N discretized points in the geometry for any value of θ between $0°$ and $90°$. In what follows, we will consider the problem of constructing the interpolation of the z-component of the electric field, E_z, and the y-component of the H-field, H_y, for all θ in the geometry points.

5.2.1 Real-Imaginary Interpolation Versus Magnitude-Phase Interpolation

Since the solutions provided by the solver are in the frequency domain, they are complex-valued functions. Complex numbers can be represented either by their real and imaginary parts or by their magnitude and phase, therefore the interpolation of complex-valued functions can be computed in multiple ways which are not equivalent. The first option is to treat the real and imaginary parts as two real-valued functions, interpolate them separately and combine the results. The second option is to treat the magnitude and phase as two real-valued functions, interpolate them separately and combine the results.

The performances of these two methods depend on the considered problem. In the case studied in this chapter, the data from the simulation have real and imaginary parts oscillating quite fast compared to the sampling frequency (Figure 5.2), hence they are not good candidates for interpolation. However the magnitude is much smoother which means it may give trustworthy interpolation results. The phase looks more chaotic but it is not a good indicator because of its natural 2π-periodicity that induced spurious discontinuities: the phase needs to be "unwrapped" before being interpolated.

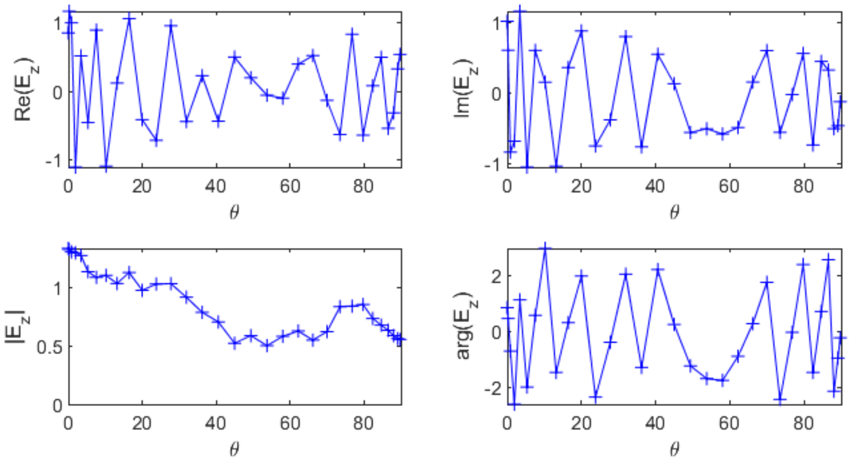

Figure 5.2 – Real and imaginary parts (top left and right respectively), magnitude and phase of E_z (bottom left ad right respectively) as a function of θ in one point of the geometry.

In figure 2.2, it can be observed how the unwrapped function is more suitable to interpolation and in Section 2.4.1, further details about the unwrapping problem were introduced

5.2.2 Stratregy Proposed

The novel phase unwrapping proposed in Section 2.4 of Chapter 2 is applied to recover the "unwrapped" electromagnetic signals. In the aforementioned Chapter, it was proved that the new strategy is more robust and able to perform accurately with much less sampling points. And not only that, but its performances were also demonstrated as well as compared with current techniques (Sections 2.4.2, 2.4.3 and 2.4.4). Therefore, with the proposed strategy, the number of snapshots is significantly reduced, finding a smooth space where interpolation and parametric functions can be constructed. Then, a non-intrusive MOR procedure, specifically the s-PGD introduced in Chapter 2 can be employed to construct the parametric model.

5.3 Antena Modelling and Simulation Details

The simulation model discussed in this chapter is illustrated in Figure 5.3. This simplified mock-up represents the receiving part of a typical automotive radar device operating at 24 GHz and located behind a plastic bumper (Blind Spot Detection).

The antenna is made of 16×8 square array elements printed on a rectangular substrate (thickness about 0.254 mm with a dielectric permittivity set equal to 2.2 and an electrical conductivity of 0.003 S/m). The average thickness of the plastic bumper is 7.5 mm and its permittivity about 2.6 (its conductivity being negligible).

As mentioned in the during this chapter, computational results were obtained using the CEM-TD product included in the CEM One® software package and based on the standard FDTD simulation technique (Finite Difference Time Domain).

Once the device is illuminated by an external plane wave, electric and magnetic field components can be thus accessed at the level of each basic antenna element and thus expressed in frequency domain (modulus and phase) using a classical Fourier transform—see for instance Figures 5.4 and 5.5.

With an incidence angle of the 24 GHz exciting wave ranging from 0° to 90° in the horizontal plane (illustrated in Figure 5.3 for a given sample of the array antenna), the spureous effect of the plastic bumper can be evaluated by comparing the fields actually received by the antenna with the reference signal obtained without any extra obstacle.

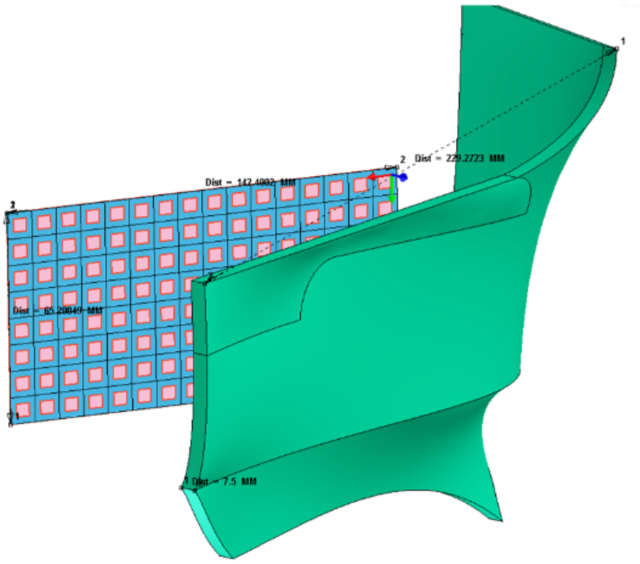

Figure 5.3 – Radar antenna and radome.

5.4 Results on the RADAR Problem

The electromagnetic field on a patch antenna (8×16 rectangular patches) has been computed for 33 different values of θ between 0° and 90°, 32 of which are used to apply our method and one as reference to compare the interpolation with the simulation. The reference electromagnetic field corresponds to the parameter value $\theta_{ref} = 79.8°$. The two closest values of theta used to compute the interpolation are 76.8° and 82.4° hence θ_{ref} lies in a gap of size $\Delta\theta = 82.4° - 76.8° = 5.6°$. The values of the electromagnetic field below 0.2 V/m for the electric component (**E**) and 0.5 mA/m for the magnetic component (**H**) are not considered in this study because the signal is not considered significant enough and the phase cannot be studied because of its singularity (See Section 5.4.1). For this reason and due to the polarization of the electromagnetic field, only the z-component of the electric field E_z and y-component of the magnetic field H_y provide results. The absolute error is calculated between the phase of the reference field and the phase of the interpolated field. Then, figures are shown with the mean error over each patch of the antenna using the proposed method (Figures 5.4 and 5.5) and the classical unwrapping algorithm for comparison (Figures 5.6 and 5.7).

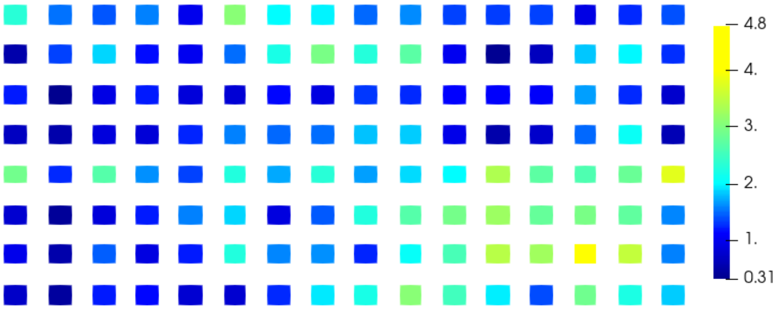

Figure 5.4 – Mean absolute error on the phase (°) of the E_z component over each patch of the antenna using the proposed method.

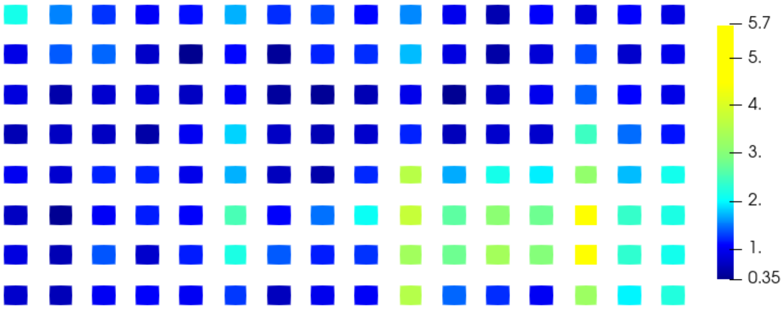

Figure 5.5 – Mean absolute error on the phase (°) of the H_y component over each patch of the antenna using the proposed method.

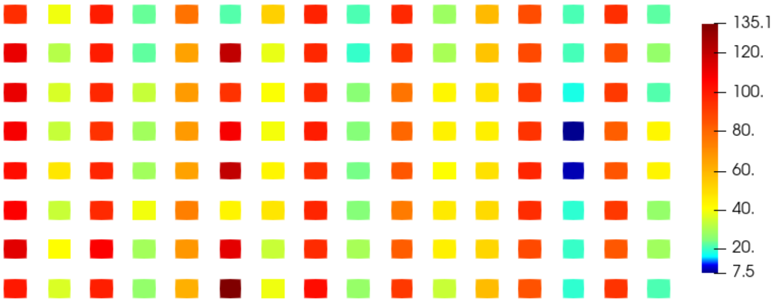

Figure 5.6 – Mean absolute error on the phase (°) of the E_z component over each patch of the antenna using the classical unwrapping algorithm.

With the proposed method, the average error over the entire antenna is 1.6° for the electric field and 1.4° for the magnetic field while with the standard unwrapping algorithm, the average error over the entire antenna is 62.0° for the electric field and 63.7° for the magnetic field. In comparison, the average error on the phase when interpolating real and imaginary parts is 166.8° for the electric field and 166.7° for the magnetic field.

The proposed approach is accurate and robust as the mean phase error is consistently under 6° on the entire antenna for both the electric and magnetic fields, whereas real and imaginary parts interpolation completely fails when dealing with such a sparse discretization of the parameter θ.

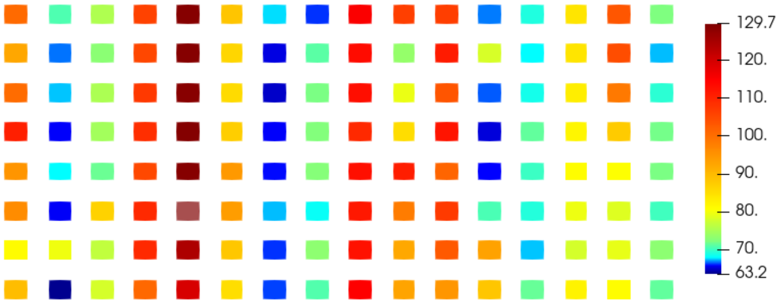

Figure 5.7 – Mean absolute error on the phase (°) of the H_y component over each patch of the antenna using the classical unwrapping algorithm.

5.4.1 Clarification. Phase Singularity

This additional section contains a clarification about the statement made during Section 5.4 concerning phase singularity.

The phase of a complex-valued function can have very fast variations when its magnitude is close to zero, even if the function is very regular (Figure 5.8). This may induce large error in the interpolation of the phase, which cannot be easily avoided. However since the magnitude is very small, a large error on the phase does not have too much impact on the complex number itself, which can usually simply be regarded as zero.

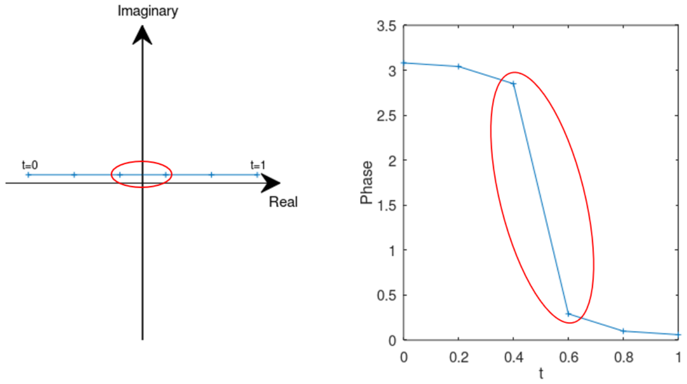

Figure 5.8 – Example of a smooth parametric curve on the complex plane (**left**) and the phase as a function of the parameter (**right**).

5.5 Conclusions

In this chapter, the computation of parametric solutions for electromagnetic wave propagation in radar applications is addressed. These simulations currently require hundreds of hours of computations to obtain suitable accuracy.

An interpolation method for complex-valued fields which allows reducing the computational cost significantly is described. By exploiting the natural regularity of electromagnetic fields, we are able to retrieve highly accurate parametric solutions from a very sparse set of simulations.

In addition, this is an example of the great advantages of the proposed unwrapping algorithm of Section 2.4. In fact, in the aforementioned section, the results already showed that a great reduction in the number of needed snapshots can be achieved. And not only that, but it was proved that the novel unwrapping algorithm can outperform current commercial software as well as provide good results in complex settings, such as the one tackled in this chapter.

Chapter 6

An aircraft Hybrid Twin: Learning stable reduced-order models for hybrid twins

Abstract The concept of "Hybrid Twin" (HT) has recently received a growing interest thanks to the availability of powerful machine learning techniques. This twin concept combines physics-based models within a model-order reduction framework—to obtain real-time feedback rates—and data science. Thus, the main idea of the HT is to develop on-the-fly data-driven models to correct possible deviations between measurements and physics-based model predictions. This chapter is focused on the computation of stable, fast and accurate corrections in the Hybrid Twin framework to address a real industrial application. Furthermore, regarding the delicate and important problem of stability, the novel approach presented in Chapter 2 of this dissertation is employed. Throughout this chapter, a comparison between the full data-driven solution and the hybrid twin strategy is also carried out. This way, the advantages of the hybrid strategy are analyzed.

Contents

6.1 Introduction . . . 140
  6.1.1 Chapter overview . . . 140
  6.1.2 Topic introduction . . . 140
6.2 System modeling . . . 141
  6.2.1 Extracting the model of the system from scratch . . . 141
  6.2.2 Enriching a physics-based model within the Hybrid Twin framework . . . 142
6.3 Application to a dynamical system: The aircraft hybrid twin 142
  6.3.1 System to model and types of data. . . . 142
  6.3.2 Extracting a model from scratch using the GT data . . . 143
    6.3.2.1 Procedure and results . . . 143
    6.3.2.2 Checking explicitly the improvements of the proposed approach to learn stable systems. Example when proceeding from the GT data. . . . 151
  6.3.3 Extracting a model from scratch using noisy data (PED). . . 151
  6.3.4 Extracting the correction model. Hybrid Twin paradigm. . . 157
6.4 Conclusions . . . 163

6.1 Introduction

6.1.1 Chapter overview

This chapter shows the thesis work done for a research project as part of the PEA MMT (Plan d'Etudes Amont Man Machine Teaming) financed by the DGA (French Government Defense procurement and technology agency) and managed by French aircraft and jets manufacturer Dassault Aviation.

The goal is to employ the HT strategy to model an air distribution system of a commercial aircraft from Dassault Aviation.

Moreover, one of the techniques proposed for hybridization in Chapter 2 is employed to address this industrial application. Specifically, the stabilized DMDc technique proposed in Section 2.5.3. In that section, the proposed strategy to obtain stable systems is described as well as the sub-variants to deal with high-dimensional systems.

The methodology is tested for the aforementioned industrial case (detailed in Section 6.3.1), where an excellent agreement was observed when employing the HT approach.

The work is organized as follows: in Section 6.1.2, a brief introduction of the topic is shown. Next, in Section 6.2, the system modeling with the HT concept is presented and compared to the direct (so to speak, from scratch) data-driven approach. An alternative approach that benefits from transfer learning, for instance, can be found in [Guastoni *et al.* 2020]. Then, in Sections 6.3 and 6.4, the results and general conclusions of the present work are discussed, respectively. In addition, throughout Sections 6.3.2, 6.3.3 and 6.3.4, a comparison between the full data-driven solution and the hybrid twin strategy is carried out.

This chapter and all the results presented in it correspond to the following published paper

- A. Sancarlos, M. Cameron, J.M. Le Peuvedic, J. Groulier, E. Cueto, F. Chinesta, J.L. Duval, " Learning stable reduced-order models for hybrid twins," *Data-Centric Engineering*, Accepted, in press.

6.1.2 Topic introduction

The Hybrid Twin (HT) paradigm is a powerful tool to make better predictions, increase control performance or improve decision-making [Chinesta *et al.* 2020, Martín *et al.* 2020]. The main idea, see Fig. 6.13, is to develop on-the-fly data-driven models to correct the gap between data (i.e., measurements) and model predictions. In other words, there are two main ingredients of a HT:

- The first one is to enrich physics description with data.
- The second one is to accelerate physics-based models using Model Order Reduction (MOR) techniques, as in [Chinesta *et al.* 2017], [Chinesta *et al.* 2011], or [Quaranta 2019].

In any case, when addressing dynamical systems in the HT framework, it is important to guarantee the stability of the system when adding corrections to the physical model. It is worth noting that this is an important issue, because sometimes the best model, computed with state-of-the-art algorithms, completely fails to obtain a stable time-integrator. For example, when considering a linear dynamical model by the Dynamic Mode Decomposition (DMD) approach [Schmid 2010, Kutz *et al.* 2016], the feasible region constrained by the stability condition is nonconvex [Huang *et al.* 2016], and no general methodology exists to solve it.

For this reason, this thesis proposes a new, fast and efficient methodology, covering several sub-variants and guaranteeing a low computational cost as well as the achievement of a stable dynamical system. This technique will therefore be used to add a stable correction term into the HT concept.

6.2 System modeling

In what follows, we consider the system as described by a vector $\mathbf{z} \in \mathbb{R}^{\mathtt{D}_\mathtt{z}}$ (with $\mathtt{D}_\mathtt{z}$ the number of variables involved in the system evolution). The state (snapshot of the system) at time $t_k = k\Delta t$ is stored at vectors $\mathbf{z}_k$, with $k \geq 0$, with $\mathbf{z}_0$ assumed known. In addition, $\mathtt{D}_\mathtt{u}$ control parameters are considered, giving rise to the input space $\mathbf{u} \in \mathbb{R}^{\mathtt{D}_\mathtt{u}}$.

We assume the existence of a model $\mathbb{M}^c(\mathbf{z}, \mathbf{u})$ which we refer to as coarse, since we assume that some form of enrichment is necessary. Often, this model is physics-based, it arises from the corresponding PDEs governing the problem and can contain non-linearities. Other times, it is based on MBSE (Model Based System Engineering) modelling. This approximate representation of the reality is sought to be computable under real-time constraints. These constraints depend on the context and can range from some seconds to the order of milliseconds. If the complexity of the model does not allow to obtain such a response under constraints, model order reduction techniques constitute an appealing alternative. These, that can be linear or not, allow us to timely integrate the state of the system.

Because of the simplifying hypotheses involved in the construction of the model $\mathbb{M}^c$, it is expected that model predictions $\mathbf{z}_k^c$ differ from measurements to some extent, i.e., $\|\mathbf{z}_k - \mathbf{z}_k^c\| > \epsilon$, for most time steps k, thus needing for a correction.

6.2.1 Extracting the model of the system from scratch

Several routes exist to construct a model for a given dynamical system. The first one consists in performing a completely data-driven approach from experimental measurements $(\mathbf{z}_k, \mathbf{u}_k)$, $k = 0,\ 1, \ldots, n_s$ A valuable option is to consider the so-called dynamic mode decomposition (DMD) to extract a matrix model of a discrete linear system [Schmid 2010]. As suggested by several works, many different systems can be well approximated using this approach [Schmid 2011, Schmid *et al.* 2011]. If problems arise due to complex system behaviours, the procedure of extending the state vector to a higher dimensional space can often solve the problem [Kutz *et al.* 2016, Eivazi *et al.* 2021].

A second alternative could be the technique presented in Section 2.5.4 (or a variant of this proposal), that consists in grouping all the states close to $\mathbf{z}_k$ and the control parameters close to $\mathbf{u}_k$ into a set $\mathcal{K}_i$. For the sake of clarity, in what follows $\mathcal{K}$ will refer to one of these generic sets. A linear model for the set $\mathcal{K}$, denoted $\mathbf{M}_\mathcal{K}$, which in this case is simply a matrix, is extracted from

$$\bar{\mathbf{M}}_\mathcal{K} = \arg\min_{\tilde{\mathbf{M}}_\mathcal{K}} \left\| \mathbf{X}_1 - \tilde{\mathbf{M}}_\mathcal{K}\tilde{\mathbf{X}}_0 \right\|_F^2, \tag{6.1}$$

with

$$\tilde{\mathbf{z}}_k = \begin{bmatrix} \mathbf{z}_k \\ \mathbf{u}_k \end{bmatrix},$$

$$\tilde{\mathbf{X}}_0 = \left[\tilde{\mathbf{z}}_0, \tilde{\mathbf{z}}_1, \ldots, \tilde{\mathbf{z}}_{n_{s-1}}\right],$$

$$\mathbf{X}_1 = \left[\mathbf{z}_1, \mathbf{z}_2, \ldots, \mathbf{z}_{n_s}\right],$$

if stability problems do not arise. Note that in this case the model is composed of local matrices defining different linear maps in each set.

Quite often, an issue can appear because of the difficulties to learn stable models when constructing these dynamical systems. For this reason, in Section 2.5.3, a new methodology is proposed when using these techniques to guarantee that the obtained systems remain stable.

6.2.2 Enriching a physics-based model within the Hybrid Twin framework

Constructing a model $\mathbb{M}$ of the physical system from scratch is not the most valuable route as discussed in former works, cf. [Chinesta *et al.* 2020]. Purely data-driven, black-box models are not popular in industry, due to the lack of interpretability and guaranteed error estimators. Thus, a more valuable option consists of constructing corrections to physics-based models—if these provide unsatisfactory results—from an additive correction of this coarse prediction.

In fact, since the coarse model is expected to perform reasonably well for predicting the state of the system, bias will in general remain reasonably small. If this is true, the correction model will be much less nonlinear, and it will accept a more accurate description from the same amount of data.

Thus, we define the correction contribution $\mathbf{c}_k$ (or, equivalently, the model enrichment) as:

$$\mathbf{z}_k - \mathbf{z}_k^c = \mathbf{c}_k, \tag{6.2}$$

where $\mathbf{z}_k^c$ refers the model prediction.

Taking as a proof of concept a dynamic linear system with control inputs, the correction term is searched as:

$$\mathbf{c}_{k+1} = \mathbf{M}_c \mathbf{c}_k + \mathbf{M}_{uc} \mathbf{u}_k, \tag{6.3}$$

where $\mathbf{M}_c$ and $\mathbf{M}_{uc}$ are the matrices defining the time evolution of the correction term. Thus, the total response of the system is finally predicted by using

$$\mathbf{z}_{k+1} \approx \mathbf{z}_{k+1}^c + \mathbf{M}_c \mathbf{c}_k + \mathbf{M}_{uc} \mathbf{u}_k. \tag{6.4}$$

By taking into consideration that $\mathbf{z}^c$ is stable and integrated independently of the correction term, the stability condition of the system should apply just on the correction term.

In next section, the novel strategy proposed in Section 2.5.3 to guarantee the construction of stable systems with low computational cost is employed. In addition, this technique can be used either to build models from scratch or the correction term of the HT approach.

6.3 Application to a dynamical system: The aircraft hybrid twin

6.3.1 System to model and types of data.

The modeled system corresponds to an air distribution system of an aircraft and is characterized by eight variables defining the state of the system: six temperatures T_k^i, $i = 1, 2, \dots, 6$, and two pressures p_k^j, $j = 1, 2$. The model should also take into account three control variables u_k^q, $q = 1, 2, 3$, for each time instant k.

With the knowledge and experience of Dassault Aviation, two models are constructed with the help of the software Dymola [Dassault Systemes 2021]:

- A coarse model (CM). This model deliberately fails to provide accurate predictions due to over-simplification. It is important to note that in industry, this type of model is often physics-based (although this is not mandatory) but still requires an important computing time.
- A high-fidelity model that will therefore be considered as the ground truth (GT), which is consequently still more time consuming. This model is going to emulate in this work the real state of the system.

Due to confidentiality issues, Dassault Aviation simulated different flights with both models and provided three different types of pseudo-experimental data which are employed in the present work:

- The CM data. These data correspond to the predictions of the CM for the given set of simulated flights.
- The GT data. These data correspond to the predictions of the GT model. It will be considered in the present work for evaluation purposes.
- Pseudo-experimental data (PED). A white noise is added artificially to the GT data. Consequently, these data will emulate experimental measurements including experimental errors.

Additionally, in Figures 6.1 and 6.2, a comparison is shown between the three types of data (CM, GT and PED) for a given flight simulation.

At this point, three different approaches were tested:

- Extracting a model from scratch from GT data (Section 6.3.2).
- Obtaining a model from scratch using the noisy pseudo-experimental data (PED) (Section 6.3.3).
- Extracting a correction term to enrich the CM, thus constructing the Hybrid Twin (Section 6.3.4).

Advantages and weaknesses of each approach will be discussed. The mathematical details of the CM anf GT models are omitted for confidentiality reasons. However, this is not important for presenting, discussing and employing the proposed methodology and, moreover, a successful outcome will be a sign that the proposed approach can address current industrial needs.

6.3.2 Extracting a model from scratch using the GT data

6.3.2.1 Procedure and results

It is interesting to analyse whether the proposed approach presented in Section 2.5.3 is able to learn a model from scratch employing the GT data. Therefore, this section is focused on this goal. In next sections, it will be analysed if the approach is able to obtain similar results when learning in the presence of noise (PED data) and finally, we will see the advantages of using the hybrid twin rational instead of the complete data-driven approach.

The technique is sketched in the diagram of Figure 6.3. As it can be noticed, the system is characterized by eight variables defining the state of the system (six temperatures T_k^i,

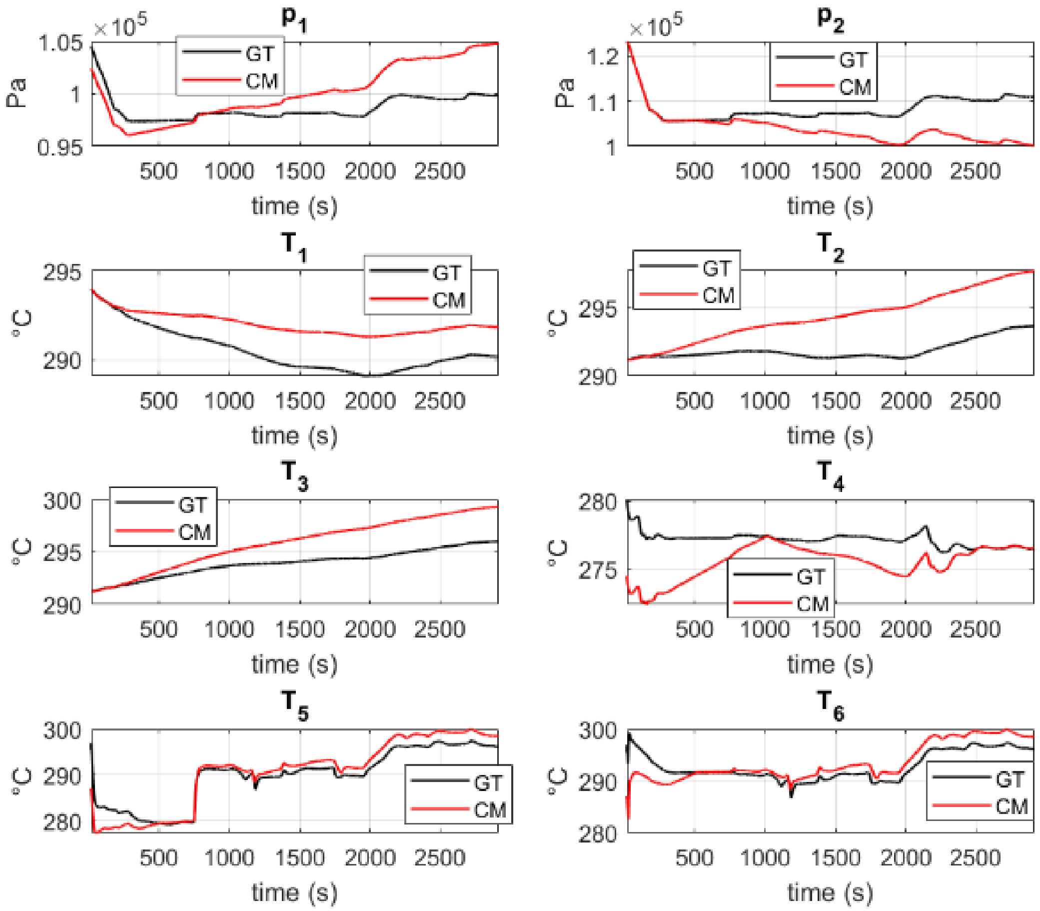

Figure 6.1 – Comparison of the state evolution $\mathbf{z}(t) = [p_1, p_2, T_1, T_2, T_3, T_4, T_5, T_6]$ for a given flight between the Coarse model (CM) and the Ground truth (GT)

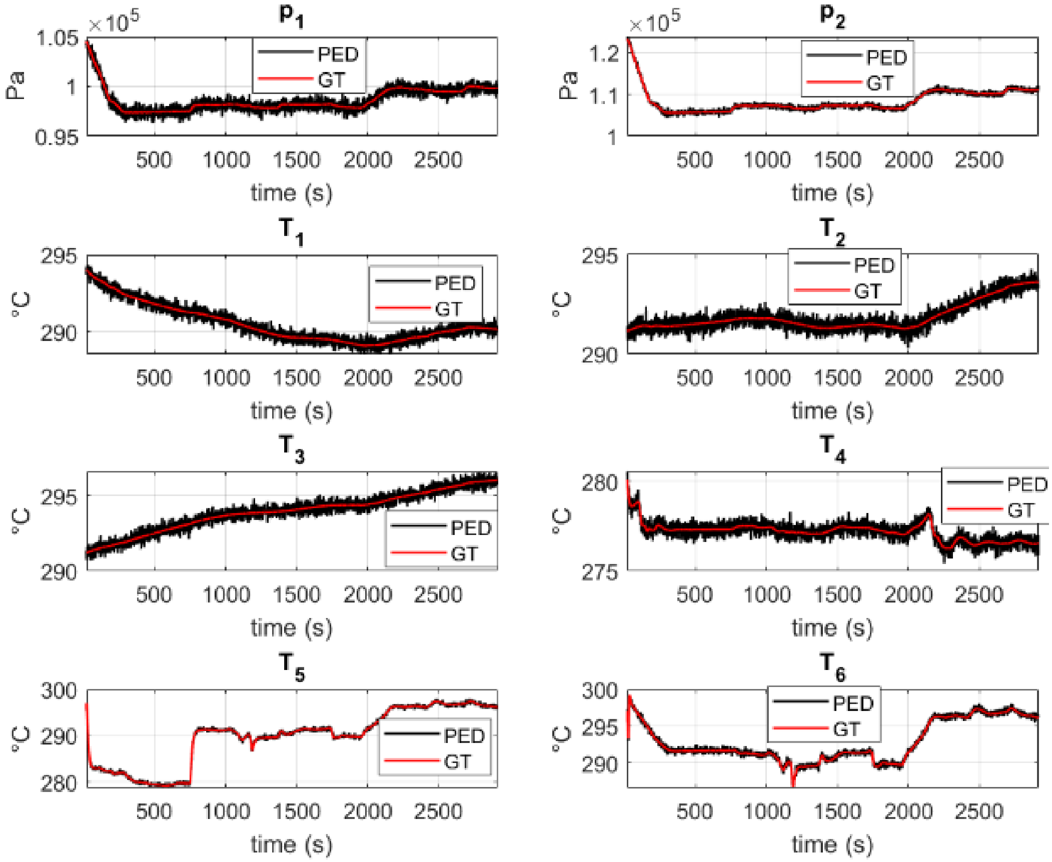

Figure 6.2 – Comparison of the system evolution, $\mathbf{z}(t) = [p_1, p_2, T_1, T_2, T_3, T_4, T_5, T_6]$, for a given flight between the Ground truth (GT) and the pseudo-experimental (noisy) data, PED

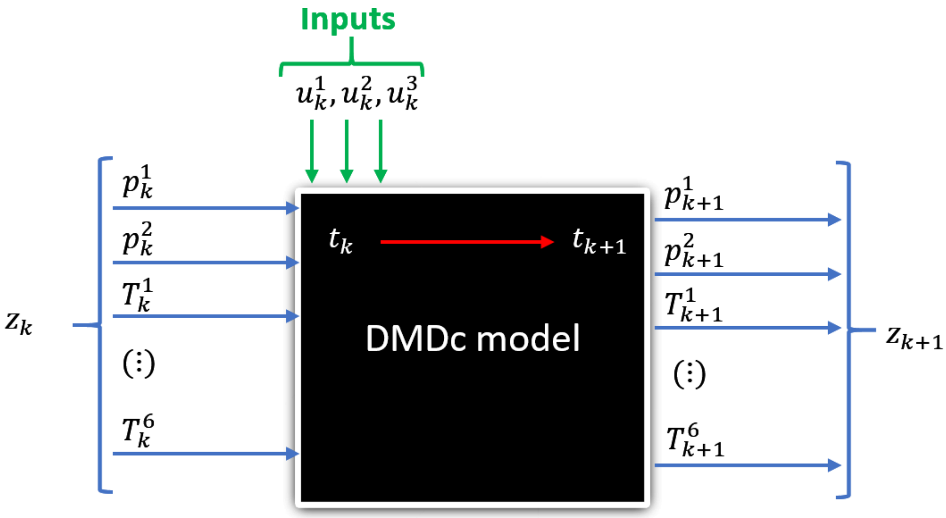

Figure 6.3 – Diagram illustrating the inputs and the state vector of the proposed DMDc model to reproduce the pruned data of the system.

$i = 1, 2, \ldots, 6$, and two pressures p_k^j, $j = 1, 2$) and three control variables u_k^q, $q = 1, 2, 3$ for each time instant k.

In the present case, it is considered the simplest modeling approach in which the model consists in a simple linear application that maps the present state and control parameters $\mathbf{z}_k$ and $\mathbf{u}_k$, respectively, onto the next system state $\mathbf{z}_{k+1}$.

The available data consist in $\mathtt{F} = 82$ flights, each one leading to eight time series $\mathbf{z}_k^{\mathtt{f}}$, with $\mathtt{f} = 1, \ldots, \mathtt{F}$, and $k = 1, \ldots, \mathtt{n}^{\mathtt{f}}$ (the number of collected data depends on the flight, these having different duration). It is important to note that, for any flight $t_{k+1} - t_k = \Delta t$, with constant Δt, for any component state and any flight.

The extended state is defined as shown in Section 2.5.3:

$$\tilde{\mathbf{z}}_k = \begin{pmatrix} \mathbf{z}_k \\ \mathbf{u}_k \end{pmatrix}. \tag{6.5}$$

To learn the model, we select arbitrarily two flights from the $\mathtt{F}$ available, $\mathtt{f} = \mathtt{r}$ and $\mathtt{f} = \mathtt{s}$, and define the training matrices

$$\tilde{\mathbf{X}}_0 = \begin{pmatrix} \mathbf{z}_0^{\mathtt{r}} & \cdots & \mathbf{z}_{\mathtt{n}^{\mathtt{r}}-1}^{\mathtt{r}} & \mathbf{z}_0^{\mathtt{s}} & \cdots & \mathbf{z}_{\mathtt{n}^{\mathtt{s}}-1}^{\mathtt{s}} \\ \mathbf{u}_0^{\mathtt{r}} & \cdots & \mathbf{u}_{\mathtt{n}^{\mathtt{r}}-1}^{\mathtt{r}} & \mathbf{u}_0^{\mathtt{s}} & \cdots & \mathbf{u}_{\mathtt{n}^{\mathtt{s}}-1}^{\mathtt{s}} \end{pmatrix}, \tag{6.6}$$

and

$$\mathbf{X}_1 = \begin{bmatrix} \mathbf{z}_1^{\mathtt{r}} & \cdots & \mathbf{z}_{\mathtt{n}^{\mathtt{r}}}^{\mathtt{r}} & \mathbf{z}_1^{\mathtt{s}} & \cdots & \mathbf{z}_{\mathtt{n}^{\mathtt{s}}}^{\mathtt{s}} \end{bmatrix}, \tag{6.7}$$

that allows extracting the model by solving the problem indicated in Eq. (2.27) or its reduced counterpart (2.28).

Then, as soon as the model is extracted, we proceed to predict the state evolution for each one of the $\mathtt{F}$ flights, from their initial states, by simply writing at each time t_k, $k = 1, \ldots, \mathtt{n}^{\mathtt{f}}$,

$$\tilde{\mathbf{z}}_k^{\mathtt{f}} = \begin{pmatrix} \mathbf{z}_k^{\mathtt{f}} \\ \mathbf{u}_k^{\mathtt{f}} \end{pmatrix}, \tag{6.8}$$

and applying the updating of Equations (2.22) or (2.28). Training data are composed of two flights while the other eighty are used to test the performance of the present approach.

Figure 6.4 compares the predicted states at each time instant by integrating the just unveiled model from the initial condition. It employs a GT data series corresponding to one particular, previously unseen flight. It can be observed that the proposed approach achieves an excellent agreement for variables p_1, p_2, T_1, T_2, T_3 and T_4.

On the other hand, although the error in variables T_5 and T_6 is larger it achieves to follow the general trend, despite the fast time evolutions that these variables exhibit. The same tendency is observed in all the flights as Fig. 6.5 proves. To better capture the fast evolutions of these two variables, the procedure described in Section 2.5.4 for addressing nonlinear behaviors could be employed. However, in this work it is preferred to improve the accuracy in the prediction of these special variables by employing a Hybrid approach, for the reasons exposed in Section 6.3.4.

In Figure 6.6, it is observed that a similar accuracy is obtained for more than 85 % of the flights in the testing set (concerning variables p_1, p_2, T_1 and T_2). A similar conclusion follows from Figure 6.7 for variables T_3 and T_4. Therefore, it is concluded that the model has a good ability for generalization taking into consideration that just two flights are considered in the training.

However, the error in variables T_5 and T_6 can reach high values in a considerable part of the testing set. To adress that, the HT rationale will be proposed and discussed.

Before that, we will see what happens if stability is not enforced when extracting the GT model from scratch in the following subsection 6.3.2.2 as well as the improvements of the proposed procedure.

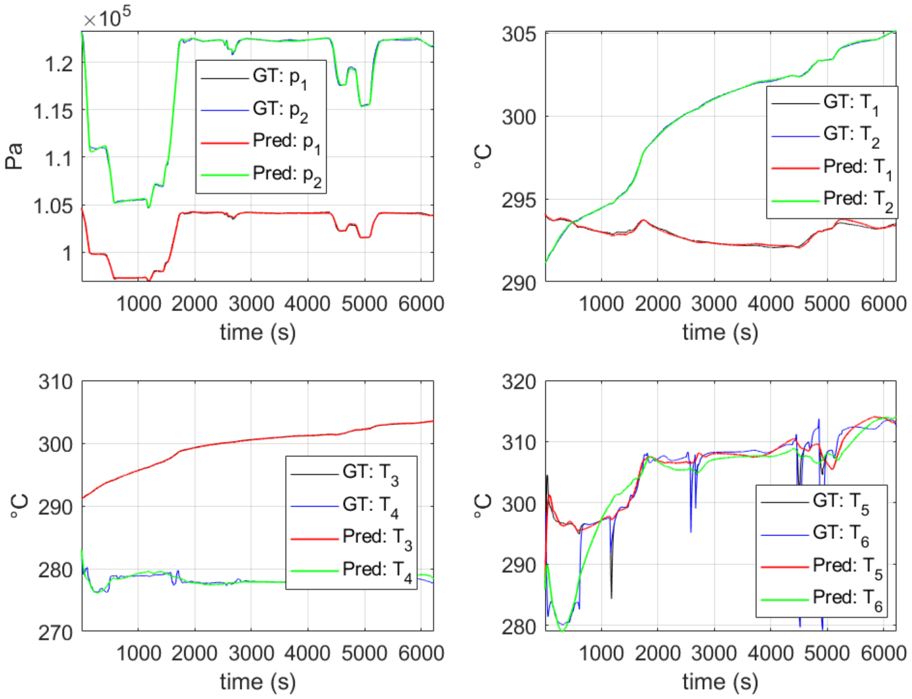

Figure 6.4 – Prediction of the GT data using the proposed technique for a flight which is not used in the training set. “GT" refers to GT data series described in Section 6.3.1 and “Pred" refers to the stabilized DMDc model obtained with the proposed approach discussed in Section 2.5.3

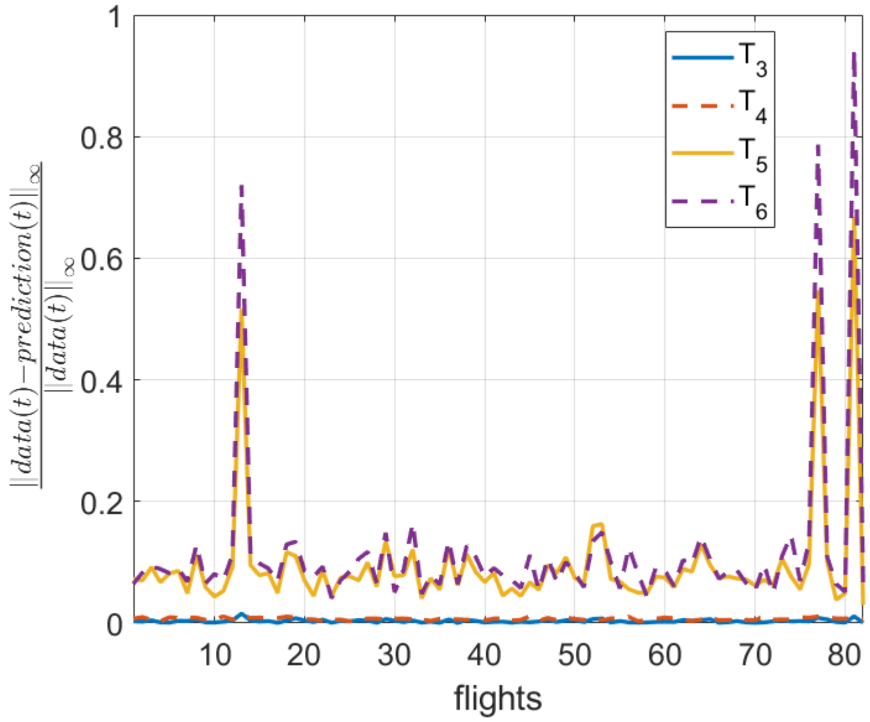

Figure 6.5 – Error in the prediction of T_3, T_4, T_5 and T_6 for different flights which are not in the training set. The prediction error in variables T_5 and T_6 is higher than the other ones due to their fast time evolution

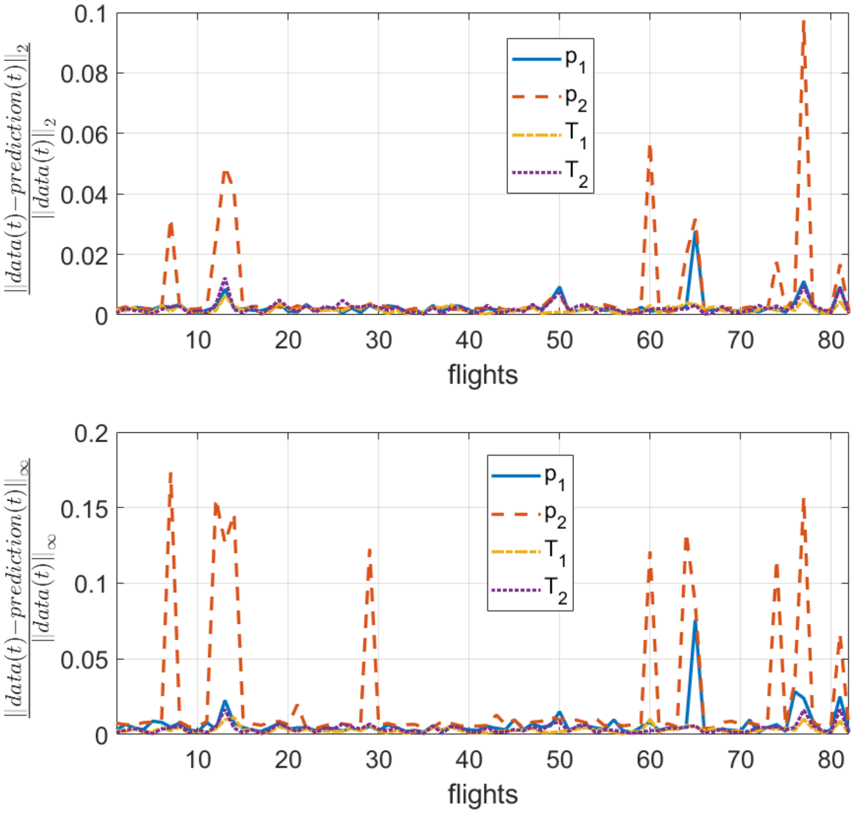

Figure 6.6 – Error in the prediction of p_1, p_2, T_1 and T_2 of the proposed technique for lights which are not in the training set

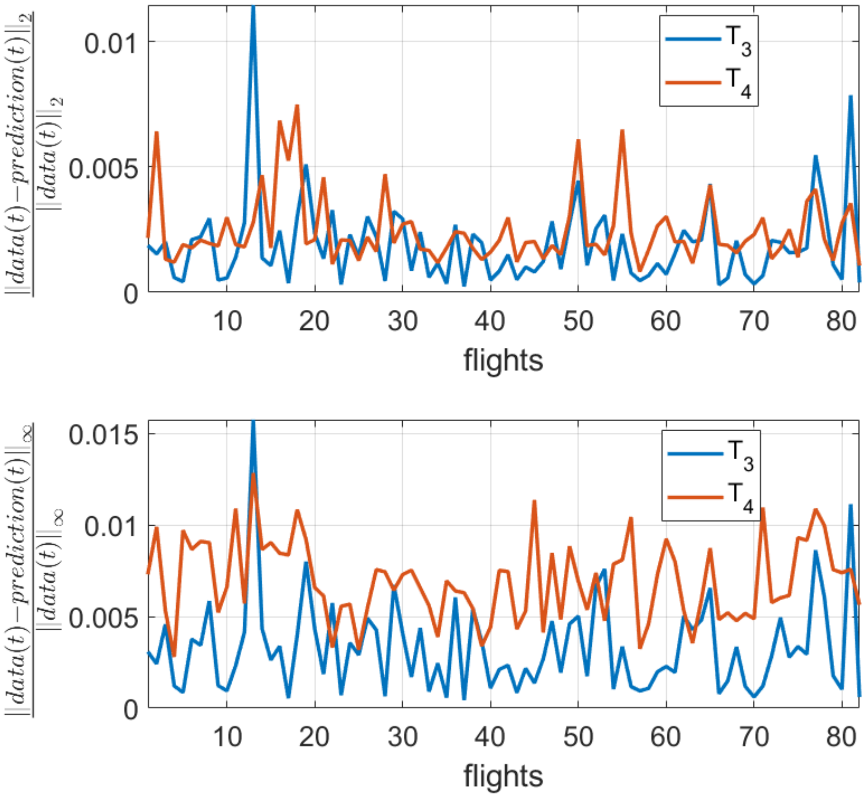

Figure 6.7 – Error in the prediction of T_3 and T_4 of the proposed technique for flights which are not in the training set

6.3.2.2 Checking explicitly the improvements of the proposed approach to learn stable systems. Example when proceeding from the GT data.

In the above Section, the results when modelling the GT data were shown when using the stabilization procedure for the DMDc proposed in this work. However, it is interesting to analyze whats happens when using other algorithms or by simply using standard procedures to observe the benefits of the proposed stabilization.

To this end, the GT data for a particular flight is considered. The time evolution of the system can be observed in Figure 6.8.

The first objective is to see if we can approximate the dynamics of Figure 6.8 by constructing a standard DMDc model without stabilizing it. Moreover, we are interested in observing if stability issues arise.

Therefore, a model is constructed following the DMDc procedure with the state vector and inputs exposed in Section 6.3.2.1.

As shown in Figure 6.9 below, the DMDc model reports stability issues giving useless predictions.

Nevertheless, by applying the proposed stabilization approach to the DMDc algorithm (as discussed in Section 2.5.3), a stable model is easily obtained quick and fast. The flight predicted by the proposed approach is shown in Figure 6.10. It is worth noting the great improvement observed by comparing the standard non-stabilized DMDc model (Figure 6.9) with the stabilized one (Figure 6.10) able to capture complex dynamics while completely overcoming the stability issues.

Now, in the next section, we will examine the possibility of unveiling an accurate model from noisy data. In this way, two important aspects will be analysed: the interest of employing a Hybrid Twin approach and the ability of the proposed technique to filter noise.

6.3.3 Extracting a model from scratch using noisy data (PED).

In this section, the goal is to unveil a model from scratch using noisy data. This will allow us to study the robustness of the approach in the filtering process.

After applying the technique in different flights and studying the reconstruction error by considering different extended states $\tilde{\mathbf{z}}$, the proposed model is composed of:

$$\tilde{\mathbf{z}}_k = \begin{pmatrix} \mathbf{z}_k \\ \mathbf{u}_k \\ \mathbf{u}_{k-1} \\ \boldsymbol{\omega}_k \\ \mathbf{W}_k \end{pmatrix}, \tag{6.9}$$

where:

$$\boldsymbol{\omega}_k = \sum_{i=0}^{k} \mathbf{u}_i (t_{i+1} - t_i),$$

and

$$\mathbf{W}_k = \sum_{i=0}^{k} \boldsymbol{\omega}_i (t_{i+1} - t_i).$$

The same methodology of the previous Section is applied, by using the new extended states $\tilde{\mathbf{z}}$. This way, the more complex behavior of the noisy data can be addressed. In this case, nine flights of different duration are used for the training set.

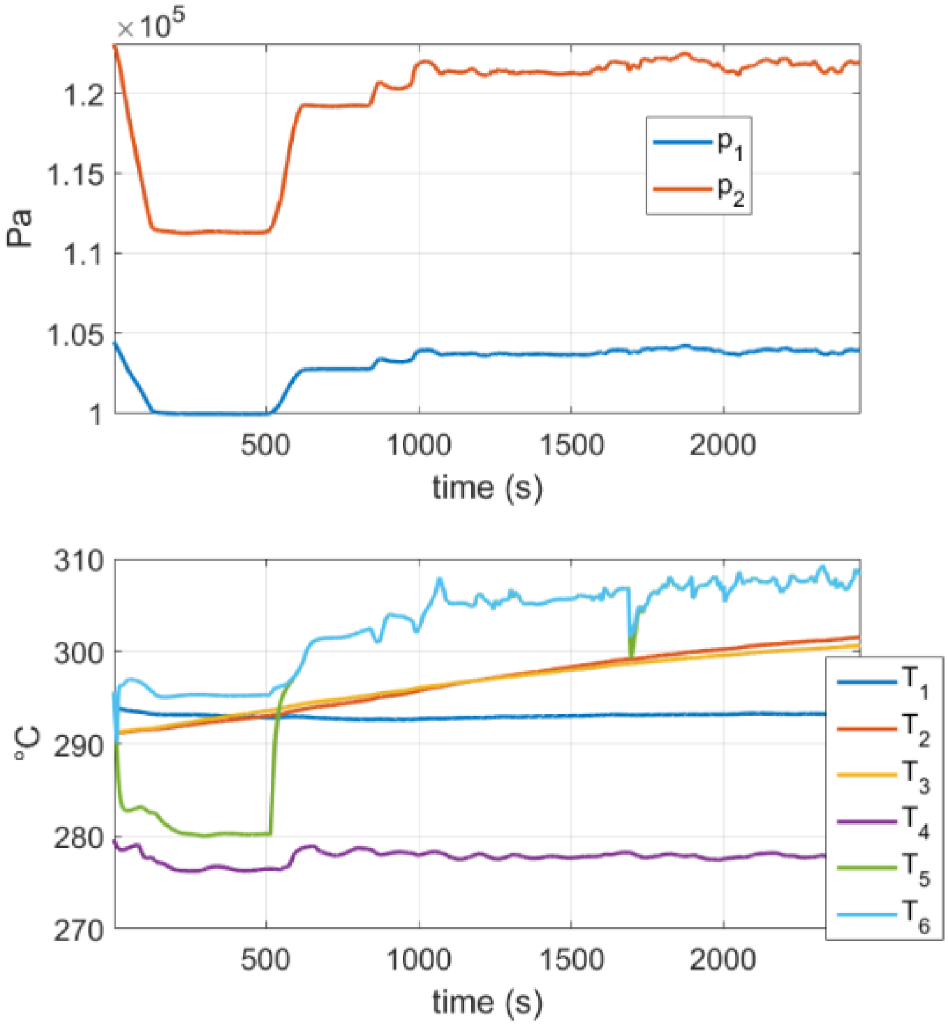

Figure 6.8 – GT data for the example in Section 6.3.2.2

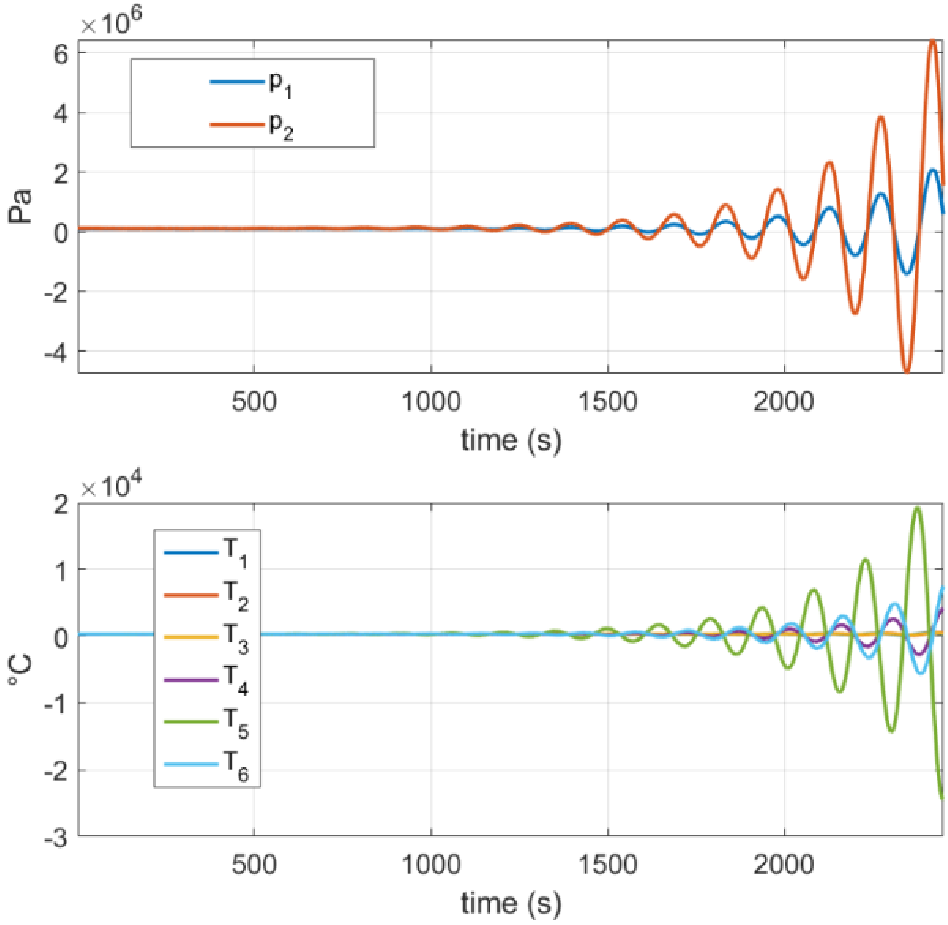

Figure 6.9 – Prediction $\mathbf{z}(t) = [p_1, p_2, T_1, T_2, T_3, T_4, T_5, T_6]$ of the GT obtained through DMDc. This prediction tries to reproduce the flight of Figure 6.8 but fails to provide with stable results

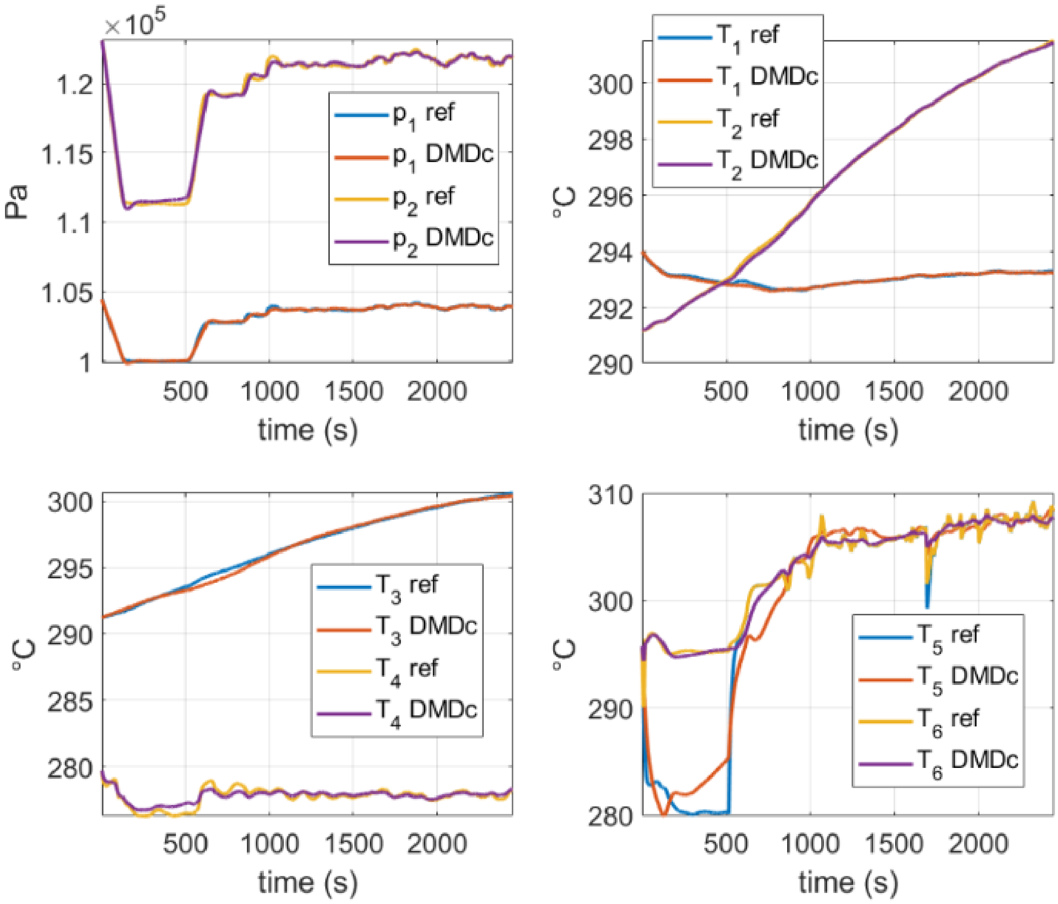

Figure 6.10 – Comparison between the reference dynamics of Figure 6.8 and the prediction of the modified, stable DMDc model. Huge improvements are observed when comparing with Figure 6.9. The state vector of the system is $\mathbf{z}(t) = [p_1, p_2, T_1, T_2, T_3, T_4, T_5, T_6]$

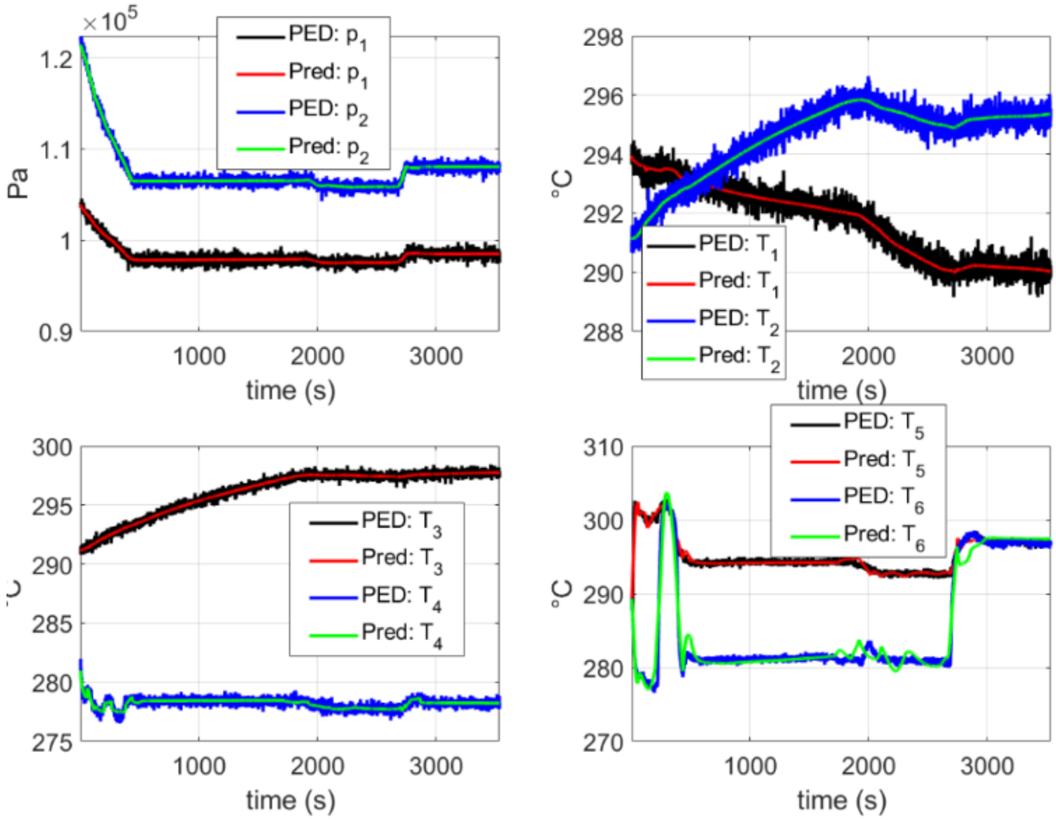

Figure 6.11 – Comparison between the model obtained from scratch using PED data and the PED data itself. In this figure, the reconstruction of a flight contained in the training set is shown. “PED" refers to the pseudo-experimental data with noise described in Section 6.3.1 and “Pred" refers to the stabilized DMDc model obtained with the proposed approach discussed in Section 2.5.3. It can be observed that an excellent agreement is obtained for every variable while filtering the noise

In Fig. 6.11, a comparison is shown between the dynamics predicted by the DMDc model obtained from scratch using the PED and the PED itself (see Section 6.3.1), for a flight contained in the training set. Here, it is observed that the model can capture the dynamics of the system with an excellent accuracy, by just employing the initial state of the system and the corresponding control inputs while filtering the noise contained in the training data.

In Fig. 6.12 a comparison is shown between the dynamics predicted by the DMDc model obtained from scratch using the PED and the PED itself (see Section 6.3.1), for a flight contained in the testing set (never considered in the model construction). In these plots, it is shown that a good agreement is obtained for all the variables with the exception of T_5 and T_6. Similar results are reported in the other flights of the testing set.

Variables T_5 and T_6 are more challenging to predict because of their fast time evolution. Nevertheless, we are going to deal with them in the next section. Therefore, the Hybrid Twin concept, which follows, is expected leading to more accurate results.

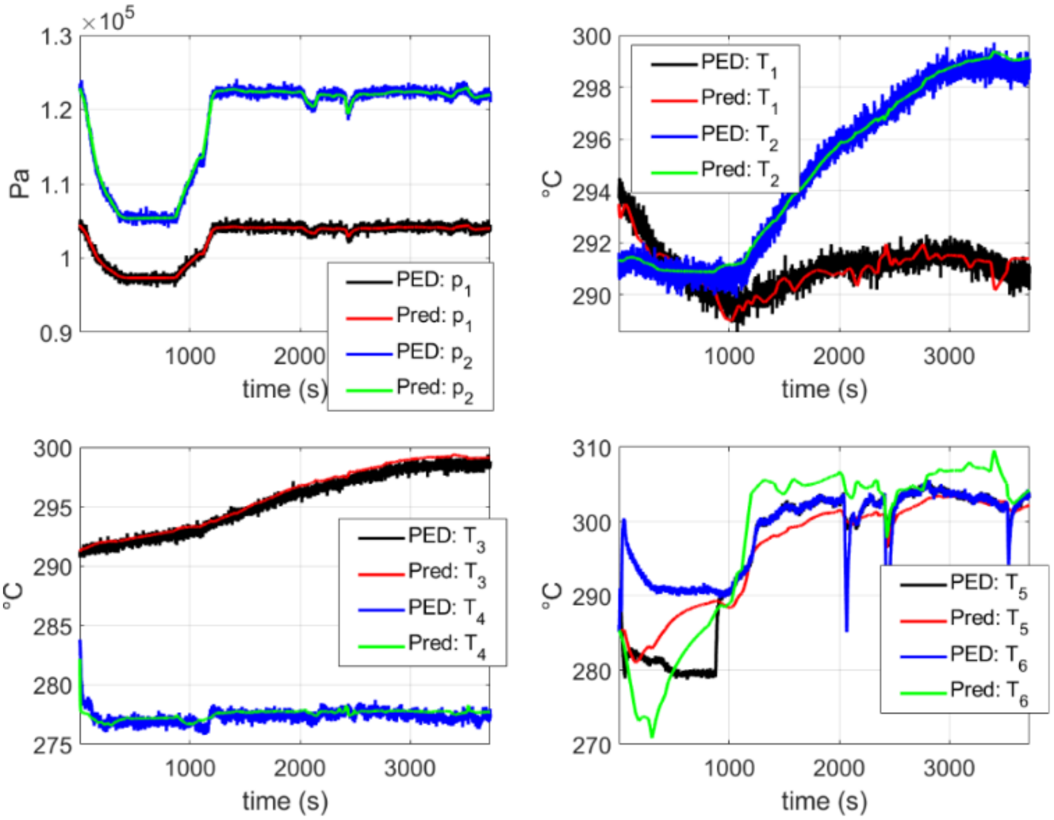

Figure 6.12 – Comparison between the model obtained from scratch using PED data and the PED data itself. In this figure, the reconstruction of a flight which is not contained in the training set is shown. “PED" refers to the pseudo-experimental data with noise described in Section 6.3.1 and “Pred" refers to the stabilized DMDc model obtained with the proposed approach discussed in Section 2.5.3. It can be observed that a good agreement is obtained for all the variables with the exception of T_5 and T_6

6.3.4 Extracting the correction model. Hybrid Twin paradigm.

As discussed in Section 6.2.2, constructing a model of the real system from scratch is not the most valuable route when addressing complex systems. For the system analyzed in the present work, outputs p_1, p_2, T_1, T_2, T_3 and T_4 are predicted to a great accuracy for the approaches shown in Sections 6.3.2 and 6.3.3. On the other hand, outputs T_5 and T_6 present difficulties. In these cases, an interesting option consists in expressing the state of the system from an additive correction of the coarse model. Therefore, in this case, the proposed model is going to capture just the ignorance that the coarse model contains.

One of the advantages of this concept is that the main response is provided by the physics-based model, thus guaranteeing that the model is going to exhibit a behavior coherent with the physical phenomenon under scrutiny as well as being explained by practitioners. In addition, the part of the response which has difficulties in being modeled—for instance, the appearance of degradation of the system—can be approximated by the data-driven model.

The Hybrid Twin (HT) concept is illustrated in Figure 6.13. Note that only the first measurement is mandatory to run the model coined as the $\Delta\mathbb{M}$. Therefore, knowing the initial state of the system, the real response can be reproduced adding the correction model to the CM without further measurements.

Again, the extended state $\Delta\tilde{\mathbf{z}}$ for the discrepancy model is:

$$\Delta\tilde{\mathbf{z}}_k = \begin{pmatrix} \Delta\mathbf{z}_k \\ \mathbf{u}_k \\ \mathbf{u}_{k-1} \\ \boldsymbol{\omega}_k \\ \mathbf{W}_k \end{pmatrix}. \tag{6.10}$$

Nine flights are considered in the training set. As expected for a real-life application, the measured data (that is, the PED) is employed to obtain the discrepancy to be modeled within the HT concept.

Figures 6.14, 6.15 and 6.16 are obtained by just integrating from the initial state of the system and by employing and enriching the CM prediction without any further measurement. This proves the excellent agreement that can be achieved within the HT rationale.

In Fig. 6.14, a comparison is shown between the HT prediction and the PED for a previously unseen flight. In these plots, an excellent agreement is noticed for all the variables. Moreover, predictions filter the noisy measurements.

An error criterion is defined to compare the prediction of the HT approach with the accuracy of the measuring instruments:

$$\mathrm{err}_i(t) = \frac{|z_i^{\mathrm{GT}}(t) - z_i^{HT}(t)|}{\Delta z_i^{\max,\mathrm{GT}}}, \tag{6.11}$$

$$\mathrm{err}_{\mathrm{meas}}^{\max} = \frac{\max\left(|z_i^{\mathrm{GT}} - z_i^{m}|\right)}{\Delta z_i^{\max,\mathrm{GT}}}, \tag{6.12}$$

where:

- i refers to the i-th variable z_i of the state vector.
- z_i^{HT} is the predicted value of the HT for z_i.

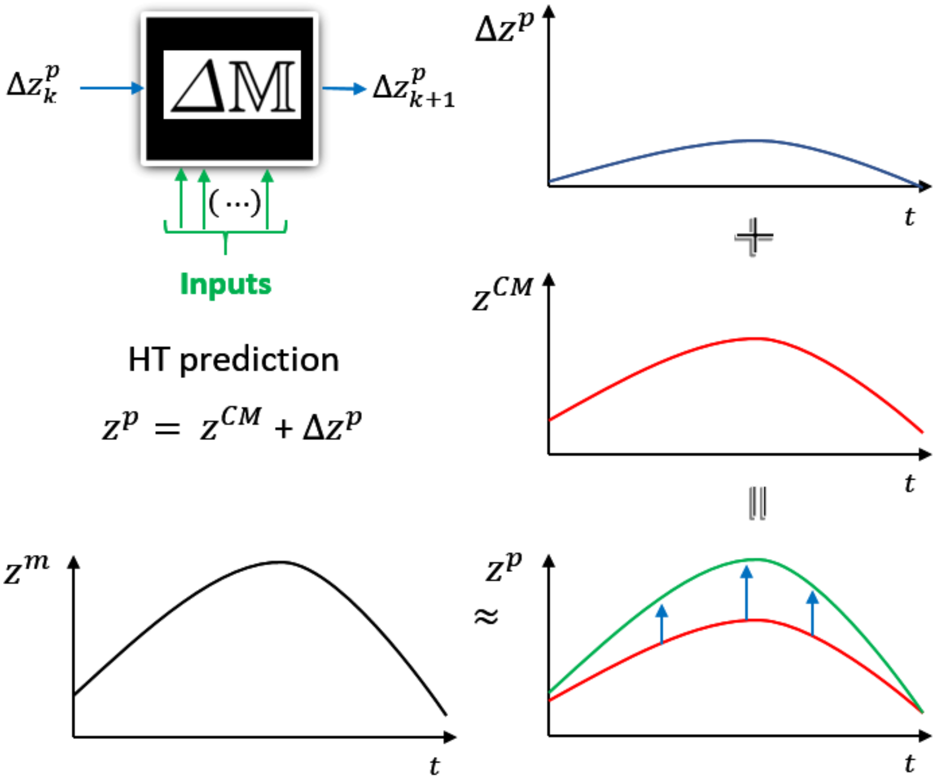

Figure 6.13 – Diagram illustrating the HT concept. The HT is able to correct the discrepancy between the coarse model (CM) and the pseudo-experimental data (denoted by a superscript m, that is, the PED). Its prediction is here denoted by a superscript HT whereas the enrichment model is denoted by Δz. Note that z^m can be filtered to have a better estimate of the GT when applying the HT approach.

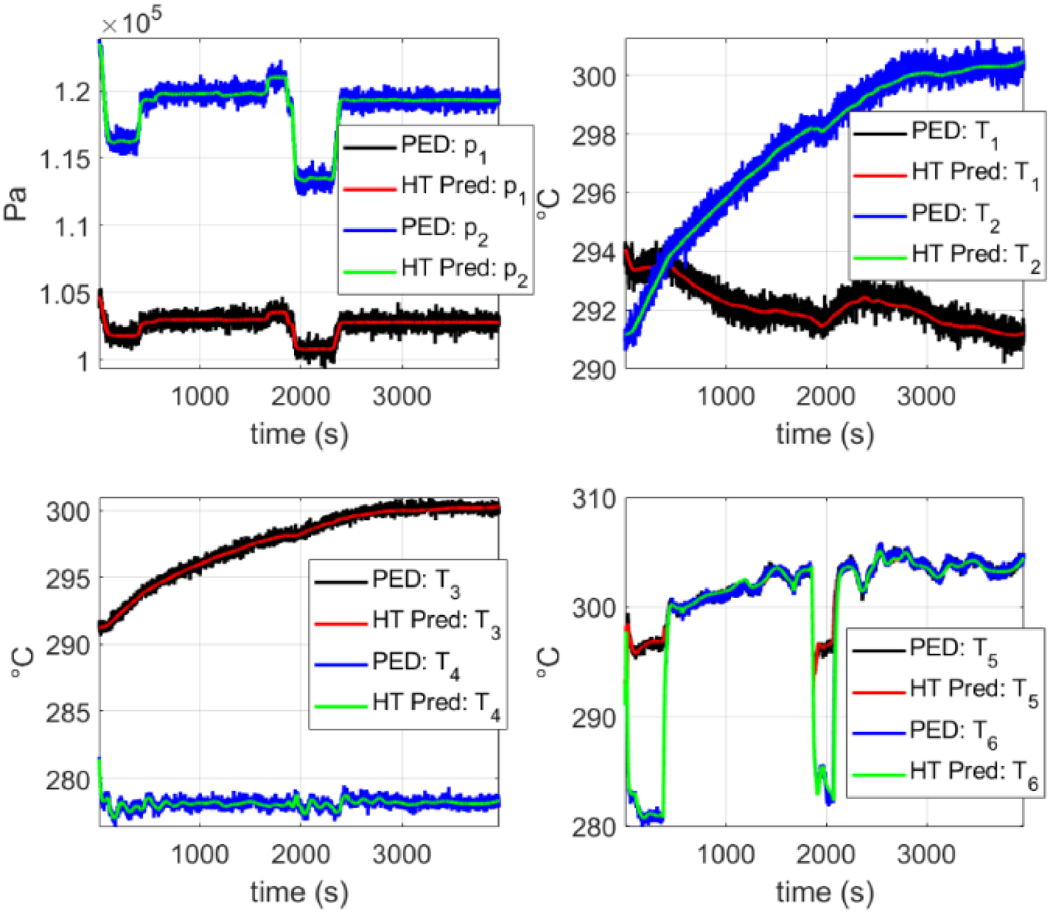

Figure 6.14 – Prediction of the HT approach considering a flight in the testing set. “PED" refers to the pseudo-experimental data with noise described in Section 6.3.1 and “HT Pred" refers to the HT approach whose correction term corresponds to a stabilized DMDc model obtained with the methodology discussed in Section 2.5.3. The correction term was constructed using the PED. It can be observed that an excellent agreement is obtained for all the variables

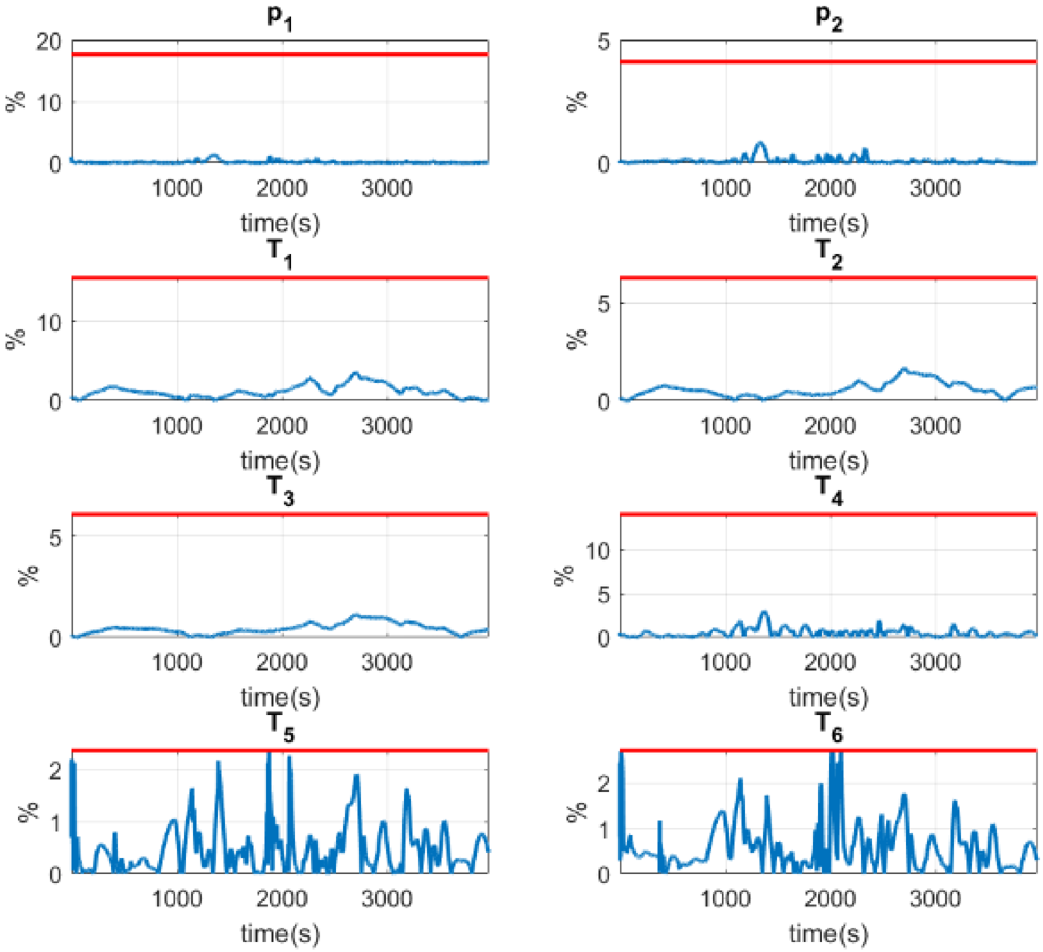

Figure 6.15 – Error of the HT approach (blue line) considering a flight which is not used for the training. The red line refers to the maximum error in the pseudo measurements (PED). The error criterion is defined in Eqs (6.11) (blue line) and (6.12) (red line)

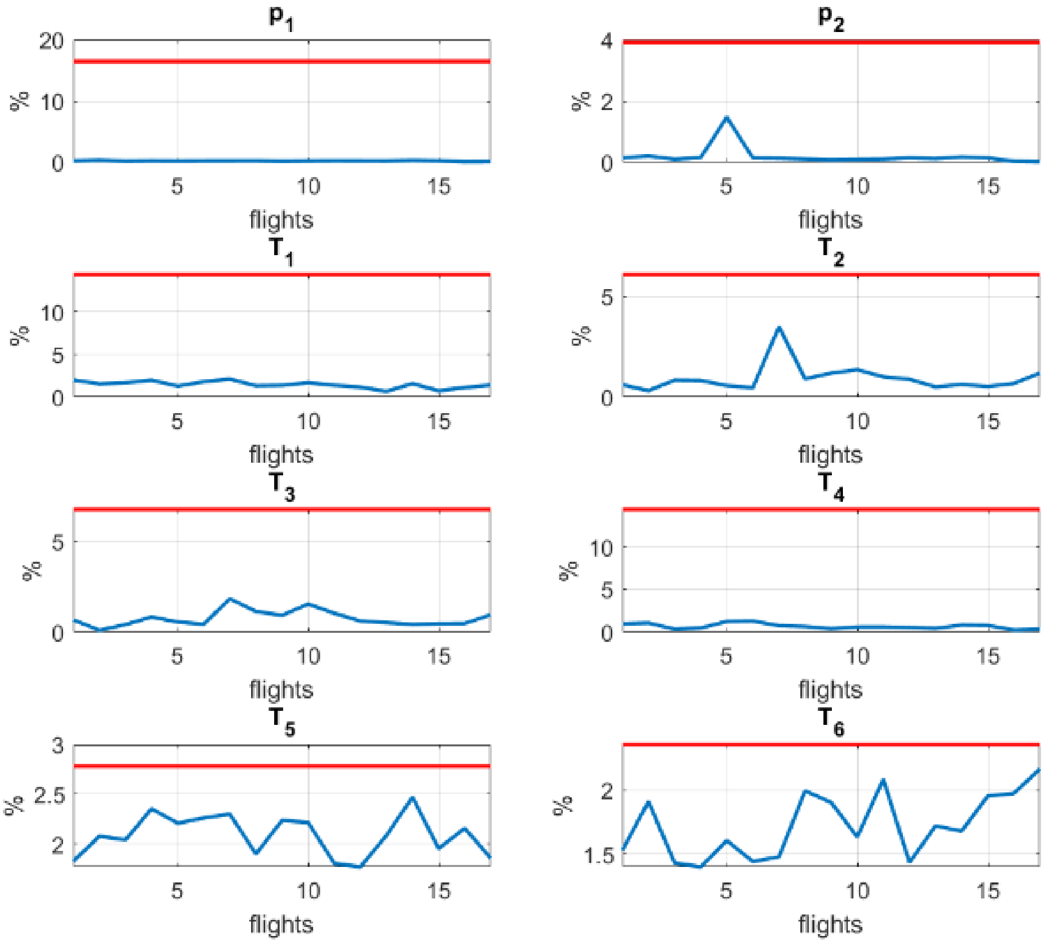

Figure 6.16 – Error of the HT approach (blue line) considering different flights which are not used for the training. The red line refers to the maximum error in the pseudo measurements. The error assigned to a flight is the mean value of the error defined in Eq. (6.11)

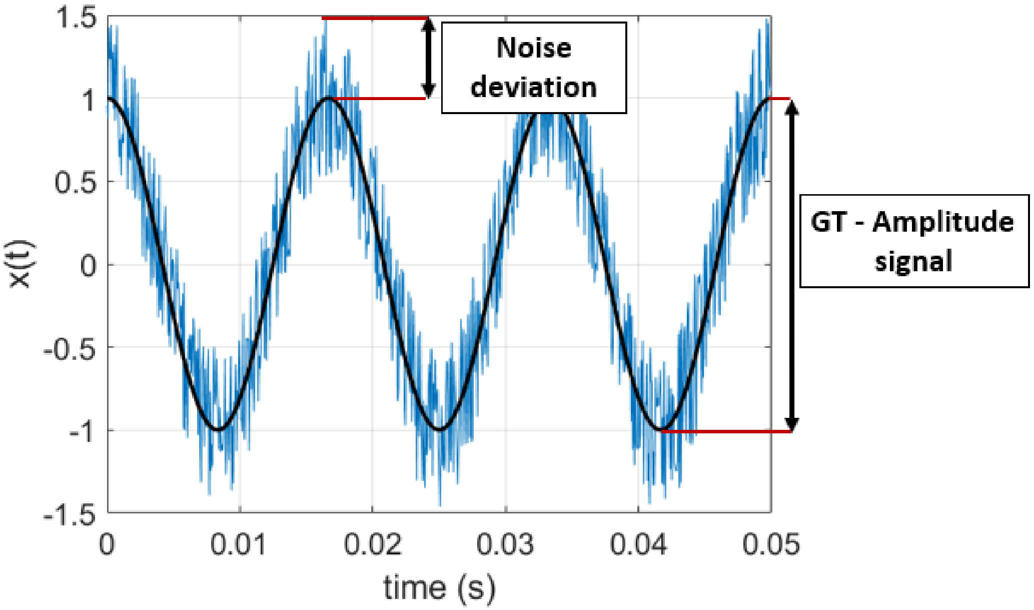

Figure 6.17 – Sine wave with noise. In the plot, the maximum variation of the signal is indicated as well as the deviation caused by the noise to illustrate the concept used to define the error criterion

- z_i^m is the measured value of z_i. These data include the corresponding noise. In other words, these data are the PED.

- z_i^{GT} is the true value of z_i which is theoretically unknown and cannot be accessed by an observer in a real application. This value is used for evaluation purposes.

- $\Delta z_i^{\max,\mathrm{GT}}$ is the difference between the maximum and the minimum value of z_i^{GT} considering all the flights.

Using Eqs. (6.11) and (6.12), it is possible to compare the accuracy of the HT with the one obtained by measuring the data (that is, the PED). Moreover, the relative errors are computed taking as a base the maximum variation of each variable when regarding all the available flights. Fig. 6.17 shows the maximum variation of a signal as well as the deviation caused by the noise to illustrate the concept.

Observing Figs. 6.15 and 6.16, we can confirm that the HT concept allow us to improve, not only the accuracy of the CM but the accuracy of the measuring instruments regardless of whether or not flights come from training by filtering the noise. In this way, two goals are achieved at the same time: enriching the CM by learning the difference with the measured data while filtering the noise.

Therefore, the HT concept is a valuable route to enrich physics-based models with data-driven corrections. It is important to note that for HT to be applied, the CM must not be extremely bad, since in this case a direct data-driven or reduced-order modeling approach would be preferred (because there is no point in correcting such a model).

6.4 Conclusions

This work presents a fast and efficient methodology, covering several variants to learn dynamical models while guaranteeing a low computational cost as well as the achievement of stable dynamical time integrations. This technique was used with success to predict a practical scenario under the HT rationale, being able to impose stability in the correction term. In addition, the proposed technique filters noise improving the knowledge of the system state.

We also compared the proposed technique in two scenarios: *when it is employed to obtain models from scratch* versus *when it is employed for an enrichment in the HT rationale.*

We concluded that for more complex systems the HT paradigm seems advantageous for two reasons. The first one is that more complex behaviors can be captured (as variables T_5 and T_6). The second one is that, in the HT, the main response is relied on the physics-based model thus guaranteeing that the model is going to exhibit a behavior coherent with the physical phenomenon at hand. Consequently, just the part of the response which has difficulties in being modeled is carried out by the data-driven model, for instance, degradation or aging.

CHAPTER 7

From ROM of electrochemistry to AI-based battery digital and hybrid twin

---

Abstract Lithium-ion batteries are widely used in the automobile industry (electric vehicles and hybrid electric vehicles) due to their high energy and power density. However, this raises new safety and reliability challenges which require development of novel sophisticated Battery Management Systems (BMS). A BMS ensures the safe and reliable operation of a battery pack and to realize it a model must be solved. However, current BMSs are not adapted to the specifications of the automotive industry, as they are unable to give accurate results at real-time rates and during a wide operation range. For this reason, the main focus of this work is to develop a Hybrid Twin, as introduced throughout this dissertation, so as to meet the requirements of the new generation of BMS. To achieve this, three Reduced Order Model (ROM) techniques are applied to the most commonly used physics-based models, each one for a different range of application. In addition to the above, an innovative planning algorithm is developed to make decisions based on predictions of the whole EV, taking into consideration the fast and accurate predictions of the proposed ROMs. Furthermore, the algorithm is also capable of proposing changes in the driving behavior if it detects that battery problems can arise.

Contents

7.1 Introduction 167
    7.1.1 Chapter overview 167
    7.1.2 Topic introduction and chapter structure 168
7.2 Electrochemical model: Newman's P2D model 170
    7.2.1 Newman's P2D model 170
    7.2.2 Definitions of the State of Charge (SoC) 174
7.3 Solving Newman's P2D model 175
7.4 Proper Orthogonal Decomposition of the P2D model 176
    7.4.1 Reasons to use the POD 176
    7.4.2 POD of the electrochemical model 178
    7.4.3 Results 180
7.5 PGD regression. Learning the cell behavior from data . . . 184
    7.5.1 Introduction 184
    7.5.2 Proposed model 184
    7.5.3 Results 187
7.6 Innovative planning algorithm with EV simulation and results 197
    7.6.1 Introduction 197

7.6.2 Constructing a digital twin of the electric vehicle system . . . 197
7.6.3 Adapting driving behaviour in function of an accurate and fast computation of battery needs 202
7.6.4 Algorithm to select the best itinerary 210
7.6.5 BMS: cell balancing example 213
7.6.6 Summary results 216
7.7 Constructing a hybrid twin 216
7.7.1 Introduction 216
7.7.2 Dictionary Model for the Electrochemical Model: Correcting the gap 216
7.7.3 Results 218
7.8 Conclusions 228

7.1 Introduction

7.1.1 Chapter overview

This chapter address an important industrial application nowadays: the need of fast an accurate models for lithium-ion batteries. European projects strategically launched by the European Comission, such as Batteries Europe [Alliance 2019], are a sign of the great importance of this topic today.

In particular, three Reduced Order Model (ROM) techniques are applied to the most commonly used physics-based models, each one for a different range of application.

First, a POD model is used to greatly reduce the simulation time and the computational effort for the Newman's pseudo-2D cell model, while maintaining its accuracy. In this way, cell design, optimization of parameters, and simulation of battery packs can be done while saving time and computational resources. In addition, its real-time performance has been studied.

Next, a regression model is constructed from data by using the sparse-Proper Generalized Decomposition (s-PGD). It is shown that it achieves real-time performance for the whole Electric Vehicle (EV) system with a battery pack. In addition, this regression model can be used in a BMS without issues because of the simple algebraic expression obtained. Thanks to that, an innovative planning algorithm is developed to make decisions based on predictions of the whole EV, taking into consideration the fast and accurate s-PGD model. Furthermore, the algorithm is also capable of proposing changes in the driving behavior if it detects that battery problems can arise.

Finally, the last ROM is a data-driven model based on the novel hybridation techniques of Chapter 2. It is developed to extract an on-line model that corrects the gap between prediction and measurement, thus constructing the first (to our knowledge) hybrid twin of a Li-ion battery able to self-correct from data. In addition, thanks to this model, the above gap is corrected during the driving process, taking into consideration real-time restrictions.

Now, in Section 7.1.2, the topic and the content is introduced in detail as well as the structure of the chapter.

This chapter and all the results presented in it correspond to the published papers:

- A. Sancarlos, M. Cameron, A. Abel, E. Cueto, J.L. Duval, F. Chinesta, "From ROM of Electrochemistry to AI-Based Battery Digital and Hybrid Twin," *Archives of Computational Methods in Engineering* , vol. 28, pp. 979–1015, 2021. DOI: https://doi.org/10.1007/s11831-020-09404-6.
- A. Sancarlos, A. Abel, F. Chinesta, "Batteriemanagementsysteme mit Hybrid Twin für Lithium-Ionen-Batterien," *ATZextra* , Springer Vieweg, vol. 26, Edition: Special issue 3/2021, pp. 20–23, Juni 2021. URL: `https://www.springerprofessional.de/batteriemanagementsysteme-mit-hybrid-twin-fuer-lithium-ionen-bat/19313538`.

as well as the following Conference Proceedings paper:

- A. Sancarlos, P. De Miguel, M. Cameron, E. Cueto, F. Chinesta, J.L. Duval, "Battery Hybrid Twin in Electrical Vehicle Monitoring and Planning ," *FISITA 2021 World Congress – Conference Proceedings*, 2021.

7.1.2 Topic introduction and chapter structure

After nearly a century with the Internal Combustion Engine (ICE) dominating the personal transportation sector, it now appears that the Electric Vehicle (EV) is on the verge of becoming its successor. We have witnessed important movements and actions in this direction both at commercial and (inter-)national level in recent years. The former, through research and development of the market, the latter by changing legislation for these purposes. Needless to say, the electric battery sector is expected to become of utmost importance in the years to come.

One key issue in the EV is that its performance is closely tied to the performance of the battery. For this reason, it is fundamental to analyze this component of the car. Most EV have an on-board Battery Management System (BMS) that maintains safe and consistent operation of the battery module and optimize the performance of the battery system.

In order to infer micro-scale, unmeasurable states from the available, macro-scale measurements, a model must be solved for the BMS. In automotive applications, this model should accurately describe the battery behavior under the wide range of possible operating conditions encountered in practice.

Current BMS often use empirical or phenomenological models, such as the Equivalent-Circuit Models (ECM) for battery state estimation and control [Plett 2004, Hu *et al.* 2012]. These models have a relatively low computational cost, but they can only be used within the narrow operating conditions in which they have been parametrized. If the range of validity wants to be extended, a large amount of experimental data is required under a wide range of operating conditions. Furthermore, making predictions when degradation happens is challenging or simply impossible.

Alternatively, there exist different physics-based models describing the thermodynamics, reaction kinetics and transport within the cell [Doyle *et al.* 1993, Fuller *et al.* 1994, Doyle & Fuentes 2003]. These models are more accurate and also valid over a wide range of operating conditions. In addition, they can be directly coupled to degradation models. However, they are highly time-consuming to be of practical use in real-time applications due to the limited computational resources of an embedded BMS. A good summary of thermal-electrochemical models and ECM used in literature can be found in [Wang *et al.* 2016].

The physics-based model most commonly used is Newman's pseudo-2D (P2D) Model [Doyle *et al.* 1993]. The P2D model can accurately describe lithium-ion battery time evolution responses over a wide operating range [Forman *et al.* 2012], and it is therefore an excellent starting point for the following generation of BMS [Bizeray *et al.* 2015].

Nevertheless, the P2D model needs a bigger computation effort than ECM does. For this reason, several attempts to obtain simplified models derived from the P2D model to guarantee its use in real-time applications can be found in the literature .

One of the most commonly used simplifications is known as the Single Particle Model (SPM) [Santhanagopalan & White 2006, Moura *et al.* 2014, Domenico *et al.* 2009, Moura *et al.* 2017]. It assumes that each electrode can be represented by a unique solid-phase particle and considers that the concentration in the electrolyte does not vary spatially or temporally. State estimation using the SPM and similar approximations often include the use of an Extended Kalman Filter (EKF) algorithm [Santhanagopalan & White 2006]—for which reduced-order versions exist, see [González *et al.* 2017]—, or a backstepping PDE state estimator [Moura *et al.* 2014].

In [Domenico *et al.* 2009], an averaged electrochemical model similar to the SPM was used, by applying also the EKF, and in [Moura *et al.* 2017], an improvement of the SPM was made to include the dynamics of the concentration in the electrolyte. Nevertheless, these approaches are inherently limited because of the low current validity range of the SPM.

Other approaches include state estimation on reduced-order models derived from the P2D model [A. Smith *et al.* 2007, A. Smith *et al.* 2008, D. Stetzel *et al.* 2015, L. Lee *et al.* 2012b, L. Lee *et al.* 2012a, L. Lee *et al.* 2014]. For example, in [D. Stetzel *et al.* 2015], the EKF is applied to a state space reduced-order model computed from the P2D model using a discrete-time realization algorithm [L. Lee *et al.* 2012b, L. Lee *et al.* 2012a, L. Lee *et al.* 2014]. However, as [Bizeray *et al.* 2015] remarks, the parameters of such reduced-order models may be difficult to interpret or have no direct physical meaning, which makes accounting for degradation effects difficult.

Most recent works have shown that the use of spectral numerical methods to discretize the P2D model produces a high model reduction without losing accuracy or physical significance of parameters [Bizeray *et al.* 2015]. However, the reduction depends on the choice of the basis. Therefore, if the maximum possible reduction is looked for, the best possible basis must be found (efficiency criteria). This is a goal which can be achieved with the POD approach proposed in this work.

For these reason, the main objective of this work is to develop a Hybrid Twin (HT), as introduced in [Chinesta *et al.* 2020], for lithium-ion batteries. In this way, a new generation of BMS for the automotive industry can be developed according to the expected necessities in this industrial application. The HT concept is based on Newman's P2D Model previously mentioned. This model is presented in detail in Section 7.2.

To that end, the first step is to achieve a simulation time for the model compatible with both the real-time feedback rates of the BMS and the available computer power in the car. To achieve this, the following Model Order Reduction (MOR) technique is first employed: the Proper Orthogonal Decomposition (POD) [Chinesta *et al.* 2017]. The analysis shows that the results of the POD model are indistinguishable, to the naked eye, to the original ones (without using the MOR).

In addition, POD results are compared with the software Lithium-ION SIMulation BAttery Toolbox (LIONSIMBA), see `https://github.com/lionsimbatoolbox/LIONSIMBA`. This is a reliable tool to compare results because a validation of the software was done with respect to the COMSOL MultiPhysics commercial software (COMSOL, Inc., Stockholm, Sweden) and the Newman's DUALFOIL code [Robinson & García 2015].

The POD results and the methodology of the technique are detailed in Section 7.4. It is shown that by utilizing the proposed model, cell design, optimization of parameters and simulation of battery packs can be achieved while saving time and computational resources.

The second step is to integrate the developed model with all the other systems which constitute the EV under real-time constraints. The POD model may not be suitable or the best option to achieve this, so alternatives are explored.

Here the use of the sparse Proper Generalized Decomposition, s-PGD [Ibáñez Pinillo *et al.* 2018] is proposed to obtain an algebraic expression for the behavior of a battery cell according to different possible itineraries. This chapter proves that we can model the behavior of the lithium-ion cell analyzed for such a wide range of itineraries using polynomials with the proposed approach. Since the discussed proposal transforms the problem of the cell model to the evaluation of a polynomial, there are no problems in coupling the battery model with the other systems in the EV. A detailed example of the accuracy and the range of use of the approach is discussed. The results and the explanation of the technique used in the regression (s-PGD) can be found in Section 7.5. To simulate the EV, the ESI system simulation software SimulationX (ESI ITI GmbH, Dresden, Germany) was used. The results of this study can be found in Section 7.6.2.

The Digital Twin created in the above section does not only allow real-time simulations, but can also adapt its predictions taking into consideration the real driving conditions and the real driving cycle to change the planning in real-time.

For this reason, an innovative planning algorithm is created taking the s-PGD model. The great added value of this algorithm is its ability to make quick decisions based on very accurate predictions of the battery system while simulating the entire EV. To do that and as previosuly introduced, the s-PGD battery model is first integrated into an EV system using SimulationX (Section 7.6.2). Then, a procedure to adapt and modify the driving cycle is designed to keep the battery state in the correct operation range in function of the planned itinerary (Section 7.6.3). This way, driving profiles can be recommended or imposed on the driver to guarantee durability and good long-life performance of the battery pack. Furthermore, the planning algorithm can decide on the best possible itinerary considering different battery criteria (Section 7.6.4). To achieve that, different routes are simulated in real-time using the created EV model. In addition, other proof of concept is carried out simulating a BMS in SimulationX (Section 7.6.5), proving that a BMS could be developed using the present approach.

The next section (Section 7.7) is devoted to the data-driven modeling concept of the HT methodology. The main idea here is that biased deviations (between the model and the measurements) show hidden physics not considered in the model. These deviations therefore require a particular treatment, namely their on-line modeling by assimilating collected data. On the other hand, the unbiased deviation contribution is associated with noise and is addressed by using adequate filters. For this reason, a data-driven model based upon the novel strategies proposed in Chapter 2 is developed. In particular, the stabilized DMD (Section 2.5.3) and the DMD Dictionary Method (Section 2.5.4). They are employed to extract an on-line model to correct the gap between predictions and measurements. Thanks to the HT model, we can eliminate this gap during the driving process and take into consideration real-time restrictions. The results can be found in Section 7.7.

Finally, in Section 7.8 the general conclusions of the present work are shown.

7.2 Electrochemical model: Newman's P2D model

7.2.1 Newman's P2D model

There exists a vast collection of models for the battery in the literature. Those related to the equivalent circuit of the battery are often simple enough to achieve a good computational time. However, they are typically limited to a narrow operational range. In addition, the battery models based on electrochemistry laws are generally preferred to the equivalent circuit or to other kinds of simplified models, because they also predict the physical cell limitations, which have a relevant effect in the automotive application, where the battery suffers very often the stress of very high transient loads. In addition, they are more accurate and have a wide operational range. The literature on electrochemical modeling of batteries is quite extensive, including both full order and simplified models.

Newman's group developed a physics-based model using porous electrode and concentrated solution theories [Doyle *et al.* 1993]. This model can accurately capture the battery response and has been widely used in the literature. However, there are problems to use the model in real-time applications or to achieve fast simulations and predictions because of the large computational effort needed to solve it. A method to reduce the computational resources required to solve the model is presented in Sect. 7.4.

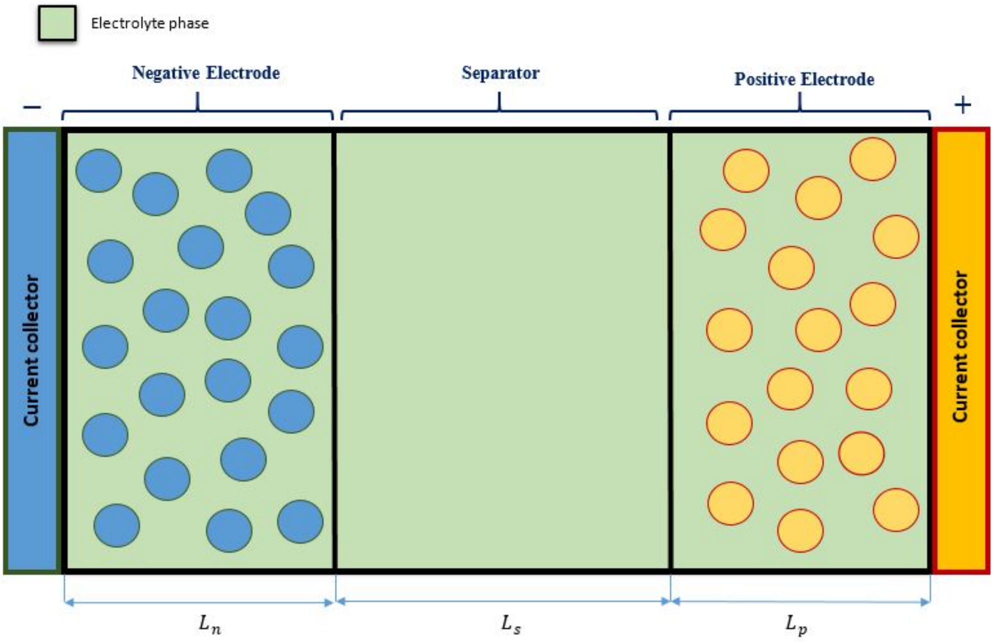

Figure 7.1 – Schematic of electrochemical cell model with coupled solid diffusion submodel.

The lithium-ion cell model shown in Figure 7.1 consists of two porous electrodes composed of an active material (that can store lithium intercalated in the solid material) and a separator. The electrodes and the separator are soaked in an electrolyte that allows the transport of ions. During discharge, lithium stored in the anode is de-inserted from the active material and released as ions in the electrolyte. Driven by diffusion (concentration gradient) and migration (potential gradient), lithium ions travel through the separator to the cathode where they enter the lattice of the cathode active material.

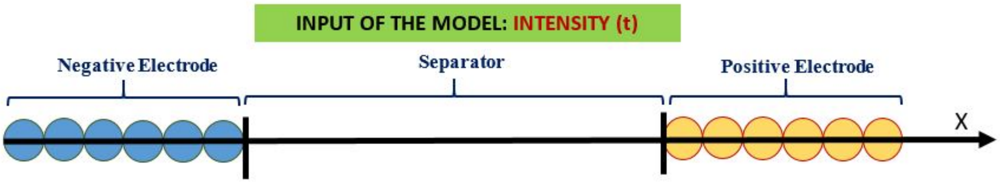

Figure 7.2 – Schematic of the P2D model.

The separator, while conductive to ions, is an electronic insulator, thus forcing electrons to follow an opposite path through an external circuit or load. On the other hand, the path of electrons and lithium-ions is reversed when the battery is charging (due to the fact that the physical reactions are made in the opposite sign).

In the domains of the problem, two phases are considered, the solid phase and the electrolyte phase, and they are treated as superimposed continua using porous electrode theory [Bizeray *et al.* 2015].

It is important to note that the x-dimension refers to the spatial dimension through the electrodes and the separator, according to Figures 7.1, 7.2, and 7.3, and the r dimension refers to the depth in the particle where the diffusion of the lithium happens. The r-dimension of the spherical particles is called the pseudo second dimension. This is why the model is often referred to as Newman's P2D model in the literature.

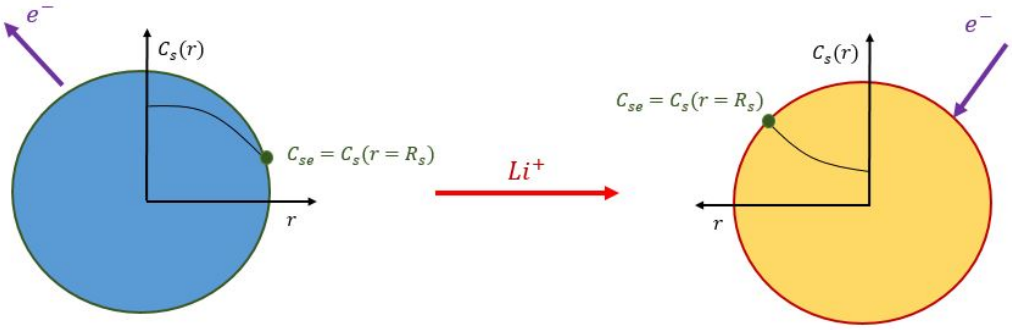

Figure 7.3 – Detail of the solid diffusion submodel. The path of electrons and the graphs of $c_s(r)$ showed are the ones for the discharging process

The P2D model consists of a set of partial differential equations (PDEs) and algebraic constraints governing the evolution of lithium concentration and electric potential within the cell. The equations of the model describe the battery system with four quantities, i.e., concentration of lithium in solid and electrolyte phase, $c_s(r, x, t)$ and $c_e(x, t)$, respectively, and the volume-averaged electrical potential in the solid and electrolyte phase, $\phi_s(x, t)$ and $\phi_e(x, t)$. All the equations are coupled by the term $j^{\mathrm{Li}}(x, t)$ which is the reaction current resulting in production or consumption of Li.

The complete set of equations for the micro-macroscopic model is:

$$\frac{\partial c_s}{\partial t} = \frac{D_s}{r^2} \cdot \frac{\partial}{\partial r}\left(r^2 \frac{\partial c_s}{\partial r}\right), \tag{7.1}$$

$$\frac{\partial\left(\varepsilon_e \cdot c_e\right)}{\partial t} = \frac{\partial}{\partial x}\left(D_e^{\mathrm{eff}} \frac{\partial c_e}{\partial x}\right) + \frac{1 - t_+}{F} \cdot j^{\mathrm{Li}}, \tag{7.2}$$

$$j^{\mathrm{Li}} = \frac{\partial}{\partial x}\left(\sigma^{\mathrm{eff}} \frac{\partial \phi_s}{\partial x}\right), \tag{7.3}$$

$$j^{\mathrm{Li}} = -\frac{\partial}{\partial x}\left(K^{\mathrm{eff}} \frac{\partial \phi_e}{\partial x}\right) - \frac{\partial}{\partial x}\left(K_D^{\mathrm{eff}} \frac{\partial \ln c_e}{\partial x}\right), \tag{7.4}$$

$$j^{\mathrm{Li}}(x) = a_s \cdot i_0 \cdot \left[\exp\left(\frac{\alpha_a \cdot F}{R \cdot T} \cdot \eta\right) - \exp\left(-\frac{\alpha_c \cdot F}{R \cdot T} \cdot \eta\right)\right]. \tag{7.5}$$

These equations are supplemented with appropriate boundary conditions:

$$\left.\frac{\partial c_s}{\partial r}\right|_{r=R_s} = \frac{-j^{\mathrm{Li}}}{F \cdot a_s \cdot D_s}, \quad \left.\frac{\partial c_s}{\partial r}\right|_{r=0} = 0,$$
$$\left.\frac{\partial c_e}{\partial x}\right|_{x=0} = 0, \quad \left.\frac{\partial c_e}{\partial x}\right|_{x=L_t} = 0,$$
$$\left.\sigma\varepsilon_s \frac{\partial \phi_s}{\partial x}\right|_{x=0} = \left.\sigma\varepsilon_s \frac{\partial \phi_s}{\partial x}\right|_{x=L_t} = -\frac{I}{A}$$
$$\left.\frac{\partial \phi_s}{\partial x}\right|_{x=L_n} = \left.\frac{\partial \phi_s}{\partial x}\right|_{x=L_n+L_s} = 0,$$
$$\left.\frac{\partial \phi_e}{\partial x}\right|_{x=0} = 0, \left.\frac{\partial \phi_e}{\partial x}\right|_{x=L_t} = 0$$

In addition, c_s and c_e are known at the initial time. The definition and the terminology used in the variables shown is summarized in Appendix D.

Eq. (7.1) enforces the lithium conservation in the solid phase. Similarly, Eq.(7.2) enforces the lithium conservation in the electrolyte phase. In contrast, Eq. (7.3) refers to the charge conservation in the solid phase. Similarly, Eq. (7.4) refers to the charge conservation in the electrolyte phase.

Finally, the Butler-Volmer Eq. (7.5) is used to couple the charge and species governing equations: The four unknowns c_s, c_e, ϕ_s and ϕ_e are coupled in the nonlinear definition of j^{Li}, resulting in a nonlinear problem. In addition, other variables which appear in the equations are defined empirically. These definitions are often nonlinear—such as, for example, the open circuit voltage U—thus adding more difficulties in the resolution.

The overpotential of Eq. (7.5) is obtained as:

$$\eta(x) = \phi_s(x) - \phi_e(x) - U(c_{se}(x)), \tag{7.6}$$

where $c_{se} = c_s(r = R_s, x)$ and therefore, the open circuit voltage U depends on the electrode.

In Eq. (7.5), exchange current density, i_0, is related to both solid surface and electrolyte concentrations according to

$$i_o = k_o \cdot c_e^{\alpha_a} \cdot (c_{s,\max} - c_{se})^{\alpha_a} \cdot c_{se}^{\alpha_c}, \tag{7.7}$$

where k_0 is a kinetic rate constant that depends on the temperature. Its value is often obtained using the initial exchange current density and concentrations.

Finally, the cell potential is computed as:

$$V = \phi_s\left(x = L_t\right) - \phi_s\left(x = 0\right) - R_f \cdot I. \tag{7.8}$$

There are additional secondary equations to solve the model in the definition of some variables. The reader can find a detailed description of these equations in Appendix E.

It is worth noting that there are as many equations (7.1) as particles in the x domain. Therefore, the discretization on the electrodes affects the number of equations to solve. This is caused by the fact that usually there is one particle in each x node in the electrode domains.

If it is taken into account that the just-introduced model is one-dimensional in the cell space, the scheme of the model would be as depicted shown in Figure 7.2 where the reader is reminded that there will be as many particles as nodes in x in the anode and cathode domain.

As previously stated, Eq. (7.1) is solved in the r-dimension of the spherical particles—the pseudo-second dimension—. For an in-depth analysis of this electrochemical model, the reading of [Hariharan *et al.* 2018] is recommended.

7.2.2 Definitions of the State of Charge (SoC)

We can find a lot of definitions of the SoC in the literature, and each one has its particular use and meaning. Fundamentally, the concept of SoC is related to the transport of lithium from one electrode to the other. A cell with a highly lithiated negative electrode and relatively delithiated positive electrode should correspond to a high SoC, since this implies that the cell has most of its stored charge.

The more extended definition is the bulk SoC. The bulk SoC counts the total lithium entering or exiting the electrode particles. Therefore, knowing the maximum and minimum concentration of lithium in each electrode (related to a correct operation of the cell), we can estimate the bulk SoC. The bulk SoC is computed using the following expression:

$$\mathrm{SoC} = \frac{\frac{c_{s,\mathrm{av}}}{c_{s,\mathrm{max}}} - \theta_{0\%}}{\theta_{100\%} - \theta_{0\%}}, \tag{7.9}$$

where $\theta_{100\%}$ and $\theta_{0\%}$ are the relation $\frac{c_{se}}{c_{s,\mathrm{max}}}$ on one electrode when the battery is fully charged and completely discharged respectively. $c_{s,\mathrm{av}}$ is the average value of the concentration in the electrode. It is computed as follows (for the anode):

$$c_{s,\mathrm{av}} = \frac{3}{L_n \cdot R_s^3} \int_0^{L_n} \int_0^{R_s} r^2 \cdot c_s(r,x) \cdot dr \cdot dx. \tag{7.10}$$

The first integral is used to compute the mean value of concentration of each particle and the second computes the mean value of all the particles along the electrode (since the lithium concentration varies spatially in the electrode).

It is important to note that the meaning of SoC depends on the choice of $c_{s,\mathrm{av}}$. For example, the voltage depends directly on the concentration at the particle surface and not on the mean value in the particles. Therefore, we can define the surface SoC redefining $c_{s,\mathrm{av}}$ as follows: The $c_{s,\mathrm{av}}$ is computed using (with respect to the negative electrode):

$$c_{s,\mathrm{av}} = \frac{1}{L_n} \int_{\Omega_n} c_{se}(x) \cdot dx. \tag{7.11}$$

where Ω_n refers to the domain of the anode.

Furthermore, the surface SoC can also be computed for each spatial position on the electrodes (therefore: $c_{s,\mathrm{av}} = c_s(x, r = R_s)$). This way, the surface SoC would be a function depending on time and space $\mathrm{SoC}(x,t)$. This is an interesting definition to see where depletion and saturation occur on the electrodes.

In addition, the surface SoC has implications in the available power that can be extracted at a given time, since the redox reactions are limited by the reactant concentrations at the particle surface [Bartlett 2015]. The bulk and surface SoC converge to the same value at steady state (because at steady state the concentration profiles are stabilized), but it can be useful to track both metrics during dynamic current profiles.

For example, in a high discharge rate, there will be a significant difference between bulk and surface SoC. However the latter has the information about the quantity of lithium instantaneously available to move from one electrode to the other and the quantity of lithium that can be deposed in a given time on an electrode.

Despite the usefulness of Eq. (7.11), the profile of the surface concentration on the electrodes can have big variations and irregularities depending on the properties of the cell. In these cases, the mean value of Eq. (7.11) may not be suitable to approximate the dynamic behavior of the SoC in the electrodes.

The reason for this is that the critical points in the electrodes can reach the values of depletion or saturation much sooner than the average value of the electrode concentration. This can cause problems such as a sudden loss of power.

For this reason, control strategies normally try to avoid this [Smith 2010]. In these cases, we may be interested in the surface SoC at the critical points.

In this case we redefine $c_{s,\mathrm{av}}$ as $c_{s,\mathrm{av}} = c_s(x = x_c, r = R_s)$, where R_s is the particle radius and x_c is the critical point on the electrode. In this way we can, for example, stop charging if the critical point in the electrode is close to a dangerous surface SoC [1]. In order to clarify the terminology employed, this dissertation will refer to the above definition as critical SoC and to the definition of Eq. 7.11 as surface SoC.

Another important issue is the voltage limits of the cell. Usually the operation of the cell has to work between a given range of voltage. Trying to work outside this limits can have undesirable effects. The operational limits of the battery can come from a variety of sources: voltage limits, suitable concentration limits and limits to avoid depletion and saturation effects. In some way, the effects are related, for example the voltage depends on the surface concentration and their distribution on the electrodes as well as the current profile.

Finally, sometimes the cell voltage distributions are plotted as a function of the depth of discharge (DoD), a term which is used to describe how deeply the battery is discharged and it can be calculated as

$$\mathrm{DoD} = 1 - \mathrm{SoC}. \tag{7.12}$$

7.3 Solving Newman's P2D model

The reader is reminded that one of the goals of this work is to reduce, by means of a reduced-order model, the computational effort and the simulation time of the full-order model, FOM, explained in Sect. 7.2. Results of the ROM will therefore be checked against the FOM. This section is devoted to explaining the method used to solve the model. In particular, a strategy to solve Eqs. (7.1), (7.2), (7.3), (7.4) and (7.5) is needed, because all equations are coupled and there is not a direct way to compute a solution.

Firstly, it can be noticed that the system of equations is nonlinear, so an algorithm for the solution of nonlinear systems is required. The Newton-Raphson method will be employed for the necessary linearization of these equations.

Secondly, it is noted that Eqs. (7.1) and (7.2) are the only ones which allow us to advance in the time domain. This can be accomplished in an implicit or explicit scheme. As a first approximation, and to avoid cumbersome expressions for the Jacobian matrix, only the spatial derivatives of c_s and c_e will be cast in an implicit scheme. The variable j^{Li} will be cast in an explicit way, allowing us to separate the nonlinear problem in Eqs. (7.3), (7.4) and (7.5). This scheme is sketched in Figure 7.4.

The just-introduced approach can be further improved. For example, an additional iterative loop can be added (as shown in Fig. 7.5) to compute j^{Li} in an implicit way.

---

[1] The measure to control depletion and saturation on the electrodes is $0 < c_{se}(x)/c_{s,\max} < 1$. On the other hand, the measure to control depletion in the electrolyte is $c_e(x) > 0$ [Smith 2010].

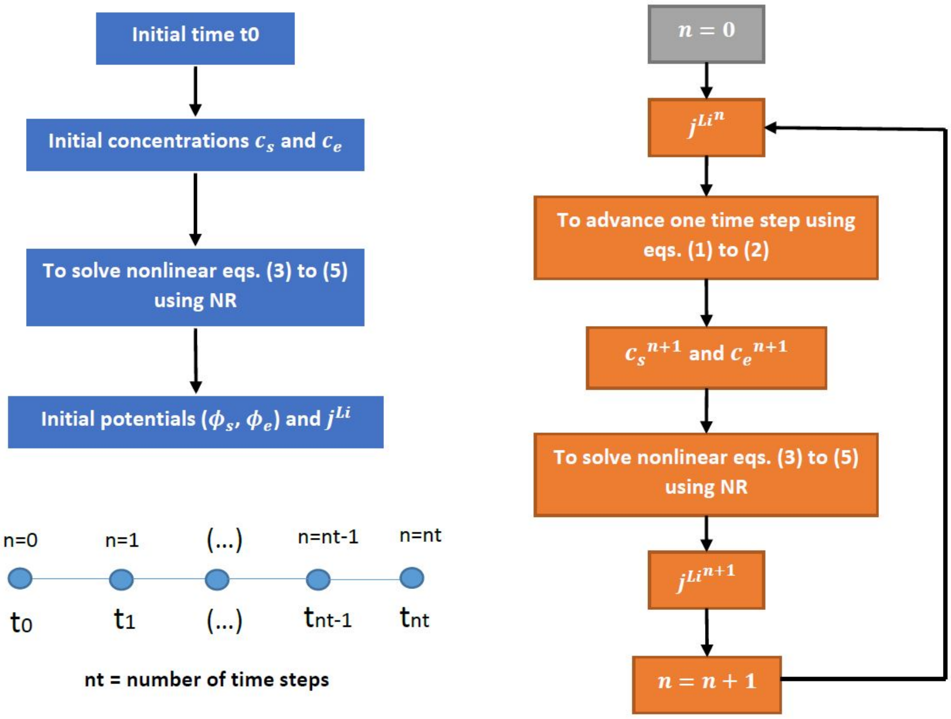

Figure 7.4 – Scheme to solve the electrochemical model.

This allows the augmentation of the size of the time steps without the introduction of any perceived instability.

The PDEs (7.2), (7.3) and (7.4) always contain a term of the form $\frac{\partial}{\partial x}\left(k\frac{\partial u}{\partial x}\right)$ where k is a discontinuos function. A finite element discretization is used for these equations, namely, a weak formulation of the problem, to avoid problems in the derivative of a discontinuos function. In contrast, Eq. (7.1) can be discretized using the FDM (Finite Difference Method), which is easier to implement than FEM.

To compute the value of the functions c_s and c_e at each time step, a Crank–Nicolson scheme is used to discretize Eq. (7.1) and an implicit Euler scheme for Eq.(7.2). The reason of using the implicit Euler scheme is its enhanced stability properties. Conversely, the Crank-Nicolson method is used to take advantage of the benefits of the implicit methods as well as an order of accuracy of $\mathcal{O}(\Delta t^2)$.

In the r-domain, two different step sizes are used to adapt the mesh to the shape of the solution. In addition, a finite difference formula of an order of accuracy of $\mathcal{O}(\Delta r^4)$ is used in the area where the function changes faster and abruptly. In the other areas, the classical formulas of an order of accuracy of $\mathcal{O}(\Delta r^2)$ are used.

7.4 Proper Orthogonal Decomposition of the P2D model

7.4.1 Reasons to use the POD

In general, the solution of the model described in Section 7.2 requires a large computational effort in terms of both time and memory. Under such situations, classical methods are not

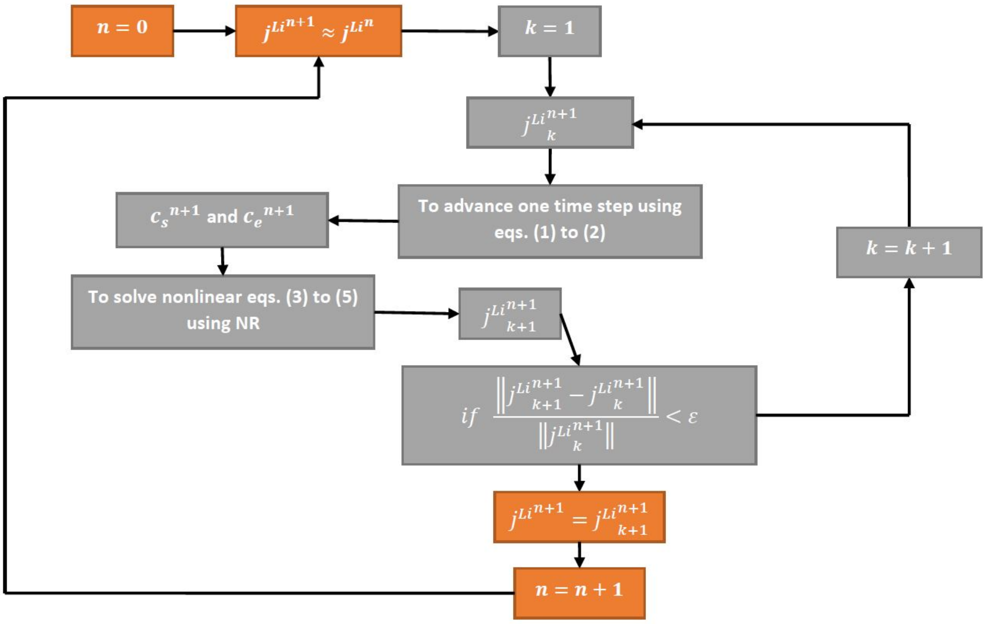

Figure 7.5 – Improved scheme to solve the electrochemical model.

able to provide satisfactory results under the stringent conditions imposed by real-time feedback rates.

Analyzing different batteries, it can be observed that the parameters of the model can influence significantly the stability and accuracy needed to solve the model and therefore also in the amount of computational resources. For example, some tests to simulate some seconds of battery life usually took times in the order of minutes to compute. Hence, the computational effort has to be reduced several orders of magnitude and to achieve that, Proper Orthogonal Decomposition is proposed [Karhunen 1946] [Loève 1963] [Meyer & Matthies 2003] [Niroomandi *et al.* 2008] [Rozza *et al.* 2008].

In the simulations carried out, it is observed that roughly 90 % of the time is used in solving Eqs. (7.1). In addition, a big computational effort is needed to save and to compute the time evolution of the $c_s(r)$ functions at each particle. So it is clear that it is necessary to focus on this part of the model.

The problem in Eq. (7.1) is the large number of nodes along the r-domain needed to achieve an accurate solution without losing stability. This number of nodes has to be multiplied for the number of particles distributed along the x-domain. Therefore, one possible solution to the problem can be to reduce drastically the number of unknowns needed along r. For that purpose, a reduced basis is extracted to project all the possible functions $c_s(r)$. If the cardinality of the basis, $\mathtt{n}$, is small enough, the number of unknowns in Eq. (7.1) can be greatly reduced:

$$c_s(r) \approx \sum_{i=1}^{\mathtt{n}} \mathbf{F}_i(r) \cdot \alpha_i. \tag{7.13}$$

Now, if the reduced basis $\mathbf{F}_i(r)$ is known, we require only $\mathtt{n}$ coefficients α_i to determine the function c_s by Galerkin projection. It is important to keep in mind that in a Finite

Element basis (for example) we may need hundreds of coefficients (or even more) to determine the function we are evaluating because of the refined mesh used.

Note that Eq. (7.13) can be expressed in a more compact form:

$$c_s(r) = \begin{bmatrix}\mathbf{F}_1(r) & \cdots & \mathbf{F}_\mathrm{n}(r)\end{bmatrix} \begin{bmatrix}\alpha_1 \\ \vdots \\ \alpha_\mathrm{n}(r)\end{bmatrix} = \mathbf{F}\cdot\alpha. \tag{7.14}$$

To obtain the set of reduced basis,the method of the snapshots detailed in Section 1.2.1 is employed.

Imagine that a set of experimental values or snapshots of the $c_s(r)$ functions are collected in a matrix $\mathbf{Y}$ during a battery simulation. The SVD can be used (according to the aforementioned Section 1.2.1) to extract a reduced basis $\{\mathbf{u}_i\}_{i=1}^{l}$, which better approximates the $c_s(r)$ functions. If the extracted basis is small enough, a drastic reduction of unknowns will be achieved.

If the snapshots reflect well all the possible shapes and degrees of freedom of the $c_s(r)$ functions, this reduced basis can be used to perform simulations different from the ones used to extract the reduced basis. The reason for this is that the $c_s(r)$ functions of other scenarios will be well approximated because their projection into the reduced basis is good enough to reproduce them. However, if there is a scenario which produces c_s functions which are not well reproduced by the reduced basis, the accuracy of the ROM will be severely affected.

7.4.2 POD of the electrochemical model

To use the POD methodology, the matrix $\mathbf{Y}$ which contains the snapshots has to be constructed (see Section 7.4.1). Each snapshot is a function $c_s(r)$ for a particle at a given time. However, our experience indicates that only the $c_s(r)$ functions in the particles placed at the boundaries of the electrodes are needed to construct a good reduced basis. In this way, the size of the $\mathbf{Y}$ matrix is greatly reduced to reproduce long-time dynamics. So, from Eq.(7.1):

$$\frac{\partial c_s}{\partial t} = \frac{D_s}{r^2}\cdot\frac{\partial}{\partial r}\left(r^2\frac{\partial c_s}{\partial r}\right) = \frac{2\cdot D_s}{r}\cdot\frac{\partial c_s}{\partial r} + D_s\cdot\frac{\partial^2 c_s}{\partial r^2}.$$

Using a Crank–Nicolson scheme:

$$\frac{c_s^{n+1}-c_s^n}{\Delta t} = \frac{1}{2}D_s\cdot\left(\frac{2}{r}\cdot\frac{\partial c_s^{n+1}}{\partial r} + \frac{\partial^2 c_s^{n+1}}{\partial r^2} + \frac{2}{r}\cdot\frac{\partial c_s^n}{\partial r} + \frac{\partial^2 c_s^n}{\partial r^2}\right). \tag{7.15}$$

By further discretizing Eq. (7.15) in space, we obtain the following algebraic expression:

$$\mathbf{L}\cdot\mathbf{c}_s^{n+1} = \mathbf{J}\cdot\mathbf{c}_s^n + \frac{1}{2}\left(\mathbf{b}^{n+1}+\mathbf{b}^n\right) = \mathbf{J}\cdot\mathbf{c}_s^n + \mathbf{p}(\mathbf{b}^{n+1},\mathbf{b}^n). \tag{7.16}$$

where $\mathbf{p}$ is a vector which depends on the boundaries $(\mathbf{b}^{n+1},\mathbf{b}^n)$, namely, the $j^{\mathrm{Li}}(x)$ in the n- and $n+1$-th time steps, according to the following finite difference discretization.

The matrices in Eq. (7.16) $(\mathbf{L},\mathbf{J})$ are obtained by using a Finite Difference scheme of order $\mathcal{O}(\Delta r^4)$ between $R_s > r > 0.91\cdot R_s$ and of order $\mathcal{O}(\Delta r^2)$ between $0.91\cdot R_s > r > 0$ [Kutz 2013]. Two different Δr are used. A larger one (Δr_1) between $0.89\cdot R_s > r > 0$ and a smaller one (Δr_2) between $R_s > r > 0.89\cdot R_s$. The values of $\Delta r_1, \Delta r_2$ depend on the parameters of the cell analyzed.

To obtain the second-derivative formula when changing from Δr_1 to Δr_2, we look for $\frac{d^2u_i}{dr^2}$ as in Fig. 7.6. In addition, the points $i-1, i, i+1$ and $i+2$ are the ones which will be used in the expression searched according to Figure 7.6 where h is defined as Δr_1 and $\gamma \cdot h$ as Δr_2.

Given a smooth function $f : \mathbb{R} \to \mathbb{R}$, its Taylor series around a is

$$\sum_{n=0}^{\infty} \frac{f^{(n)}(a)\,(x-a)^n}{n!}.$$

Therefore, according to the Taylor series, the following system of equations can be found:

$$\begin{aligned}\begin{pmatrix} u_{i-1} \\ u_{i+1} \\ u_{i+2} \end{pmatrix} = u_i \cdot \begin{pmatrix} 1 \\ 1 \\ 1 \end{pmatrix} + h \cdot \frac{du_i}{dr} \cdot \begin{pmatrix} -1 \\ \gamma \\ 2 \cdot \gamma \end{pmatrix} + h^2/2 \cdot \frac{du_i^2}{dr^2} \cdot \begin{pmatrix} 1 \\ \gamma^2 \\ 4 \cdot \gamma^2 \end{pmatrix} \\ + h^3/6 \cdot \frac{du_i^3}{dr^3} \cdot \begin{pmatrix} -1 \\ \gamma^3 \\ 8 \cdot \gamma^3 \end{pmatrix} + h^4/24 \cdot \frac{du_i^4}{dr^4} \cdot \begin{pmatrix} 1 \\ \gamma^4 \\ 16 \cdot \gamma^4 \end{pmatrix} + \cdots\end{aligned}$$

Now, we form a weighted sum of the equations with the coefficients $1, A, B$:

$$\begin{aligned} u_{i-1} + A \cdot u_{i+1} + B \cdot u_{i+2} = u_i \cdot (1 + A + B) & \\ + h \cdot \frac{du_i}{dr} \cdot (2 \cdot B \cdot \gamma + A \cdot \gamma - 1) & \\ + h^2/2 \cdot \frac{du_i^2}{dr^2} \cdot (4 \cdot B \cdot \gamma^2 + A \cdot \gamma^2 + 1) & \\ + h^3/6 \cdot \frac{du_i^3}{dr^3} \cdot (8 \cdot B \cdot \gamma^3 + A \cdot \gamma^3 - 1) & \qquad + \quad \cdots \end{aligned}$$

removing the addends related to the third and first derivatives gives:

$$\begin{aligned} 2 \cdot B \cdot \gamma + A \cdot \gamma &= 1, \\ 8 \cdot B \cdot \gamma^3 + A \cdot \gamma^3 &= 1. \end{aligned}$$

Solving the system:

$$B = \frac{1 - \gamma^2}{6 \cdot \gamma^3}; \quad A = \frac{1 - 2 \cdot B \cdot \gamma}{\gamma}.$$

So, finally the sought expression is:

$$\frac{d^2 u_i}{dr^2} = 2 \cdot \frac{B \cdot u_{i+2} + A \cdot u_{i+1} - u_i \cdot (1 + A + B) + u_{i-1}}{h^2 \cdot (4 \cdot B \cdot \gamma^2 + A \cdot \gamma^2 + 1)} + \mathcal{O}(h^2). \tag{7.17}$$

Returning to Eq.(7.16), adding the terminology introduced in Eq. (7.14), we change Eq. (7.16) to introduce the reduced basis in the formulation of the problem as well as the new unknowns.

$$\mathbf{L} \cdot \mathbf{F} \cdot \alpha^{n+1} = \mathbf{J} \cdot \mathbf{F} \cdot \alpha^n + \mathbf{p}(\mathbf{b}^{n+1}, \mathbf{b}^n). \tag{7.18}$$

There are different strategies to solve the overdetermined system in Eq. (7.18). In this dissertation, the Ordinary Least Squares is chosen. This method minimizes the sum of squared residuals, and leads to a closed-form expression for the estimated value of the unknown vector. Therefore, the solution can be written as:

$$\begin{aligned} \mathbf{L}_F = \mathbf{L} \cdot F, \qquad & \mathbf{J}_F = \mathbf{J} \cdot F, \\ \mathbf{R} = \mathbf{L}_F^\top \cdot \mathbf{L}_F, \quad & \mathbf{M} = \mathbf{L}_F^\top \cdot \mathbf{J}_F, \end{aligned}$$

$$\begin{aligned} \alpha^{n+1} &= \mathbf{R}^{-1} \cdot \mathbf{L}_F^\top \cdot \left(\mathbf{J}_F \cdot \alpha^n + \mathbf{p}(\mathbf{b}^{n+1}, \mathbf{b}^n)\right), \\ \alpha^{n+1} &= \mathbf{R}^{-1} \cdot \left(\mathbf{M} \cdot \alpha^{\mathbf{n}} + \mathbf{L}_F^\top \cdot \mathbf{p}(\mathbf{b}^{n+1}, \mathbf{b}^n)\right). \end{aligned} \tag{7.19}$$

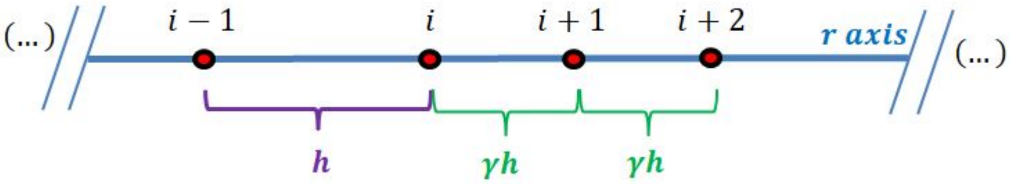

Figure 7.6 – Reference mesh to obtain the finite difference formula when the spatial step changes.

7.4.3 Results

To validate the robustness of the proposed scheme, two different batteries are studied, each one with different parameters. The parameters of the first cell are taken from [Domenico *et al.* 2009, Smith & Wang 2006]. This is a 6 Ah cell, designed for its application to Hybrid Electric Vehicles (HEV). For this battery, a POD basis is extracted using a constant 12 A discharge current. To check the accuracy of the reduced model, a comparison between the POD model and the original, full-order model is done. Results of this comparison are detailed in Figure 7.7, where a validation is done with a current profile according to the Freedom CAR test procedure, a U.S. Department of Energy program for the zero-emission vehicle and technology Research.

Other current profiles provided similar results, thus proving the validity of the approach. On the other hand, a reduction factor of 50 in the number of unknowns in this cell is achieved by using the POD basis. The simulation time and the computational effort to solve the problem is reduced by this factor approximately—note that roughly 90 % of the time was used to solve Eq. (7.1).

The second cell parameters are taken from [Torchio *et al.* 2016]. This type of cell is suitable for both HEV and EV applications, as we can notice in the types of simulations done in these references. The main parameters of this cell are detailed in Appendix E.

For this second battery, a POD basis is extracted using a constant current discharge of 60 A. Figure 7.8 shows a comparison between the POD model and the original full order model. This figure shows the accuracy for the POD model to perform simulations with current profiles different from the one used to extract the basis. We remind ourselves that the basis is extracted with a constant current profile, while in the simulation of Figure 7.8, the current used has a linear profile between different points. Despite the current differences, a good accuracy is achieved by the POD model as we can see in the comparison.

The reduced-order results are also compared to those provided by the software LIONSIMBA [Torchio *et al.* 2016]. These results are shown in Fig. 7.9.

In addition to obtaining a good comparison in terms of results, a reduction factor of 40 in the number of unknowns in this cell is achieved using the POD basis. The simulation time and the computational effort to solve the problem is reduced by this factor approximately. In fact, for both cells, the time for a simulation of an interval t is less or equal than the elapsed time t. These results were tested on a laptop running an Intel Core Kabylake i7-7700HQ+HM175, with 8GB DDR4 RAM running at 2400MHz.

Based on the experience of our simulations, we conclude that the key issue to obtaining a good reduced basis is to collect the $c_s(r)$ functions from an off-line simulation of a complete discharge-charge cycle at constant current. As it is shown in Fig. 7.8, this basis is good

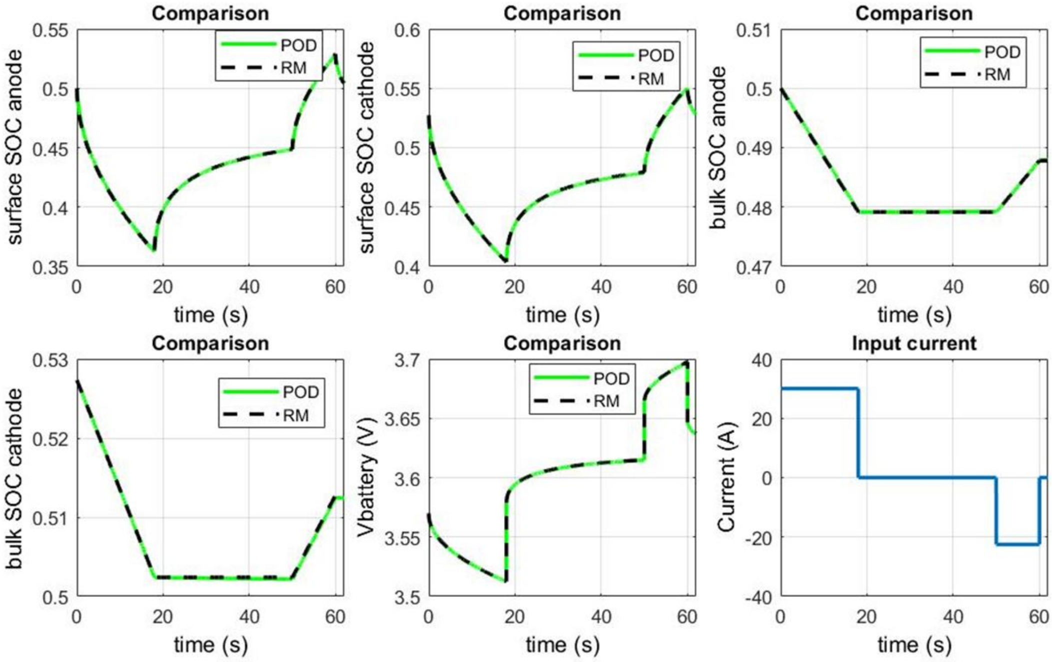

Figure 7.7 – Simulation of the reduced order model for the first cell. Comparison of the evolution in time between the POD model and the original, full-order electrochemical mode, of the different variables of the cell. The different SoC and cell voltages are compared and the input current used during the simulation is shown in the last picture. Legend: RM = Results of the full P2D model; POD = Results of the POD model.

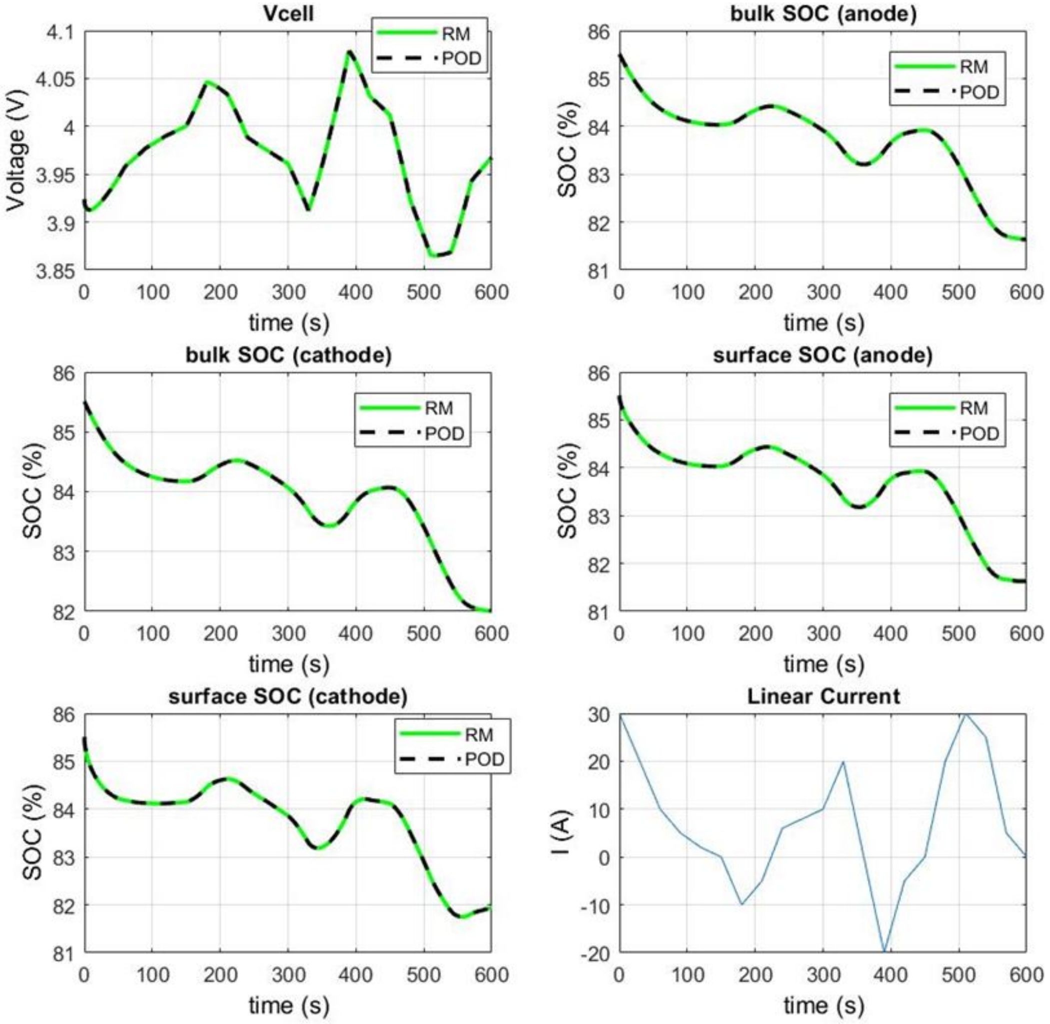

Figure 7.8 – Comparison of full- and reducer-order simulations of the second cell. . The different SoC and the cell voltage are compared and the input current used during the simulation is shown in the last picture. Legend: RM = Results of the full P2D model; POD = Results of the POD model.

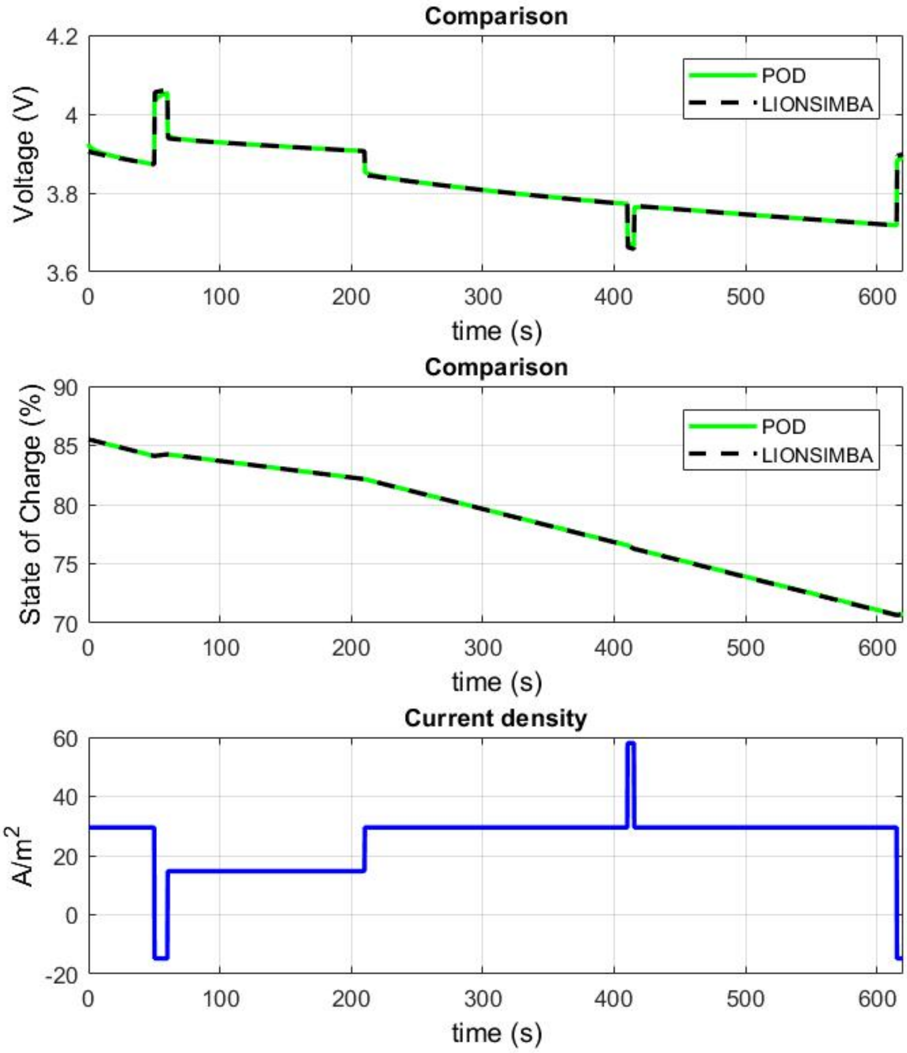

Figure 7.9 – Comparison of the reduced-order results with those provided by the software LIONSIMBA for the second cell.

enough to reproduce other current profiles with good accuracy.

Another important consideration is the value of the constant current used to extract the basis. Normally, a high value will produce more variations in the c_s functions, which will better enrich the reduced basis. However, in this case, the simulation will typically stop sooner due to, for example, reaching the cut-off voltage.

In these circumstances, the depth of the diffusion in the particles can be smaller because of the shorter simulation time. This provides a dilemma for selecting the appropriate value.

The reader is reminded that the cut-off voltage is one of the limits imposed on the cell, as explained in Section 7.2.2, to ensure a suitable operation of the component. In this case, the cut-off voltage is referred to the limit assigned to the lowest value of the cell voltage.

7.5 PGD regression. Learning the cell behavior from data

7.5.1 Introduction

In Section 7.4, a ROM is developed to allow fast simulations of the electrochemical model using less computational resources. As we saw, excellent agreement with existing, full-order models are obtained. However, the POD model is not necessarily the best option to achieve a full simulation of all the systems which constitute the EV or indeed to be used in a BMS. For this reason, several alternatives are explored, leading us to the approach presented in this section.

This method allows to easily couple the battery model with the other subsystems of the vehicle. It can likewise be used in a BMS without issue because of the simple algebraic expression(s) obtained.

Furthermore, this PGD approach could be developed, in which batteries can be modeled from data. One motivation for the use of the latter approach is that, by working directly with data, no parameter fitting is necessary. This conceptualization has been tested successfully in other branches of scientific computing, see, for instance, [Kevrekidis & Samaey 2010] [Kirchdoerfer & Ortiz 2016] [Brunton *et al.* 2016] [Kaiser *et al.* 2018] [González *et al.* 2018a] [Moya *et al.* 2019], to name but a few. This methodology can be specially convenient if it is expected that, for some reason, the model for the battery will change during its operating life, for instance.

As presented in Section 7.3, the response of the cell depends on the micro-scale, where many parameters are involved in the description of its dynamics. If a response surface-like approach is chosen under this setting, a large sampling effort is to be expected, that grows exponentially with the number of parameters. For this reason, a method able to circumvent the curse of dimensionality should be used [Laughlin & Pines 2000]. Here, the so-called sparse Proper Generalized Decomposition (s-PGD in what follows) is employed. The reader unfamiliar with this methodology is directed to review Section 2.2 where it is introduced. The constructed model is explained in Section 7.5.2. Finally, results are presented in Section 7.5.3.

7.5.2 Proposed model

This chapter is focused on the battery application in the EV. In this application, the main objective is to construct a regression model able to provide the response of the cell/battery for an arbitrary itinerary of the EV.

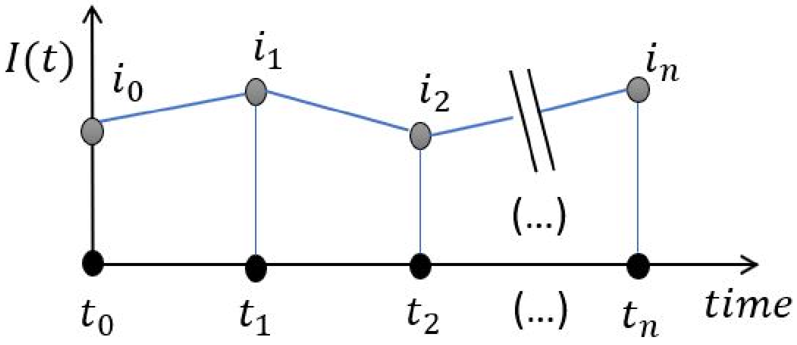

Figure 7.10 – Construction of a piece-wise linear intensity as a function of time.

The itinerary depends on the initial State of Charge (SoC), the loading and the environmental conditions. Therefore, the goal is to build a mathematical model which give us functions f_1 and f_2 as follows:

$$\begin{aligned} \mathrm{SoC}(t) &= f_1(\mathrm{SoC}(t=0), \mathrm{Load}, \mathrm{Environment}), \\ V(t) &= f_2(\mathrm{SoC}(t=0), \mathrm{Load}, \mathrm{Environment}). \end{aligned} \tag{7.20}$$

There are two immediate issues in developing the model in Eq. (7.20). The first is the high-dimensional problem of defining such an itinerary. The second is that the electrochemical model depends on a micro state. This implies that the dynamical evolution of the response depends on the time evolution of a large number of variables.

Considering the isothermal model of the cell and neglecting its time evolution, the load and the environment of an itinerary can be translated as the $I(t)$ demanded by the battery. In this way, the different itineraries can be modeled as different $I(t)$ for a given initial SoC.

It follows that a possible way to obtain a model by data regression is to parameterize the current instead. To this end, a piece-wise linear intensity is assumed and constructed as a function of the value of the current in some nodes as sketched Figure 7.10. The problem is that this approach forces us to work in a high-dimensional space with potentially hundreds of parameters for a one-hour itinerary. This idea was therefore discarded.

Another possibility consists in parameterizing an interval of time as a function of a given initial condition and a final current at the end of the time interval. Once this interval is parameterized, the only thing we have to do to complete a simulation is to join the solutions of each interval.

The problem here is due to the micro-scale modeling of the cell. This means that we will need to follow the micro-scale evolution of parameters such as $c_s(r, x, t)$ and $c_e(x, t)$ to compute and follow the time evolution of macroscopic parameters such as $V(t)$ and the $SoC(t)$. Therefore, this second idea produces hundreds of inputs or outputs on the modeled interval.

Nevertheless, analytical means can be considered to reduce the number of input and output parameters to make this second idea feasible. Sometimes, variables at the macro scale, which depend on a high number of parameters in the micro-scale, can be reduced to a simple expression. In this way, macroscopic parameters (surface SoC, bulk SoC and voltage) are used to reproduce the battery response, assuming for now that the system will

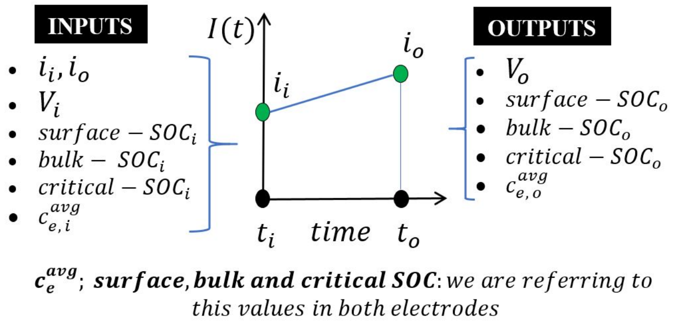

Figure 7.11 – Model of the parameterized interval. One regression is performed for each output. We will take for each output, the inputs which give us the best results. Here, subscript i refers to input values, while subscript o means output. Variable i refers to the current and the variable V refers to the voltage.

be sufficiently described by these variables. This is not a random choice. The bulk SoC, the surface SoC and the voltage for a given intensity depend on the dynamics of the micro-scale parameters c_s and c_e.

This approach is extended by predicting the micro-scale parameters of interest using only the above-mentioned macro-scale variables. Concretely, depletion and saturation are predicted adding the critical SoC defined in Section 7.2.2. Furthermore, the average electrolyte concentration at each electrode, $c_{e,\mathrm{avg}}$, is added into the s-PGD model. In this way, Li^+ depletion in the electrolyte is controlled.

To summarize, the s-PGD model retains only field variables relevant to estimation and control applications in the micro and macro scale. The great advantage of employing this approach is that the s-PGD model can predict the time evolution in all the scales observing only a few macro-scale variables. Proofs of this assertion are included in Section 7.5.3.

In Fig. 7.11, the proposed model is sketched. In this model, a time interval $\Delta t = t_o - t_i$ is parameterized as a function of given initial conditions at the beginning of the interval and the final current at the end of the interval.

A different PGD regression model will be constructed for each output. This model provides us with a forecast of the outputs Δt seconds in the future, taking the corresponding inputs into the regression. Note that it is not necessary to take all the inputs shown in Fig. 7.11 to perform the regression. For each output, the inputs which give the best results are taken.

A polynomial basis is selected to use the s-PGD explained in Section 2.2 with the electrochemical model. The motivation for this choice is the requirement for a simple model that can be integrated in the SimulationX model of the EV.

Therefore, the expression of the output voltage as a function of all the relevant parameters will take the form

$$V_o = g(s^1, ..., s^6) = \sum_{m=1}^{M} \prod_{k=1}^{6} \vartheta_m^k(s^k), \tag{7.21}$$

where:

$s^1 = i_i$, $\quad s^2 = i_o$, $\quad s^3 =$ surface SoC (anode)

$s^4 =$ surface SoC (cathode), $\quad s^5 =$ bulk SoC (anode), $\quad s^6 =$ bulk SoC (cathode), and ϑ_m^k are the one-dimensional functions constructed with different polynomial bases according to the Modal Adaptivity Strategy (MAS) explained in Section. 2.2.

7.5.3 Results

In this section, we analyze an example cell described in [Torchio *et al.* 2016]. Its parameters are detailed in Appendix E.

As already described in Section 7.5.2, polynomial bases are used for the one-dimensional functions of the s-PGD regression introduced in Sect. 2.2. The MAS is used, starting with low-degree approximations and finishing with higher-degree approximations.

The surrogate input to describe an itinerary, namely $I(t)$, is considered to be polygonal within each Δt. This assumption is made because, in principle, Δt is small enough to consider that the current has a linear profile between any two consecutive time instants.

It is observed that the method chosen to extract and to select the data for the training set has a significant impact on the regression results. The regression is done performed on sparse data, because of the high dimensionality of the problem. For this reason, the sampling strategy is critical to ensuring the good predictive capabilities in the model.

A simple way to obtain a good training set is to consider the current nodes of the itinerary $I(t)$ (defined as in Fig. 7.10) as different parameters (dimensions $i_0, \ldots, i_n$) of the problem. We remind ourselves that the real dimensions of the model proposed are the ones shown in Fig. 7.11, but for the sampling $i_0, \ldots, i_n$ are selected to be used. The reason for this choice is that it is not possible to reconstruct the whole micro-scale state with the few dimensions which are chosen in Fig. 7.11. The whole micro-scale state is needed to run the model to obtain the training set.

In order to obtain different $I(t)$ values, the Latin Hypercube Sampling (LHS) method is employed in the dimensions $i_0, \ldots, i_n$. The sampling process described is repeated for different initial SoC of the cell. Then, when sampling is finished and the itineraries of the the sampling are simulated, the different results of the variables of interest (SoC, V, ...) are split into different intervals of size Δt to perform the regression via the s-PGD.

One way to improve the sampling described above is the following. The LHS which is used in this work (Matlab function `lhsdesign()`) produces normally oscillating $I(t)$ functions. It is convenient to enrich the training set by e.g. adding some $I(t)$ with constant current profiles or formed of 2-4 step functions. In this way, the regression is more adapted to current profiles representative of a constant discharging or charging of the battery and it can take into consideration this type of behavior that otherwise would be underestimated. Furthermore, in doing this, the training set is more adapted to simulations that attain greater depths of discharge (because, for example, some high constant current profiles are added in the training set).

In the results that follow, a regression is obtained using a sampling composed of 5-minute itineraries ($\Delta t = 15$ s is used for the regression). These results are shown in Figs. 7.12, 7.13, 7.14 and 7.15. This regression turns out to be very accurate for itineraries of 5 minutes, where the relative error is always under 1 % in all the tests.

This regression model can be used for itineraries longer than 5 min, but the relative error starts to increase up to 1 %. In Figs. 7.14 and 7.15 we can see that the error can be acceptable for 10 minute itineraries.

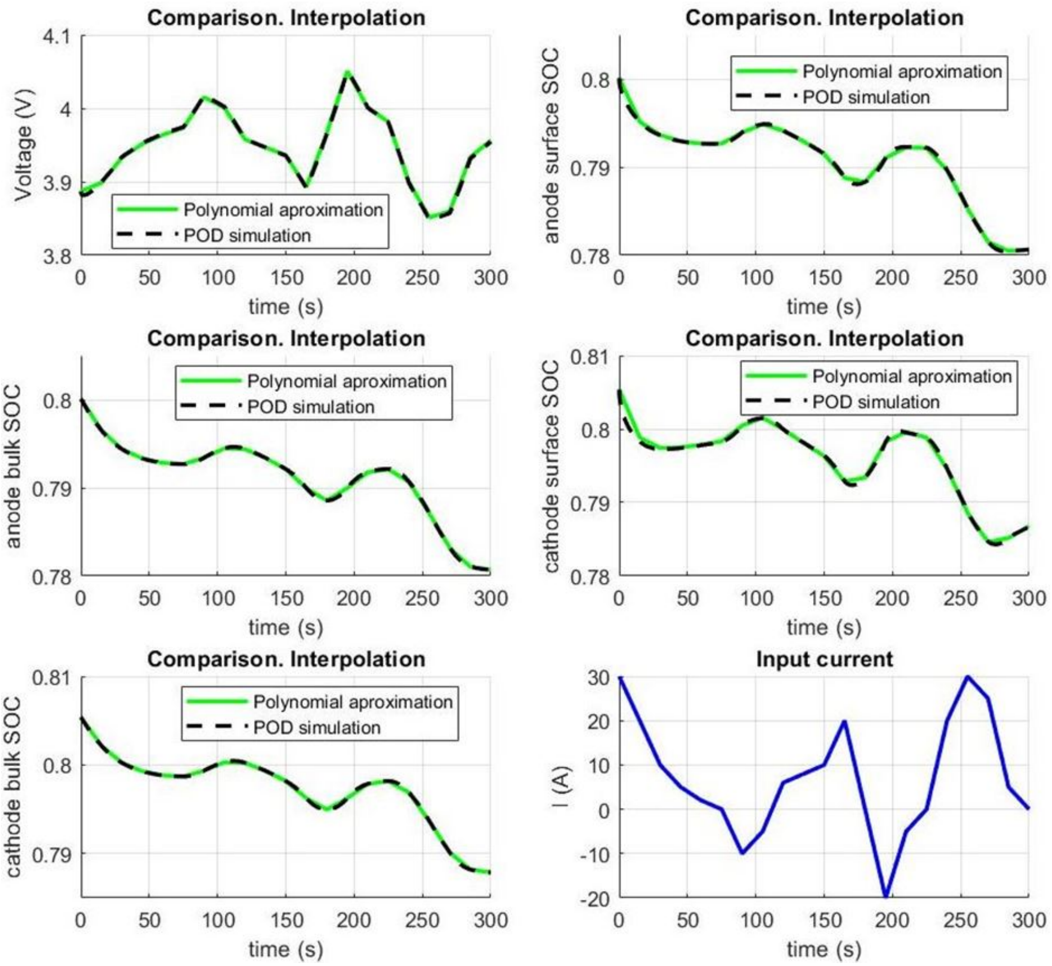

Figure 7.12 – Comparison of the results between the s-PGD model and the POD model in a 5 minute itinerary. The s-PGD model is extracted based on itineraries of 5 minutes. $\Delta t = 15s$.

The inputs used for the regression of each output were:

$$\begin{array}{rll}
V_o: & s^1 = i_o - i_i & s^2 = \dfrac{i_o + i_i}{2} \\
 & s^3 = \text{surface SoC (anode)} & s^4 = \text{bulk SoC (anode)} \\
 & s^5 = V_i & \\
\text{s-SoC}: & s^1 = i_i & s^2 = i_o \\
 & s^3 = \text{surface SoC} & s^4 = \text{bulk SoC} \\
 & s^5 = V_i & \\
\text{b-SoC}: & s^1 = i_i & s^2 = i_o \\
 & s^3 = \text{bulk SoC} &
\end{array}$$

where the s-SoC and the b-SoC refer to the surface SoC and bulk SoC respectively.

The MAS explained in Section 2.2 is used to determine the higher-degree

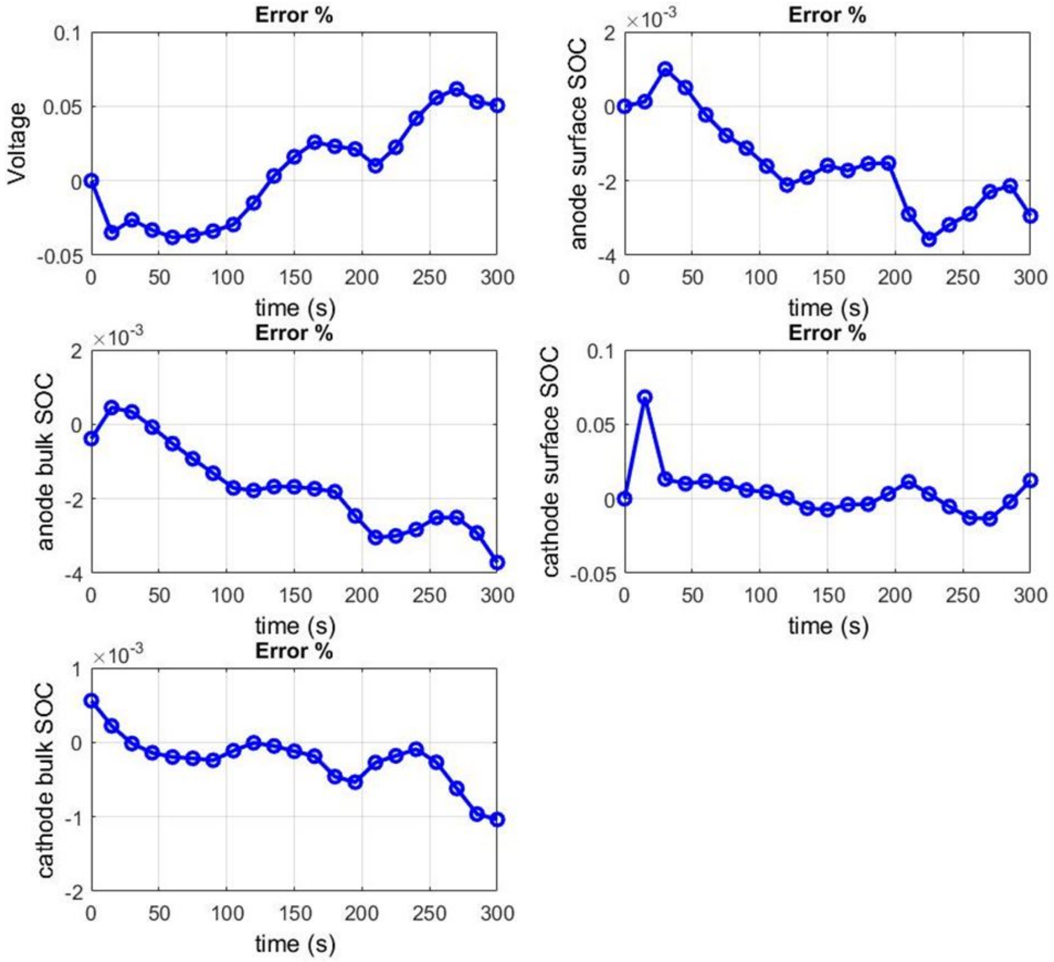

Figure 7.13 – Error between the s-PGD model and the POD model in a 5 minute itinerary. The s-PGD model is extracted based on itineraries of 5 minutes. $\Delta t = 15s$

approximations used. The results to apply the MAS are:

1. For the surface and bulk SoC, only polynomial basis of degree one (thus, linear) are used.

2. For the Voltage: a first group of modes is created with one-dimensional functions based on polynomial basis of degree one. Then, a second group of modes is created with one-dimensional functions based on polynomial bases of degree two.

This methodology can also be used with longer trajectories or smaller Δt. Consider, for instance, a regression obtained with a sampling composed of 10-minute itineraries ($\Delta t = 5$ s is used for this regression). The results are shown in Figs. 7.16 and 7.17. This regression is very accurate to compute 10-minute itineraries, where the relative error is under 1 % in almost all the checking set of data points.

Trajectories longer than 10 minutes can also be computed. While the error will naturally increase, it can be acceptable if the difference between T_{sim} and T_{reg} is not too large. Note

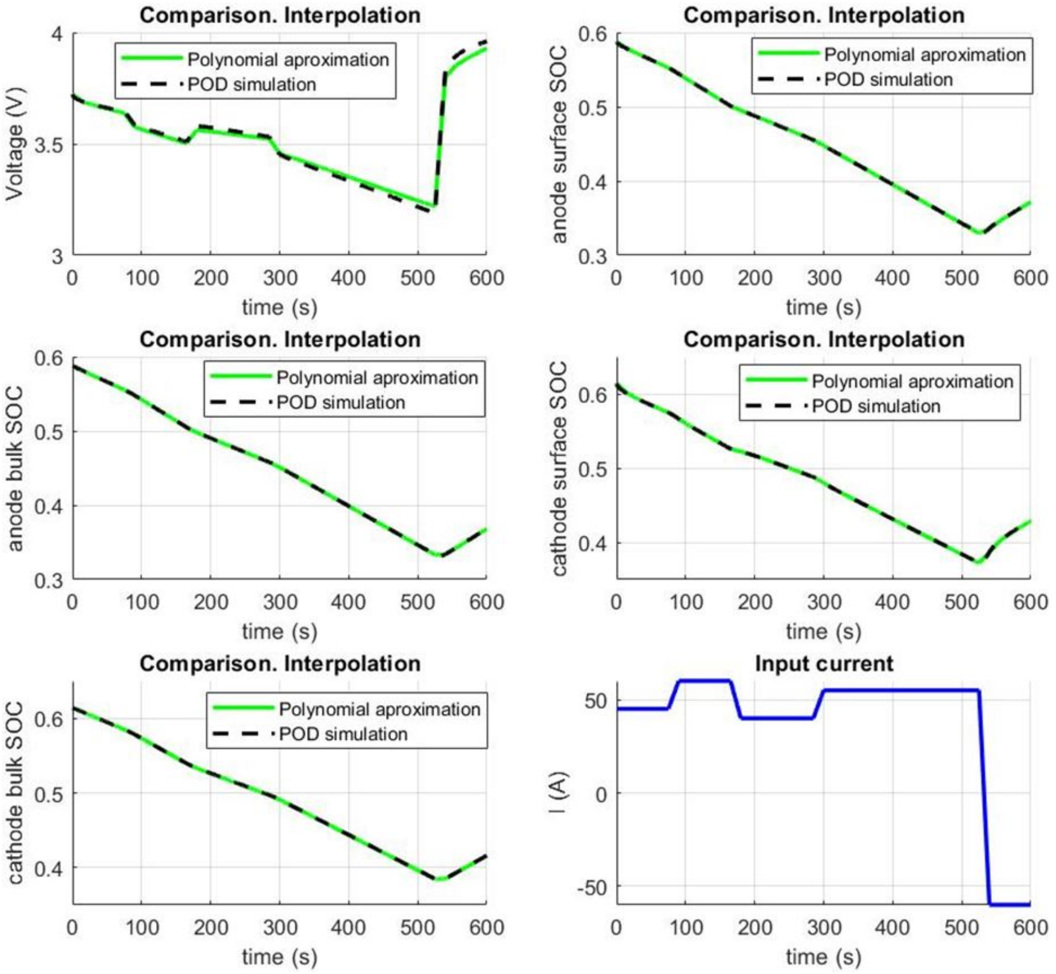

Figure 7.14 – Comparison of the results between the s-PGD model and the POD model in a 10 minute itinerary. The s-PGD model is extracted based on itineraries of 5 minutes. $\Delta t = 15s$

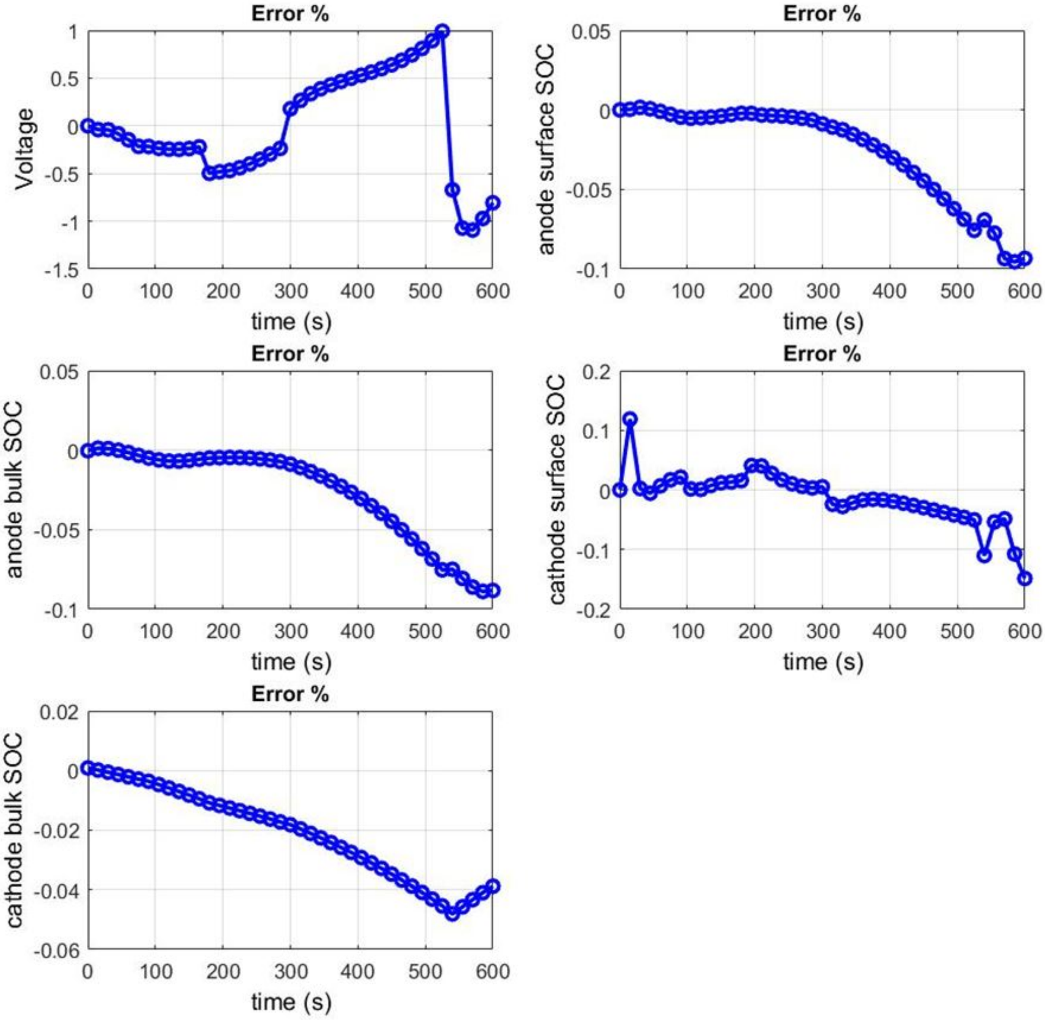

Figure 7.15 – Error between the s-PGD model and the POD model in a 10 minute itinerary. The s-PGD model is extracted based on itineraries of 5 minutes. $\Delta t = 15s$

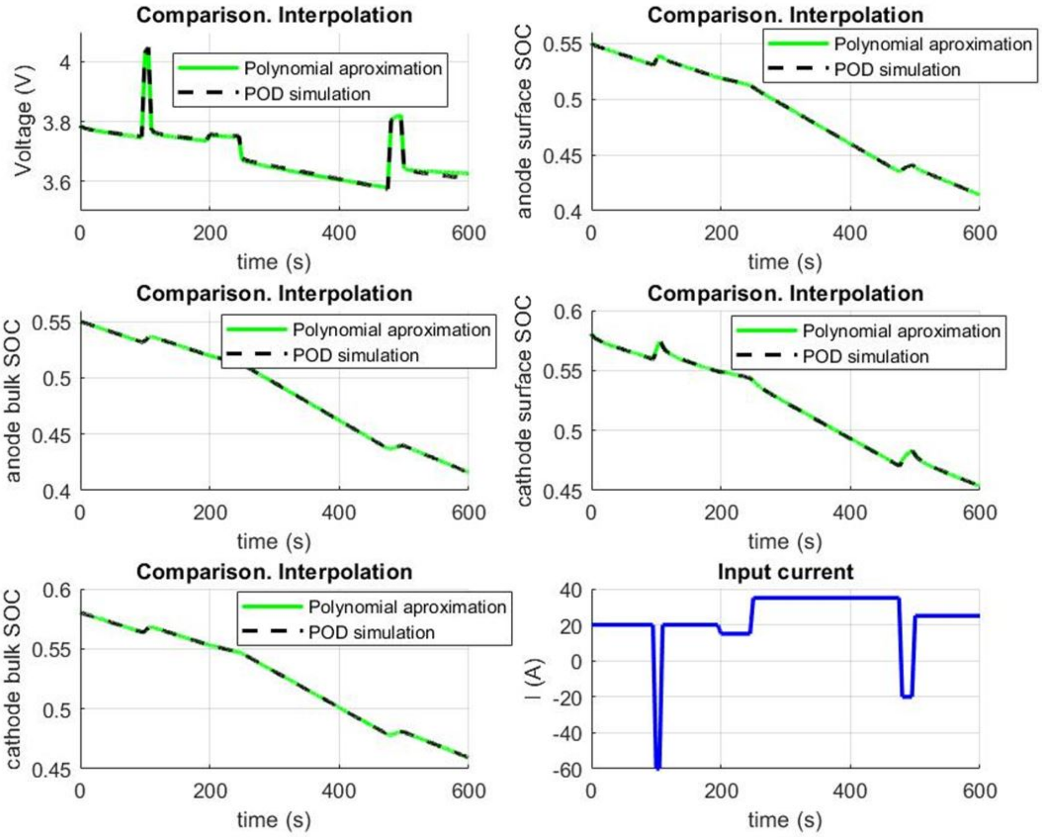

Figure 7.16 – Comparison of the results between the s-PGD model and the POD model in a 10 minute itinerary. The s-PGD model is extracted based on itineraries of 10 minutes. $\Delta t = 5s$

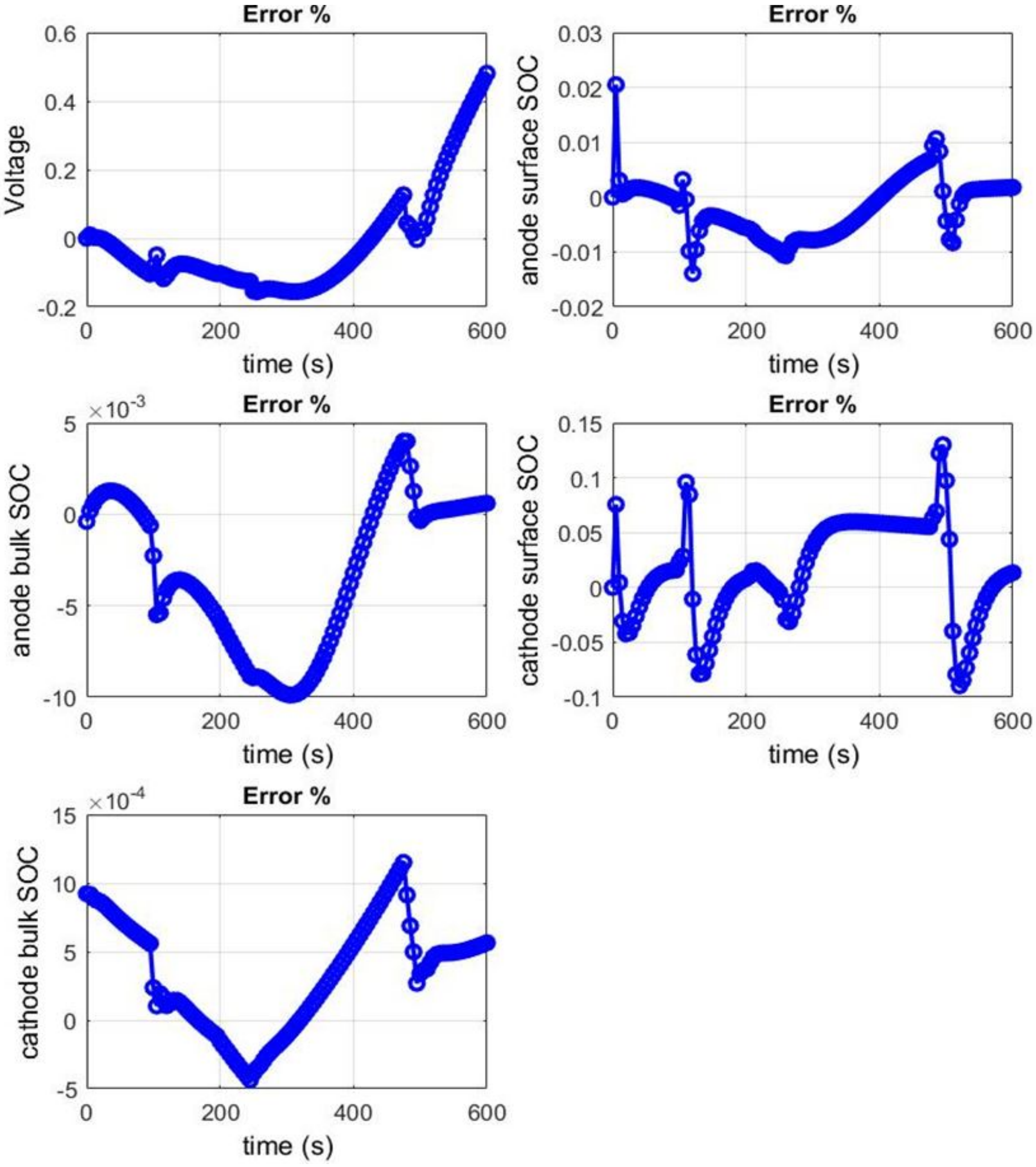

Figure 7.17 – Error between the s-PGD model and the POD model in a 10 minute itinerary. The s-PGD model is extracted based on itineraries of 10 minutes. $\Delta t = 5s$

that T_{sim} is the duration of the simulated itinerary, while T_{reg} is the equivalent for the sampling itineraries for the PGD regression.

The results for the regression shown in Figs. 7.16 and 7.17 are

1. For the surface and bulk SoC, only polynomial bases of degree one are used.
2. For the voltage, a first group of modes is created with one-dimensional functions based on polynomial bases of degree one. Then, a second group of modes is created with one-dimensional functions based on polynomial bases of degree two. Finally, a third group of modes is created with one-dimensional functions based on polynomial bases of degree three.

To summarize, the results of using the s-PGD in the critical SoC and in the c_e^{avg} are shown according to Section 7.5.2 (where their importance was discussed). Here, $\Delta t = 2s$ is used. The values are with respect to the negative electrode.

Results are shown in Figs. 7.18 and 7.19. These regressions are intended to reproduce ten-minute itineraries with an initial SoC of 85 %. We can observe that we can reproduce the results with a high degree of accuracy. Inputs used for these regressions are the same as those used in the voltage regression with $\Delta t = 15s$ (but using c_e^{avg} or the critical SoC instead for the voltage input), while polynomials of degree two were employed in the approximation.

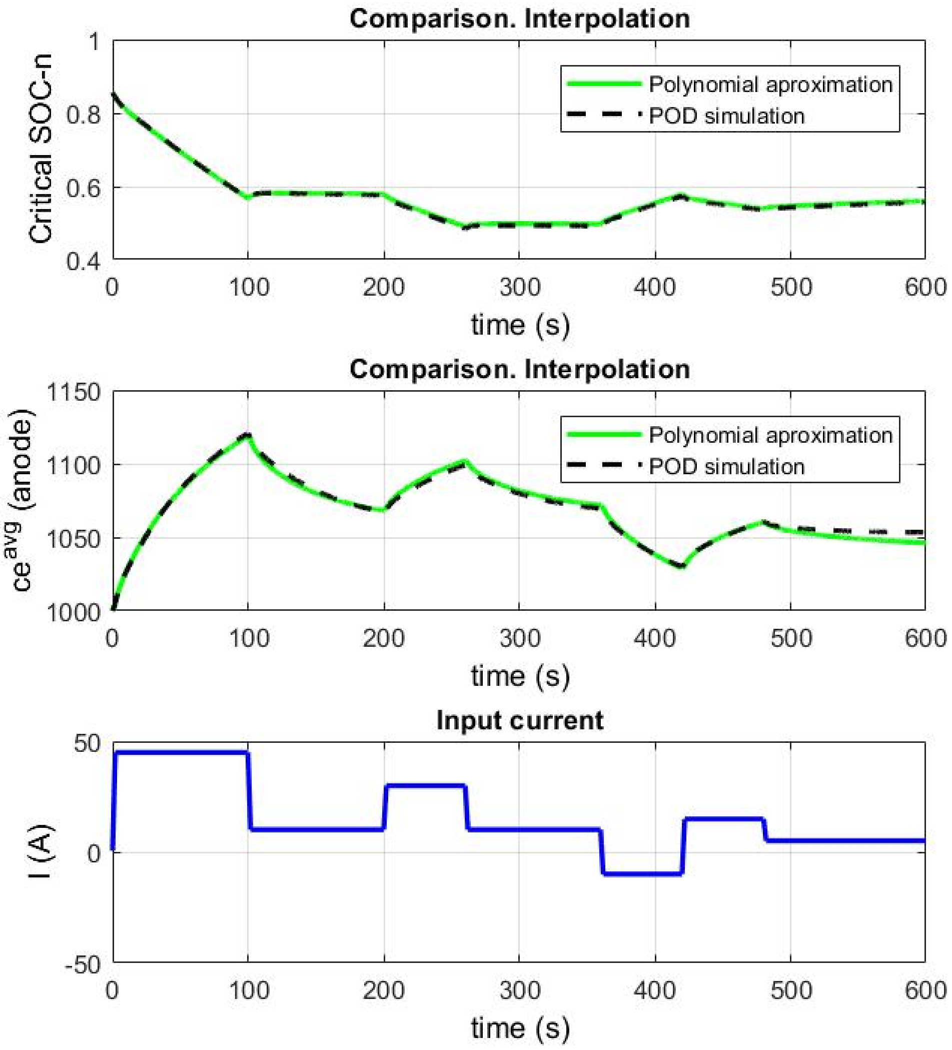

Figure 7.18 – Comparison of the results between the s-PGD model and the POD model in a 10-minute itinerary (critical SoC and c_e^{avg}). The s-PGD model is extracted based on itineraries of 10 minutes. $\Delta t = 2s$.

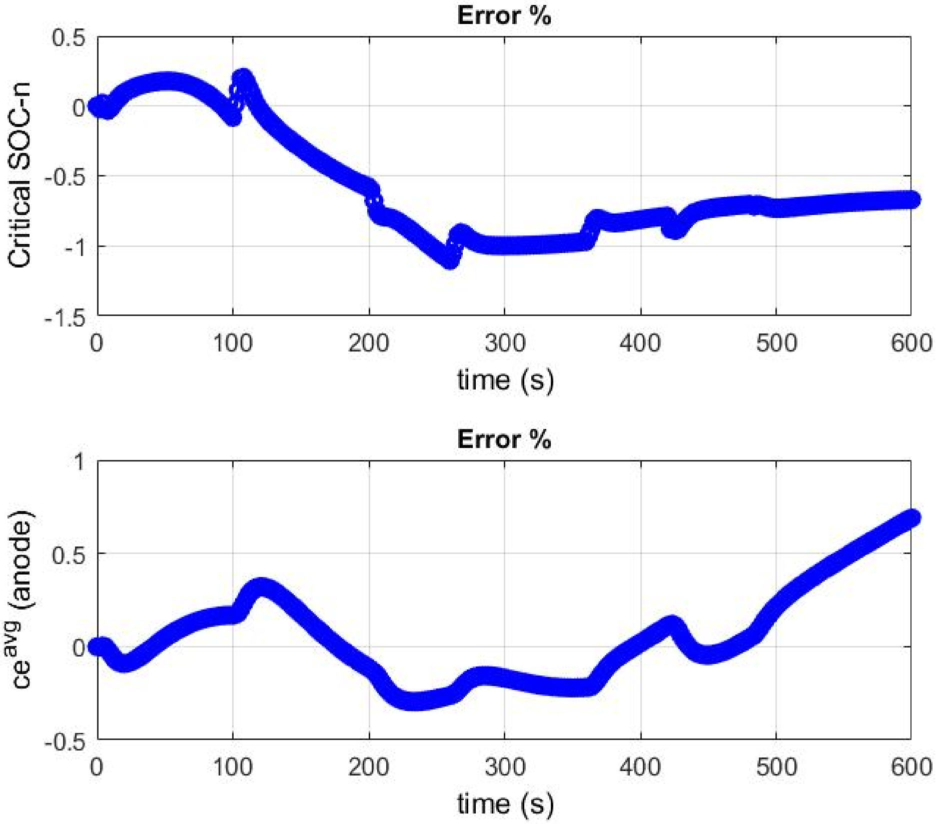

Figure 7.19 – Error between the s-PGD model and the POD model in a 10 minute itinerary (critical SoC and c_e^{avg}). The s-PGD model is extracted based on itineraries of 10 minutes. $\Delta t = 2s$.

7.6 Innovative planning algorithm with EV simulation and results

7.6.1 Introduction

In previous Section 7.5, an accurate s-PGD model of a battery cell is developed.

Due to its low computational cost, it can be perfectly integrated on-board of the EV as well as in system simulation tools such as SimulationX [*ESI ITI GmbH. Dresden, Germany*].

In fact, an innovative planning algorithm is created taking the above model in the following sections of this work. The great added value of this algorithm is its ability to make quick decisions based on very accurate predictions of the battery system while simulating the entire EV.

To do that, the s-PGD battery model is first integrated into an EV system using SimulationX (Section 7.6.2). Then, a procedure to adapt and modify the driving cycle is designed to keep the battery state in the correct operation range in function of the planned itinerary (Section 7.6.3). The big succcess here is being able to make fast decisions employing the highly-accurate predictions provided by the s-PGD model. This way, driving profiles can be recommended or imposed on the driver to guarantee durability and good long-life performance of the battery pack.

Furthermore, the planning algorithm can decide on the best possible itinerary considering different battery criteria (Section 7.6.4). To achieve that, different routes are simulated in real-time using the EV model created in SimulationX. As the simulation times of the s-PGD model are extremely fast, this goal is perfectly reached.

Two criteria are tested:

The first one is based on choosing the fastest itinerary by imposing a maximum allowable depth of discharge. Furthermore, the driving cycle is also corrected to fit an appropiate operation range for the battery cells.

On the other hand, the second criterion is based on choosing the itinerary which achieves the minimum depth of discharge while monitoring that the travel time does not exceed a maximum specified value. In addition, the driving cycle is corrected as done in the first criterion.

In addition, other proof of concept is carried out simulating a BMS in SimulationX (Section 7.6.5). This proves that a BMS industrial application can be developed using the present approach. Therefore, the methodology is discused to be an excellent first step to implement the required new generation of BMS for the automotive industry due to the accuracy of the proposed model and the low computational resources required.

7.6.2 Constructing a digital twin of the electric vehicle system

In this section, the s-PGD model developed in Section 7.5 (specifically the model with $\Delta t = 2$ s) is inserted in a HEV/EV model to simulate the whole vehicle under realistic operating conditions. To this end, the system simulation software *SimulationX* (ESI ITI GmbH, Dresden, Germany) is used. This is a tool in the field of multi-physics system simulation. It is based on the *Modelica* language, an object-oriented, declarative, multi-domain modeling language for component-oriented modeling of complex systems. See `http://modelica.org` for more information.

The neessary steps to insert the s-PGD model into a SimulationX model of the EV are summarized in Fig. 7.20.

Firstly, a battery package is created with all the elements needed for the battery model. This package is written using Modelica and encapsulates all elements needed to run the

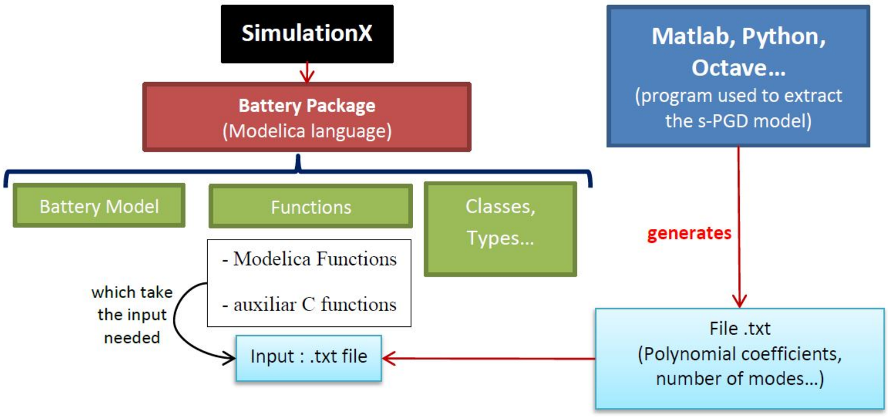

Figure 7.20 – Diagram showing the data flow for the *s*-PGD model when embedding in a SimulationX model.

model such as types, classes and functions. In addition to describing equations in its native, equation-based form, Modelica provides a means of interfacing components to external C functions. A number of utility functions are created in C language such as functions for reading the input file containing the polynomial coefficients of the *s*-PGD solution. This file is generated by the program used to compute the *s*-PGD solution. By exploiting the Modelica external C interface, the regression information stored in the file can be tranparently loaded into the Modelica battery modeling components as a battery component that reproduces the *s*-PGD model in the full EV system simulation, Fig. 7.20.

Induction motors (for example the Tesla Model S) or synchronous motors (for example the Renault Zoe) are more widely used than the DC motors in the EV. However, for simplicity, and without loss of generality, we will model in this example the electric motor as a DC motor, which can be more often found in HEV applications.

A DC/DC converter is used to control the motor through the applied voltage. The model used in the converter is taken from [Winter *et al.* 2015]. Elements such as damping, inertias, springs, transmissions, rotational transformations and masses are used to model the mechanical part of the vehicle.

The main forces acting against the movement of the car are the aerodynamic resistance, the rolling resistance and the grade resistance. Therefore, the tractive effort must be higher than these resistance forces to achieve the desired acceleration.

In Appendix F the interested reader can find the main parameters used in this example. An actual ten-minute itinerary is used between Avenida de Valencia, E-46891 El Palomar and Plaza Barranc Marques, E-46890 Agullent, both in Spain. This itinerary is shown in Fig. 7.21.

Moreover, the SimulationX model of the vehicle is connected to OpenStreetMap (OSM) [OpenStreetMap contributors 2017] to download the data for an specified itinerary such as maximum speed limitations or the different sections of the road. This way, an expected driving cycle (expected speed curve in function of the trajectory position; $v(s)$) can be designed for a given itinerary. To do that, a specific interface was created with HTML and JavaScript to extract the OSM data. Then, these data are communicated to SimulationX with Python.

Figure 7.21 – Picture of the itinerary simulated by the SimulationX EV model. It corrsponds to a ten-minute itinerary between Avenida de Valencia, E-46891 El Palomar and Plaza Barranc Marques, E-46890 Agullent, both in Spain.

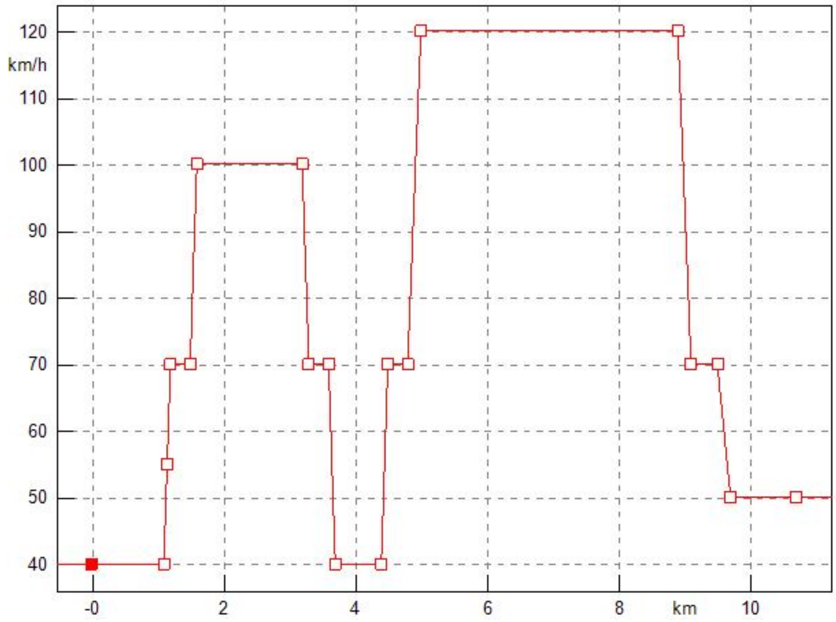

Figure 7.22 – Velocity(position) of the itinerary

The expected driving cycle $v(s)$ is obtained considering that the speed in each road section is the permitted maximum speed. In Fig. 7.22, this velocity function is shown, while in Fig. 7.23 the velocity demanded by the driver as a function of time is shown.

A PI controller is used to ensure that the system follows the response $v(s)$. In our case, the controller sends a signal to the actuator of the control system as a function of the error between the sensed speed and the desired speed. The controller output can be expressed as:

$$u(t) = K_p \cdot e(t) + K_i \cdot \int_0^t e(\tau)d\tau,$$

where $e(t)$ is the error between the sensed speed and the desired speed and K_p and K_i are the proportional and integral gains respectively. In this way, the driver behavior is modeled by the PI controller which must be correctly parameterized to follow the desired speed response $v(s)$.

In addition, the hill gradient angle γ is also obtained taking the altitude of each point in the road provided in the OSM data:

$$\gamma(s_i) = \arctan(\frac{h_{i+1} - h_i}{s_{i+1} - s_i}), \tag{7.22}$$

where s_i refers to the discretized i-th point of the trajectory position and h_i is the discretized i-th point of the altitude function for the itinerary.

This way, the rolling and grade resistance can be updated and computed for each road position in function of the selected itinerary:

$$R_r(s) = C_r \cdot m \cdot g \cdot \cos(\gamma(s)),$$

$$R_{\text{grade}}(s) = m \cdot g \cdot \sin(\gamma(s)),$$

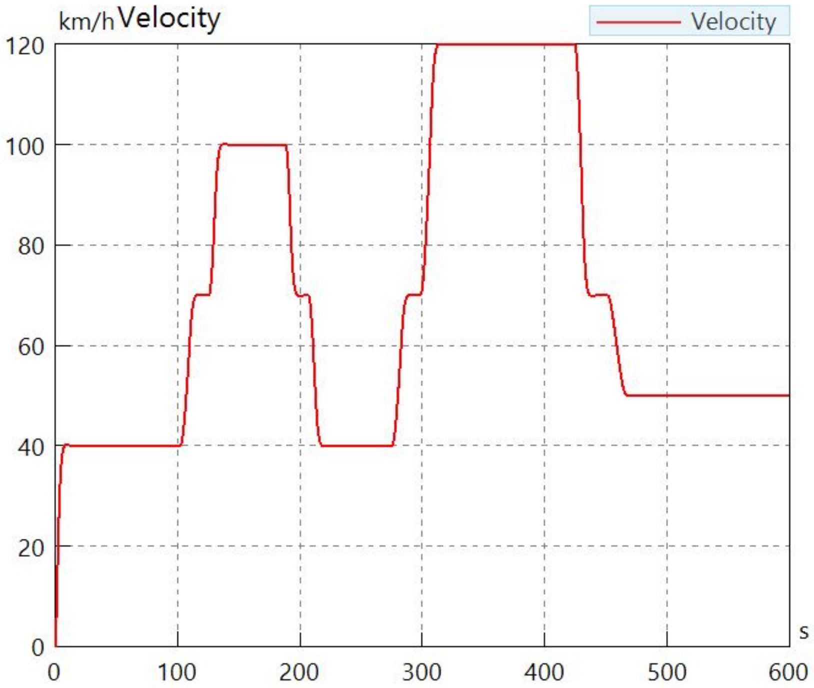

Figure 7.23 – Velocity response demanded by the driver

.

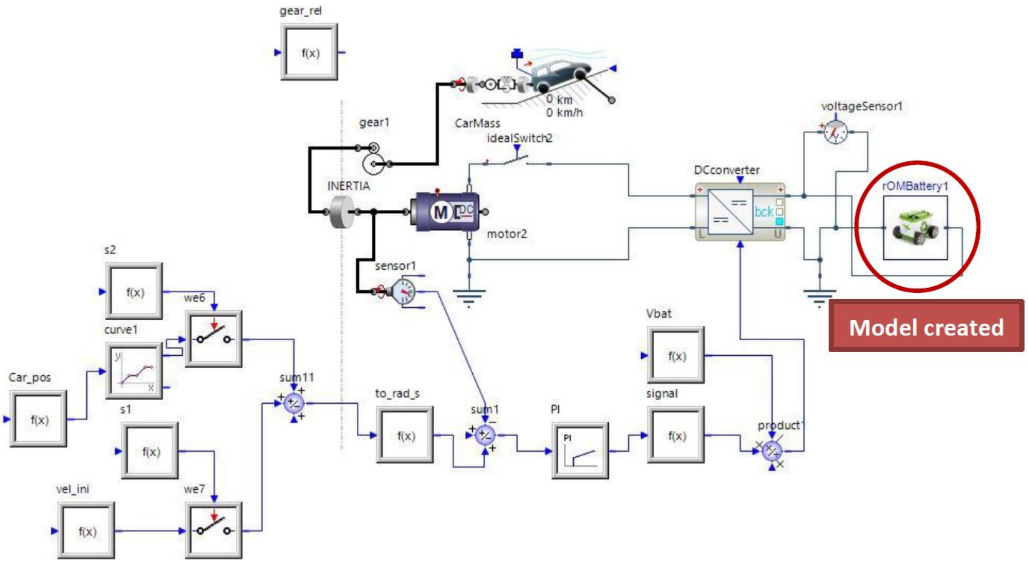

Figure 7.24 – Graphical view of the EV model created in SimulationX. In the red circle, the battery box created with the s-PGD solution is highlighted

where m is the vehicle mass and C_r is the rolling resistance coefficient.

On the other hand, the aerodynamic resistance is also considered in function of the real speed of the vehicle, which depends on the expected driving cycle obtained with OSM:

$$R_{\text{aero}}(s) = \rho/2 \cdot A_{ref} \cdot C_w \cdot v(s)^2,$$

where ρ is the air density, C_w is the air drag coefficient, V is the vehicle speed and A_{ref} is the reference area.

The parameter values and the details of the vehicle simulated in this work can be found in Appendix F.

In Fig. 7.24, the SimulationX battery box model is shown. In Fig. 7.25, the SimulationX user parameter interface demonstrates how a user can select the number of (identical) cells are connected in series and in parallel. More than one type of cell can be used to create the battery by joining different battery boxes.

Furthermore, the possibility of adding an internal resistance to the model is created. In this way, the user can model linear voltage drops such as the contact resistance when the cells are connected through the collectors. In Fig. 7.26, we observe voltage variation in a cell due to the electrochemical model. In Fig. 7.27, we can observe the voltage variation in a cell due to the internal resistance (A resistance $R = 0.001\ \Omega$ is selected). In Fig. 7.28, a comparison of the bulk SoC and the surface SoC is shown. Finally, the critical SoC and the $c_{e,\text{avg}}$ in the negative electrode can be noticed from Fig. 7.29.

7.6.3 Adapting driving behaviour in function of an accurate and fast computation of battery needs

Durability and good long-life performance of battery cells is a crucial property to ensure. To achieve that, it is important to guarantee that cells are maintained in a suitable operation range. For example, it is important to accurately predict when depletion and saturation

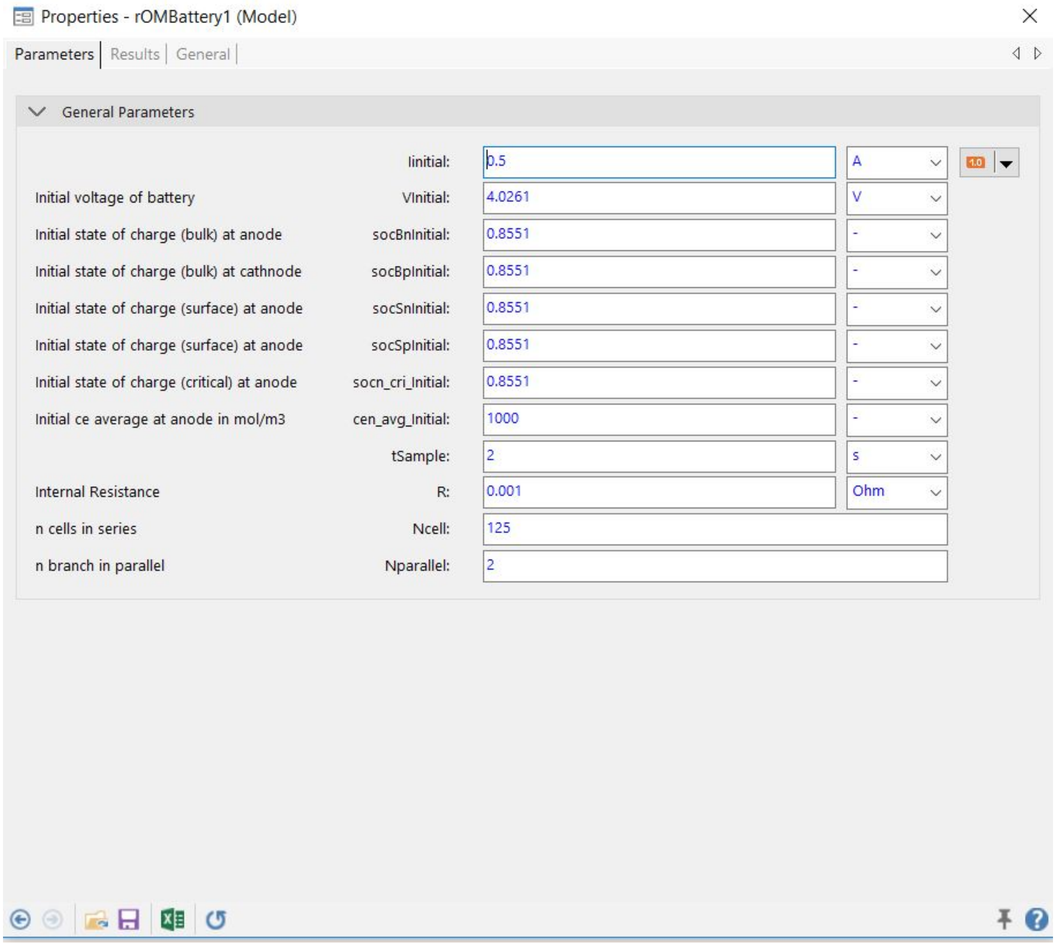

	Iinitial:	0.5	A
Initial voltage of battery	VInitial:	4.0261	V
Initial state of charge (bulk) at anode	socBnInitial:	0.8551	-
Initial state of charge (bulk) at cathnode	socBpInitial:	0.8551	-
Initial state of charge (surface) at anode	socSnInitial:	0.8551	-
Initial state of charge (surface) at anode	socSpInitial:	0.8551	-
Initial state of charge (critical) at anode	socn_cri_Initial:	0.8551	-
Initial ce average at anode in mol/m3	cen_avg_Initial:	1000	-
	tSample:	2	s
Internal Resistance	R:	0.001	Ohm
n cells in series	Ncell:	125	
n branch in parallel	Nparallel:	2	

Figure 7.25 – Parameters of the SimulationX model created using the *s*-PGD solution

Figure 7.26 – Cell voltage predicted by the *s*-PGD model during the simulated itinerary.

Figure 7.27 – Voltage drop produced by the internal resistance in a cell during the simulated. itinerary

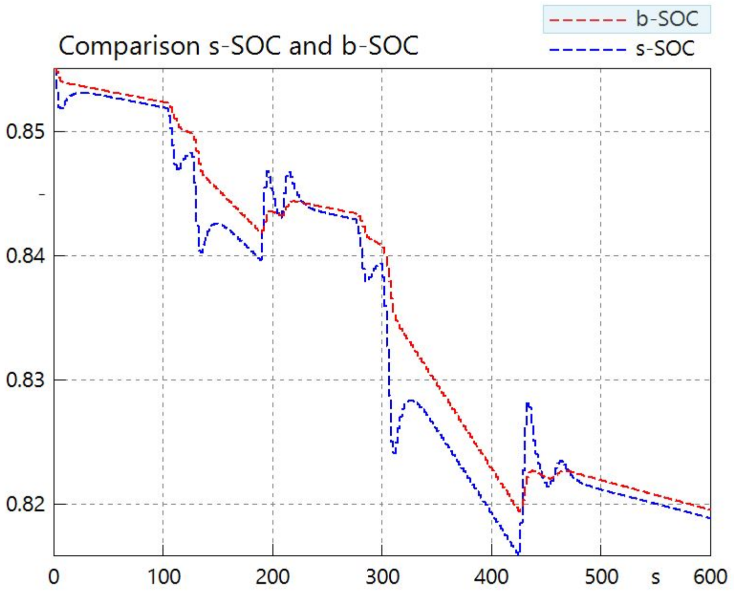

Figure 7.28 – Comparison between the bulk SoC and the surface SoC in the ten-minute itinerary.

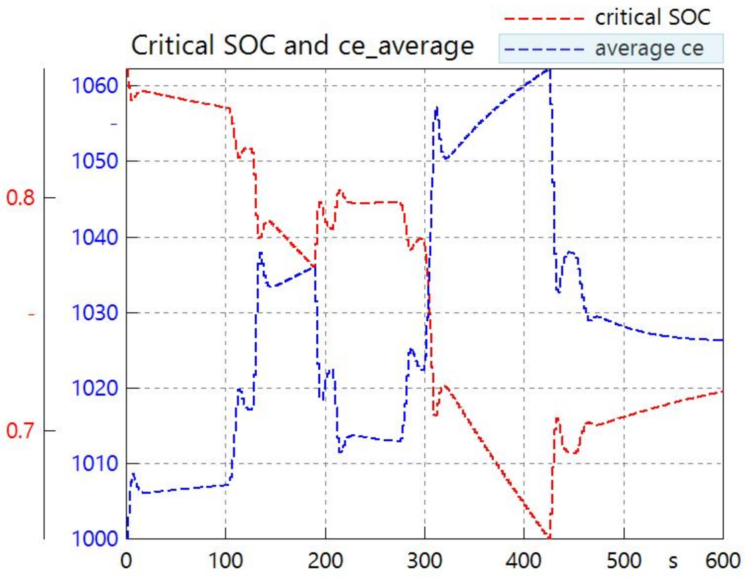

Figure 7.29 – Comparison between the critical SoC and the c_e^{avg} in the negative electrode during the simulated itinerary.

occurs in the electrodes as well as Li^+ depletion in the electrolyte. The reason is that these phenomenons can cause problems such as a sudden loss of power.

Furthermore, although it is true that a cell can supply a higher current than nominal for a short period of time, if the peaks and duration of these transient periods are not controlled, the stress to which the cell is subjected can advance its deterioration.

It is not surprising then, that industry is requiring more accurate and real-time tools to predict these effects in order to act accordingly. For this reason, we are proposing the integrated s-PGD approach to monitor these processes. In fact, this can be easily carried out supervising the variables: surface SoC, critical SoC and $c_{e,avg}$ defined in Section 7.2.2 and 7.5.2.

Therefore, the s-PGD predictions are employed to anticipate when these effects will occur and adapt the driver's driving profile accordingly, preventing the battery from entering dangerous operating zones and reducing the electrochemical stress of the cells. For this reason, an algorithm is designed in SimulationX, simulating the whole EV for the desired itinerary with the s-PGD battery model to then, change the speed driver's profile if problems are expected to arise.

The global algorithm to adapt the speed profile is composed of two steps.

First Step: Guaranteeing a minimum final SoC. The algorithm checks if the selected route can be traveled with the initial speed reference curve without overtaking a maximum pre-specified Depth of Discharge (DoC). In other words, the algorithm checks if a minimum SoC is achieved at the end of the trajectory. If the SoC is below this threshold, the expected driving cycle is changed until the condition is satisfied. Therefore, the algorithm simulates the EV model and monitors the final SoC. Furthermore, the procedure described in Algorithm 1 shows the details of this first step. In this procedure $bSoC$ refers to the bulk SoC, RS refers to road section, v_{per} refers to the maximum permitted speed in a RS, f defines a factor to determine the maximum percentage allowed to decrease the expected driving cycle and L_1 defines the SoC threshold to be satisfied at the end of the itinerary.

Algorithm 1 First Step. Guaranteeing a minimum final SoC

```
procedure FirstStep
    Simulate $s$-PGD–EV system.
    while $bSoC(t_{end}) < L_1$ do
        Identify traveled RSs when $bSoC = L$
        Define set $\mathcal{T}$ containing the above RSs
        Find RS in $\mathcal{T}$ with the highest speed.
        Take max. speed in the found RS: $v_{sect}$.
        while $v_{sect} < f v_{per}$ do
            Find next RS in $\tau$ with the highest speed.
            Take max. speed in the found RS: $v_{sect}$.
            if $v(t) < f v_{per}(t)$ for $\forall t$ then
                End algorithm. Reject itinerary.
        Reduce $p\%$ the speed in the chosen section
        Simulate $s$-PGD-EV system with new $v(s)$.
    Report final values of the $s$-PGD–EV system
```

Second Step: Finding a suitable and safe battery operation range. Firstly, the algorithm checks if depletion or saturation happens by monitoring the critical SoC and $c_{e,avg}$.

Figure 7.30 – Smoothing procedure of the reference driving cycle taken by the control $v(s)$ when high discharge/charge rates happens when accelerating. This is used by the second step (See Algorithm 2) of the general procedure to adapt the driving cycle. $v(s)$ and α refers to the values before the modification and $v'(s)$ and α' refers to the values after the modifciation.

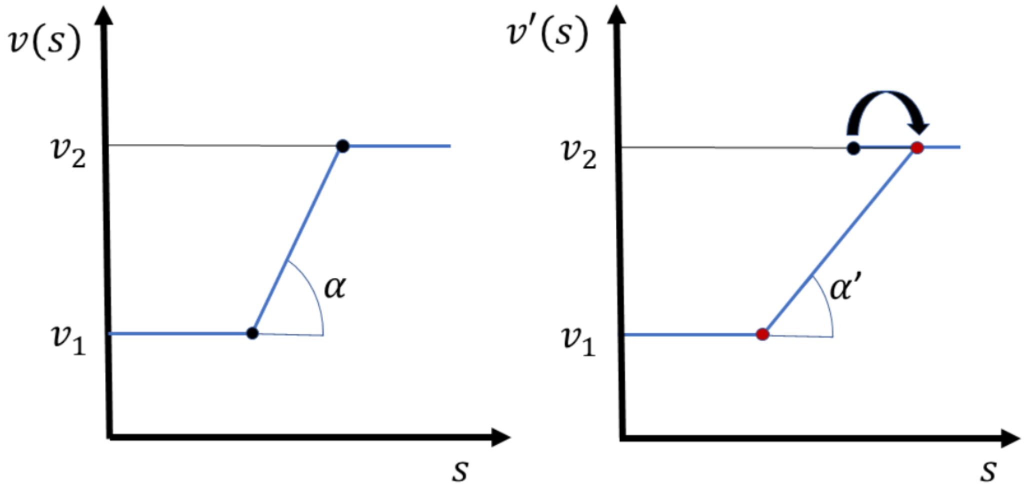

Specifically, this process verifies that the above variables do not reach a predefined threshold value. Secondly, the algorithm control the difference between the surface SoC and bulk SoC to avoid strong electrochemical stresses. The reason is that there will be a significant difference between bulk and surface SoC in high discharge and charge rates. And this relationship will be further exacerbated as the charge/discharge rates get stronger. Therefore, the measure of this difference gives a good estimator about the electrochemical stress that the cell is suffering. If the measured difference reach a predefined threshold, a trigger is activated. Then, the smoothing procedure of Figure 7.30 is employed. The idea is to reduce the acceleration demanded to the EV, decreasing accordingly the demanded intensity peaks. Therefore if the trigger is activated, the acceleration is reduced. Furthermore, the procedure described in Algorithm 2 shows the details of this second step. In this procedure *sSoC* refers to the surface SoC, RSC refers to the reference speed curve taken by the control system $v(s)$, *Dep* refers to a boolean variable that indicates if depletion happens when true, *Sat* refers to a boolean variable that indicates if saturation happens when true.

To illustrate, the algorithm, a travel example considering the following start and end points:

- Start point: Mittelstraße 14, 04838 Eilenburg, Germany
- End point: Bunitz, 04838 Doberschütz, Germany

In addition, the itinerary selected in OpenStreetMaps is the one shown in Figure 7.31.

The reference speed curve changes from the one in Figure 7.32 to the one in Figure 7.33 after applying the described algorithm. Comparing the two figures, the smoothing procedure can be observed.

Moreover, the predicted values concerning the surface and bulk SoC for the initial driving cycle are the ones in Figure 7.34.

Algorithm 2 Second Step: Finding a suitable and safe battery operation range.

```
procedure SecondStep
    Simulate $s$-PGD–EV system.
    Check depletion and saturation: $Dep$, $Sat$.
    while $Dep$ or $Sat$ are True do
        Identify problematic region: $R_i$.
        if same $R_i$ modified $n$ times in a row then
            Reduce $p\%$ the speed increment in $R_i$.
            if $v(t) < fv_{per}(t)$ for some $t$ then
                End algorithm. Reject itinerary.
        else
            Smooth the RSC in the chosen $R_i$.
        Simulate $s$-PGD–EV system with new $v(s)$.
        Check depletion and saturation: $Dep$, $Sat$.
    while $\max(bSoC - sSoC) > L_2$ do
        Identify problematic region: $R_i$.
        if same $R_i$ modified $n$ times in a row then
            Reduce $p\%$ the speed increment in $R_i$.
            if $v(t) < fv_{per}(t)$ for some $t$ then
                End algorithm. Reject itinerary.
        else
            Smooth the RSC in the chosen $R_i$.
        Simulate $s$-PGD–EV system with new $v(s)$.
    Report final values of the $s$-PGD–EV system
```

Figure 7.31 – In red: example itinerary taken for Section 7.6.3. It is also the example itinerary (number one) taken for Section 7.6.4

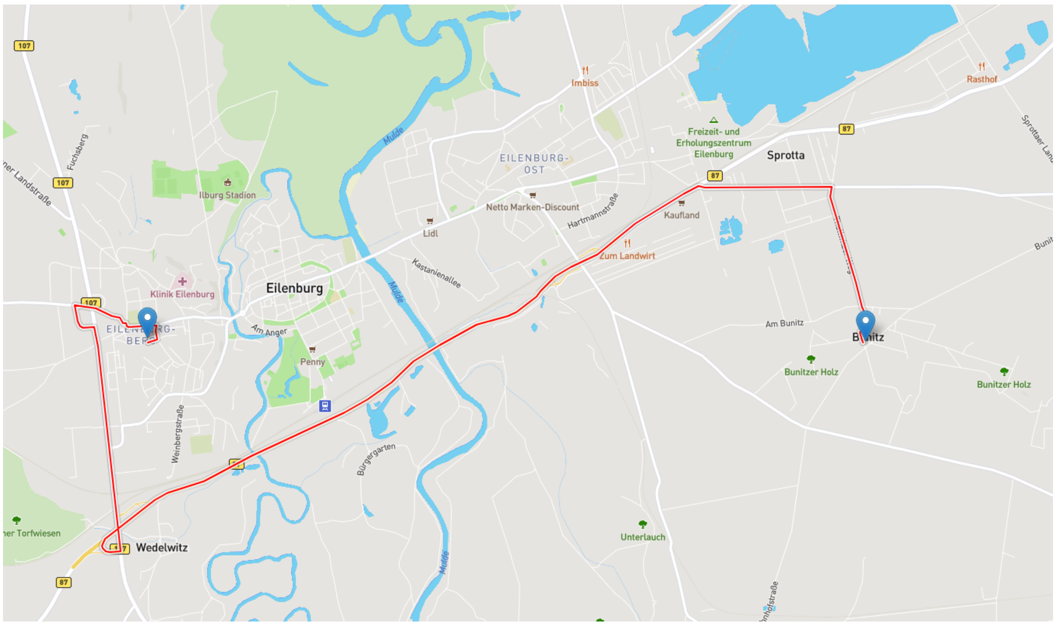

Figure 7.32 – Initial reference speed for the example of Section 7.6.3. The SimulationX model translates the reference $v(s)$ to $v(t)$. It is important to note that this is not the real speed of the EV but the reference one taken by the control. We start with this type of reference curves to minimize the travel time. If problems arise, the smooth procedure is applied.

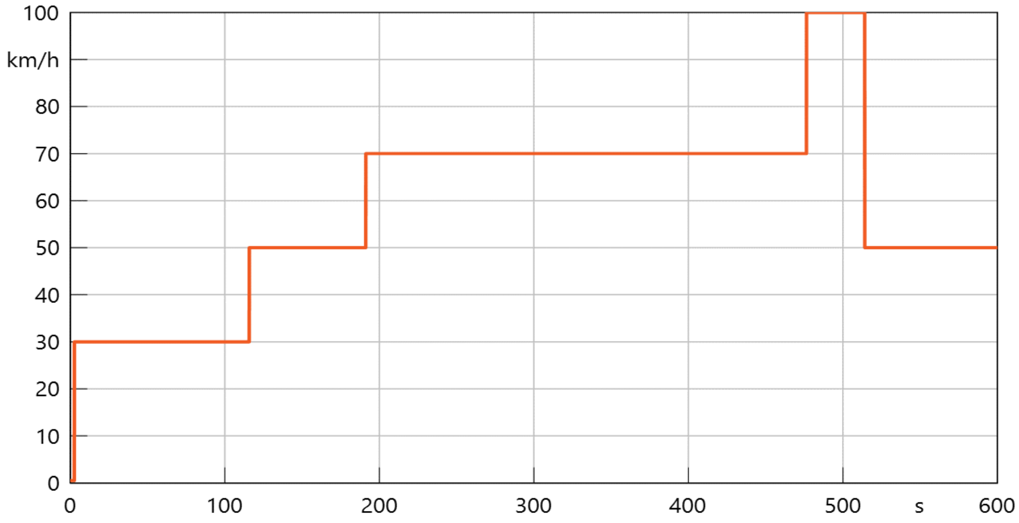

Figure 7.33 – Reference speed after applying the algorithm of Section 7.6.3. Note that the SimulationX model translates the reference $v(s)$ to $v(t)$.

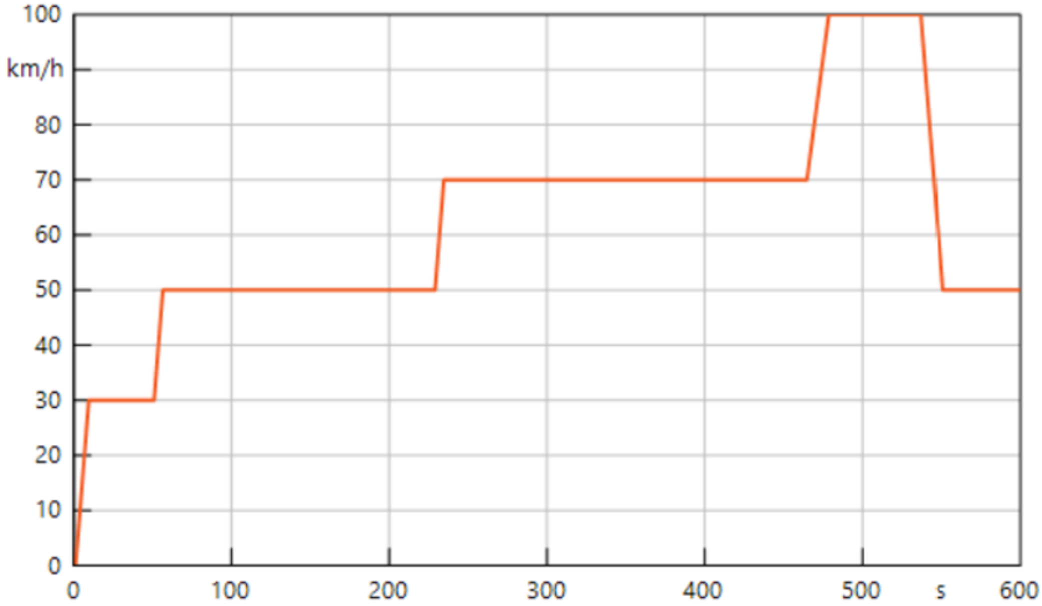

On the other hand, the time evolution of the bulk and surface SoC once the algorithm adapted the driving cycle are shown in Figure 7.35. Comparing Figures 7.34 - 7.35, it can be observed that the difference between the surface SoC and the bulk SoC is decreased thanks to the modified driving cycle. This way, as said previously, the electrochemical stress of the cell is reduced. Also, the minimum final SoC imposed by the user is satisfied (in this case 83 %) and the condition to avoid depletion or saturation was verified by the algorithm.

7.6.4 Algorithm to select the best itinerary

The EV system with the s-PGD model can also be employed to decide the best possible route when considering battery specificacions. Here, an algorithm is considered to do this choice in function of two criteria.

The first one is to look for the fastest route while ensuring a user-defined minimum final SoC. This way, the itineraries which produce an unacceptable DoC are discarded and the fastest route is taken from the remaining ones. Furthermore, the driving cycle is also corrected to fit an appropiate operation range for the battery cells.

The second is to find the route that provides the user with the minimum DoC while ensuring that the time travel takes less than a predefined maximum time. In addition, the driving cycle is corrected as done in the first criterion.

In addition, the algorithm is able to detect charging stations close to the route to suggest a stop at them if necessary.

To illustrate all this, the same start and end points of the above example are considered but now, studying different possible routes to select the best one in function of the exposed criteria.

In Figures 7.31, 7.36 and 7.37, the three different routes to study are considered. Simulating the above routes, the Table 7.1 is obtained.

Figure 7.34 – Time evolution of the surface (green line) and bulk (red line) SoC when taking speed curve of Figure 7.32.

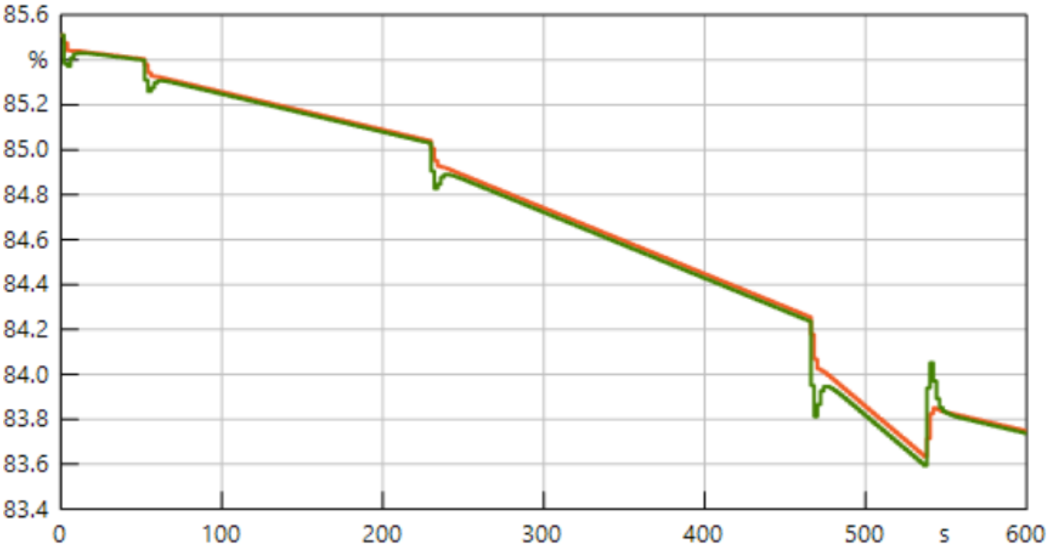

Figure 7.35 – Time evolution of the surface (green line) and bulk (red line) SoC when taking the modified speed curve of Figure 7.33.

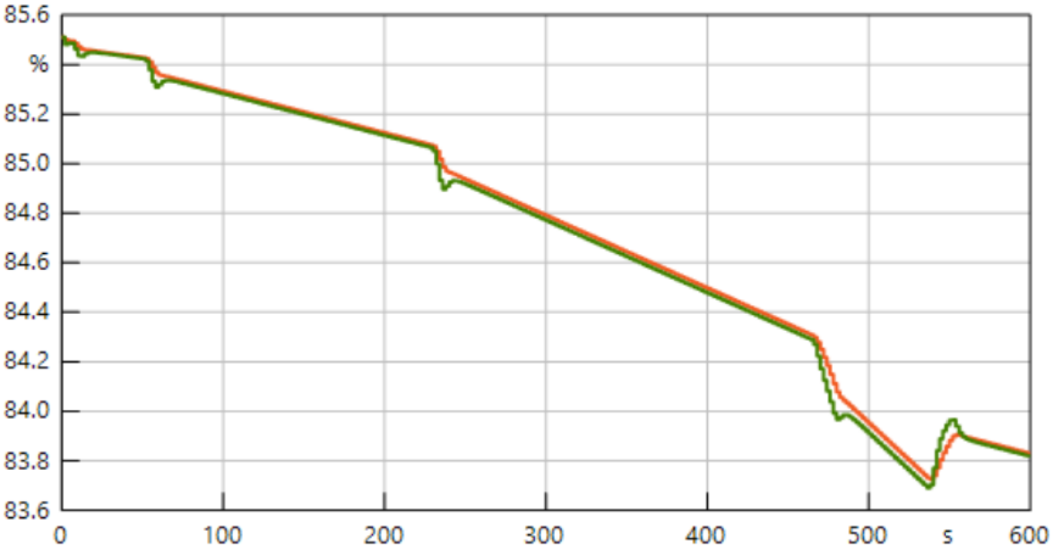

Table 7.1 – Predictions for the example of Section 7.6.4

Route	final SoC	Travel time	Distance traveled
1	83.83 %	10 min	10.7 km
2	84.56 %	8.3 min	6.7 km
3	84.49 %	8.5 min	6.8 km

Figure 7.36 – In red: example itinerary (number two) taken for Section 7.6.4.

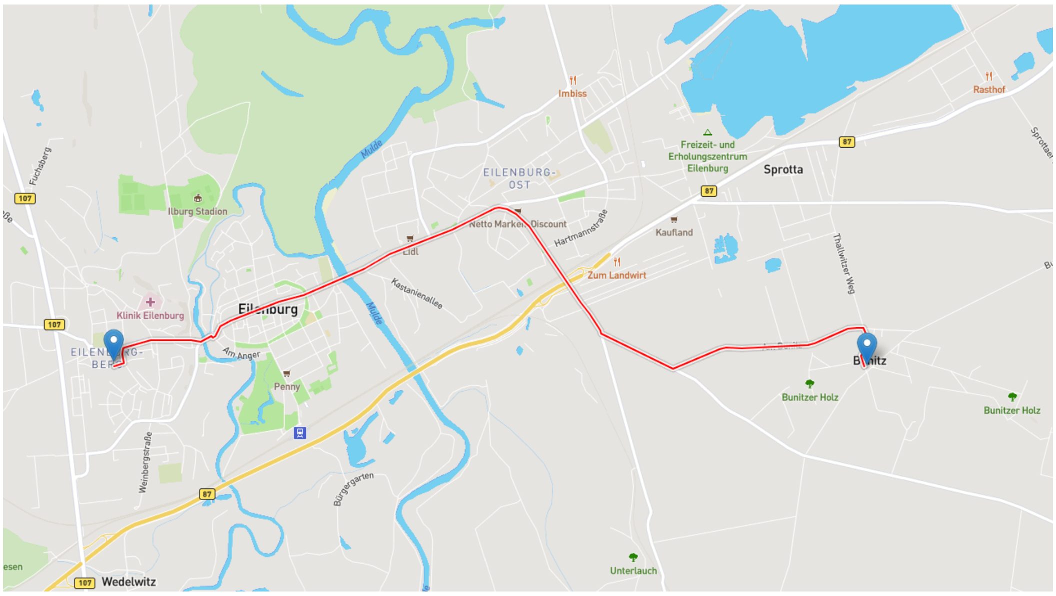

Figure 7.37 – In red: example itinerary (number three) taken for Section 7.6.4.

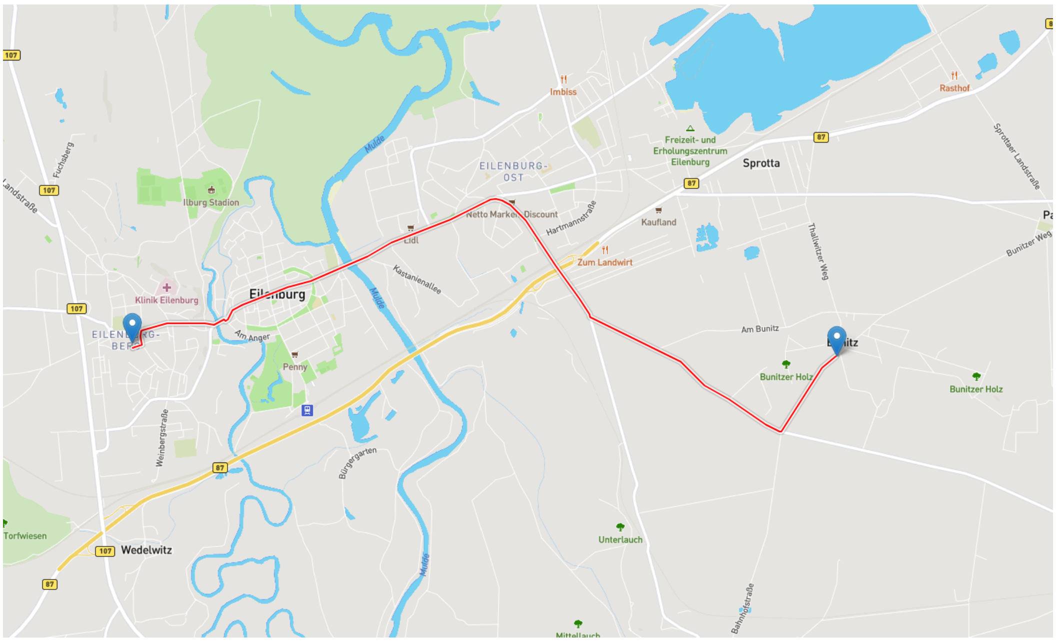

Figure 7.38 – Diagram of the cell balancing strategy employed in Section 7.6.5.

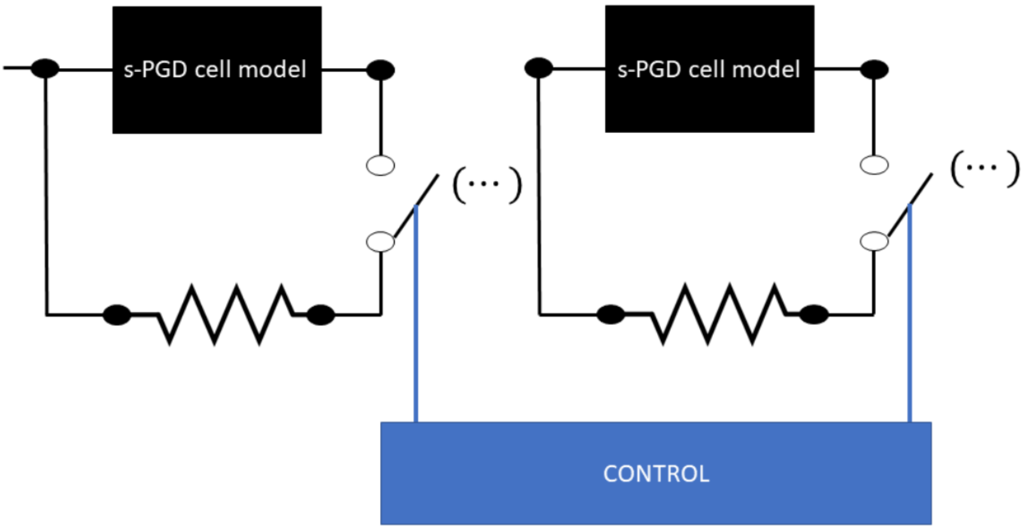

The route selected depending on the chosen criterion is:

- *First criterion.* Here, we suppose that the user wants to reach the end point with a minimum SoC of 84 %. In this case, route number 2 will be selected.
- *Second criterion.* Here, we suppose that the user wants to reach the end point with a maximum travel time of 9 minutes. In this case, route number 3 will be selected.

7.6.5 BMS: cell balancing example

As mentioned in this work, the proposed approach can be integrated in a BMS to improve the control and monitoring of battery cells. The improvement is significant: the better predictions of the cell state provided by the s-PGD model will be translated to better BMS, which is one of the topics that automotive industry is seeking. As a proof of concept, a cell balancing scheme (one of the tasks carried out by the BMS) is designed to correct the imbalance of one cell. Specifically, an example of passive balancing is employed. To do that, a switched shunt resistor is designed to balance the cells during the charging (See Figure 7.38). This way, cells with higher SoC will have a net input energy lower than cells with low SoC when charging, thus producing the balancing effect.

For this example, we consider that, after some trajectories, a cell is unbalanced respect to the others 1 %. Then, a charging procedure starts with a constant current profile and the BMS activates the mentioned cell balance strategy to correct this gap.

Figure 7.39 shows how the SoC is balanced thanks to the implemented strategy. Furthermore, the voltage responses are also tracked in Figure 7.40. For this example, the voltage of both blocks is equalised after the balancing process is finished. However, it is important to note that equal voltages do not necessarily mean the same state of charge as it observed when seeing and comparing the time evolution of both Figures.

Figure 7.39 – Balancing of the cells during charging. In this figure, the bulk SoC of the two types of unbalanced cells is shown. After approx. 770 s, the cells are balanced. The charging is done using a constant current profile.

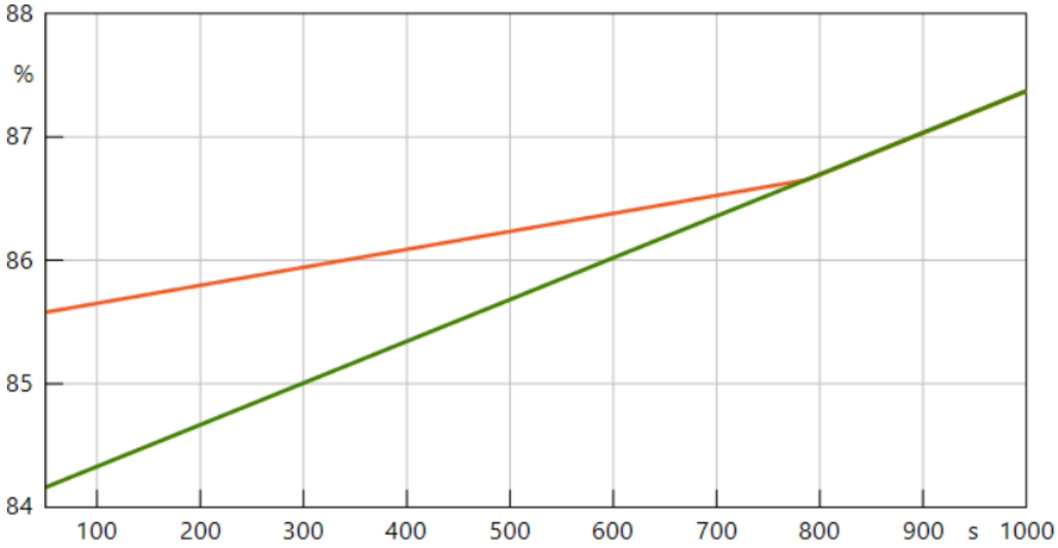

Figure 7.40 – Balancing of the cells during charging. In this figure, the voltage of the two types of unbalanced cells is shown. The voltage of both blocks is equalised after the balancing process is finished. The charging is done using a constant current profile.

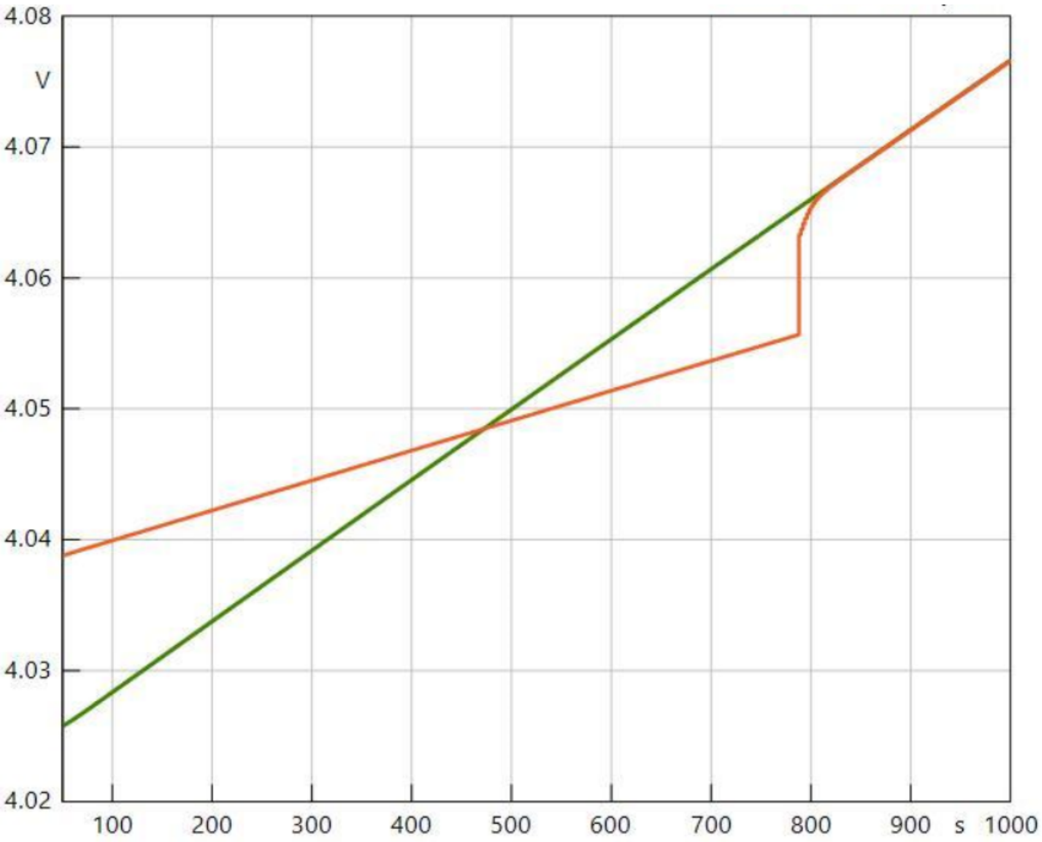

7.6.6 Summary results

It has been shown how the proposed battery approach can be employed to develop planning algorithms, to correct and adapt driving behaviours or to design new BMS thanks to its accuracy and low computational cost.

The added value is significant: the better predictions of the cell state provided by the s-PGD model will be translated to better tools for the above concepts. This is interesting for the automotive industry to improve their products and and be more competitive in the EV market.

Furthermore, we proved that fast simulations are carried out for the entire EV system when the battery s-PGD model is included with SimulationX. Not only that but multiple trajectories are quickly simulated to decide the best route or adapt/correct the driving cycle. In addition, the needed itinerary data for the simulation is extracted from OpenStreetMap (OSM). This way, problems about restrictions on use or availability of map data are avoided.

7.7 Constructing a hybrid twin

7.7.1 Introduction

In Section 7.5, a battery model is developed. It can be simulated together with all the other systems within the EV under real-time feedback constraints. With the help of this model, highly accurate results are obtained in the prediction of variables of interest as compared to the results of the original electrochemical model shown in Section 7.2.

This section aims to go further. The main objective is to develop a model for real-time applications capable to learn from data. In this way, systematic, biased deviations from the model can be attributed to deficiencies in the model. With the stream of experimental measurements the model will be corrected on-line and under real-time constraints, thus giving rise to the concept of the Hybrid Twin [Chinesta *et al.* 2020]. In this application, the correction term is contructed employing the novel procedure described in Section 2.5.4: The DMD Dictionary method. The procedure employed for this application is detailed in Section 7.7.2..

Finally, The reader is reminded that a detailed mathematical introduction to the HT is carried out in Section 2.5.2.

7.7.2 Dictionary Model for the Electrochemical Model: Correcting the gap

As introduced in Section 7.2, the electrochemical model is high-dimensional. If we use the ideas of the Dictionary Method (DM) in the micro-scale, the matrices to work will be of an intractable size. For example, if a reduction of the dimension is not used, a state vector of thousands of dimensions can be found. In this case, the DM would be unfeasible. In addition, even if a drastic reduction of the dimension in the micro-scale could be applied, there is no guarantee that good results would be obtained because the system is highly nonlinear.

For these reasons, we must change the way we think about the electrochemical model to use the DM with success. We focus only on two variables of interest: The voltage and the bulk SoC.

The isothermal Newman's P2D model presented in this work give us the voltage and the bulk SoC as a function of both the micro-scale state of, and the current demanded by the battery, $I(t)$. However, the time evolution of the micro-scale is a consequence of $I(t)$.

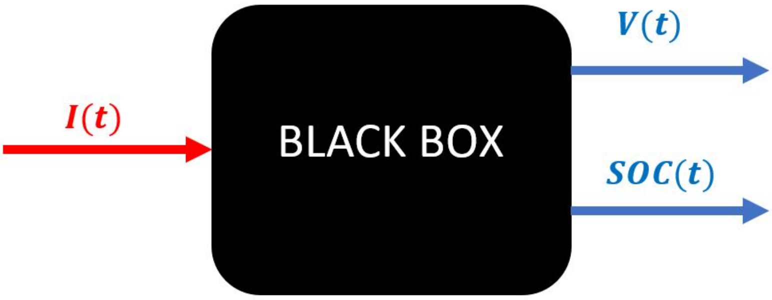

Figure 7.41 – Diagram of the approach used to apply the DM for the battery model.

Therefore, the global overview would be that the Newman's P2D gives the evolution of the variables as a function of the initial micro-scale state of the battery and the current demanded by the battery $I(t)$.

It is worth noting that implies that the variable which dictates the time evolution of the whole system is $I(t)$ (for a fixed initial state). In this way, the model can be interpreted as a black box, as sketched in Fig. 7.41.

Therefore, a dynamical system, which has only voltage and bulk SoC as variables of interest, along with the input $I(t)$, is considered. Note that $I(t)$ carries two meanings: the time evolution of the current and the time evolution of the micro scale. For this reason, the dynamical system that we are proposing must depend on the history. In this way, it takes into consideration how the micro scale is evolving, and how the response must change because of that.

Therefore, variables based on the time history of $I(t)$ must be created to measure this evolution of the micro-scale state. In addition, a transformation $\mathbf{g}(\cdot)$, introduced in Section 2.5.4, must be defined to linearize as much as possible the behavior of the system. The identified local linear systems have the form

$$\tilde{\mathbf{z}} = \begin{bmatrix} V \\ \text{bulk SoC} \\ I \\ \frac{dI}{dt} \\ \int_0^t I \, dt \\ \int_0^t \int_0^t I \, dt \, dt \end{bmatrix} \quad \longrightarrow \quad \mathbf{z} = \begin{bmatrix} V \\ \text{bulk SoC} \end{bmatrix},$$

$$\tilde{\mathbf{M}} = \begin{bmatrix} m_{(1,1)} & m_{(1,2)} & m_{(1,3)} & m_{(1,4)} & m_{(1,5)} & m_{(1,6)} \\ m_{(2,1)} & m_{(2,2)} & m_{(2,3)} & m_{(2,4)} & m_{(2,5)} & m_{(2,6)} \end{bmatrix}.$$

As we have already seen in Section 2.5.4, the dictionary $\mathcal{S}$, which allows us to reproduce a nonlinear model as a combination of local linear approaches, is obtained in two phases.

The first stage is off-line during which a training set $\mathcal{T}$ composed of a collection of snapshots $\left\{\tilde{\mathbf{z}}_1, \ldots, \tilde{\mathbf{z}}_{N_f}\right\}$ of different simulations must be obtained. Then, in the on-line stage, the model is corrected, enriching the original dictionary. In this way, the proposed model can be adapted so as to fit with unexpected experimental measurements.

Consider, for instance, a model trained to reproduce any possible 10-minute trajectory from an initial SoC of 40-60 %. If the model attempts to reproduce a trajectory of an initial SoC of 80 % (not trained), the on-line correction must be able to reproduce well this new scenario. Or imagine that an attempt is made to employ model with a twenty-minute trajectory whereas it is trained only for ten-minute journeys. Then, the on-line correction also needs to be able to reproduce well this new scenario. Gaps between reality and the electrochemical model should be corrected in the same way.

Noise is not considered in the results of Section 7.7.3. It could easily be, however, with the methodology already considered in Section 2.5.2.

7.7.3 Results

The systems to identify have the form presented in Section 7.7.2. In these, we expect our model to be able to reproduce an arbitrary 10-minute trajectory with an initial SoC of 50 %. The pseudo-experimental training set $\mathcal{T}$ is composed of a collection of snapshots obtained from the Newman's P2D electrochemical model shown in Section 7.2 using the POD methodology explained in Section 7.4. This training set $\mathcal{T}$ is obtained using ten different ten-minute trajectories. In the comparisons that follow, the results of the DM are compared with the ones extracted from the Newman's P2D electrochemical model.

Two different error criteria are used. The first one is:

$$\begin{aligned}\mathrm{err}^V_{\max} &= \max\left(100\cdot\frac{|V_{DM}(t)-V_{\mathrm{P2D}}(t)|}{V_{\mathrm{P2D}}(t)}\right),\\ \mathrm{err}^{\mathrm{SoC}}_{\max} &= \max\left(100\cdot\frac{|\mathrm{SoC}_{DM}(t)-\mathrm{SoC}_{P2D}(t)|}{\mathrm{SoC}_{P2D}(t)}\right),\end{aligned}$$

where V denotes voltage, SoC denotes the bulk state of charge, the subscript DM denotes the results obtained by the Dictionary Method and the subscript $P2D$ denotes the results obtained by Newman's P2D model.

The second error criteria used is given by

$$\begin{aligned}\mathrm{err}^V &= \frac{\|V_{DM}(t)-V_{P2D}(t)\|_2}{\|V_{P2D}(t)\|_2},\\ \mathrm{err}^{\mathrm{SoC}} &= \frac{\|\mathrm{SoC}_{DM}(t)-\mathrm{SoC}_{P2D}(t)\|_2}{\|\mathrm{SoC}_{P2D}(t)\|_2}.\end{aligned}$$

In Figs. 7.42 and 7.43, we can observe the error caused by the model extracted through the DM for 38 trajectories (without any on-line correction). The first ten trajectories correspond to the training set. The transition between the training set to the not-trained trajectories is highlighted with a red line. In these plots we can see that the voltage error is always lower than 3 % and it can be lower than 1 % in a lot of itineraries. Conversely, the SoC error is negligible (always lower than 0.08 %).

In Fig. 7.44 and 7.45 we show the comparison of the DM with and without the on-line correction for a trajectory which we have chosen deliberately to be different to those in the training set. To update the on-line dictionary we impose the criteria to limit the maximum error to 0.65 % for the voltage and to 0.05 % for the SoC. In addition, the vertical lines in the correction event plot indicate when a correction event happens. We can notice in these figures that only two corrections are needed to maintain the error level below 0.65 %.

In Fig.7.46, the on-line correction is shown to react within a region for which the model is not prepared. Here we can see the results for a trajectory with an initial SoC of 85 %. We can see that a few corrections are needed at the beginning but later, the model attains good predictability abilities.

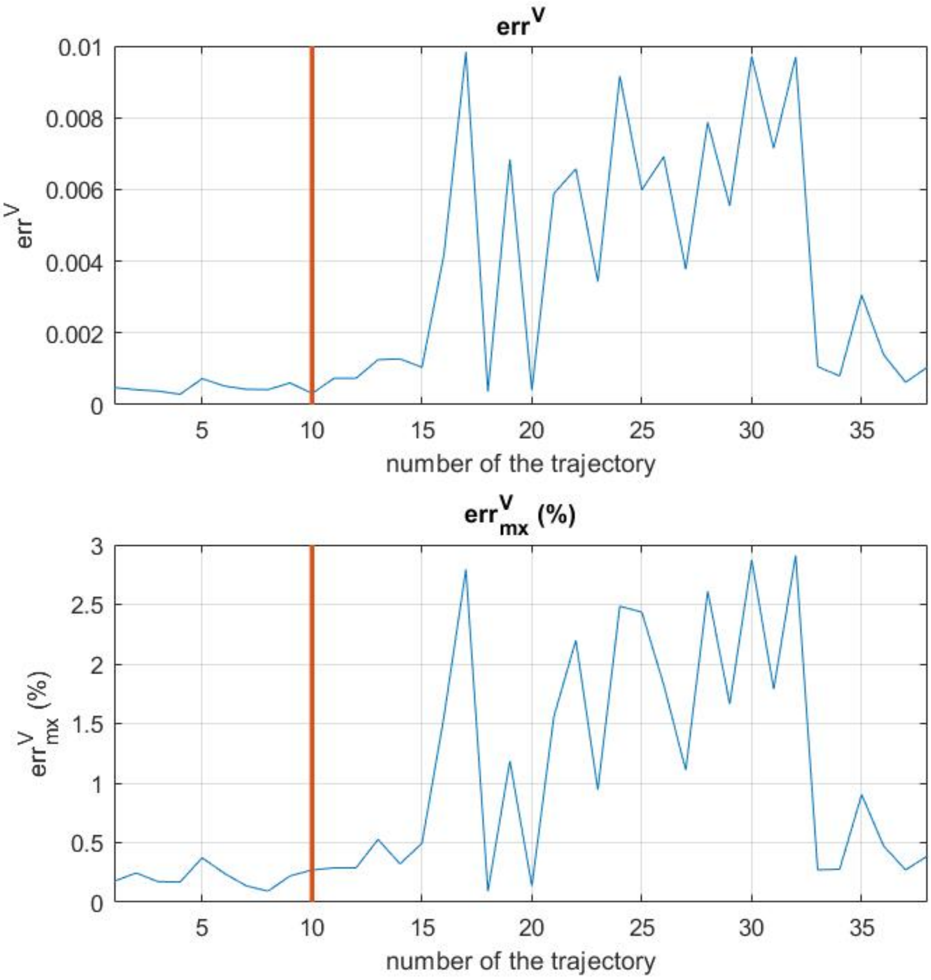

Figure 7.42 – Voltage error of using the model extracted through the DM for 38 trajectories (without any on-line correction). The first ten trajectories correspond to the training set. The transition between the training set and the not-trained trajectories is highlighted with a red line

In Fig. 7.47, we show the SoC results for the above conditions. Note that only one correction is needed for the SoC, despite the fact that the model was not trained to work in these conditions.

In Fig. 7.48, we see how the on-line correction reacts to a different trajectory with an initial SoC of 85 %. In this case, no correction is needed due to the on-line learning of the first one (see Fig. 7.46).

Finally, in Fig. 7.49 and 7.50, the number of corrections needed for six trajectories of an initial SoC of 85 % and another six for an initial SoC of 42.7 % are shown. As a result of these corrections, the error the voltage remains below 0.5 %.

As an additional measure, the dictionary is enriched at each correction. With this

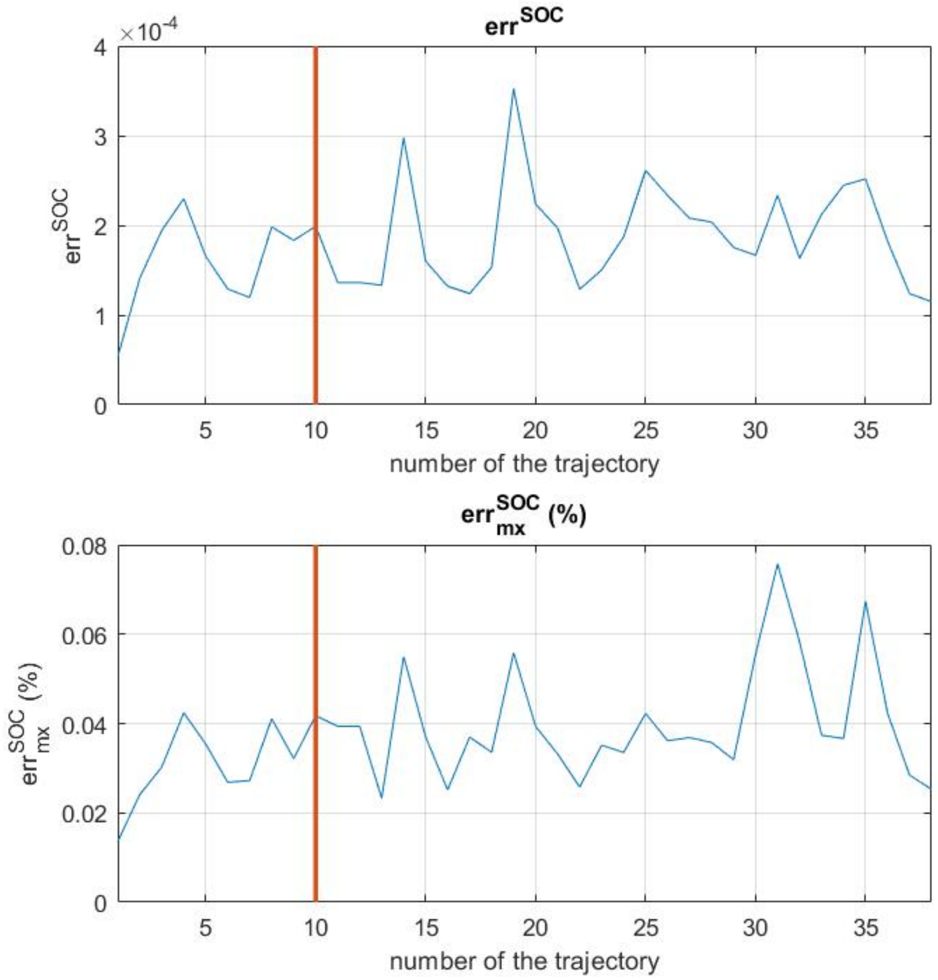

Figure 7.43 – SoC error of using the model extracted through the DM for 38 trajectories (without any on-line correction). The first ten trajectories correspond to the training set. The transition between the training set and the not-trained trajectories is highlighted with a red line

addition, the number of corrections is reduced as the model learn how to react in these new scenarios. To update the on-line dictionary, we imposed the criteria to limit the maximum error to 0.035 % for the SoC and to 0.5 % for the voltage.

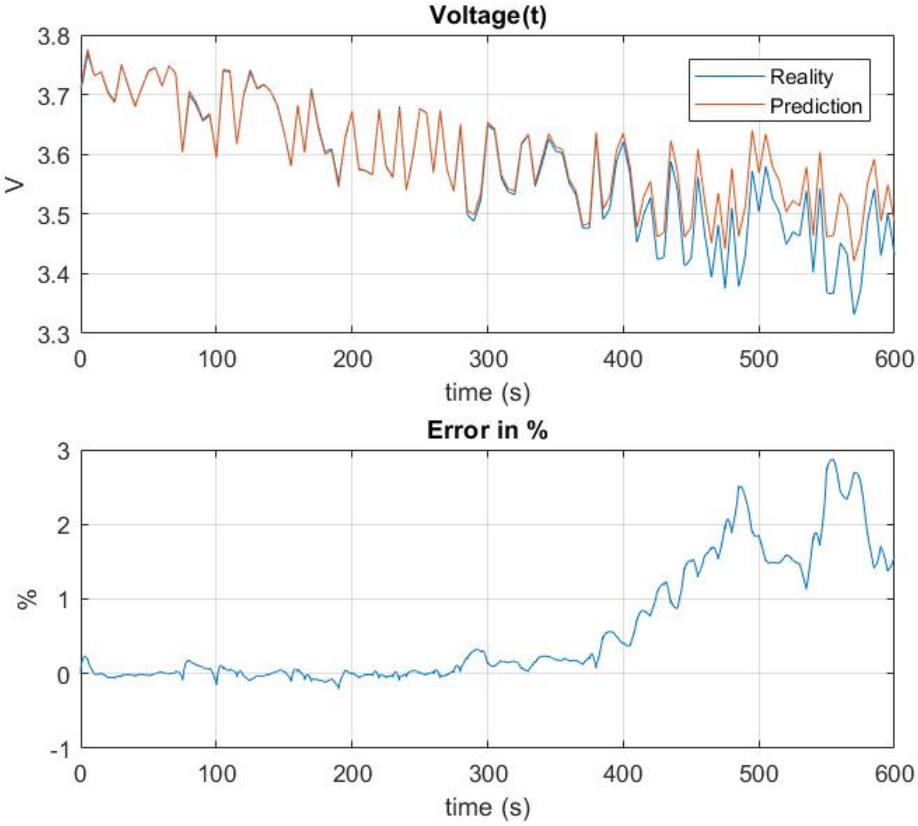

Figure 7.44 – Comparison of the results between the P2D model and the DM model for trajectory number 30. Here, the on-line correction term is not used.

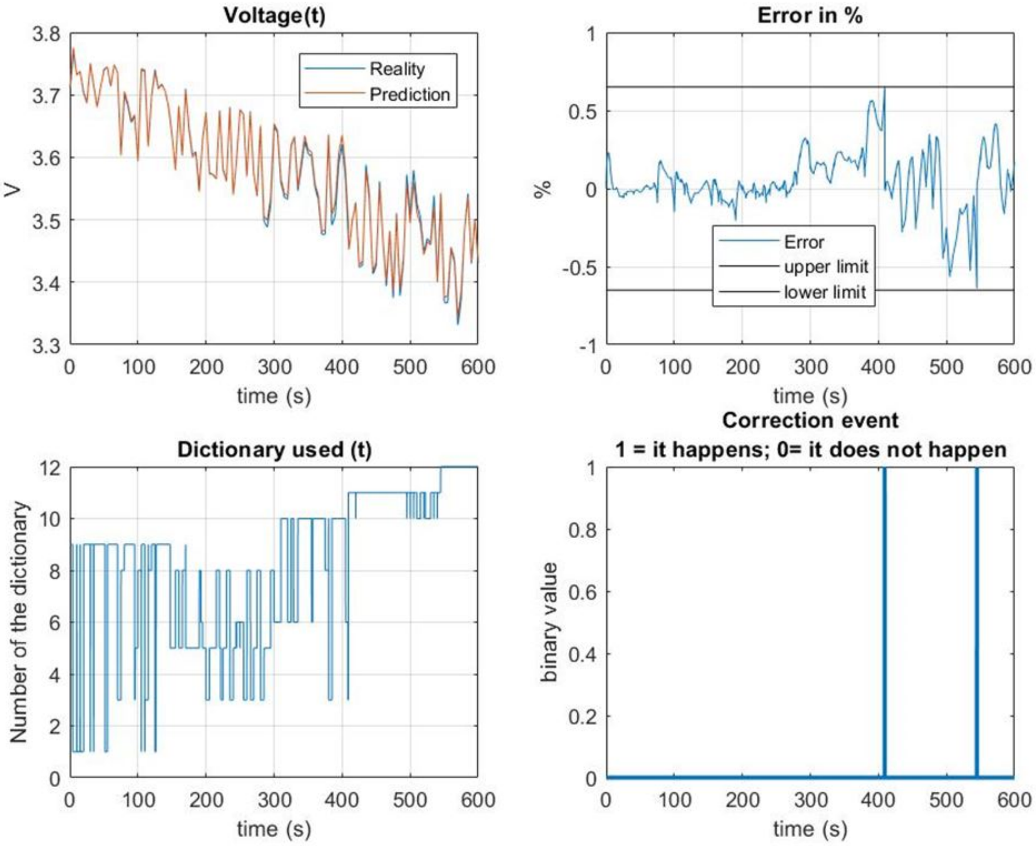

Figure 7.45 – Comparison of the results between the P2D model and the DM model for trajectory number 30. Here, the on-line correction is used. To update the on-line dictionary we impose the criteria to limit the maximum error to 0.65 % for the voltage. The vertical lines in the correction event plot indicate when the correction event happens.

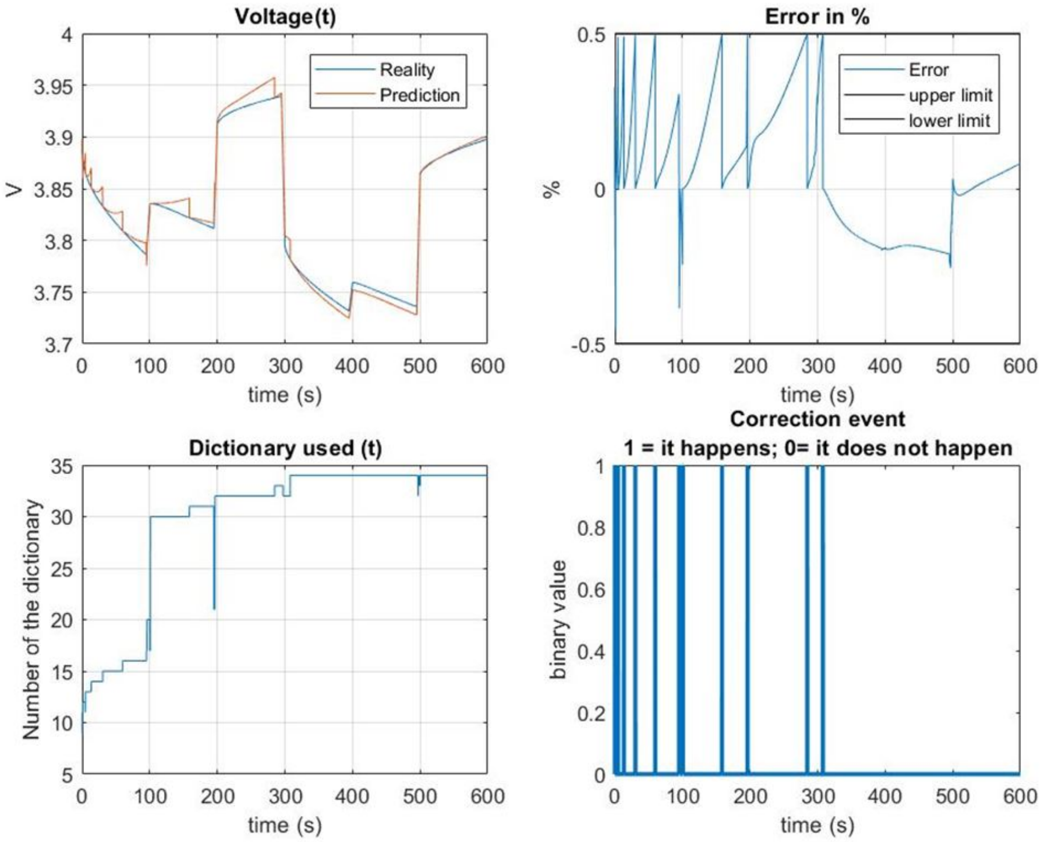

Figure 7.46 – The DM with on-line correction reacts in a region for which the model is not prepared. Results are shown for the voltage during a trajectory with an initial SoC of 85 % (not initially considered in the training set). To update the on-line dictionary, we imposed the criteria to limit the maximum error to 0.5 % for the voltage.

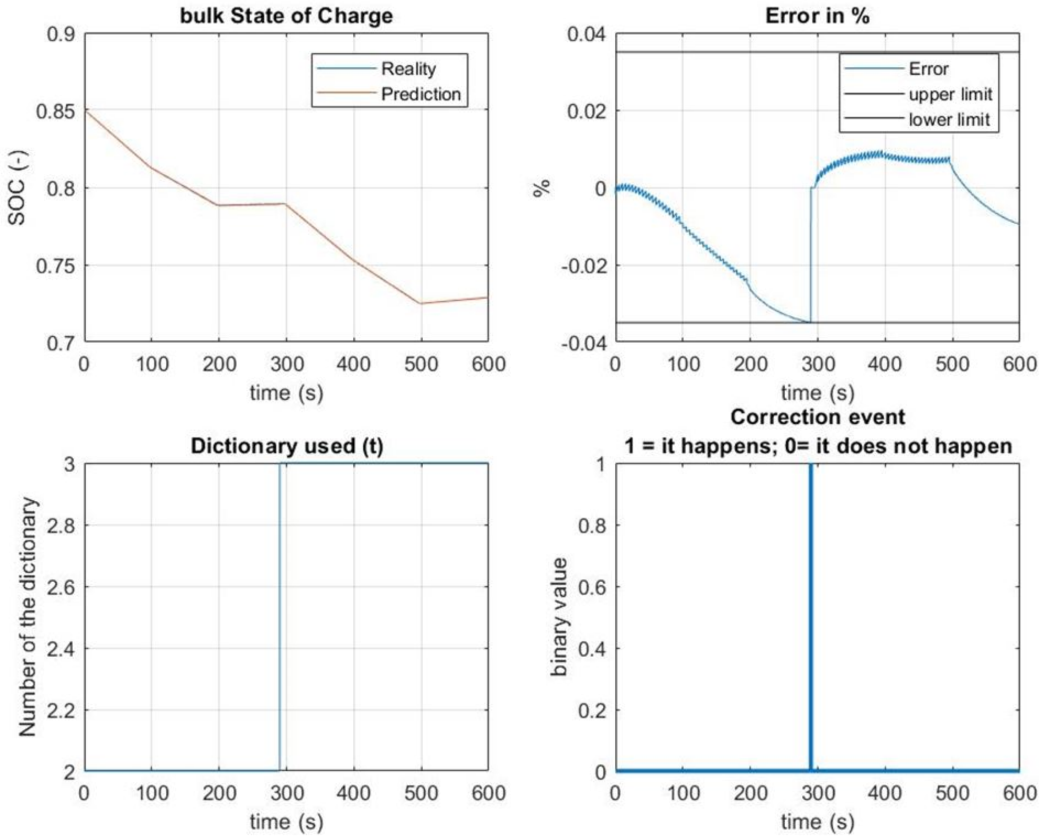

Figure 7.47 – The DM with on-line correction reacts to a region in which the model is not prepared. Here we can see the results for the SoC for a trajectory with an initial SoC of 85 % (not trained for this scenario). To update the on-line dictionary we imposed the criteria to limit the maximum error to 0.035 % for the SoC.

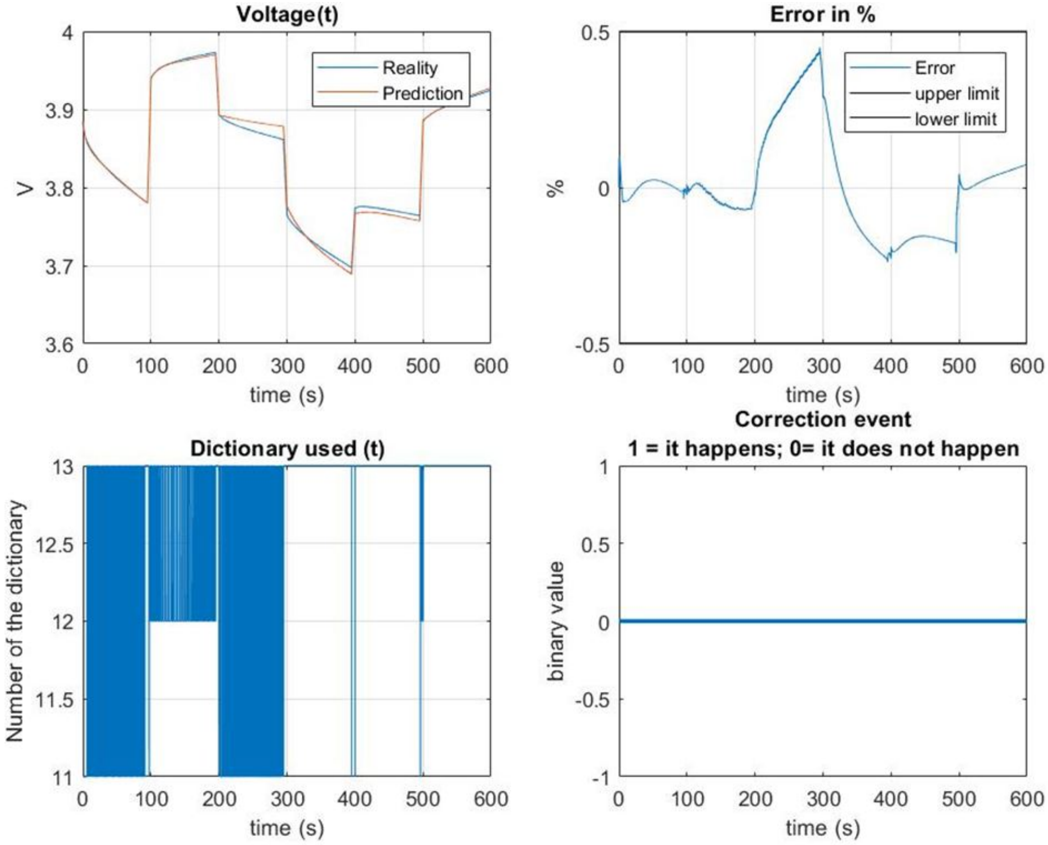

Figure 7.48 – The DM with on-line correction reacts to another trajectory with an initial SoC of 85 %. We can see that no correction is needed for the voltage in this second trajectory due to the on-line learning of the first one (Fig. 7.46). To update the on-line dictionary we imposed the criteria to limit the maximum error to 0.5 % for the voltage

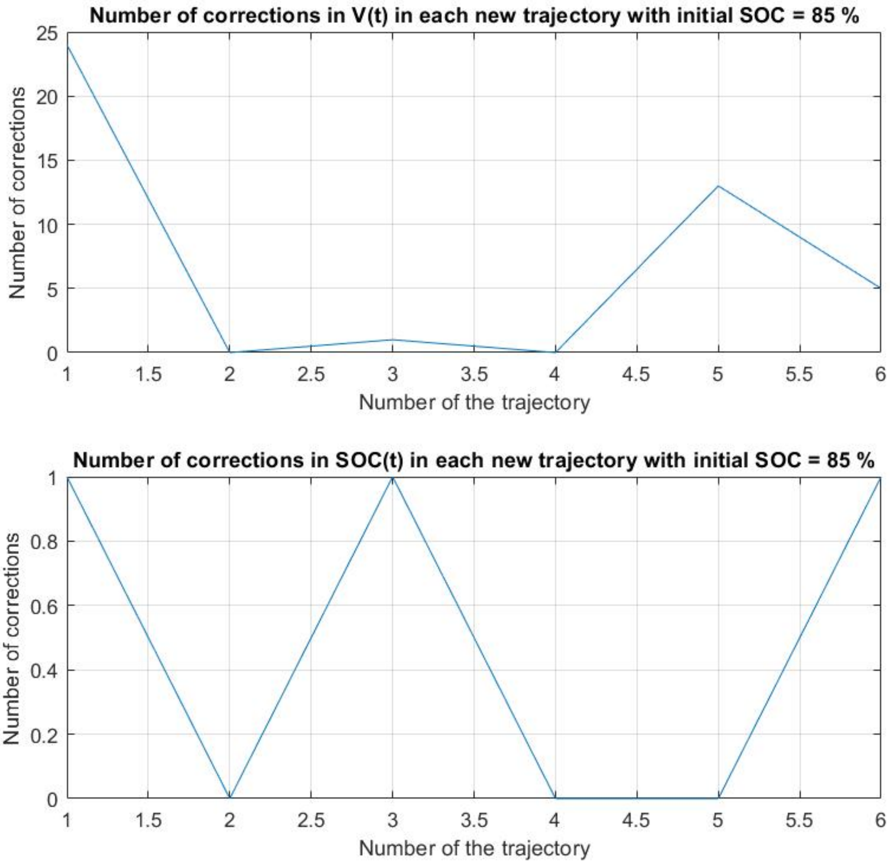

Figure 7.49 – Number of corrections needed for different trajectories with an initial SoC of 85 % (for which the original model is not trained). To update the on-line dictionary we imposed the criteria to limit the maximum error to 0.035 % for the SoC and to 0.5 % for the voltage.

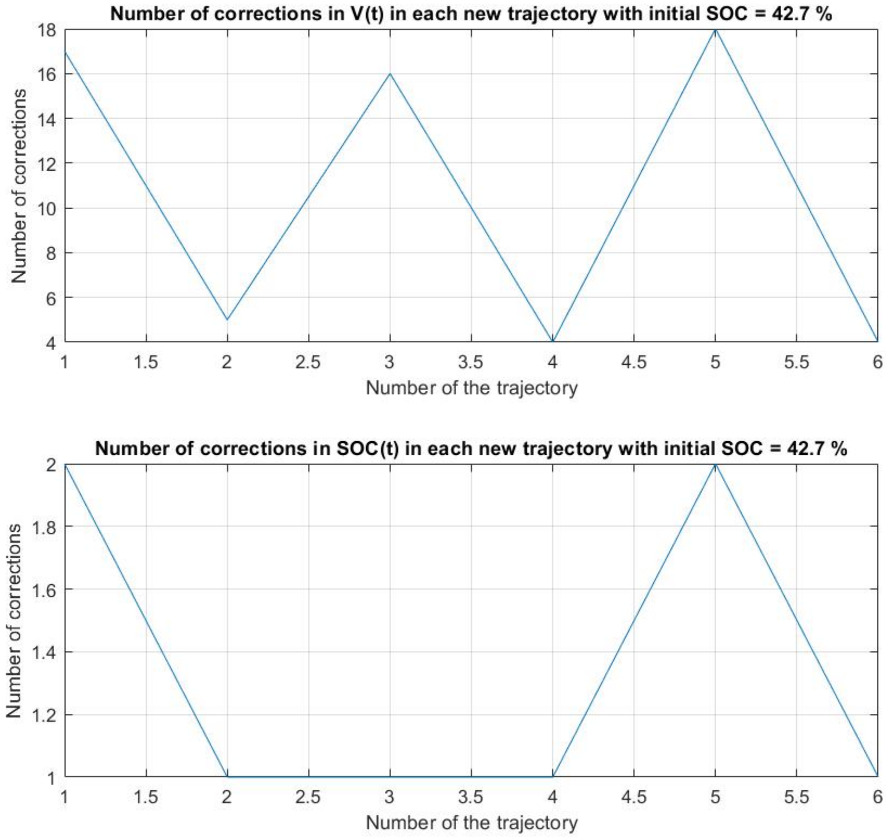

Figure 7.50 – Number of corrections needed for different trajectories with an initial SoC of 42.7 % (for which the original model is not trained). To update the on-line dictionary we imposed the criteria to limit the maximum error to 0.035 % for the SoC and to 0.5 % for the voltage.

7.8 Conclusions

In Section 7.4 a ROM is developed using the POD technique. It can be observed that the results of the full model are reproduced with a high accuracy using the POD model. A large reduction in the computational time and resources needed to solve the electrochemical model is also achieved.

The saving in computational time and resources means that cell design, parameter fitting, and simulation of battery packs can be achieved under this rationale. The key to developing this model is the extraction of the basis functions using the results of off-line simulations. As it was shown, with only an off-line simulation a wide operational range of the cell can be reproduced. To further enrich the basis, some off-line simulations close to a SoC of 100 % and 0 % are recommended.

In Section 7.5, a data-driven ROM was developed using the s-PGD regression technique which can learn either from a physics-based model or experimental data. In Section 7.6.2, it was shown that the developed model was used successfully in conjunction with the whole EV model to obtain fast results with the accuracy of the electrochemical model. This approach could be an excellent option and a good first step to develop the new generation of BMS for the automotive industry because of its accuracy and the low computational resources required. In fact, it has been shown how the proposed battery approach can be employed to develop planning algorithms, to correct and adapt driving behaviours or to design new BMS. The added value is significant: the better predictions of the cell state provided by the s-PGD model will be translated to better tools for the above concepts. This is interesting for the automotive industry to improve their products and and be more competitive in the EV market.

Furthermore, the Digital Twin created using the s-PGD does not only allow for real-time simulations, but can also adapt its predictions taking into consideration the real driving conditions and the real driving cycle to change the planning in real-time.

Indeed, it would be interesting to enrich the model with the thermal gradient or aging effects to further enhance its applicability. This would require a reformulation of the electrochemical model so that the phenomena were correctly described.

Finally, in Section 7.7, a model based on the hybrid twin paradigm is presented to correct the electrochemical model in real-time. To achieve this, a data-driven model based upon the novel hybridation strategies proposed in this dissertation is developed. Accurate results are found by using this data-driven model to reproduce the behavior of the cell. As it has been shown, the data-driven model has excellent capabilities to adapt quickly and reliably to new scenarios (situations for which the model has not been trained).

Note: Perspectives and future works will be detailed in next chapter.

Conclusions and Perspectives

The discussed work showed that the present dissertation is part of the framework based on strengthening the link between data science and numerical simulation. In fact, this thesis was devoted to the development of new methodologies and simulation tools to improve, enhance and boost virtual, digital and hybrid twins to address current industrial challenges. In particular, the MOR and the Machine Learning (ML) framework were explored, employed and enlarged by means of the new proposals done during this work.

The purpose of this thesis was threefold.

First, the development of high-fidelity and high-dimensional parametric models to strongly accelerate highly-accurate physics-based models by means of the MOR and data-driven techniques. These solutions can be evaluated online extremely fast even with real-time constraints (compulsary in many applications) and consequently, they were employed to improve existing twins. Several current industrial problems were studied (Chapters 4, 5, 6 and 7).

Second, Research and development (R&D) of novel MORTs, algorithms and data-driven models. Novel approaches were developed to improve the results when the current techniques suffer and to extend methodologies to new areas of interest. Most of the novel simulation tools proposed here were provided to address the different challenging scenarios presented throughout this dissertation. Nevertheless, they can be easily extended or, in most cases, directly applied to other settings.

Third, in the context of the DDDAS framework, the Hybrid Twin was developed and applied to an aeronautics problem as well as to a battery system of an EV. Here, the difference/gap between the physical prediction and the measurements is corrected. We observed how the physics-based response can be accelerated employing a parametric deterministic solution learned using the non-intrusive MOR framework. To make possible the hybridation, two novel techniques were successfully proposed, allowing not only to address nonlinear settings but also to ensure stability in the time integration as well as a low computational cost.

In Chapter 2, the novel techniques to successfully solve the industrial challenges of Chapters 4, 5, 6 and 7 were presented and discussed. In particular, this chapter proposed the following new techniques: the s-PGD+RB strategy, a novel unwrapping algorithm, the stabilized DMD/DMDc and the DMD Dictionary strategy. In addition, excellent results were observed when applied to their respective problems detailed below.

In Chapter 4, high-dimensional parametric solutions were obtained to quickly determine the response of rotating electric machines with accuracy. Two different approaches were successfully applied for different ranges of application. The first one employing the intrusive PGD combined with an innovative mapping to transform the motor geometry. The second one based on the proposed s-PGD+RB strategy. Excellent results were obtained when compared with the FEMM software. Furthermore, the proposed solutions can be particularized under the stringent real-time constraints and can empower industrial procedures such as the optimization, inverse analysis or simulation-based control.

The above work opened a line of research where more complex models are going to be addressed as well as the coupling of the numerical model with transient responses of circuit equations. Thus, the computational cost reduction would be even more drastic.

In fact, the electric machine articles published in this thesis, attracted the attention of multinational companies such as SKF, starting a collaboration to apply these techniques to their electromagnetic devices, in this case magnetic bearings.

Then, in Chapter 5, the novel unwrapping algorithm proposed in this dissertation was applied to the efficient and optimal design of radar-based Advanced Driver Assistant Systems (ADAS). In particular this chapter proposed a parametric solution by employing a non-intrusive formulation of the PGD, combined with a powerful phase-angle unwrapping strategy for accurately addressing the electric and magnetic fields interpolation, contributing to improve the design, the calibration and the operational use of those systems. It was proved how the number of snapshots can be greatly reduced by employing the proposed approach. This way, the computational cost is significantly reduced. And not only that, but its performance was compared with that of Matlab software, showing better results and thus improving current commercial techniques.

Next, Chapter 6 proposed a new strategy for the computation of stable, fast and accurate corrections in the Hybrid Twin framework to address an industrial application of the international company Dassault Aviation. Specifically, the stabilized DMD/DMDc was employed. It was proved how this novel strategy addresses successfully the delicate and important problem of stability. In fact, it was demonstrated that the technique is able to learn dynamical models while guaranteeing a low computational cost as well as the achievement of stable dynamical time integrations. Moreover, the experimental tests carried out showed that the proposed technique correctly filters noise, thus improving the knowledge of the system state. In addition, the experimental results reflected the advantages of the HT paradigm. Indeed, the most complex behaviors could only be captured when applying this hybrid strategy. Due to the excellent results obtained during this research project, a new line of research wants to be opened (with Dassault Aviation) to apply the aformentioned technique to an aeronautical system but explicitly taking into consideration the corresponding control strategy.

The last industrial application was addressed in Chapter 7: the need of fast an accurate models for lithium-ion batteries. In particular, three Reduced Order Model (ROM) techniques were applied to the most commonly used physics-based models, each one for a different range of application.

In Section 7.4, a POD model was proposed to greatly reduce the simulation time and the computational effort for the Newman's pseudo-2D cell model, thus proving to be an excellent tool for cell design, parameter fitting or simulation of battery packs. In addition, the results showed an excellent agreement between both modeling frameworks.

Then, Sections 7.5 and 7.6 proposed a s-PGD cell model that achieved real-time performance for the whole Electric Vehicle (EV) system with a battery pack. Moreover, results proved that a good accuracy was obtained. Indeed, it has been shown and demonstrated how the proposed battery approach can be employed to develop planning algorithms, to correct and adapt driving behaviours or to design the new generation of BMS. The added value is significant: the better predictions of the cell state provided by the s-PGD model will be translated to better tools for the above concepts. In addition, there are strong perspectives of incorporing the aforementioned s-PGD cell models in the commercial software of ESI Group. Furthermore, an interesting future line of research would be to enrich the model with the thermal gradient or aging effects to further enhance its applicability.

The last ROM was a data-driven model based on the proposed DMD Dictionary technique (Section 7.7). It was demonstrated how this approach can be used to extract an on-line model that corrects the gap between prediction and measurement. Thus, the first (to our knowledge) hybrid twin of a Li-ion battery was constructed, being able to self-correct from data. Accurate results were found by using this data-driven model to reproduce the behavior of the cell. And not only that, but excellent model capabilities were reported to adapt quickly and reliably to new scenarios. Future works would address the capabilities of the data-driven model to predict specific aging effects, to correct other possible QoI or to deal with the presence of noise (in the latter case, filters could be created if necessary whenever the inherent filter of the DMD does not give satisfactory results).

Another chapter, which is worthy to metion, is Chapter 3 where the novel PGD techniques were presented: the rs-PGD, the s^2-PGD and the ANOVA-based sparse-PGD. Each of them was designed to deal with a different issue. Moreover, we observed and discussed, through different examples, how they can improve significantly the existing sparse PGD performance, reducing overfitting and achieving great explanatory predictive capabilities when correctly applied in their respective frameworks. Therefore, the improvements carried out by these new techniques opens the door to construct better high-dimensional parametric functions in the low-data regime context, which is really appealing because of the increasing industrial interest in this type of solutions. In fact, this work opened and active line of research to address specific industrial applications where the use of these techniques can be competitively advantageous. In addition, this line of research will also study the best workflow for allying them as well as the scalability.

As we noticed during the manuscript, the topics covered in this work come from specific industrial areas, however, the work was addressed from a global point of view, offering different methodologies than can be extrapolated in different areas. For that reason, perspectives of future work (in addition to the ones previously introduced) consider capitalization of the techniques developed. Also, the industrialization and scalability of techniques such as the hybridation ones, the rs-PGD or the s^2-PGD.

To sum up, we strongly believe that this dissertation constitutes a good foundation towards the implementation of machine learning techniques combined with the MOR framework as a cornerstone to the development of disruptive and innovative technologies. As it can be appreciated in the individual conclusions of each section, the techniques and strategies proposed in this manuscript along with the exemplified applications are able to open the route to a new paradigm combining low-data artificial intelligence with physical knowledge. And not only that, but also to pave the way to the discussed new lines of research.

Appendix A

Translation of the Chapter on Conclusions and Perspectives

This appendix contains the translation into Spanish and French of the Chapter on Conclusions and Perspectives of the present dissertation.

A.1 Conclusions et Perspectives

Les travaux discutés ont montré que la présente thèse s'inscrit dans le cadre basé sur le renforcement du lien entre la science des données et la simulation numérique. En effet, cette thèse a été consacrée au développement de nouvelles méthodologies et d'outils de simulation pour améliorer, renforcer et dynamiser les jumeaux virtuels, numériques et hybrides afin de relever les défis industriels actuels. En particulier, les techniques de réduction de modèles et du Machine Learning (ML) ont été explorés, employés et élargis par le biais de nouvelles propositions faites au cours de ce travail.

L'objectif de cette thèse était triple.

Tout d'abord, le développement de modèles paramétriques haute-fidélité et haute-dimension pour accélérer fortement les modèles physiques plus précis au moyen des techniques de réduction de modèles et des techniques orientées données. Ces solutions peuvent être évaluées en ligne extrêmement rapide, même avec des contraintes de temps réel (obligatoires dans de nombreuses applications) et, par conséquent, elles ont été utilisées pour améliorer les jumeaux existants. Plusieurs problèmes industriels actuels ont été étudiés (Chapitres 4, 5, 6 et 7).

Deuxièmement, la recherche et le développement (R & D) de nouvelles techniques de réduction de modèles, algorithmes et modèles pilotés sur les données. De nouvelles approches ont été développées pour améliorer les résultats lorsque les techniques actuelles se voient limitées et pour étendre les méthodologies à de nouveaux domaines d'intérêt. La plupart des nouveaux outils de simulation proposés ici ont été fournis pour répondre aux différents scénarios difficiles présentés tout au long de cette thèse. Néanmoins, ils peuvent être facilement étendus ou, dans la plupart des cas, directement appliqués à d'autres contextes.

Troisièmement, dans le cadre de travail des DDDAS, le jumeau hybride a été développé et appliqué à un problème aéronautique ainsi qu'à un système de batterie d'un véhicule électrique. Ici, la différence/écart entre la prédiction physique et les mesures experimentales est corrigée. Nous avons observé comment la réponse basée sur la physique peut être accélérée en utilisant une solution déterministe paramétrique apprise en utilisant les techniques de réduction de modèles non-intrusives. Pour rendre possible l'hybridation, deux nouvelles techniques ont été proposées avec succès, permettant non seulement de traiter des paramètres non linéaires mais aussi d'assurer la stabilité de l'intégration temporelle ainsi qu'un faible coût de calcul.

Dans le Chapitre 2, les nouvelles techniques permettant de résoudre avec succès les défis industriels des Chapitres 4, 5, 6 et 7 ont été présentées et discutées. En particulier, ce chapitre propose les nouvelles techniques suivantes : la stratégie s-PGD+RB, un nouvel *unwrapping algorithm*, la DMD/DMDc stabilisée et la stratégie du Dictionnaire DMD. De plus, d'excellents résultats ont été observés lorsqu'elles ont été appliquées à leurs problèmes respectifs détaillés ci-dessous.

Dans le Chapitre 4, des solutions paramétriques à haute dimension ont été obtenues pour déterminer rapidement et avec précision la réponse des machines électriques tournantes. Deux approches différentes ont été appliquées avec succès pour différents domaines d'application. La première utilise la PGD intrusive combinée à un mappage innovante pour transformer la géométrie du moteur. La seconde est basée sur la stratégie s-PGD+RB proposée. D'excellents résultats ont été obtenus en comparaison avec le logiciel FEMM. En outre, les solutions proposées peuvent être adaptées aux contraintes strictes du temps réel et peuvent faciliter les procédures industrielles telles que l'optimisation, l'analyse inverse ou le contrôle par simulation.

Le travail ci-dessus a ouvert une ligne de recherche où des modèles plus complexes vont être abordés ainsi que le couplage du modèle numérique avec les réponses transitoires des équations de circuit. Ainsi, la réduction des coûts de calcul serait encore plus drastique. En pratique, les articles sur les machines électriques publiés dans cette thèse ont attiré l'attention de multinationales telles que SKF, qui ont entamé une collaboration pour appliquer ces techniques à leurs dispositifs électromagnétiques, en l'occurrence les paliers magnétiques.

Ensuite, dans le Chapitre 5, le nouvel *unwrapping algorithm* proposé dans cette thèse est appliqué à la conception efficace et optimale des systèmes avancés d'aide à la conduite (ADAS) basés sur les radars. En particulier, ce chapitre propose une solution paramétrique en employant une formulation non-intrusive de la PGD, combinée à une stratégie puissante de *unwrapping* pour traiter avec précision l'interpolation des champs électriques et magnétiques, contribuant ainsi à améliorer la conception, la calibration et l'utilisation opérationnelle de ces systèmes. Il a été démontré que le nombre de *snapshots*, peut être considérablement réduit en utilisant l'approche proposée. De cette façon, le coût de calcul est considérablement réduit. De plus, ses performances ont été comparées à celles du logiciel Matlab, montrant de meilleurs résultats et améliorant ainsi les techniques commerciales actuelles.

Ensuite, le Chapitre 6 propose une nouvelle stratégie pour le calcul de corrections stables, rapides et précises dans le cadre de l'Hybrid Twin pour répondre à une application industrielle de la société internationale Dassault Aviation. Plus précisément, la DMD/DMDc stabilisée est ici utilisée. Il a été prouvé que cette nouvelle stratégie permet de résoudre avec succès le délicat et important problème de la stabilité. Concrètement, il a été démontré que la technique est capable d'apprendre des modèles dynamiques tout en garantissant un faible coût de calcul ainsi que la réalisation d'intégrations dynamiques temporelles stables. De plus, les tests expérimentaux réalisés ont montré que la technique proposée filtre correctement le bruit, améliorant ainsi la connaissance de l'état du système. De plus, les résultats expérimentaux ont reflété les avantages du paradigme HT. En effet, les comportements les plus complexes n'ont pu être capturés qu'en appliquant cette stratégie hybride. En raison des excellents résultats obtenus au cours de ce projet, une nouvelle ligne de recherche veut être ouverte (avec Dassault Aviation) pour appliquer la technique mentionnée ci-dessus à un système aéronautique mais en prenant explicitement en considération la stratégie de contrôle correspondante.

La dernière application industrielle a été abordée dans le Chapitre 7 : le besoin de modèles rapides et précis pour les batteries lithium-ion. En particulier, trois techniques de réduction de modèles ont été appliquées aux modèles basés sur la physique les plus couramment utilisés, chacune pour un domaine d'application différent.

Dans la section 7.4, un modèle POD a été proposé pour réduire considérablement le temps de simulation et l'effort de calcul pour le modèle pseudo-2D de Newman, ce qui s'avère être un excellent outil pour la conception de cellules, l'ajustement des paramètres ou la simulation de packs de batteries. En outre, les résultats ont montré un excellent accord entre les deux cadres de modélisation.

Ensuite, les sections 7.5 et 7.6 ont proposé un modèle de cellule s-PGD qui a atteint une performance en temps réel pour l'ensemble du système du véhicule électrique (VE) avec un bloc-batterie. De plus, les résultats ont prouvé qu'une bonne précision a été obtenue. En effet, il a été montré et démontré comment l'approche de la batterie proposée peut être employée pour développer des algorithmes de planification, pour corriger et adapter les comportements de conduite ou pour concevoir la nouvelle génération de systèmes de gestion de batterie (Battery Management Systems, BMS). La valeur ajoutée est importante : les meilleures prédictions de l'état de la cellule fournies par le modèle s-PGD se traduiront par de meilleurs outils pour les concepts ci-dessus. En outre, il existe de fortes chances d'incorporer les modèles cellulaires s-PGD susmentionnés dans les logiciels commerciaux d'ESI Group. En outre, une future ligne de recherche intéressante serait d'enrichir le modèle avec le gradient thermique ou les effets du vieillissement pour améliorer encore son applicabilité.

Le dernier modèle était un modèle piloté par les données basé sur la technique proposée du dictionnaire DMD (Section 7.7). Il a été démontré comment cette approche peut être utilisée pour extraire un modèle en ligne qui corrige l'écart entre la prédiction et la mesure experimentale. Ainsi, le premier jumeau hybride (à notre connaissance) d'une batterie Li-ion a été construit, capable de s'autocorriger à partir des données. Des résultats précis ont été trouvés en utilisant ce modèle basé sur les données pour reproduire le comportement de la cellule. Et ce n'est pas tout, les capacités du modèle à s'adapter rapidement et de manière fiable à de nouveaux scénarios sont excellentes. Les travaux futurs porteront sur les capacités du modèle piloté par les données à prédire des effets de vieillissement spécifiques, à corriger d'autres quantités d'intérêt possibles ou à traiter la présence de bruit (dans ce dernier cas, des filtres pourraient être créés si nécessaire lorsque le filtre inhérent au DMD ne donne pas de résultats satisfaisants).

Un autre chapitre, qui mérite d'être mentionné, est le Chapitre 3 où les nouvelles techniques PGD ont été présentées : la rs-PGD, la s^2-PGD et la sparse-PGD basée sur l'ANOVA. Chacune d'entre elles a été conçue pour traiter un problème différent. De plus, nous avons observé et discuté, à l'aide de différents exemples, la manière dont ils peuvent améliorer de manière significative les performances de la sparse-PGD existante, en réduisant le surajustement et en atteignant de grandes capacités prédictives explicatives lorsqu'ils sont correctement appliqués dans leurs cadres respectifs. Par conséquent, les améliorations apportées par ces nouvelles techniques ouvrent la porte à la construction de meilleures fonctions paramétriques à haute dimension dans le contexte d'un régime à faibles données, ce qui est vraiment attrayant en raison de l'intérêt industriel croissant pour ce type de solutions. Ce travail a ouvert une ligne de recherche active pour aborder des applications industrielles spécifiques où l'utilisation de ces techniques peut être compétitivement avantageuse. En outre, cette ligne de recherche étudiera également le meilleur flux de travail pour les allier ainsi que l'évolutivité.

Comme nous l'avons remarqué lors de la rédaction du manuscrit, les sujets abordés dans ce travail proviennent de domaines industriels spécifiques, cependant, le travail a été abordé d'un point de vue global, offrant différentes méthodologies qui peuvent être extrapolées dans différents domaines. Pour cette raison, les perspectives de travaux futurs (en plus de celles présentées précédemment) envisagent la capitalisation des techniques développées. Il en est de même, l'industrialisation et la mise à l'échelle de techniques telles que celles de l'hybridation ou la s^2-PGD.

En résumé, nous croyons fermement que cette thèse constitue une bonne base pour la mise en œuvre de techniques d'apprentissage automatique combinées avec les techniques de réduction de modèles comme pierre angulaire du développement de technologies perturbatrices et innovantes. Comme on peut l'apprécier dans les conclusions individuelles de chaque section, les techniques et les stratégies proposées dans ce manuscrit ainsi que les applications prises en exemple sont capables d'ouvrir la voie à un nouveau paradigme combinant la connaissance physique et l'intelligence artificielle avec peu de données. Et non seulement cela, mais aussi ouvrir la voie aux nouvelles lignes de recherche discutées.

A.2 Conclusiones y perspectivas

El trabajo expuesto demostró que la presente disertación está inscrita en el marco de trabajo basado en el fortalecimiento del vínculo entre la ciencia de los datos y la simulación numérica. De hecho, esta tesis se dedicó al desarrollo de nuevas metodologías y herramientas de simulación para mejorar, potenciar e impulsar los gemelos virtuales, digitales e híbridos para abordar los retos industriales actuales. En particular, las técnicas de reducción de modelos y de *machine learning* fueron exploradas, empleadas y ampliadas mediante las nuevas propuestas realizadas durante este trabajo.

El objetivo de esta tesis ha sido triple.

Para empezar, el primer próposito ha sido el desarrollo de modelos paramétricos de alta fidelidad y dimensión para acelerar significativamente los modelos físicos de gran precisión mediante técnicas de reducción de modelos y ciencia de datos (concretamente, técnicas de *machine learning*). Este tipo de soluciones pueden evaluarse en línea de forma extremadamente rápida, incluso con restricciones de tiempo real (obligatorias en muchas aplicaciones) y, en consecuencia, se emplearon para mejorar los gemelos existentes (virtuales, digitales y híbridos). Varios problemas industriales actuales han sido estudiados en la presente disertación (Capítulos 4, 5, 6 y 7).

El segundo próposito ha consistido en la investigación y el desarrollo (I+D) de nuevas técnicas de reducción de modelos, algoritmos y modelos basados en datos. De hecho, se han desarrollado nuevos enfoques para mejorar los resultados cuando las técnicas actuales sufren o se ven limitidas, así como para ampliar las metodologías a nuevas áreas de interés. La mayoría de las herramientas de simulación novedosas propuestas aquí se proporcionaron para abordar los diferentes escenarios desafiantes presentados a lo largo de esta disertación. No obstante, pueden extenderse fácilmente o, en la mayoría de los casos, aplicarse directamente a otros escenarios.

En tercer lugar, en el marco de trabajo de los DDDAS, el próposito ha consistido en desarrollar el Gemelo Híbrido (Hybrid Twin, HT) y aplicarlo a un problema aeronáutico, así como a un sistema de baterías de un vehículo eléctrico. En este marco de trabajo, la diferencia o la desviación entre la predicción física y las mediciones experimentales es exitosamente corregida. Además, observamos cómo la respuesta basada en la física puede acelerarse empleando una solución determinista paramétrica aprendida utilizando técnicas de reducción de modelos no intrusivas. Para hacer posible la hibridación, se propusieron con éxito dos técnicas novedosas, que permiten no sólo abordar configuraciones no lineales, sino también garantizar la estabilidad en la integración temporal, así como un bajo coste computacional.

En el Capítulo 2, se presentaron y discutieron las nuevas técnicas para resolver con éxito los retos industriales de los Capítulos 4, 5, 6 y 7. En particular, en este capítulo se propusieron las siguientes técnicas novedosas: la estrategia s-PGD+RB, un novedoso algoritmo de *unwrapping*, la DMD/DMDc estabilizada y la estrategia del Diccionario DMD. Además, se observaron excelentes resultados cuando se aplicaron a sus respectivos problemas que se detallan a continuación.

En el Capítulo 4, se obtuvieron soluciones paramétricas de alta dimensión para determinar rápidamente la respuesta de las máquinas eléctricas rotativas con precisión. Se aplicaron con éxito dos enfoques diferentes para distintos rangos de aplicación. El primero empleando la PGD intrusiva combinada con un mapeo innovador para transformar la geometría del motor. El segundo, basado en la estrategia s-PGD+RB propuesta. Se obtuvieron excelentes resultados cuando se compararon con el software FEMM. Además, las soluciones propuestas pueden particularizarse bajo las estrictas restricciones de tiempo real y pueden potenciar procedimientos industriales como la optimización, el análisis inverso o el control basado en la simulación.

El trabajo anterior abrió una línea de investigación en la que se van a abordar modelos más complejos, así como el acoplamiento del modelo numérico con las respuestas transitorias de las ecuaciones del circuito. De este modo, la reducción del coste computacional sería aún más drástica. De hecho, los artículos sobre máquinas eléctricas publicados en esta tesis, atrajeron la atención de empresas multinacionales como SKF, con la que se ha iniciado una colaboración para aplicar estas técnicas a sus dispositivos electromagnéticos, en este caso rodamientos magnéticos.

A continuación, en el Capítulo 5, se aplicó el novedoso algoritmo de *unwrapping* propuesto en esta tesis al diseño eficiente y óptimo de sistemas avanzados de asistencia al conductor (ADAS) basados en radar. En particular, este capítulo propuso una solución paramétrica empleando una formulación no intrusiva de la PGD, combinada con una potente estrategia de *unwrapping* para abordar con precisión la interpolación de los campos eléctricos y magnéticos, contribuyendo a mejorar el diseño, la calibración y el uso operativo de dichos sistemas. Se demostró cómo el número de *snapshots*, puede reducirse en gran medida empleando el enfoque propuesto. De este modo, el coste computacional se reduce significativamente. Y no sólo eso, sino que su rendimiento se comparó con el del software Matlab, mostrando mejores resultados y mejorando así las técnicas comerciales actuales.

Más adelante, en el Capítulo 6 se propuso una nueva estrategia para el cálculo de correcciones estables, rápidas y precisas en el marco de trabajo del Hybrid Twin para abordar una aplicación industrial de la empresa internacional Dassault Aviation. En concreto, se empleó la DMD/DMDc estabilizada. Se demostró cómo esta novedosa estrategia aborda con éxito el delicado e importante problema de la estabilidad. De hecho, se demostró que la técnica es capaz de aprender modelos dinámicos garantizando un bajo coste computacional, así como la consecución de integraciones dinámicas temporales estables. Además, las pruebas experimentales realizadas mostraron que la técnica propuesta filtra correctamente el ruido, mejorando así el conocimiento del estado del sistema. Además, los resultados experimentales reflejaron las ventajas del paradigma HT. De hecho, los comportamientos más complejos sólo pudieron ser capturados al aplicar esta estrategia híbrida. Debido a los excelentes resultados obtenidos durante este proyecto de investigación, se quiere abrir una nueva línea de investigación (con Dassault Aviation) para aplicar dicha técnica a un sistema aeronáutico, pero teniendo en cuenta explícitamente la estrategia de control correspondiente.

La última aplicación industrial se abordó en el Capítulo 7: la necesidad de modelos rápidos y precisos para las baterías de iones de litio. En concreto, se aplicaron tres técnicas de reducción de modelos a los modelos físicos más utilizados, cada uno para un rango de aplicación diferente.

En la sección 7.4, se propuso un modelo POD para reducir en gran medida el tiempo de simulación y el esfuerzo computacional para el modelo pseudo-2D de Newman, demostrando así ser una excelente herramienta para el diseño de celdas, el ajuste de parámetros o la simulación de paquetes de baterías. Además, los resultados mostraron una excelente concordancia entre ambos marcos de modelado.

A continuación, las secciones 7.5 y 7.6 propusieron un modelo de celda s-PGD que logró un rendimiento en tiempo real para todo el sistema del vehículo eléctrico con un paquete de baterías. Además, los resultados demostraron que se obtuvo una buena precisión. De hecho, se ha mostrado y demostrado cómo el enfoque propuesto para las baterías puede emplearse para desarrollar algoritmos de planificación, para corregir y adaptar los comportamientos de conducción o para diseñar la nueva generación de sistemas de gestión de baterías (Battery Management System, BMS). El valor añadido es significativo: las mejores predicciones del estado de la célula proporcionadas por el modelo s-PGD se traducirán en mejores herramientas para los conceptos mencionados. Además, existen grandes perspectivas de incorporar los mencionados modelos s-PGD en el software comercial del Grupo ESI. Además, una interesante línea de investigación futura sería enriquecer el modelo con el gradiente térmico o los efectos del envejecimiento para mejorar aún más su aplicabilidad.

El último modelo fue uno basado en datos y en la técnica propuesta del Diccionario DMD (Sección 7.7). Se demostró cómo este enfoque puede utilizarse para extraer un modelo en línea que corrija el desfase entre la predicción y la medición experimental. Así, se construyó el primer gemelo híbrido (hasta donde sabemos) de una batería de iones de litio, capaz de autocorregirse a partir de los datos. Se obtuvieron resultados precisos utilizando este modelo basado en datos para reproducir el comportamiento de una celda. Y no sólo eso, sino que se mostró la excelente capacidad del modelo para adaptarse de forma rápida y fiable a nuevos escenarios. En futuros trabajos se abordarán las capacidades del modelo impulsado por datos para predecir efectos específicos del envejecimiento, para corregir otras posibles cantidades de interés o para hacer frente a la presencia de ruido (en este último caso, se podrían crear filtros si fuera necesario siempre que el filtro inherente de la DMD no diera resultados satisfactorios).

Otro capítulo digno de mención es el Capítulo 3 donde se presentaron las nuevas técnicas PGD: la rs-PGD, la s^2-PGD y la ANOVA-based sparse-PGD. Cada una de ellas fue diseñada para tratar un problema diferente. Además, observamos y discutimos, a través de diferentes ejemplos, cómo pueden mejorar significativamente el rendimiento de la s-PGD existente, reduciendo el sobreajuste y logrando una gran capacidad predictiva cuando se aplican correctamente en sus respectivos marcos. Por lo tanto, las mejoras llevadas a cabo por estas nuevas técnicas abren la puerta a la construcción de mejores funciones paramétricas de alta dimensión en el contexto del régimen de datos escasos, lo cual es realmente atractivo debido al creciente interés industrial en este tipo de soluciones. De hecho, este trabajo abre una línea de investigación activa para abordar aplicaciones industriales específicas en las que el uso de estas técnicas puede ser competitivamente ventajoso. Además, esta línea de investigación también estudiará el mejor flujo de trabajo para aliarlas así como la escalabilidad.

Como se ha podido comprobar a lo largo del manuscrito, los temas tratados en este trabajo provienen de áreas industriales concretas, sin embargo, el trabajo se ha abordado desde un punto de vista global, ofreciendo diferentes metodologías que pueden ser extrapoladas a diferentes áreas. Por ello, las perspectivas de trabajo futuro (además de las introducidas anteriormente) contemplan la capitalización de las técnicas desarrolladas, así como la industrialización y escalabilidad de técnicas como las de hibridación o la s^2-PGD.

En resumen, creemos firmemente que esta disertación constituye una buena base hacia la implementación de técnicas de aprendizaje automático combinadas con las técnicas de reducción de modelos como piedra angular para el desarrollo de tecnologías disruptivas e innovadoras. Como se puede apreciar en las conclusiones individuales de cada sección, las técnicas y estrategias propuestas en este manuscrito junto con las aplicaciones tomadas como ejemplo son capaces de abrir una ruta hacia un nuevo paradigma que combine el conocimiento físico con la inteligencia artificial aplicada a la ingeniería. Y no sólo eso, sino también allanar el camino a las nuevas líneas de investigación discutidas.

Appendix B

EM parameters

B.1 Units

The units employed in the chapter and appendices which address rotating electrical machines are introduced in the following table.

Unit	Symbol	Unit	Symbol
millimeters	mm	meters	m
degrees	$deg.$	radians	rad
horsepower	HP	ampere	A
Hertz	Hz	revolutions per minute	rpm
Tesla	T	megasiemens	MS
Pascal	$N/m^2 = Pa$	-	-

Table B.1 – Units

B.2 Induction motor

An example from the FEMM software manual [Meeker 2018] is borrowed, where geometry and further details can be found. The main parameters and features of the motor are as follows:

- 2 HP motor, 50 Hz, 3-phase supply. It is a 4-pole machine (i.e., p = 2).
- The winding configuration for one pole of the machine is: A+, A+, A+, C-, C-, C-, B+, B+, B+ (the nine slots from 0 to 90 geometrical degrees).
- There are a total of 36 slots on the stator and 28 slots on the rotor. A total of 44 turns sit inside each stator slot.
- The rotor's diameter is 80 mm, and the air gap between the rotor and stator is 0.375 mm. The length of the machine in the into-the-page direction is 100 mm.

Materials used:

- Aluminum for rotor bars ($\sigma = 34.45$ MS/m)
- Air ($\mu_r = 1$)
- Stator Winding ($\mu_r = 1$)
- For the Case 1. Linear B-H relationship.
  - Silicon Core Iron for the ferromagnetic materials ($\mu_r = 7000$)

- For the Case 2. Nonlinear B-H relationship.
    - Carpenter Silicon Core Iron "A", 1066C Anneal (B-H curve taken from FEMM library)

B.3 Synchronous machine.

An example from the FEMM software manual [Meeker 2018] is borrowed, where geometry and further details can be found. The main parameters and features of the motor are as follows:

- 3-phase supply. It is a 8-pole machine (i.e. p = 4)
- The winding configuration for one pole of the machine is: A+, B-, C+ (the three slots from 0 to 45 geometrical degrees).

Geometry:

- Rotor Inner Diameter: 22.8 mm.
- Rotor Iron Outer Diameter: 50.5 mm.
- Rotor Outer Diameter: 55.1 mm.
- Air Gap Length: 0.7 mm.
- Stator Outer Diameter: 100 mm.
- Angle Spanned by Tooth: 11.9 deg.
- Turns/Slot: 46.
- The complete geometry of the machine is reconstructed in Figure 4.18.

Materials:

- Winding Wire: 4X20AWG copper wire
- Magnet Material: Sm2Co17 24MGOe
- Stator Material: 24 Gauge M19 NGO Steel @ 98% fill
- Rotor Material: 1018 steel

Appendix C

EM models

C.1 Induction motor

In this machine, a 2D current-based formulation for a squirrel-cage induction motor is considered. According to [Bianchi 2005, Salon 1995], the 2D problem is given by the following PDE:

$$\frac{\partial}{\partial x}\left(\frac{1}{\mu}\frac{\partial A_z}{\partial x}\right)+\frac{\partial}{\partial y}\left(\frac{1}{\mu}\frac{\partial A_z}{\partial y}\right)=-J_0+\sigma\frac{\partial A_z}{\partial t}-\sigma\mathbf{v}\times\Big(\nabla\times\mathbf{A}\Big), \tag{C.1}$$

where $\mathbf{A}$ is the magnetic vector potential, $\mathbf{v}$ is the velocity, A_z is the z-component of the magnetic vector potential, J_0 is the applied density current source, σ is the electric conductivity and μ represents the permeability.

Considering $J_0(t) = \mathrm{Re}(\hat{J}_0 e^{j\omega t})$, $A_z(t) = \mathrm{Re}(\hat{A}_z e^{j\varphi t} e^{j\omega t})$ and $\tilde{A}_z = \hat{A}_z e^{j\varphi t}$ (where φ is the phase angle between $A_z(t)$ and $J_0(t)$) as well as the assumptions and mathematical procedure shown in [Bianchi 2005, Salon 1995], the above problem can be simplified to the following expression for an harmonic analysis:

$$\frac{\partial}{\partial x}\left(\frac{1}{\mu}\frac{\partial \tilde{A}_z}{\partial x}\right)+\frac{\partial}{\partial y}\left(\frac{1}{\mu}\frac{\partial \tilde{A}_z}{\partial y}\right)=-\hat{J}_0+j\omega\sigma_{eq}\tilde{A}_z, \tag{C.2}$$

where $\tilde{A}_z$ is a complex number, j is the unit imaginary number, $\omega = 2\pi f$, f is the supply frequency, σ_{eq} is an equivalent conductivity computed as $\sigma_{eq} = \sigma s$ and s is the slip. The slip in induction motors is defined as $s = \frac{n_s - n_r}{n_s}$, where n_s is the synchronous speed and n_r is the rotor speed.

This formulation transforms the magneto-dynamic field problem expressed by Eq. (C.1) to a magnetostatic complex field problem with induced currents. In the chosen approach the rotor is fixed in the stator reference frame and an equivalent conductivity is assigned to the rotor bars to take into consideration the motional term of the current density, that is, the induced current density due to the movement.

Therefore, we can represent the motor at any operation point by multiplying the rotor conductivities by the slip. This is similar to the procedure used in the standard motor equivalent circuit where the rotor resistance is divided by the slip.

The choice of solving Eq. (C.2) was done to adapt the problem to the free FEMM software and its capabilities. In addition, to take into consideration the nonlinear relationship B-H in Eq. (C.2), FEMM includes a nonlinear time harmonic solver that it is used in this work. This nonlinear time harmonic analysis seeks to include the effects of nonlinearities like saturation and hysteresis on the fundamental of the response, while ignoring higher harmonic content.

There are several subtly different variations of the formulation that can yield slightly different results, so documentation of what has actually been implement is important to the correct interpretation of the results from this solver. An excellent description of this formulation is contained in [Jack & Mecrow 1990, Meeker 2018].

C.2 Synchronous machine

In this machine, a two-dimensional steady state analysis is carried out to adapt us to the capabilities of the open source FEMM. In Section 4.2.2, the weak form was described. Here, the strong form employed in FEMM as well as the choice of certain modeling details are introduced. In addition, at the end of the appendix, references are included to further elaborate on the modelling of electrical machines and on the details presented here.

In three-phase motors, as in the other polyphase configurations of synchronous machines, the stator-produced magnetomotive force (MMF) rotates at synchronous speed. Since the rotor is also rotating at synchronous speed in the steady state, an observer on the rotor experiences a constant field ($\frac{\partial B}{\partial t} = 0$), and therefore, there are no eddy currents on the rotor.

On the other hand, an observer on the stator experiences a time varying field whose fundamental is at the system frequency. Since the stator is laminated and the stator windings are stranded and transposed, the eddy currents are resistance limited and can be neglected in the field computation. Hence the term ($\sigma \frac{\partial A_z}{\partial t}$) in the diffusion equation is neglected also in this frame since σ can be considered zero.

If we take into consideration the above assumptions in Eq. (C.1) as well as adding the modeling term for the permanent magnets, it will lead us to the Poisson's equation for a magnetostatic analysis:

$$\frac{\partial}{\partial x}\left(\frac{1}{\mu}\frac{\partial A_z}{\partial x}\right) + \frac{\partial}{\partial y}\left(\frac{1}{\mu}\frac{\partial A_z}{\partial y}\right) = -J_0 - \frac{\partial}{\partial x}\left(\frac{B_{r,y}}{\mu}\right) + \frac{\partial}{\partial y}\left(\frac{B_{r,x}}{\mu}\right), \tag{C.3}$$

where $B_{r,x}$ and $B_{r,y}$ are respectively the x and y components of the remanent flux density.

A fixed reference frame is used in the above equation where the PDE is solved for each rotor position. To further details in electric machine modeling, we kindly suggest the reading of [Salon 1995], [Bianchi 2005]. Note also that Eqs. (C.2) and (C.3) are solved in Cartesian coordinates.

APPENDIX D

Nomenclature for the Electrochemical Model

Symbol	Definition	Unit
a_s	Active surface area per electrode unit volume	$\frac{m^2}{m^3}$
A	Electrode plate area	m^2
c	Concentration of lithium in a phase	$\frac{mol}{m^3}$
D	Diffusion coefficient of lithium species	$\frac{m^2}{s}$
F	Faraday's constant	$\frac{C}{mol}$
i_o	Exchange current density of an electrode reaction	$\frac{A}{m^2}$
I	Applied current	A
j^{Li}	Reaction current resulting in production or consumption of Li	$\frac{A}{m^3}$
L_n	Length of the anode	m
L_s	Length of the separator	m
L_p	Length of the cathode	m
L_t	Length of the cell	m
p	Bruggeman exponent	-
R	Universal gas constant	$\frac{J}{mol \cdot K}$
R_f	Film resistance on an electrode surface	$\Omega \cdot m^2$
R_s	Radius of solid active material particles	m
t_+^0	Transference number of lithium ion with respect to the vel. of solvent	-
T	Absolute temperature	K
U	Open-circuit potential of an electrode reaction	V
α_a	Anodic transfer coefficient for an electrode reaction	-
α_c	Cathodic transfer coefficient for an electrode reaction	-
η	Surface overpotential of an electrode reaction	V
K	Conductivity of an electrolyte	$\frac{S}{m}$
K_D	Diffusional conductivity of an electrolyte	$\frac{A}{m}$
ϕ	Volume-averaged electrical potential in a phase	V
σ	Conductivity of solid active materials in an electrode	$\frac{S}{m}$
c_{se}	Concentration of litium in the solid phase at solid/electrolyte interface	$\frac{mol}{m^3}$
k_o	kinetic rate constant	$\frac{m^{2.5}}{mol^{0.5}s}$
ε	Volume fraction or porosity of a phase	-

$\theta_{100\%}$	Stoichiometry at 100 %	-
$\theta_{0\%}$	Stoichiometry at 0 %	-
θ	$\frac{c_{se}}{c_{s,\max}}$	-
Symbol	Definition	Unit

Table D.1 – Nomenclature used

Notes:

1. The subscript s refers to the solid phase with the exception of L_s.
2. The subscript e refers to the electrolyte phase.
3. The subscript n refers to the anode.
4. The subscript p refers to the cathode.
5. The subscript “max” refers to maximum.
6. The superscript “eff” refers to effective.
7. The superscript “init” refers to initial.

Appendix E

Cell parameters and additional equations

Parameter	Cathode	Separator	Anode
c_e^{init}	1000	1000	1000
c_s^{init}	25751	-	26128
$c_{s,\max}$	51554	-	30555
D_e	$7.5 \cdot 10^{-10}$	$7.5 \cdot 10^{-10}$	$7.5 \cdot 10^{-10}$
D_s	10^{-14}	-	$3.9 \cdot 10^{-14}$
k_o	$2.25196 \cdot 10^{-6}$	-	$4.85416 \cdot 10^{-6}$
L	$8 \cdot 10^{-5}$	$2.5 \cdot 10^{-5}$	$8.8 \cdot 10^{-5}$
R_s	$2 \cdot 10^{-6}$	-	$2 \cdot 10^{-6}$
ε_s	0.59	-	0.4824
ε_e	0.385	0.724	0.485
σ	100	-	100
a_s	885000	-	723600
p	4	4	4
F	96485	96485	96485
R	8.314472	8.314472	8.314472
T	298.15	298.15	298.15
α_a	-	-	0.5
α_c	0.5	-	-
$\theta_{100\%}$	0.4955	-	0.8551
$\theta_{0\%}$	0.99174	-	0.01429
A	1	-	1
t_+^0	0.364	0.364	0.364
Parameter	Cathode	Separator	Anode

Table E.1 – Cell parameters

The units of the values shown in the table above are the same as those used in Table D.1.

Additional equations:

$$
\begin{aligned}
&D_e^{\text{eff}} = \varepsilon_e^p \cdot D_e, \quad K^{\text{eff}} = \varepsilon_e^p \cdot K, \quad K_D^{\text{eff}} = \frac{2 \cdot R \cdot T \cdot K^{\text{eff}}}{F} \cdot (t_+^0 - 1),\\
&\sigma^{\text{eff}} = \varepsilon_s \cdot \sigma, \qquad a_s = \frac{3 \cdot \varepsilon_s}{R_s}.
\end{aligned}
$$

K, U_n and U_p are usually computed using empirical equations according to the simulated cell. The empirical equations for this cell are:

$$
\begin{aligned}
U_n(\theta_n) = 0.7222 + 0.1387 \cdot \theta_n + 0.029 \cdot \theta_n^{0.5} - \frac{0.0172}{\theta_n} + \frac{0.0019}{\theta_n^{1.5}}\\
+ 0.2808 \cdot \exp(0.9 - 15 \cdot \theta_n) - 0.7984 \cdot \exp(0.4465 \cdot \theta_n - 0.4108),
\end{aligned}
$$

$$
U_p(\theta_p) = \frac{-4.656 + 88.669 \cdot \theta_p^2 - 401.119 \cdot \theta_p^4 + 342.909 \cdot \theta_p^6 - 462.471 \cdot \theta_p^8 + 433.434 \cdot \theta_p^{10}}{-1 + 18.933 \cdot \theta_p^2 - 79.532 \cdot \theta_p^4 + 37.311 \cdot \theta_p^6 - 73.083 \cdot \theta_p^8 + 95.96 \cdot \theta_p^{10}},
$$

$$
\begin{aligned}
K(c_e) = 4.1253 \cdot 10^{-2} + 5.007 \cdot 10^{-4} \cdot c_e - 4.7212 \cdot 10^{-7} \cdot c_e^2\\
+ 1.5094 \cdot 10^{-10} \cdot c_e^3 - 1.6018 \cdot 10^{-14} \cdot c_e^4.
\end{aligned}
$$

Appendix F

Parameters used in the SimulationX model

Parameter	Value	Parameter	Value
Vehicle mass m	1300 kg	Initial Displacement	0 km
Initial Velocity	0 km/h	Driving Shaft Inertia	0.9 $kg \cdot m^2$
Inertia Side Shafts	0.5 $kg \cdot m^2$	Inertia Driving Wheels	1.42 $kg \cdot m^2$
Wheel radius	300 mm	Axle Transmission ratio	3
Air Drag Coefficient C_w	0.3	Rolling resistance Coef. C_r	0.01
Air density ρ	1.293 kg/m^3	Reference Area A_{ref}	1.5 m^2
Hill Gradient Angle γ	0	PI controller G	$1.39 \cdot 10^{-3}$
PI controller T_i	0.0011	Armature resistance R_a	0.537 Ω
Armature inductance L_a	1 mH	-	-
Parameter	Value	Parameter	Value

Table F.1 – Main parameters

The parameters of the PI controller are assumed to have the following form:

$$G \cdot \Big(1 + \frac{1}{Ti \cdot s}\Big).$$

The parameters of the DC/DC converter are the default parameters in the SimulationX model described in [Winter *et al.* 2015]. The main forces considered for the linear movement of the vehicle are:

$$F_t = m \cdot a + R_{aero} + R_r + R_{grade},$$

where F_t is the tractive effort, and

$$R_{\text{aero}} = \rho/2 \cdot A_{ref} \cdot C_w \cdot V^2,$$

represents the aerodynamic resistance. Likewise,

$$R_r = C_r \cdot m \cdot g \cdot \cos(\gamma),$$

represents the rolling resistance and, finally,

$$R_{\text{grade}} = m \cdot g \cdot \sin(\gamma),$$

is the grade resistance.

Bibliography

[A. Smith *et al.* 2007] Kandler A. Smith, Chris Rahn and Chao-Yang Wang. *Control oriented ID electrochemical model of lithium ion battery.* Energy Conversion and Management, **48**, 2565–2578, 2007.

[A. Smith *et al.* 2008] Kandler A. Smith, Chris Rahn and Chao-Yang Wang. *Model-based electrochemical estimation of lithium-ion batteries.* 714 – 719, 2008.

[Allery *et al.* 2004] Cyrille Allery, S. Guerin, Aziz Hamdouni and Anas Sakout. *Experimental and numerical POD study of the Coanda effect used to reduce self-sustained tones.* Mechanics Research Communications, **31**, 105–120, 2004.

[Allery 2002] Cyrille Allery. *Contribution à l'identification des bifurcations et à l'étude des écoulements fluides par des systèmes dynamiques d'ordre faible (P. O. D.).* 2002.

[Alliance 2019] European Energy Research Alliance. *European Energy Research Alliance - EU projects - Batteries Europe.* `https://www.eera-set.eu/eu-projects/batteries-europe/`, 2019. Accessed: 2019-10-24.

[Ammar *et al.* 2006] Amine Ammar, Béchir Mokdad, Francisco Chinesta and Roland Keunings. *A New Family of Solvers for Some Classes of Multidimensional Partial Differential Equations Encountered in Kinetic Theory Modeling of Complex Fluids.* Journal of Non-Newtonian Fluid Mechanics, 2006.

[Ammar *et al.* 2007] Amine Ammar, Béchir Mokdad, Francisco Chinesta and Roland Keunings. *A new family of solvers for some classes of multidimensional partial differential equations encountered in kinetic theory modelling of complex fluids. Part II: Transient simulation using space-time separated representations.* Journal of Non-Newtonian Fluid Mechanics, **144**, 98–121, 2007.

[Amsallem & Farhat 2008] David Amsallem and Charbel Farhat. *Interpolation Method for Adapting Reduced-Order Models and Application to Aeroelasticity.* AIAA Journal, **46**, 1803–1813, 2008.

[Amsallem *et al.* 2014] David Amsallem, Matthew Zahr, Youngsoo Choi and Charbel Farhat. *Design optimization using hyper-reduced-order models.* Structural and Multidisciplinary Optimization, **51**, 919–940, 2014.

[Anandkumar *et al.* 2014] Animashree Anandkumar, Rong Ge, Daniel Hsu, Sham M. Kakade and Matus Telgarsky. *Tensor Decompositions for Learning Latent Variable Models.* Journal of Machine Learning Research, **15**, 2773–2832, 2014.

[Argerich 2020] C. Argerich. *Study and development of new acoustic technologies for nacelle products.* PhD thesis, Universitat Politecnica de Catalunya, 2020.

[Arthur & Vassilvitskii 2007] David Arthur and Sergei Vassilvitskii. *K-means++: The Advantages of Careful Seeding.* In Proceedings of the Eighteenth Annual ACM-SIAM Symposium on Discrete Algorithms, SODA '07, 1027–1035, Philadelphia, PA, USA, 2007. Society for Industrial and Applied Mathematics.

[Astrid *et al.* 2008] Patricia Astrid, Siep Weiland, Karen Willcox and Ton Backx. *Missing Point Estimation in Models Described by Proper Orthogonal Decomposition.* IEEE Transactions on Automatic Control, **53**, 2237–2251, 2008.

[Badías *et al.* 2019] Alberto Badías, Sarah Curtit, David González, Icíar Alfaro, Francisco Chinesta and Elías G. Cueto. *An augmented reality platform for interactive aerodynamic design and analysis.* International Journal for Numerical Methods in Engineering, **120**, 125–138, 2019.

[Badias *et al.* 2020a] Alberto Badias, Icíar Alfaro, David González, Francisco Chinesta and Elías Cueto. *MORPH-DSLAM: Model Order Reduction for PHysics-based Deformable SLAM.* CoRR, **abs/2009.00576**, 2020.

[Badías *et al.* 2020b] Alberto Badías, David González, Icíar Alfaro, Francisco Chinesta and Elías Cueto. *Real-time interaction of virtual and physical objects in mixed reality applications.* International Journal for Numerical Methods in Engineering, **121**, 3849–3868, 2020.

[Bai 2018] Gai Bai. *Numerical simulation and optimization for electromagnetic noises of permanent magnet synchronous motors in vehicles.* Journal of Vibroengineering, **20**, 2018.

[Barrault *et al.* 2004] M. Barrault, Cong Tu Nguyen, A. Patera and Yvon Maday. *An 'empirical interpolation' method: application to efficient reduced-basis discretization of partial differential equations.* Comptes rendus de l'Académie des sciences. Série I, Mathématique, **339-9**, 667–672, 2004.

[Bartlett 2015] A Bartlett. *Electrochemical Model-Based State of Charge and State of Health Estimation of Lithium-Ion Batteries.* PhD thesis, Ohio State University, 2015.

[Baudat & Anouar 2001] G. Baudat and F. Anouar. *Kernel-based methods and function approximation.* In IJCNN'01. International Joint Conference on Neural Networks. Proceedings (Cat. No.01CH37222), volume 2, 1244–1249 vol.2, 2001.

[Beddek 2012] Karim Beddek. *Propagation d'incertitudes dans les modèles éléments finis en électromagnétisme : application au contrôle non destructif par courants de Foucault.* PhD thesis, Ecole doctorale Sciences pour l'Ingenieur (Lille) - L2EP, 2012. Thèse de doctorat dirigée par Clénet, StéphaneLe Menach, Yvonnick et Moreau, Olivier Génie électrique Lille 1 2012.

[Ben Abdallah & Abdelfattah 2015] Wajih Ben Abdallah and Riadh Abdelfattah. *A generalized form of the InSAR phase unwrapping problem based on a compressed sensing technique.* In 2015 IEEE International Conference on Image Processing (ICIP), 3225–3229, 2015.

[Benner *et al.* 2015] Peter Benner, Serkan Gugercin and Karen Willcox. *A Survey of Projection-Based Model Reduction Methods for Parametric Dynamical Systems.* SIAM Review, **57**, 483–531, 2015.

[Bianchi 2005] Nicola Bianchi. Electrical machine analysis using finite elements. CRC Press Taylor & Francis Group, 2005.

[Bizeray *et al.* 2015] A.M. Bizeray, S. Zhao, S.R. Duncan and D.A. Howey. *Lithium-ion battery thermal-electrochemical model-based state estimation using orthogonal collocation and a modified extended Kalman filter.* Journal of Power Sources, **296**, 400 – 412, 2015.

[Blöecher *et al.* 2012] H.-L. Blöecher, M. Andres, C. Fischer, A. Sailer, M. Goppelt and J. Dickmann. *Impact of system parameter selection on radar sensor performance in automotive applications.* Advances in Radio Science, **10**, 33–37, 2012.

[Bognet *et al.* 2012] Brice Bognet, Felipe Bordeu, Francisco Chinesta, Adrien Leygue and Arnaud Poitou. *Advanced simulation of models defined in plate geometries: 3D solutions with 2D computational complexity.* Computer Methods in Applied Mechanics and Engineering, **201**, 1–12, 2012.

[Borzacchiello *et al.* 2019] Domenico Borzacchiello, Jose V. Aguado and Francisco Chinesta. *Non-intrusive Sparse Subspace Learning for Parametrized Problems.* Archives of Computational Methods in Engineering, **26**, 303–326, 2019.

[Breiman *et al.* 1984] L. Breiman, J. Friedman, C.J. Stone and R.A. Olshen. Classification and regression trees. Taylor & Francis, 1984.

[Breiman 2001] L. Breiman. *Random Forests.* Machine Learning, **45**, 5–32, 2001.

[Brunton & Kutz 2019] Steven L. Brunton and J. Nathan Kutz. Data-driven science and engineering: Machine learning, dynamical systems, and control. Cambridge University Press, 2019.

[Brunton *et al.* 2015] Steven Brunton, Joshua Proctor and J. Kutz. *Discovering governing equations from data: Sparse identification of nonlinear dynamical systems.* Proceedings of the National Academy of Sciences, **113**, 3932–3937, 2015.

[Brunton *et al.* 2016] Steven L. Brunton, Joshua L. Proctor and J. Nathan Kutz. *Discovering governing equations from data by sparse identification of nonlinear dynamical systems.* Proceedings of the National Academy of Sciences, 2016.

[Bui-Thanh *et al.* 2008] T. Bui-Thanh, K. Willcox and O. Ghattas. *Model Reduction for Large-Scale Systems with High-Dimensional Parametric Input Space.* SIAM J. Sci. Comput., **30**, 3270–3288, 2008.

[Buitrago *et al.* 2019] Santi Buitrago, Sebastian Blanch Boris and Jordi Romeu. *Imaging System for Automotive Radome Characterization.* In 2019 13th European Conference on Antennas and Propagation (EuCAP), 1–5, 2019.

[Bur *et al.* 2016] Nicolas Bur, Pierre Joyot, Chady Ghnatios, Pierre Villon, Elías Cueto and Francisco Chinesta. *On the use of model order reduction for simulating automated fibre placement processes.* Advanced Modeling and Simulation in Engineering Sciences, **3**, 4, 2016.

[Burges 1998] Christopher J.C. Burges. *A Tutorial on Support Vector Machines for Pattern Recognition.* Data Mining and Knowledge Discovery, **2**, 121–167, 1998.

[Cardillo & Caddemi 2019a] Emanuele Cardillo and Alina Caddemi. *Feasibility Study to Preserve the Health of an Industry 4.0 Worker: a Radar System for Monitoring the Sitting-Time.* In 2019 II Workshop on Metrology for Industry 4.0 and IoT (MetroInd4.0 IoT), 254–258, 2019.

[Cardillo & Caddemi 2019b] Emanuele Cardillo and Alina Caddemi. *Insight on Electronic Travel Aids for Visually Impaired People: A Review on the Electromagnetic Technology.* Electronics, **8**, 2019.

[Carlberg & Farhat 2008] Kevin Carlberg and Charbel Farhat. *A Compact Proper Orthogonal Decomposition Basis for Optimization-Oriented Reduced-Order Models.* volume 5964, 2008.

[Carlberg & Farhat 2011] K. Carlberg and C. Farhat. *A low-cost, goal-oriented 'compact proper orthogonal decomposition' basis for model reduction of static systems.* International Journal for Numerical Methods in Engineering, **86**, 381–402, 2011.

[Carlberg *et al.* 2013] Kevin Carlberg, Charbel Farhat, Julien Cortial and David Amsallem. *The GNAT method for nonlinear model reduction: Effective implementation and application to computational fluid dynamics and turbulent flows.* Journal of Computational Physics, **242**, 623–647, 2013.

[Chapman *et al.* 2017] Todd Chapman, Philip Avery, Pat Collins and Charbel Farhat. *Accelerated mesh sampling for the hyper reduction of nonlinear computational models.* International Journal for Numerical Methods in Engineering, **109**, 1623–1654, 2017.

[Chaqués Herraiz 2015] Gustavo Chaqués Herraiz. Diseño de dispositivos electromagnéticos mediante el uso de técnicas avanzadas de simulación y optimización numérica (pgd). Master's thesis, Universitat Politècnica de València, 2015.

[Chaturantabut & Sorensen 2010] Saifon Chaturantabut and D. Sorensen. *Nonlinear Model Reduction via Discrete Empirical Interpolation.* SIAM J. Sci. Comput., **32**, 2737–2764, 2010.

[Chinesta & Cueto 2014] F. Chinesta and E. Cueto. Pgd-based modeling of materials, structures and processes. Springer International Publishing, 2014.

[Chinesta & Ladevèze 2014] F. Chinesta and P. Ladevèze. Separated representations and pgd-based model reduction. Springer-Verlag Wien, 2014.

[Chinesta *et al.* 2010] F. Chinesta, A. Ammar and E. Cueto. *Recent Advances and New Challenges in the Use of the Proper Generalized Decomposition for Solving Multidimensional Models.* Arch Computat Methods Eng, **17**, 327–350, 2010.

[Chinesta *et al.* 2011] F. Chinesta, P. Ladeveze and E. Cueto. *A Short Review on Model Order Reduction Based on Proper Generalized Decomposition.* Arch Computat Methods Eng, **18**, 2011.

[Chinesta *et al.* 2013a] Francisco Chinesta, Roland Keunings and Adrien Leygue. The proper generalized decomposition for advanced numerical simulations: A primer. Springer Publishing Company, Incorporated, 2013.

[Chinesta *et al.* 2013b] Francisco Chinesta, Adrien Leygue, Felipe Bordeu, Elías Cueto, David Gonzalez, Amine Ammar and Antonio Huerta. *PGD-Based Computational Vademecum for Efficient Design, Optimization and Control.* Archives of Computational Methods in Engineering, **20**, 31 – 59, 2013.

[Chinesta *et al.* 2014] Francisco Chinesta, Adrien Leygue, Brice Bognet, Chady Ghnatios, Fabien Poulhaon, Felipe Bordeu, Anaïs Barasinski, Arnaud Poitou, Sylvain Chatel and Serge Maison-Le Poëc. *First steps towards an advanced simulation of composites manufacturing by automated tape placement.* International Journal of Material Forming, **7**, 81–92, 2014.

[Chinesta *et al.* 2017] Francisco Chinesta, Antonio Huerta, Gianluigi Rozza and Karen Willcox. Model reduction methods, 1–36. American Cancer Society, 2017.

[Chinesta *et al.* 2018] Francisco Chinesta, Elias Cueto, Emmanuelle Abisset-Chavanne, Jean Louis Duval and Fouad El Khaldi. *Virtual, Digital and Hybrid Twins: A New Paradigm in Data-Based Engineering and Engineered Data.* Archives of Computational Methods in Engineering, 2018.

[Chinesta *et al.* 2020] Francisco Chinesta, Elias Cueto, Emmanuelle Abisset-Chavanne, Jean Louis Duval and Fouad El Khaldi. *Virtual, digital and hybrid twins: a new paradigm in data-based engineering and engineered data.* Archives of computational methods in engineering, **27**, 105–134, 2020.

[Chkifa *et al.* 2014] Abdellah Chkifa, Albert Cohen and Christoph Schwab. *High-Dimensional Adaptive Sparse Polynomial Interpolation and Applications to Parametric PDEs.* Foundations of Computational Mathematics, **14**, 601–633, 2014.

[Cli 2015] *Paris Declaration on Electro-Mobility and Climate Change & Call to Action.* `https://unfccc.int/media/521376/paris-electro-mobility-declaration.pdf`, 2015. Accessed: 2019-10-24.

[Costantini *et al.* 2012] Mario Costantini, Fabio Malvarosa and Federico Minati. *A General Formulation for Redundant Integration of Finite Differences and Phase Unwrapping on a Sparse Multidimensional Domain.* IEEE Transactions on Geoscience and Remote Sensing, **50**, 758–768, 2012.

[Criminisi *et al.* 2011] Antonio Criminisi, Ender Konukoglu and Jamie Shotton. *Decision Forests for Classification, Regression, Density Estimation, Manifold Learning and Semi-Supervised Learning.* Technical report MSR-TR-2011-114, 2011.

[Criminisi *et al.* 2012] Antonio Criminisi, Jamie Shotton and Ender Konukoglu. *Decision Forests: A Unified Framework for Classification, Regression, Density Estimation, Manifold Learning and Semi-Supervised Learning.* Technical report 2-3, 2012.

[Cueto *et al.* 2014] E. Cueto, C. Ghnatios, F. Chinesta, N. Montes, F. Sanchez and A. Falco. *Improving computational efficiency in LCM by using computational geometry and model reduction techniques.* Key Engineering Materials, **611-612**, 339–343, 2014.

[Cueto *et al.* 2016] Elas Cueto, David Gonzlez and Icar Alfaro. Proper generalized decompositions: An introduction to computer implementation with matlab. Springer Publishing Company, Incorporated, 1st édition, 2016.

[D. Stetzel *et al.* 2015] Kirk D. Stetzel, Lukas L. Aldrich, M Trimboli and Gregory Plett. *Electrochemical state and internal variables estimation using a reduced-order physics-based model of a lithium-ion cell and an extended Kalman filter.* Journal of Power Sources, **278**, 2015.

[Darema 2015] Frederica Darema. *DDDAS, A Key Driver for Large-Scale-Big-Data and Large-Scale-Big-Computing.* Procedia Computer Science, **51**, 2463, 2015. International Conference On Computational Science, ICCS 2015.

[Dassault Systemes 2021] Dassault Systemes. *Dymola 2021 x*, 2021.

[de Almeida 2013] J. P. Moitinho de Almeida. *A basis for bounding the errors of proper generalised decomposition solutions in solid mechanics.* International Journal for Numerical Methods in Engineering, **94**, 961–984, 2013.

[Domenico *et al.* 2009] Domenico Di Domenico, Anna Stefanopoulou and Giovanni Fiengo. *PSM: Lithium-Ion Battery State of Charge (SOC) and Critical Surface Charge (CSC) Estimation using an Electrochemical Model-driven Extended Kalman and Filter.* ASME Journal of Dynamic Systems, Measurements and Control, 2009.

[Dowell & Hall 2001] Earl H Dowell and Kenneth C Hall. *Modeling of fluid-structure interaction.* Annual Review of Fluid Mechanics, **33**, 445–490, 2001.

[Doyle & Fuentes 2003] Marc Doyle and Yuris Fuentes. *Computer Simulations of a Lithium-Ion Polymer Battery and Implications for Higher Capacity Next-Generation Battery Designs.* Journal of The Electrochemical Society, **150**, A706–A713, 2003.

[Doyle *et al.* 1993] Marc Doyle, Thomas F. Fuller and John Newman. *Modeling of Galvanostatic Charge and Discharge of the Lithium/Polymer/Insertion Cell.* Journal of The Electrochemical Society, **140**, 1526–1533, 1993.

[Dumon *et al.* 2011] A. Dumon, C. Allery and A. Ammar. *Proper general decomposition (PGD) for the resolution of Navier–Stokes equations.* Journal of Computational Physics, **230**, 1387–1407, 2011.

[Dupont & Bouvet 2013] J.-B. Dupont and Philippe Bouvet. *Noise radiated by an electrical powertrain: multiphysical simulation.* In CFM2013, 2013. CFM 2013.

[Dupont & Saucy 2019] Jean-Baptiste Dupont and Henri Saucy. Noise radiated by electric motors – simulation process and overview of the optimization approaches, 107–121. Springer Vieweg, Wiesbaden, 2019.

[Eivazi *et al.* 2021] Hamidreza Eivazi, Luca Guastoni, Philipp Schlatter, Hossein Azizpour and Ricardo Vinuesa. *Recurrent neural networks and Koopman-based frameworks for temporal predictions in a low-order model of turbulence.* International Journal of Heat and Fluid Flow, **90**, 108816, 2021.

[Erichson *et al.* 2019] N. Benjamin Erichson, Lionel Mathelin, J. Nathan Kutz and Steven L. Brunton. *Randomized Dynamic Mode Decomposition.* SIAM Journal on Applied Dynamical Systems, **18**, 1867–1891, 2019.

[Everson & Sirovich 1995] R. Everson and L. Sirovich. *Karhunen-Loeve procedure for gappy data.* Journal of the Optical Society of America A, **12**, 1657–1664, 1995.

[Falco & Nouy 2012] A. Falco and A. Nouy. *Proper generalized decomposition for nonlinear convex problems in tensor Banach spaces.* Numer. Math., **121**, 503–530, 2012.

[Farhat *et al.* 2015] Charbel Farhat, Todd Chapman and Philip Avery. *Structure-preserving, stability, and accuracy properties of the energy-conserving sampling and weighting method for the hyper reduction of nonlinear finite element dynamic models.* International Journal for Numerical Methods in Engineering, **102**, 1077–1110, 2015.

[Farzamfar *et al.* 2016] M. Farzamfar, Anouar Belahcen, Paavo Rasilo, Stephane Clenet and A. Pierquin. *Model order reduction of electrical machines with multiple inputs.* 1882–1887, 2016.

[Fish & Belytschko 2007] Jacob Fish and Ted Belytschko. A first course in finite elements. John Wiley & Sons, Inc., USA, 2007.

[Forman *et al.* 2012] Joel C. Forman, Scott J. Moura, Jeffrey L. Stein and Hosam K. Fathy. *Genetic identification and fisher identifiability analysis of the Doyle–Fuller–Newman model from experimental cycling of a LiFePO4 cell.* Journal of Power Sources, **210**, 263–275, 2012.

[Forrester *et al.* 2008] A.I.J. Forrester, A. Sobester and A.J. Keane. Engineering design via surrogate modelling: A practical guide. John Wiley & Sons, Ltd, 2008.

[Fritzen *et al.* 2016] F. Fritzen, Bernhard Haasdonk, D. Ryckelynck and S. Schöps. *An algorithmic comparison of the Hyper-Reduction and the Discrete Empirical Interpolation Method for a nonlinear thermal problem.* ArXiv, **abs/1610.05029**, 2016.

[F.R.S. 1901] Karl Pearson F.R.S. *LIII. On lines and planes of closest fit to systems of points in space.* The London, Edinburgh, and Dublin Philosophical Magazine and Journal of Science, **2**, 559–572, 1901.

[Fuller *et al.* 1994] Thomas F. Fuller, Marc Doyle and John Newman. *Simulation and Optimization of the Dual Lithium Ion Insertion Cell.* Journal of The Electrochemical Society, **141**, 1–10, 1994.

[Gao *et al.* 2016] Xiaomeng Gao, Ehsaneh Shahhaidar, Christopher Stickley and Olga Boric-Lubecke. *Respiratory Angle of Thoracic Wall Movement During Lung Ventilation.* IEEE Sensors Journal, **16**, 5195–5201, 2016.

[Ghnatios *et al.* 2012a] C. Ghnatios, A. Ammar, A. Cimetiere, A. Hamdouni, A. Leygue and F. Chinesta. *First steps in the space separated representation of models defined in complex domains.* In 11th Biennial Conference on Engineering Systems Design and Analysis, volume 1, 37–42, 2012.

[Ghnatios *et al.* 2012b] Ch. Ghnatios, F. Masson, A. Huerta, A. Leygue, E. Cueto and F. Chinesta. *Proper Generalized Decomposition based dynamic data-driven control of thermal processes.* Computer Methods in Applied Mechanics and Engineering, **213-216**, 29–41, 2012.

[Ghnatios *et al.* 2017] Chady Ghnatios, Christian H. Mathis, Rok Simic, Nicholas D. Spencer and Francisco Chinesta. *Modeling soft, permeable matter with the proper generalized decomposition (PGD) approach, and verification by means of nanoindentation.* Soft Matter, **13**, 4482–4493, 2017.

[Ghnatios *et al.* 2019a] C. Ghnatios, E. Abisset, A. Ammar, E. Cueto, J.-L. Duval and F. Chinesta. *Advanced separated spatial representations for hardly separable domains.* Computer Methods in Applied Mechanics and Engineering, **354**, 802–819, 2019.

[Ghnatios *et al.* 2019b] C. Ghnatios, N. Montes, H. Tertrais, J.L. Duval, E. Abisset-Chavanne, A. Falco and F. Chinesta. *Towards parametric RTM processes: The interpolative mapping.* American Institute of Physics proceedings, 2019.

[Ghnatios *et al.* 2021] C. Ghnatios, E. Cueto, A. Falco, J.-L. Duval and F. Chinesta. *Spurious-free interpolations for non-intrusive PGD-based parametric solutions: Application to composites forming processes.* International journal of material forming, **14**, 83–95, 2021.

[Ghnatios 2012] C. Ghnatios. *Simulation avancée des problèmes thermiques rencontrés lors de la mise en forme des composites.* PhD thesis, Ecole Centrale Nantes, 2012.

[Gieras *et al.* 2006] Jacek F. Gieras, Chong Rui Wang and Joseph C. S. Lai. Noise of polyphase electric motors. CRC Press Taylor & Francis Group, 2006.

[Gonzáles *et al.* 2012] David Gonzáles, Françoise Masson, Fabien Poulhaon, Adrien Leygue, Elías Cueto and Francisco Chinesta. *Proper Generalized Decomposition based dynamic data driven inverse identification.* Mathematics and Computers in Simulation, **82**, 1677 – 1695, 2012.

[González *et al.* 2017] David González, Alberto Badías, Icíar Alfaro, Francisco Chinesta and Elías Cueto. *Model order reduction for real-time data assimilation through Extended Kalman Filters.* Computer Methods in Applied Mechanics and Engineering, **326**, 679 – 693, 2017.

[González *et al.* 2018a] D. González, F. Chinesta and E. Cueto. *Thermodynamically consistent data-driven computational mechanics.* Continuum Mechanics and Thermodynamics, **DOI: 10.1007/s00161-018-0677-z**, 2018.

[Gonzalez *et al.* 2018b] David Gonzalez, Francisco Chinesta and Elias Cueto. *Learning corrections for hyperelastic models from data.* Submitted, 2018.

[Goodfellow *et al.* 2016] Ian Goodfellow, Yoshua Bengio and Aaron Courville. Deep learning. MIT Press, 2016. `http://www.deeplearningbook.org`.

[Guastoni *et al.* 2020] L. Guastoni, A. Güemes, A. Ianiro, S. Discetti, P. Schlatter, H. Azizpour and R. Vinuesa. *Convolutional-network models to predict wall-bounded turbulence from wall quantities*, 2020.

[Haas & Ellermann 2017] Stefan Haas and K. Ellermann. *Development and Analysis of Radial Force Waves in Electrical Rotating Machines.* Technische Mechanik, **37**, 218–225, 2017.

[Ham *et al.* 2004] Jihun Ham, Daniel D. Lee, Sebastian Mika and Bernhard Schölkopf. *A Kernel View of the Dimensionality Reduction of Manifolds.* In Proceedings of the Twenty-first International Conference on Machine Learning, ICML '04, 47–, New York, NY, USA, 2004. ACM.

[Hariharan *et al.* 2018] Krishnan S. Hariharan, Piyush Tagade and Dr. Sanoop Ramachandran. Mathematical modeling of lithium batteries - from electrochemical models to state estimator algorithms. Springer International Publishing, 2018.

[Harter *et al.* 2016] Marlene Harter, Jürgen Hildebrandt, Andreas Ziroff and Thomas Zwick. *Self-Calibration of a 3-D-Digital Beamforming Radar System for Automotive Applications With Installation Behind Automotive Covers.* IEEE Transactions on Microwave Theory and Techniques, **64**, 2994–3000, 2016.

[Hastie *et al.* 2009] T. Hastie, R. Tibshirani and J. H. Friedman. The elements of statistical learning: data mining, inference, and prediction. New York: Springer., 2009.

[Henneron & Clenet 2014] Thomas Henneron and Stéphane Clenet. *Proper Generalized Decomposition method applied to solve 3D Magneto Quasistatic Field Problems coupling with External Electric Circuits.* IEEE Transactions on Magnetics, **51**, 1–10, 2014.

[Henneron & Clenet 2017] Thomas Henneron and Stephane Clenet. *Application of the Proper Generalized Decomposition to Solve MagnetoElectric Problem.* IEEE Transactions on Magnetics, **PP**, 1–4, 2017.

[Hernandez *et al.* 2021a] Quercus Hernandez, Alberto Badías, David González, Francisco Chinesta and Elías Cueto. *Deep learning of thermodynamics-aware reduced-order models from data.* Computer Methods in Applied Mechanics and Engineering, **379**, 113763, 2021.

[Hernández *et al.* 2021b] Quercus Hernández, Alberto Badías, David González, Francisco Chinesta and Elías Cueto. *Structure-preserving neural networks.* Journal of Computational Physics, **426**, 109950, 2021.

[Hernández *et al.* 2014] J.A. Hernández, J. Oliver, A.E. Huespe, M.A. Caicedo and J.C. Cante. *High-performance model reduction techniques in computational multiscale homogenization.* Computer Methods in Applied Mechanics and Engineering, **276**, 149–189, 2014.

[Hey *et al.* 2009] Tony Hey, Stewart Tansley and Kristin Tolle. The fourth paradigm: Data-intensive scientific discovery. Microsoft Research, 2009.

[Hofmann *et al.* 2008] Thomas Hofmann, Bernhard Schölkopf and Alexander J. Smola. *Kernel Methods in Machine Learning.* The Annals of Statistics, **36**, 1171–1220, 2008.

[Hu *et al.* 2012] Xiaosong Hu, Shengbo Li and Huei Peng. *A comparative study of equivalent circuit models for Li-ion batteries.* Journal of Power Sources, **198**, 359 – 367, 2012.

[Huang *et al.* 2016] Wenbing Huang, Lele Cao, Fuchun Sun, Deli Zhao, Huaping Liu and Shanshan Yu. *Learning Stable Linear Dynamical Systems with the Weighted Least Square Method.* In Proceedings of the Twenty-Fifth International Joint Conference on Artificial Intelligence, IJCAI'16, 1599–1605. AAAI Press, 2016.

[Huang *et al.* 2017] Wenbing Huang, Mehrtash Harandi, Tong Zhang, Lijie Fan, Fuchun Sun and Junzhou Huang. *Efficient Optimization for Linear Dynamical Systems with Applications to Clustering and Sparse Coding.* In I. Guyon, U. V. Luxburg, S. Bengio, H. Wallach, R. Fergus, S. Vishwanathan and R. Garnett, editors, Advances in Neural Information Processing Systems 30, 3444–3454. Curran Associates, Inc., 2017.

[Ibáñez Pinillo *et al.* 2018] Rubén Ibáñez Pinillo, Emmanuelle Abisset-Chavanne, Amine Ammar, David González, Elias Cueto, Antonio Huerta, Jean Louis Duval and Francisco Chinesta. *A Multidimensional Data-Driven Sparse Identification Technique: The Sparse Proper Generalized Decomposition.* Complexity, **2018**, 1–11, 2018.

[Ibanez Pinillo 2019] Ruben Ibanez Pinillo. *Advanced physics-based and data-driven strategies.* PhD thesis, 2019. Thèse de doctorat dirigée par Chinesta, Francisco et Huerta, Antonio Génie mécanique Ecole centrale de Nantes 2019.

[Ibanez *et al.* 2019] R Ibanez, E Abisset-Chavanne, E Cueto, A Ammar, J-L Duval and F Chinesta. *Some applications of compressed sensing in computational mechanics: model order reduction, manifold learning, data-driven applications and nonlinear dimensionality reduction.* Computational Mechanics, **64**, 1259–1271, 2019.

[Ida & Bastos 1992] Nathan Ida and J. P. A. Bastos. Electromagnetics and calculation of fields. Springer-Verlag New York, 1992.

[Islam *et al.* 2020] Shekh Md Mahmudul Islam, Olga Borić-Lubecke, Yao Zheng and Victor M. Lubecke. *Radar-Based Non-Contact Continuous Identity Authentication.* Remote Sensing, **12**, 2020.

[Jack & Mecrow 1990] A. G. Jack and B. C. Mecrow. *Methods for magnetically nonlinear problems involving significant hysteresis and eddy currents.* IEEE Transactions on Magnetics, **26**, 424–429, 1990.

[Jean-Baptiste & Bouvet 2012] Dupont Jean-Baptiste and Pascal Bouvet. *Multiphysics Modelling to Simulate the Noise of an Automotive Electric Motor.* In 7th International Styrian Noise, Vibration & Harshness Congress: The European Automotive Noise Conference. SAE International, 2012.

[Kaarnioja 2013] Vesa Kaarnioja. *Smolyak Quadrature.* mathesis, University of Helsinki, 2013.

[Kaiser *et al.* 2018] Eurika Kaiser, J Nathan Kutz and Steven L Brunton. *Discovering conservation laws from data for control.* arXiv preprint arXiv:1811.00961, 2018.

[Kambhatla & Leen 1997] Nanda Kambhatla and Todd Leen. *Dimension Reduction by Local Principal Component Analysis.* Neural Computation, **9**, 1493–1516, 1997.

[Karhunen 1946] K. Karhunen. *Uber lineare methoden in der wahrscheinlichkeitsrechnung.* Ann. Acad. Sci. Fennicae, ser. Al. Math. Phys., **37**, 1946.

[Kawashima & Matsuyama 2005] Hiroaki Kawashima and Takashi Matsuyama. *Hierarchical Clustering of Dynamical Systems Based on Eigenvalue Constraints.* In Sameer Singh, Maneesha Singh, Chid Apte and Petra Perner, editors, Pattern Recognition and Data Mining, 229–238, Berlin, Heidelberg, 2005. Springer Berlin Heidelberg.

[Kevrekidis & Samaey 2010] Yannis Kevrekidis and Giovanni Samaey. *Equation-free modeling.* Scholarpedia, **5**, 4847, 2010.

[Kirchdoerfer & Ortiz 2016] T. Kirchdoerfer and M. Ortiz. *Data-driven computational mechanics.* Computer Methods in Applied Mechanics and Engineering, **304**, 81 – 101, 2016.

[Kumar *et al.* 2017] D. Kumar, S. Kottalgi, T. Sambharam and P. Mandloi. *A multiphysics optimization approach to design low noise and light weight electric powertrain noise, vibration and harshness (NVH) prediction of electric powertrain using finite element analysis (FEA) and optimization.* In IECON 2017 - 43rd Annual Conference of the IEEE Industrial Electronics Society, 1692–1697, 2017.

[Kunisch, Karl & Volkwein, Stefan 2010] Kunisch, Karl and Volkwein, Stefan. *Optimal snapshot location for computing POD basis functions.* ESAIM: M2AN, **44**, 509–529, 2010.

[Kutz *et al.* 2016] J. Nathan Kutz, Steven L. Brunton, Bingni W. Brunton and Joshua L. Proctor. Dynamic mode decomposition: Data-driven modeling of complex systems. SIAM-Society for Industrial and Applied Mathematics, USA, 2016.

[Kutz 2013] J. Nathan Kutz. Data-driven modeling & scientific computation: Methods for complex systems & big data. Oxford University Press, Inc., New York, NY, USA, 2013.

[L. Lee *et al.* 2012a] James L. Lee, Andrew Chemistruck and Gregory Plett. *Discrete-Time Realization of Transcendental Impedance Functions, with Application to Modeling Spherical Solid Diffusion.* Journal of Power Sources, **206**, 367–377, 2012.

[L. Lee *et al.* 2012b] James L. Lee, Andrew Chemistruck and Gregory Plett. *One-dimensional physics-based reduced-order model of lithium-ion dynamics.* Journal of Power Sources, **220**, 430–448, 2012.

[L. Lee *et al.* 2014] James L. Lee, Lukas L. Aldrich, Kirk D. Stetzel and Gregory Plett. *Extended operating range for reduced-order model of lithium-ion cells.* Journal of Power Sources, **255**, 85–100, 2014.

[Ladevèze & Chamoin 2011] Pierre Ladevèze and Ludovic Chamoin. *On the verification of model reduction methods based on the Proper Generalized Decomposition.* Computer Methods in Applied Mechanics and Engineering, **200**, 2032–2047, 2011.

[Ladevèze *et al.* 2001] Pierre Ladevèze, Lionel Arnaud, Philippe Rouch and Claude Blanzé. *The variational theory of complex rays for the calculation of medium-frequency vibrations.* Engineering Computations, **vol. 18**, pp. 193–214, 2001.

[Ladevèze 1989] P. Ladevèze. *The large time increment method for the analyze of structures with nonlinear constitutive relation described by internal variables.* C. R. Acad. Sci. Paris, **309**, 1095–1099, 1989.

[Ladeveze 1999] Pierre Ladeveze. Nonlinear computational structural mechanics. Springer-Verlag New York, 1999.

[Laughlin & Pines 2000] R. B. Laughlin and David Pines. *The Theory of Everything.* Proceedings of the National Academy of Sciences, **97**, 28–31, 2000.

[LeCun *et al.* 2015] Y. LeCun, Y. Bengio and G. Hinton. *Deep learning.* Nature, **521**, 436–444, 2015.

[Lee & Verleysen 2007] J.A. Lee and M. Verleysen. Nonlinear dimensionality reduction. Springer-Verlag New York, 2007.

[Lloyd 2006] S. Lloyd. *Least Squares Quantization in PCM.* IEEE Trans. Inf. Theor., **28**, 129–137, 2006.

[Loève 1963] M. M. Loève. Probability theory. The University Series in Higher Mathematics, 3rd ed. Van Nostrand, Princeton, NJ, 1963.

[Lorenz 1963] Edward N Lorenz. *Deterministic nonperiodic flow.* Journal of the Atmospheric Sciences, **20**, 130–141, 1963.

[Ly & Tran 2001] H.V. Ly and H.T. Tran. *Modeling and control of physical processes using Proper Orthogonal Decomposition.* Journal of Mathematical and Computer Modeling, **33**, 223–236, 2001.

[M. Sudheer Kumar & Apparao 2015] S. Harish M. Sudheer Kumar and A.Dhanamjay Apparao. *Design of PID controller via novel model order reduction technique.* IJARCCE, **4**, 278–281, 2015.

[Malik 2017] M.H. Malik. *Reduced Order Modeling for Smart Grids' Simulation and Optimization.* PhD thesis, Ecole Centrale Nantes, 2017.

[Mallat 2016] Stéphane Mallat. *Understanding deep convolutional networks.* Philosophical Transactions of the Royal Society A: Mathematical, Physical and Engineering Sciences, **374**, 20150203, 2016.

[Martín *et al.* 2020] Clara Argerich Martín, Arnulfo Carazo Méndez, Olivier Sainges, Emilie Petiot, Anais Barasinski, Mathieu Piana, Louis Ratier and Francisco Chinesta. *Empowering Design Based on Hybrid TwinTM: Application to Acoustic Resonators.* Designs, **4**, 2020.

[MathWorks 2020] MathWorks. *Documentation unwrap function.* `https://uk.mathworks.com/help/matlab/ref/unwrap.html`, 2020. Accessed: 2020-09-30.

[Mazgaonkar *et al.* 2019] Numair Mazgaonkar, Mazharul Chowdhury and Linus Francis Fernandes. *Design of Electric Motor Using Coupled Electromagnetic and Structural Analysis and Optimization.* In SAE Technical Paper. SAE International, 2019.

[Meeker 2018] D. C. Meeker. *Finite Element Method Magnetics User's Manual*, version 4.2 édition, 2018.

[Meyer & Matthies 2003] M. Meyer and H. G. Matthies. *Efficient model reduction in non-linear dynamics using the Karhunen-Loève expansion and dual-weighted-residual methods.* Computational Mechanics, **31**, 179–191, 2003.

[Modesto *et al.* 2015] David Modesto, Sergio Zlotnik and Antonio Huerta. *Proper generalized decomposition for parameterized Helmholtz problems in heterogeneous and unbounded domains: Application to harbor agitation.* Computer Methods in Applied Mechanics and Engineering, **295**, 127–149, 2015.

[Moitra 2018] Ankur Moitra. Algorithmic aspects of machine learning. Cambridge University Press, 2018.

[Moura *et al.* 2014] Scott Moura, N Chaturvedi and M Krstic. *Adaptive PDE Observer for Battery SOC/SOH Estimation via an Electrochemical Model.* ASME Journal of Dynamic Systems, Measurement, and Control, **136**, 011015–011026, 2014.

[Moura *et al.* 2017] Scott J. Moura, Federico Bribiesca Argomedo, Reinhardt Klein, Anahita Mirtabatabaei and Miroslav Krstic. *Battery State Estimation for a Single Particle Model With Electrolyte Dynamics.* IEEE Transactions on Control Systems Technology, **25**, 453–468, 2017.

[Moya *et al.* 2019] B. Moya, D. Gonzalez, I Alfaro, F. Chinesta and E. Cueto. *Learning slosh dynamics by means of data.* Computational Mechanics, **64**, 511–523, 2019.

[Moya *et al.* 2020a] Beatriz Moya, Iciar Alfaro, David Gonzalez, Francisco Chinesta and Elías Cueto. *Physically sound, self-learning digital twins for sloshing fluids.* PLOS ONE, **15**, 1–16, 2020.

[Moya *et al.* 2020b] Beatriz Moya, Alberto Badías, Icíar Alfaro, Francisco Chinesta and Elías Cueto. *Digital twins that learn and correct themselves.* International Journal for Numerical Methods in Engineering, 2020.

[Moya *et al.* 2021] Beatriz Moya, Alberto Badias, David Gonzalez, Francisco Chinesta and Elias Cueto. *Physics perception in sloshing scenes with guaranteed thermodynamic consistency*, 2021.

[Nadal *et al.* 2015a] E. Nadal, F. Chinesta, P. Díez, F.J. Fuenmayor and F.D. Denia. *Real time parameter identification and solution reconstruction from experimental data using the Proper Generalized Decomposition.* Computer Methods in Applied Mechanics and Engineering, **296**, 113–128, 2015.

[Nadal *et al.* 2015b] E Nadal, A Leygue, F Chinesta, M Beringhier, J J Ródenas and F J Fuenmayor. *A separated representation of an error indicator for the mesh refinement process under the proper generalized decomposition framework.* Computational mechanics, **55**, 251–266, 2015.

[Niroomandi *et al.* 2008] S. Niroomandi, I. Alfaro, E. Cueto and F. Chinesta. *Real-time deformable models of non-linear tissues by model reduction techniques.* Computer Methods and Programs in Biomedicine, **91**, 223 – 231, 2008.

[Niroomandi *et al.* 2013] Siamak Niroomandi, Icíar Alfaro, David González, Elías Cueto and Francisco Chinesta. *Model order reduction in hyperelasticity: a proper generalized decomposition approach.* International Journal for Numerical Methods in Engineering, **96**, 129–149, 2013.

[Norouzian *et al.* 2016] Fatemeh Norouzian, Rui Du, Marina Gashinova, Edward Hoare, Costas Constantinou, Mike Lancaster, Peter Gardner and Mikhail Cherniakov. *Signal reduction due to radome contamination in low-THz automotive radar.* In 2016 IEEE Radar Conference (RadarConf), 1–4, 2016.

[OpenStreetMap contributors 2017] OpenStreetMap contributors. *Planet dump retrieved from https://planet.osm.org* . `https://www.openstreetmap.org`, 2017.

[P. Jiang *et al.* 2020] P. P. Jiang, Q. Zhou and X. Shao. Surrogate model-based engineering design and optimization. Springer, 2020.

[Panel 2006] National Science Foundation (NSF) Blue Ribbon Panel. *Report on Simulation-Based Engineering Science.* `https://www.nsf.gov/pubs/reports/sbes_final_report.pdf`, 2006. Accessed: 2020-09-30.

[Papritz & Stein 1999] A. Papritz and A. Stein. Surrogate model-based engineering design and optimization. Stein A., Van der Meer F., Gorte B. (eds) Spatial Statistics for Remote Sensing. Remote Sensing and Digital Image Processing, vol 1. Springer, Dordrecht, 1999.

[Parsa *et al.* 2018] Behnoosh Parsa, Keshav Rajasekaran, Franziska Meier and Ashis Gopal Banerjee. *A Hierarchical Bayesian Linear Regression Model with Local Features for Stochastic Dynamics Approximation.* CoRR, **abs/1807.03931**, 2018.

[Patankar 1980] Suhas V Patankar. Numerical heat transfer and fluid flow. Series on Computational Methods in Mechanics and Thermal Science. Hemisphere Publishing Corporation (CRC Press, Taylor & Francis Group), 1980.

[Peng & Li 2019] Zhengyu Peng and Changzhi Li. *Portable Microwave Radar Systems for Short-Range Localization and Life Tracking: A Review.* Sensors, **19**, 2019.

[Pérez 2013] Pareja Pérez. Modelización de puestas a tierra en parques eólicos para frecuencia 50 hz y descargas de rayo. Master's thesis, Universitat Politècnica de València, 2013.

[Pfeiffer & Biebl 2009] Florian Pfeiffer and Erwin M. Biebl. *Inductive Compensation of High-Permittivity Coatings on Automobile Long-Range Radar Radomes.* IEEE Transactions on Microwave Theory and Techniques, **57**, 2627–2632, 2009.

[Pile *et al.* 2018] R. Pile, E. devillers and J. Le Besnerais. *Comparison of Main Magnetic Force Computation Methods for Noise and Vibration Assessment in Electrical Machines.* IEEE Transactions on Magnetics, **54**, 1–13, 2018.

[Plett 2004] Gregory L. Plett. *Extended Kalman filtering for battery management systems of LiPB-based HEV battery packs: Part 2. Modeling and identification.* Journal of Power Sources, **134**, 262 – 276, 2004.

[Quaranta 2019] Giacomo Quaranta. *Efficient simulation tools for real-time monitoring and control using model order reduction and data-driven techniques.* PhD thesis, 2019. Thèse de doctorat dirigée par Chinesta, Francisco et Huerta, Antonio Génie mécanique Ecole centrale de Nantes 2019.

[Quesada *et al.* 2018] C. Quesada, I. Alfaro, D. González, F. Chinesta and E. Cueto. *Haptic simulation of tissue tearing during surgery.* International Journal for Numerical Methods in Biomedical Engineering, **34**, e2926, 2018. e2926 cnm.2926.

[Raissi *et al.* 2017a] Maziar Raissi, Paris Perdikaris and George E. Karniadakis. *Physics Informed Deep Learning (Part I): Data-driven Solutions of Nonlinear Partial Differential Equations.* CoRR, **abs/1711.10561**, 2017.

[Raissi *et al.* 2017b] Maziar Raissi, Paris Perdikaris and George E. Karniadakis. *Physics Informed Deep Learning (Part II): Data-driven Discovery of Nonlinear Partial Differential Equations.* CoRR, **abs/1711.10566**, 2017.

[Raissi *et al.* 2019] M. Raissi, P. Perdikaris and G.E. Karniadakis. *Physics-informed neural networks: A deep learning framework for solving forward and inverse problems involving nonlinear partial differential equations.* Journal of Computational Physics, **378**, 686–707, 2019.

[Robinson & García 2015] Lucas Darby Robinson and R. Edwin García. *Dualfoil.py: Porous Electrochemistry for Rechargeable Batteries*, 2015.

[Rodriguez & Li 2019] Daniel Rodriguez and Changzhi Li. *Sensitivity and Distortion Analysis of a 125-GHz Interferometry Radar for Submicrometer Motion Sensing Applications.* IEEE Transactions on Microwave Theory and Techniques, **67**, 5384–5395, 2019.

[Rohling 2006] H. Rohling. *Some radar topics: waveform design, range CFAR and target recognition.* In Jim Byrnes and Gerald Ostheimer, editors, Advances in Sensing with Security Applications, 293–322, Dordrecht, 2006. Springer Netherlands.

[Roweis & Saul 2000] Sam T. Roweis and Lawrence K. Saul. *Nonlinear Dimensionality Reduction by Locally Linear Embedding.* Science, **290**, 2323–2326, 2000.

[Rozza *et al.* 2008] G. Rozza, D.B.P. Huynh and A.T. Patera. *Reduced basis approximation and a posteriori error estimation for affinely parametrized elliptic coercive partial differential equations – application to transport and continuum mechanics.* Archives of Computational Methods in Engineering, **15/3**, 229–275, 2008.

[Ryckelynck 2005] D. Ryckelynck. *A priori hyperreduction method: an adaptive approach.* Journal of Computational Physics, **202**, 346–366, 2005.

[Salon 1995] S. J. Salon. Finite element analysis of electrical machines. New York : Springer Science+Business Media, 1995.

[Sancarlos-González *et al.* 2017] Abel Sancarlos-González, Manuel pineda sanchez, Ruben Puche-Panadero, Angel Sapena-Bañó, Martin Riera-Guasp, J. Martinez-Roman, Juan Perez-Cruz and Jose Roger-Folch. *Application of the parametric proper generalized decomposition to the frequency-dependent calculation of the impedance of an AC line with rectangular conductors.* Open Physics, **15**, 2017.

[Sancarlos *et al.* 2020] Abel Sancarlos, Morgan Cameron, Andreas Abel, Elias Cueto, Jean-Louis Duval and Francisco Chinesta. *From ROM of Electrochemistry to AI-Based Battery Digital and Hybrid Twin.* Archives of Computational Methods in Engineering, 1–37, 2020.

[Sancarlos 2017] Abel Sancarlos. Cálculo de parámetros en líneas eléctricas utilizando métodos numéricos avanzados (pgd). Master's thesis, Universitat Politècnica de València, 2017.

[Santhanagopalan & White 2006] Shriram Santhanagopalan and Ralph E. White. *Online estimation of the state of charge of a lithium ion cell.* Journal of Power Sources, **161**, 1346 – 1355, 2006.

[Sapena-Bano *et al.* 2019] A. Sapena-Bano, F. Chinesta, M. Pineda-Sanchez, J.V. Aguado, D. Borzacchiello and R. Puche-Panadero. *Induction machine model with finite element accuracy for condition monitoring running in real time using hardware in the loop system.* International Journal of Electrical Power & Energy Systems, **111**, 315–324, 2019.

[Sathyan *et al.* 2020] Sabin Sathyan, Ugur Aydin and Anouar Belahcen. *Acoustic Noise Computation of Electrical Motors Using the Boundary Element Method.* Energies, **13**, 2020.

[Schapire 1990] R.E Schapire. *The strength of weak learnability.* Machine Learning, **5**, 197–227, 1990.

[Schölkopf *et al.* 1998] Bernhard Schölkopf, Alex Smola and Klaus-Robert Müller. *Nonlinear Component Analysis as a Kernel Eigenvalue Problem.* Neural Computation, **10**, 1299–1319, 1998.

[Schmid *et al.* 2011] P.J. Schmid, L. Li, M.P. Juniper and O. Pust. *Applications of the dynamic mode decomposition.* Theoretical and Computational Fluid Dynamics, **25**, 249–259, 2011.

[Schmid 2010] P.J. Schmid. *Dynamic mode decomposition of numerical and experimental data.* J. Fluid. Mech., 2010.

[Schmid 2011] P.J. Schmid. *Application of the dynamic mode decomposition to experimental data.* Exp Fluids, 2011.

[Schnabel *et al.* 2013] Raik Schnabel, Raphael Hellinger, Dirk Steinbuch, Joachim Selinger, Michael Klar and Bernhard Lucas. *Development of a mid range automotive radar sensor for future driver assistance systems.* International Journal of Microwave and Wireless Technologies, **5**, 15–23, 2013.

[Schölkopf *et al.* 1999] Bernhard Schölkopf, Alexander J. Smola and Klaus-Robert Müller. Kernel principal component analysis, 327–352. MIT Press, Cambridge, MA, USA, 1999.

[Schwarz 1978] Gideon Schwarz. *Estimating the Dimension of a Model.* Annals Statist., **6**, 461–464, 1978.

[Sempey *et al.* 2009] A. Sempey, C. Inard, C. Ghiaus and C. Allery. *Fast simulation of temperature distribution in air conditioned rooms by using proper orthogonal decomposition.* Building and Environment, **44**, 280–289, 2009.

[Shanker & Zebker 2010] A. Piyush Shanker and Howard Zebker. *Edgelist phase unwrapping algorithm for time series InSAR analysis.* J. Opt. Soc. Am. A, **27**, 605–612, 2010.

[Shiffrin *et al.* 2020] Richard M Shiffrin, Danielle S Bassett, Nikolaus Kriegeskorte and Joshua B Tenenbaum. *The brain produces mind by modeling.* Proceedings of the National Academy of Sciences, **117**, 29299–29301, 2020.

[Smith & Wang 2006] Kandler Smith and Chao-Yang Wang. *Solid-state diffusion limitations on pulse operation of a lithium ion cell for hybrid electric vehicles.* Journal of Power Sources, **161**, 628 – 639, 2006.

[Smith 2010] K. A. Smith. *Electrochemical Control of Lithium-Ion Batteries [Applications of Control].* IEEE Control Systems Magazine, **30**, 18–25, 2010.

[Stateczny *et al.* 2019] Andrzej Stateczny, Witold Kazimierski, Daria Gronska-Sledz and Weronika Motyl. *The Empirical Application of Automotive 3D Radar Sensor for Target Detection for an Autonomous Surface Vehicle's Navigation.* Remote Sensing, **11**, 1–18, 2019.

[Steinbaeck *et al.* 2017] Josef Steinbaeck, Christian Steger, Gerald Holweg and Norbert Druml. *Next generation radar sensors in automotive sensor fusion systems.* In 2017 Sensor Data Fusion: Trends, Solutions, Applications (SDF), 1–6, 2017.

[Torchio *et al.* 2016] Marcello Torchio, Lalo Magni, Bhushan Gopaluni, Richard Braatz and D.M. Raimondo. *LIONSIMBA: A Matlab Framework Based on a Finite Volume Model Suitable for Li-Ion Battery Design, Simulation, and Control.* Journal of The Electrochemical Society, **163**, A1192–A1205, 2016.

[Udrescu *et al.* 2020] Silviu-Marian Udrescu, Andrew Tan, Jiahai Feng, Orisvaldo Neto, Tailin Wu and Max Tegmark. *AI Feynman 2.0: Pareto-optimal symbolic regression exploiting graph modularity.* arXiv preprint arXiv:2006.10782, 2020.

[Vasanelli *et al.* 2017] Claudia Vasanelli, Rahul Batra and Christian Waldschmidt. *Optimization of a MIMO radar antenna system for automotive applications.* In 2017 11th European Conference on Antennas and Propagation (EUCAP), 1113–1117, 2017.

[Wang *et al.* 2016] Qian Wang, Bin Jiang, Bo Li and Yuying Yan. *A critical review of thermal management models and solutions of lithium-ion batteries for the development of pure electric vehicles.* Renewable and Sustainable Energy Reviews, **64**, 106 – 128, 2016.

[Wasserman 2018] Larry Wasserman. *Topological Data Analysis.* Annual Review of Statistics and Its Application, **5**, 501–532, 2018.

[Winner *et al.* 2016] H. Winner, S. Hakuli, F. Lotz and C. Singer. Handbook of driver assistance systems. Springer International Publishing, 2016.

[Winter *et al.* 2015] Michael Winter, Sascha Moser, Stefan Schoenewolf, Julian Taube and Hans-Georg Herzog. *Average model of a synchronous half-bridge DC/DC converter considering losses and dynamics.* In Proceedings of the 11th International Modelica Conference, 2015.

[Wu *et al.* 2008] X. Wu, V. Kumar, J. Ross Quinlan, J. Ghosh, Q. Yang, H. Motoda, McLachlan, A. Ng, B. Liu, Yu, Zhou, M. Steinbach, Hand and D. Steinberg. *Top 10 algorithms in data mining.* Knowledge and information systems, **14**, 1–37, 2008.

[Xu *et al.* 2018] Xueping Xu, Qinkai Han and Fulei Chu. *Review of Electromagnetic Vibration in Electrical Machines.* Energies, **11**, 1779, 2018.

[Zhang & Zha 2003] Zhenyue Zhang and Hongyuan Zha. *Principal Manifolds and Nonlinear Dimension Reduction via Local Tangent Space Alignment.* SIAM J. Sci. Comput., **26**, 2003.

[Zlotnik *et al.* 2015] Sergio Zlotnik, Pedro Díez, David Modesto and Antonio Huerta. *Proper generalized decomposition of a geometrically parametrized heat problem with geophysical applications.* International Journal for Numerical Methods in Engineering, **103**, 737–758, 2015.